Information quantique photonique haute fidélité : protocoles et contrôle de circuits universels

Andreas Fyrillas

université PARIS-SACLAY

High-fidelity photonic quantum information: protocols and universal circuit control

Information quantique photonique haute fidélité: protocoles et contrôle de circuits universels

Thèse de doctorat de l'université Paris-Saclay

École doctorale n° 572, Ondes et Matière (EDOM)
Spécialité de doctorat: Physique
Graduate School : Physique. Référent : Faculté des Sciences d'Orsay

Thèse préparée dans l'unité de recherche Centre de Nanosciences et de Nanotechnologies, C2N, UMR 9001 (Université Paris-Saclay, CNRS), sous la direction de **Nadia BELABAS**, chargée de recherche au C2N, et le co-encadrement de **Olivier KREBS**, directeur de recherche au CNRS.

Thèse soutenue à Paris-Saclay, le 21 mars 2025, par

Andreas FYRILLAS

Composition du jury

Membres du jury avec voix délibérative

Rachel GRANGE Professeure à Eidgenössische Technische Hochschule Zürich	Présidente
Stefanie BARZ Professeure à University of Stuttgart	Rapporteuse & Examinatrice
Val ZWILLER Professeur à Kungliga Tekniska högskolan Royal Institute of Technology	Rapporteur & Examinateur
Alberto PERUZZO Responsable informatique quantique à Qubit Pharmaceuticals (Paris, France), entreprise	Examinateur
Benoît VALIRON Professeur adjoint à Université Paris-Saclay	Examinateur

THESE DE DOCTORAT

NNT : 2025UPASP021

université PARIS-SACLAY | ÉCOLE DOCTORALE Ondes et matière (EDOM)

Titre: Information quantique photonique haute fidélité: protocoles et contrôle de circuits universels
Mots clés: Circuit photonique intégré; Traitement de l'information quantique photonique; Apprentissage machine; Contrôle optimal

Résumé: Dans cette thèse de doctorat, nous contribuons au domaine de la photonique quantique intégrée pour le traitement de l'information quantique, notamment via la caractérisation, le contrôle et les applications de circuits photoniques intégrés (PIC). Les PICs permettent une manipulation compacte et stable de la lumière quantique. Nous interfaçons des sources brillantes de photons uniques à base de boites quantiques semi-conductrices avec des PICs en silice ou en nitrure de silicium, afin d'implémenter des protocoles d'information quantique.

Nous réalisons d'abord des protocoles quantiques à l'aide de PICs spécialisés. Avec deux photons uniques et une intrication post-sélectionnée encodée en chemin, nous démontrons pour la première fois la génération sur puce d'aléa certifié. Grâce à la stabilité du système optique et la calibration fine des déphaseurs du PIC, nous obtenons un débit de 21 bits certifiés par seconde sur une acquisition de 94 heures. Avec la manipulation précise et stable de quatre qubits photoniques, nous générons un état 4-GHZ post-sélectionné sur puce intégrée avec une fidélité de 86 % et une pureté de 76 %, établissant ainsi de nouvelles références pour la génération et la tomographie d'états photoniques de haute fidélité.

En passant aux architectures PIC universelles, nous relevons le défi du contrôle optimal d'interféromètres comportant plusieurs centaines de composants intégrés. Nous développons une technique de caractérisation assistée par apprentissage machine, qui identifie avec précision les imperfections du PIC telles que la diaphonie thermique entre déphaseurs, les erreurs de réflectivité des séparateurs de faisceaux et les pertes en sortie. L'estimation de ces paramètres permet de mettre en œuvre des compensations efficaces d'imperfections de fabrication et d'atteindre expérimentalement une fidélité moyenne en amplitude record de 99,77 % entre les opérations unitaires photoniques ciblées et celles implémentées. Le PIC utilisé pour cette démonstration est un interféromètre de Clements sur 12 modes, l'un des plus grands PIC disponibles, comprenant 132 séparateurs de faisceaux et 126 déphaseurs.

Enfin, en tirant parti de l'interprétabilité de notre modèle d'apprentissage machine, nous explorons la physique des PICs afin de cibler un contrôle des PICs limité par le bruit. Nous affinons les modèles de diaphonie pour les PICs, en tenant compte des variations des propriétés physiques des guides d'ondes intégrés lorsque des déphaseurs adjacents sont activés. Nous introduisons une méthode générale de compensation de diaphonie, et proposons un critère graphique permettant d'identifier les schémas d'interféromètres robustes vis-à-vis de la diaphonie. Il s'agit d'une étape importante pour le passage à l'échelle du nombre de qubits photoniques manipulés à l'aide d'interféromètres spécialisés. Notre contribution garantit une précision optimale des opérations appliquées sur la lumière.

Nos résultats ouvrent la voie à des architectures quantiques photoniques plus fiables, rapprochant ainsi l'objectif technologique d'un ordinateur quantique photonique tolérant aux erreurs. Les avancées réalisées en caractérisation et en contrôle optimal de PICs, grâce à une technique que nous avons brevetée reposant sur l'apprentissage machine, dépassent le cadre de la photonique quantique et contribuent également à l'essor de la photonique intégrée classique.

Title: High-fidelity photonic quantum information: protocols and universal circuit control

Keywords: Photonic integrated circuit; Photonic quantum information processing; Machine learning; Optimal control

Abstract: In this PhD thesis, we advance the field of integrated photonics for quantum information processing, focusing on the characterization, control, and applications of photonic integrated circuits (PICs). PICs enable the compact and stable manipulation of light. Integrated photonics is crucial for realizing scalable, fault-tolerant photonic quantum computers. We interface bright single-photon sources based on semiconductor quantum dots with silica or silicon nitride PICs, to implement quantum information protocols.

We firstly perform quantum protocols using specialized PICs. Harnessing two single photons and postselected path-encoded entanglement, we perform the first demonstration of on-chip certified randomness generation. Through stabilization of the optical setup and accurate calibration of the PIC phase shifters, we achieve a certified bit rate of 21 bits/s on a 94-hour long acquisition. Scaling up to the precise and stable manipulation of four photonic qubits, we further generate and perform the full tomography of a postselected 4-GHZ state with 86 % fidelity and 76 % purity, setting new benchmarks for high-fidelity photonic state generation.

Shifting to universal PIC architectures, we address the challenge of optimally controlling large-scale interferometers. We develop a machine learning-assisted characterization technique, that accurately identifies PIC imperfections such as thermal crosstalk between phase shifters, beamsplitter reflectivity errors and output losses. The knowledge of these parameters opens the door to effective hardware error mitigation strategies. We experimentally achieve a record average amplitude fidelity of 99.77 % between targeted and implemented unitary operations on light. The hardware PIC used for this demonstration is a 12-mode Clements interferometer, one of the biggest available PICs, featuring 132 beamsplitters and 126 thermo-optic phase shifters.

Finally, leveraging the interpretability of our machine learning model, we explore the physics of PICs in order to target noise-limited PIC control. We refine crosstalk models for PICs by accounting for crosstalk modifying the physical properties of waveguides. We introduce a novel, more general crosstalk cancellation framework and propose a graphical criterion to certify the robustness of interferometer designs against crosstalk. This is a significant step towards scaling the number of processed photonic qubits using specialized interferometer meshes, while maintaining high accuracy of implemented operations on light.

Our results pave the way for more reliable and scalable photonic quantum architectures, narrowing the technological gap required for an error-tolerant photonic quantum computer. The advances in characterization and optimal control of PICs, thanks to a method that we patented relying on machine learning, go beyond quantum photonics and also contribute to the development of classical integrated photonics.

Contents

Acknowledgments

First and foremost, I would like to express my deepest gratitude to my jury for taking the time to review this work and for attending the defense in person. Your engagement and feedback have been invaluable.

I owe a tremendous debt of gratitude to Nadia Belabas, whose unwavering support and exceptionally insightful guidance have shaped every step of this journey. Nadia has mentored me not only through the subtleties of quantum optics but also in becoming a better scientist, colleague, and person. Her dedication and thoroughness created a synergy that enabled us to achieve things I will always be proud of, and deeply miss.

This thesis would not have been possible without the mentorship and encouragement of Nicolas Maring and Jean Senellart. They ensured that I had the time, tools, and freedom to pursue high-quality research on Quandela hardware, and I am truly thankful for their trust.

I am also grateful to Valérian Giesz, Pascale Senellart, and Niccolo Somaschi for offering me the opportunity to join this remarkable adventure with a PhD on a topic I could not have dreamed better.

Many thanks to Shane Mansfield and Olivier Krebs, for always making sure things ran smoothly throughout my doctoral years.

To Céline and Michel, thank you for being the crème de la crème of HR teams. Your support made a real difference.

Thank you also to the EDOM doctoral school, Nadia Chapiteau, Denis Boiron, and Laurent Vivien, for the administrative assistance and support.

To my colleagues

I am incredibly lucky to have worked with such inspiring and supportive colleagues. In no particular order:

To Nicolas: countless hours solving impossible problems (P=NP, Jacobian, Omega...) over junk food, poke bowls and questionable drinks have become some of my favorite memories from this PhD. It's an honor to count you among both my colleagues and my close friends.

Grégoire: please never change your sense of humor. Discussing quantum, music and muscles with you is always insightful and instructive. May your vertical jump one day reign supreme.

A special thanks to Mathias Pont, whose energy, skills in experimental optics, and pedagogy have shaped this research more than words can say.

Ozan, I've come to terms with the fact that I will neither have bigger arms, nor play the guitar as well as you, nor align optical setups with the utmost precision like you do.

Antoine, you were the first person to supervise me at C2N, and left a durable impression by possibly traumatizing me permanently. That is quite an accomplishment!

Valentin, the BG among BGs. From baby PhD students to full-fledged BG doctors, it's been a ride. Never stop living for the camera.

Edouard, you are my favorite colleague on the Massytadel (paragon + 5). You significantly leveled up my programming skills, at the cost of exposing me to jokes so bad, they loop back into brilliance.

Simone, thank you for your infinite everyday kindness and patience with my repetitive questions on integrated photonics. I'll never forget that you see everything as a capacitor... and that you stole my desk.

Marion: you call me a theorist, but offer free food. Acceptable.

Eric: you also call me a theorist, no food involved. Unacceptable.

Fatima and Guillaume P., my dear early-bird office comrades, how could I ever forget those quiet, focused mornings?

Boris: I can certify that our signaling is flawless. No loopholes here. 10/10 recommend measuring PR boxes with you.

Pierre-Emmanuel, thank you for appreciating my memes at their true value. If only it could be the same for my experimental skills.

Alexandre, you never missed a chance to praise the beauty of the plots on my screen, thank you for that.

Filipa, our Bellevue exploration during the conference is a highlight I won't forget.

Special thanks to my amazing interns—Kayleigh, Elianor, Boubacar, Olivier, Hugo, and Robin. Your presence made this journey all the more rewarding and exciting.

To the rest of the Quandela team who make it a joy to come to work every day: Anne-Claire, Alexia, Aurélien, Cassandre, Eliott, Emilio, Guillaume M., Hugo, Jean-Jacques, Johan, Luka, Marie, Mario, Maxence, Maxime, Moad, Nico, Petr, Raksha, Rayan "buddy", Sébastien, Selena (print('poney')), Sonia, Stephen, Timothée, Tommaso, and Vivien. Thank you.

To my C2N colleagues, Daniel, Dario, Etienne, George, Hêlio, Hubert, Juan, Lara, Loïc and Thibaut. Thank you for the lively and insightful weekly journal clubs.

PhD life also means conferences. Thank you to my conference buddy Frank and his team for organizing a surprise birthday celebration in Rotterdam, what a memory!

Thanks to Antoine, Les Houches Spring School will always live in my mind as an intense table tennis training camp. Good times!

To my friends

To my friends who stayed by my side through every high and low, thank you for grounding me.

Dihia and Augustin: spending time with you and making insane music is the secret ingredient to my farina. I was very touched by your presence and kindness during these years. Ready for the next trek to the stars?

Elise and Mathieu, is there a more perfect combination than spinning cups of tea, fast food at midnight with B2O blasting in the car? Maybe if you ventilate créances, sure.

Irène, thank you for the endless stream of memes on Star Wars, quantum mechanics and muscle building.

Alexandre May: getting lost in Cité U with you and your bike has been unexpectedly therapeutic.

Fabien, don't sprawl at les Mouilles. There, I said it, the place is famous now.

Alexandre Mercier and Julien, best saturday gaming nights of my life, even though we are not very strong at strategy games

Nicolas, Gregoire, Edouard, Valentin, hello again in this section.

To my family

Words cannot express my gratitude to my family for their unconditional love and encouragement.

I am forever grateful to my parents, who gave me the opportunity to follow my dreams under the best conditions one could ever dream of. Thank you for pushing me during my studies, piano lessons and sports practice. Your unconditional love and support, especially in difficult moments, means everything to me. And mom's food as well.

I am equally grateful to my sister Cassiani, whose presence I could not live without and who has objectively the best sense of humor in the world. Just poke a hole in it.

To Michel: thank you for making weekends in Livry-Gargan feel like home, through our endless conversations and shared passions. It's offline!

To my uncle Yotis: thank you for teaching me the value of perseverance and the courage to follow one's own path.

To my aunt Myra and uncle Serge: thank you for your deep, grounding life lessons.

To uncle Jean, aunt Michaela, Sophie, Myra and Anna, thank you for your warmth and endless hospitality.

To my grandmothers, thank you for feeding me with the best apple pies in the world.

Synthèse en français

Dans cette thèse de doctorat, nous contribuons au domaine de la photonique quantique intégrée pour le traitement de l'information quantique. Nous nous intéressons en particulier à l'utilisation expérimentale de circuits photoniques intégrés (PICs), qui permettent de manipuler la lumière quantique de manière compacte, stable et passant à l'échelle. Nos travaux s'inscrivent dans une approche alliant la génération de lumière quantique à partir de sources de photons uniques, la mise en œuvre de protocoles d'information quantique, le contrôle précis et fiable de la lumière quantique à l'aide de PICs, ainsi que la compréhension physique des limitations de ces dispositifs optiques miniaturisés.

Nous réalisons dans un premier temps des expériences à l'aide de PICs spécialisés, optimisés pour des tâches quantiques spécifiques. En interfaçant des sources brillantes de photons uniques, issues de boîtes quantiques semi-conductrices, avec des PICs en silice, nous démontrons la capacité de ces dispositifs à réaliser des protocoles quantiques avec un haut degré de stabilité et de précision. Nous réalisons notamment, pour la première fois, la génération d'aléa quantique certifié sur puce, en exploitant l'intrication post-sélectionnée de deux photons uniques encodés en chemin. Grâce à une calibration fine des quatre déphaseurs intégrés et la stabilité accrue obtenue pour l'expérience, nous obtenons un débit de 21 bits certifiés par seconde sur une acquisition continue de 94 heures.

Nous poursuivons avec la génération et la caractérisation d'un état intriqué multipartite de type GHZ à quatre photons, obtenus par post-sélection sur un PIC à 8 modes comportant 8 déphaseurs. Grâce à la qualité de la source de photons, à la stabilité de la plateforme optique et au contrôle précis du circuit, nous réalisons une tomographie complète de l'état, atteignant une fidélité de 86 % et une pureté de 76 %, établissant ainsi un nouveau record pour la génération d'états 4-GHZ en optique intégrée. Ces résultats soulignent le potentiel des PICs spécialisés pour la mise en œuvre de protocoles quantiques avec une haute fidélité.

Dans une seconde partie, nous abordons les circuits photoniques dits universels, capables de réaliser toute opération d'optique linéaire sur les photons en entrée. Ces circuits, plus génériques et beaucoup plus complexes, sont particulièrement prometteurs pour les applications de calcul quantique à court terme, comme l'échantillonnage bosonique. Afin de relever les défis associés au contrôle de tels PICs, qui peuvent contenir plusieurs centaines de composants (jusqu'à 132 séparateurs de faisceaux et 126 déphaseurs dans nos expériences), nous développons une méthode de caractérisation assistée par apprentissage machine. Cette approche, que nous avons brevetée, combine des modèles physiques détaillés avec des algorithmes d'optimisation alimentés par des données expérimentales. Elle permet de mesurer avec précision les imperfections du circuit, notamment la diaphonie thermique entre les déphaseurs, les erreurs de fabrication des séparateurs de faisceaux, ainsi que les pertes de transmission.

En exploitant ces paramètres reconstruits, nous parvenons à compenser efficacement les défauts du circuit, et à implémenter expérimentalement des matrices unitaires avec une fidélité moyenne en amplitude record de 99,77 %. Cette démonstration est réalisée sur un interféromètre universel à 12 modes de type Clements, l'un des plus grands circuits photoniques intégrés jamais utilisés dans ce contexte. Ce PIC a fait partie d'un dispositif quantique accessible via le cloud, qui a servi de plateforme de test pour différentes applications de traitement quantique de l'information.

Dans la dernière partie de la thèse, nous approfondissons la compréhension des limitations physiques fondamentales affectant le contrôle des PICs. En particulier, nous développons une modélisation plus fine de la diaphonie thermique, qui prend en compte les effets sur les guides d'ondes sans composants actifs, négligés

dans les modèles de la littérature. À partir de ce modèle étendu, nous introduisons une méthode générale de compensation de la diaphonie et proposons un critère graphique permettant d'identifier les topologies d'interféromètres robustes à cet effet indésirable. Ce cadre théorique permet d'orienter la conception de circuits spécialisés résistants à la diaphonie, une étape cruciale pour la mise à l'échelle des architectures photoniques.

Cette thèse propose une démarche expérimentale complète allant de la génération de qubits photoniques à leur manipulation précise dans des circuits complexes, jusqu'à la compréhension et la correction des limitations physiques de ces dispositifs. Les résultats obtenus ouvrent la voie à des architectures photoniques quantiques plus fiables, constituant un pas important vers un ordinateur quantique photonique tolérant aux erreurs. Par ailleurs, les avancées proposées en caractérisation et en contrôle optimal de PICs, via des techniques de modélisation et d'apprentissage machine, trouvent également des applications en combinant photonique intégrée et lumière classique, contribuant ainsi au développement global de la photonique intégrée.

Glossary and abbreviations

Abbreviation / Notation	Meaning
CNOT	Controlled-NOT
C-QRNG	Certified quantum random number generation / generator
CZ	Controlled-Z
$g^{(2)}(0)$	Normalized 2$^{\text{nd}}$-order correlation at zero delay (see Section I.3.1.B)
GHZ	Greenberger–Horne–Zeilinger
HOM	Hong-Ou-Mandel
M_s	Wave-packet overlap (see Section I.3.1.C)
MZI	Mach-Zehnder interferometer
PIC	Photonic integrated circuit *(in this manuscript, designates integrated linear-optical circuits for on-chip light manipulation)*
PS	Phase shifter
QI	Quantum information
QRNG	Quantum random number generation / generator
SPDC	Spontaneous parametric down-conversion
V_{HOM}	HOM visibility (see Section I.3.1.C)

Quantities with hats indicate matrices and operators in Chapter I, while they refer to predicted quantities in Chapters III and IV.

Contributions

Research publications

2023

- [1] Heurtel, N., **Fyrillas, A.**, Gliniasty, G. de, Bihan, R.L., Malherbe, S., Pailhas, M., Bertasi, E., Bourdoncle, B., Emeriau, P.-E., Mezher, R., Music, L., Belabas, N., Valiron, B., Senellart, P., Mansfield, S., Senellart, J., 2023. **Perceval: A Software Platform for Discrete Variable Photonic Quantum Computing.** Quantum 7, 931.

  https://doi.org/10.22331/q-2023-02-21-931

- [2] Maring, N., **Fyrillas, A.**, Pont, M., Ivanov, E., Bertasi, E., Valdivia, M., Senellart, J., 2023. **One Nine Availability of a Photonic Quantum Computer on the Cloud Toward HPC Integration**, in: 2023 IEEE International Conference on Quantum Computing and Engineering (QCE). Presented at the 2023 IEEE International Conference on Quantum Computing and Engineering (QCE), pp. 112–116.

  https://doi.org/10.1109/QCE57702.2023.10193

2024

- [3] **Fyrillas, A.**, Bourdoncle, B., Maïnos, A., Emeriau, P.-E., Start, K., Margaria, N., Morassi, M., Lemaître, A., Sagnes, I., Stepanov, P., Au, T.H., Boissier, S., Somaschi, N., Maring, N., Belabas, N., Mansfield, S., 2024. **Certified Randomness in Tight Space**. PRX Quantum 5, 020348.

  https://doi.org/10.1103/PRXQuantum.5.020348

- [4] Pont, M., Corrielli, G., **Fyrillas, A.**, Agresti, I., Carvacho, G., Maring, N., Emeriau, P.-E., Ceccarelli, F., Albiero, R., Dias Ferreira, P.H., Somaschi, N., Senellart, J., Sagnes, I., Morassi, M., Lemaître, A., Senellart, P., Sciarrino, F., Liscidini, M., Belabas, N., Osellame, R., 2024. **High-fidelity four-photon GHZ states on chip.** npj Quantum Inf 10, 1–7.

  https://doi.org/10.1038/s41534-024-00830-z

- [5] Maring, N., **Fyrillas, A.**, Pont, M., Ivanov, E., Stepanov, P., Margaria, N., Hease, W., Pishchagin, A., Lemaître, A., Sagnes, I., Au, T.H., Boissier, S., Bertasi, E., Baert, A., Valdivia, M., Billard, M., Acar, O., Brieussel, A., Mezher, R., Wein, S.C., Salavrakos, A., Sinnott, P., Fioretto, D.A., Emeriau, P.-E., Belabas, N., Mansfield, S., Senellart, P., Senellart, J., Somaschi, N., 2024. **A versatile single-photon-based quantum computing platform.** Nat. Photon. 1–7.

  https://doi.org/10.1038/s41566-024-01403-4

- [6] **Fyrillas, A.**, Faure, O., Maring, N., Senellart, J., Belabas, N., 2024. **Scalable machine learning-assisted clear-box characterization for optimally controlled photonic circuits.** Optica, OPTICA 11, 427–436.

  https://doi.org/10.1364/OPTICA.512148

- [7] (In preparation, included in App. E) **Fyrillas, A.**, Heurtel, N., Piacentini, S., Maring, N., Senellart, J., Belabas, N. **Resource-efficient crosstalk mitigation for the high-fidelity operation of photonic integrated circuits with induced phase shifters**

Patents

- **Method and system for characterization of a photonic circuit** (filing in progress)

Open-access code

- **2-mode Grover's search algorithm.** Introductory notebook for `Perceval`.
  `https://perceval.quandela.net/docs/v0.11/notebooks/2-mode_Grover_algorithm.html`

Software[1]

- **Unravel**, graphical real-time single-photon source characterization (see App. A).
- **PhotoGrad**, Python package for PIC calibration using machine-learning (see Chap. III).

Conferences

2022

- **Bristol Quantum Information Technologies Workshop 2022** (poster) Device-independent on-chip quantum random number generation with a bright and stable single-photon source. Bristol, UK. 25 - 28 April 2022.
- **OPTIQUE Nice 2022** (poster) Device-independent on-chip quantum random number generation with a bright and stable single-photon source. Nice, France. 4 - 8 July 2022.
- **Quantum Engineering, Fundamental Aspects to Applications 13** (poster) Device-independent on-chip quantum random number generation with a bright and stable single-photon source. Palaiseau, France. 16 - 18 November 2022.

2023

- **IEEE Quantum Week 2023** (contributed talk) One nine availability of a photonic quantum computer on the cloud toward HPC integration. Bellevue, USA. 17 - 22 September 2023.

2024

- **QUANTUMatter 2024** (contributed talk) High-fidelity quantum information with machine learning-characterized SiN photonic circuits. San Sebastian, Spain. 07 - 10 May 2024.
- **Quantum 2.0** (contributed talk) High-fidelity quantum information with machine learning-characterized photonic circuits. Rotterdam, Netherlands. 23 - 27 June 2024.

[1] Property of Quandela.

Internship supervisions

2021

- **Kayleigh Start**, M2, 3 months. Randomness extraction with the Toeplitz hashing algorithm.

2022

- **Elianor Hoffmann**, M1, 3 months. Experimental characterization of a 12-mode Clements interferometer.
- **Boubacar Ngom**, L2, 1 month. Motorized control of polarization.

2023

- **Olivier Faure**, M1, 6 months. Algorithmic generation of characterization protocols.

2024

- **Hugo Wei**, L3, 2 months. Advanced unitary matrix compilation.
- **Robin Le Meur**, M1, 6 months. Adaptive crosstalk characterization.

Context, motivation and outline of the work

Quantum information (QI) processing represents a transformative paradigm shift in computational methods, promising to solve specific problems considered intractable for classical computers. By leveraging the distinctive features of quantum mechanics, QI processing enables tasks such as factorization and quantum system simulations [8] to be performed exponentially faster than by classical methods. QI processing also opens the door to higher standards of cryptographic security and certification [9]. However, realizing scalable and fault-tolerant quantum computers is a major scientific challenge, that can be addressed on various physical platforms, such as superconducting qubits [10], trapped ions [11] and neutral atoms, each with its own specificities and technological challenges to overcome.

Among these platforms, photonics has emerged as a viable platform for QI processing [12, 13], with already several demonstrations of quantum advantage [14, 15, 16]. Photons, as carriers of quantum information, provide several compelling advantages such as mostly coherent interactions with the environment, preserving the purity of quantum states. Photons are also a natural suit for high-speed transmission, making them ideal for implementing quantum communication protocols.

In addition, photonics benefits from centuries of acquired know-how in engineering, manipulation and manufacturing of optical equipment. The practical implementation of optical circuits requiring hundreds of perfectly aligned low-loss free-space components remains however a daunting endeavor. A decade of advances in photonic integrated circuits (PICs) now allows for the miniaturization and integration of complex free-space optical systems on a single chip, providing the scalability and stability necessary for manipulating large-scale photonic systems [17, 18]. However, photonic quantum computing with PICs faces certain challenges. The manipulation of photons for quantum gates, circuits, and entanglement requires precise control over integrated components such as phase shifters and beamsplitters [19, 20]. Accurately controlling PICs by compensating internal imperfections to precisely implement targeted operations on light is not a straightforward process [21, 22, 23, 24].

Furthermore, the overall optical transmission of the system, from photon emission to detection, plays a pivotal role in scaling QI processing experiments to larger numbers of qubits. Indeed, the rate at which an n-photon computation is performed scales like T^n, with T the overall optical transmission, because all n photons must be successfully detected. Consequently, the development of ultra-low-loss integrated platforms [25, 26] and high-efficiency detectors [27] are a necessity. The brightness of single-photon sources, that is their rate of emission, plays also an essential role. Most photonic qubits in the litterature are generated from probabilistic single-photon sources, with fundamental limitations imposed on the brightness [28]. QI protocols with such sources rarely exceed the four-qubit regime [29, 30, 31]. Significant progress has been made in bright on-demand sources [32, 33], enabling to perform QI processing with more photons [34, 35, 5].

This thesis explores various aspects of photonic QI processing, focusing on the experimental challenges of harnessing photonic qubit systems for QI protocols, which includes the accurate control of PICs and the operation of optical setups on large time scales. The outline of the manuscript is as follows:

- Chapter I: **QI processing with photonic integrated circuits**.
  This chapter provides an introduction to the fundamental principles of QI processing, setting the stage for the experimental results presented in subsequent chapters. We also cover single-photon sources and integrated photonics, which constitute the backbone of the hardware used in this thesis.

- Chapter II: **Small-scale dedicated circuits for QI processing: Certified randomness generation and entangled state tomography**.
  The first part of this thesis focuses on quantum information protocols using specialized PICs, i.e. dedicated to a specific set of tasks. We begin by generating and manipulating path-encoded qubit states, entangled by postselection and controlled through arbitrary single-qubit gates on PICs. A key achievement in this section is the demonstration of certified quantum random number generation (C-QRNG) using Bell states generated on a 4-mode PIC featuring 4 reconfigurable phase shifters. This experiment represents the first on-chip certified randomness generation, delivering a certified bit rate of 21 bits per second in a 94-hour experimental acquisition. These results, published in [3], mark a significant milestone in the use of integrated photonics for secure QI processing tasks.

  Building on this work, we proceed to the generation and manipulation of a high-fidelity post-selected 4-photon Greenberger-Horne-Zeilinger (GHZ) state. This experiment, performed on a dedicated 8-mode PIC with 8 phase shifters, achieved full quantum state tomography with a state fidelity of 86 % and a purity of 76 %. The experiment was completed in approximately 50 hours, surpassing prior benchmarks in integrated platforms due to the stability of our optical setup and the brightness of the single-photon source, as reported in [4]. Together, these achievements demonstrate the potential of specialized PICs for performing complex quantum information tasks with high fidelity and stability, provided that a high-quality single-photon source operation, robust setup motorization, and accurate control of the PIC are ensured.

- Chapter III: **Towards high-fidelity photonic QI processing: circuit characterization and control using machine learning**.
  In this chapter, we transition from specialized to universal photonic circuits. Universal circuits are particularly useful for near-term quantum computing tasks, consisting in sampling from the output distribution of an implemented unitary matrix. These universal PICs, far more complex than their specialized counterparts, comprise interconnected beamsplitters and phase shifters enabling the implementation of any unitary matrix [36, 37, 38]. To tackle the control challenges posed by these circuits, we introduce a machine learning-based characterization process that we patented and that combines machine learning with physical models. By using a fully modeled virtual replica of the physical PIC, we retrieve critical physical parameters and achieve a 99.77 % amplitude fidelity on implemented unitary matrices with respect to the target, in a 12-mode Clements interferometer with 126 phase shifters. This showcases high-fidelity photonic quantum computing on large-scale devices. Our results on characterization are reported in [6]. The characterized PIC was then built into a photonic quantum device accessible on the cloud, demonstrating beyond-state-of-the-art results in QI processing published in [5] and [2].

- Chapter IV: **Targeting noise-limited circuit control with physical model extensions**.
  The final chapter delves into the physics of photonic circuits, to refine the physical model of our machine learning-assisted PIC characterization. We introduce an improved physical model for describing phase shifter crosstalk in PICs, accounting for crosstalk effects on waveguides without components. Additionally, we develop a framework to fully mitigate crosstalk in this new model, leading to the discovery of a graphical criterion for certifying

the resilience of interferometer meshes against crosstalk. Our findings are reported in [7] (in preparation, included in App. E).

I - Quantum information (QI) processing with photonic integrated circuits

> I'm not interested in color. It's light I'm after.
>
> Mark Rothko

In this PhD thesis, we investigate experimental aspects photonic quantum information (QI) using integrated circuits, focusing on the manipulation and control of quantum states of light. Throughout this work, we use **on-demand quantum dot-based single-photon sources** interfaced with **reconfigurable integrated linear optical circuits**, allowing for precise, stable and compact manipulation of photonic states. For reliable photon detection, high-efficiency **superconducting nanowire single-photon detectors** are employed throughout our experiments.

This chapter details the essential concepts that underpin our research. In Section I.1, we introduce the key principles of QI, starting with the transition from classical bits to qubits and highlighting the unique properties of quantum systems. Section I.2 delves into the quantum description of light, culminating with the photonic realization of a qubit. The generation of photonic qubits relies on bright single-photon sources that produce pure and indistinguishable single photons, which are discussed in Section I.3. Section I.4 presents the working principles of photonic integrated circuits, a fundamental resource for implementing scalable and reconfigurable QI protocols. Finally, I.5 provides an overview of the state of the art in photonic QI with integrated circuits, and introduces the main photonic QI computing paradigms.

I.1 - Foundations and formalism of QI

Quantum information (QI) explores the use of quantum systems as novel means for encoding and processing information. According to the axioms of quantum mechanics [39], the state space of a quantum system is a complex **Hilbert space**, that is an inner product space with a complete metric space structure. As a result, QI operates within a more sophisticated mathematical framework compared to classical information theory [40], whose foundations and original framework rests on discrete random variables.

In Section I.1.1, we introduce the formalism for single-qubit systems. Section I.1.2 delves into multi-qubit systems, emergence of nonclassicality and multi-qubit gates. We discuss universal sets of gates in Section I.1.3. Finally, Section I.1.4 concludes by summarizing the distinctive characteristics of QI compared to classical information processing. We use the Dirac formalism and assume familiarity with quantum mechanics [39] and linear algebra [41].

I.1.1 - From bits to qubits

Classical information processing is usually formalized in terms of **bits**: digits that can assume the value 0 or 1. The rationale for a binary computing system is that representing in a classical computer a bit state by a low (< 0.8 V) or high (> 2 V) voltage protects the apparatus against spurious electrical noise, which could flip the bit state [42] and corrupt the process execution. We discuss this aspect further in Chapter III.

Similarly, the basic information storage unit of QI is the **qubit**, a two-level quantum mechanical system with logical basis states $|0\rangle$ and $|1\rangle$ (**computational basis**). **Pure** single-qubit states, that is linear combinations of the basis states, are expressed as

$$\left|\psi\right\rangle = \alpha_0 \left|0\right\rangle + \alpha_1 \left|1\right\rangle \tag{I.1}$$

with $|\alpha_0|^2 + |\alpha_1|^2 = 1$. Pure states represent a system that is nonclassically "simultaneously" in two basis states. In contrast, **mixed** states describe a situation where a system is in one of the basis states, but the specific state is not known. Mixed states are formalized in terms of a **density matrix**, which provides the most general description of a quantum system. From the density matrix, we can compute the **purity** of a state, that quantifies its departure from a pure state. The density matrix formalism is particularly important for treating open quantum systems and understanding the loss of purity in quantum systems due to environmental interactions, a phenomenon known as **decoherence** [43]. In experimental QI processing, it is crucial to isolate qubits from their environment to minimize decoherence and maintain their quantum properties. Since light primarily interacts **coherently** with its environment, that is without loss of purity, we will focus on pure states for simplicity in this chapter, without using the density matrix. We will encounter the density matrix in Section II.6 when discussing the tomography of a quantum state.

The temporal evolution of the qubit state $\left|\psi\right\rangle$ obeys the far-famed Schrödinger equation, governing the dynamics of any pure quantum system [44]

$$i\hbar \frac{\mathrm{d}}{\mathrm{d}t} \left|\psi(t)\right\rangle = \hat{H}(t) \left|\psi(t)\right\rangle \tag{I.2}$$

where $\hat{H}$ is the **Hamiltonian** of the system (**in this chapter, operators are denoted with a hat**). The Hamiltonian operator is **self-adjoint**: $H^\dagger = H$, with † the conjugate transpose. The formal solution is

$$\left|\psi(t)\right\rangle = e^{-\frac{i}{\hbar}\int \hat{H}(t')\mathrm{d}t'} \left|\psi(t=0)\right\rangle \tag{I.3}$$

$$= \hat{U}(t) \left|\psi(t=0)\right\rangle. \tag{I.4}$$

with the operator exponential defined as $e^{\hat{A}} = \sum_{k=0}^{\infty} \frac{\hat{A}^k}{k!}$. The operator $\hat{U}$ is shown to be **unitary**, i.e. $\hat{U}^{-1} = \hat{U}^\dagger$, by the properties of the Lie group of unitary matrices [45].

As a result, coherent operations on single qubits are unitary matrices acting on the 2-dimensional Hilbert space spanned by the computational basis. Examples of canonical single-qubit gates are [46]

- the identity $\hat{\mathbb{1}} = \begin{bmatrix} 1 & 0 \\ 0 & 1 \end{bmatrix}$
- the Pauli-X gate $\hat{X} = \begin{bmatrix} 0 & 1 \\ 1 & 0 \end{bmatrix}$, Pauli-Y gate $\hat{Y} = \begin{bmatrix} 0 & -i \\ i & 0 \end{bmatrix}$ and Pauli-Z gate $\hat{Z} = \begin{bmatrix} 1 & 0 \\ 0 & -1 \end{bmatrix}$
- the Hadamard gate $\hat{H} = \frac{1}{\sqrt{2}} \begin{bmatrix} 1 & 1 \\ 1 & -1 \end{bmatrix}$
- the T gate $\hat{T} = \begin{bmatrix} 1 & 0 \\ 0 & e^{i\pi/4} \end{bmatrix}$
- and the phase gate $\hat{P} = \begin{bmatrix} 1 & 0 \\ 0 & i \end{bmatrix}$.

We now proceed with the treatment of multi-partite qubit systems.

I.1.2 - Multi-qubit gates and entanglement

The mathematical structure associated to multiqubit systems is the **tensor product** $\otimes$ [39]. Every pure state belonging to the bipartite system of two qubits labelled "A" and "B" is of the form

$$|\psi_{A\otimes B}\rangle = \sum_{k,l=0}^{1} c_{kl} |k_A\rangle \otimes |k_B\rangle \tag{I.5}$$

where $\{|0_{A/B}\rangle, |1_{A/B}\rangle\}$ is the computational basis of qubit A/B. Some states can be factorized into the separable form

$$|\psi_{A\otimes B}\rangle = \left(\alpha_0 |0_A\rangle + \alpha_1 |1_A\rangle\right) \otimes \left(\beta_0 |0_B\rangle + \beta_1 |1_B\rangle\right) \tag{I.6}$$

which is the juxtaposition of two single-qubit states. In contrast, **entangled states** cannot be expressed as a tensor product of individual states of the subsystems as in Eq. I.6. The **Bell states**

$$|\Phi^\pm\rangle = \frac{|0_A, 0_B\rangle \pm |1_A, 1_B\rangle}{\sqrt{2}} \tag{I.7}$$

$$|\Psi^\pm\rangle = \frac{|0_A, 1_B\rangle \pm |1_A, 0_B\rangle}{\sqrt{2}} \tag{I.8}$$

are examples of maximally entangled states. We argue in Section I.1.4 that quantum entanglement is a capital resource for QI processing.

Separable multi-qubit gates such as

$$\hat{U}_{A\otimes B} = \hat{U}_A \otimes \hat{U}_B \tag{I.9}$$

where $\hat{U}_A$ and $\hat{U}_B$ are applied separately on qubits A and B cannot generate entanglement by themselves. To generate entanglement, multi-qubit gates whose action cannot be decomposed as a separate evolution of both qubits are needed. This is the case of the **controlled-NOT (CNOT) gate** defined on the computational basis as

$$\widehat{\text{CNOT}} |x, y\rangle = \begin{cases} |0, y\rangle & \text{if } x = 0 \\ |1, \overline{y}\rangle & \text{if } x = 1 \end{cases} \tag{I.10}$$

with $\overline{y}$ the Boolean negation of y ($\overline{0}=1$ and $\overline{1}=0$). For instance, the Bell state $|\Phi^+\rangle$ is obtained using a Hadamard gate on qubit A followed by a CNOT gate:

$$|0_A 0_B\rangle \xrightarrow{\hat{H}_A} \frac{1}{\sqrt{2}}(|0_A 0_B\rangle + |1_A 0_B\rangle) \xrightarrow{\widehat{\text{CNOT}}} \frac{1}{\sqrt{2}}(|0_A 0_B\rangle + |1_A 1_B\rangle) = |\Phi^+\rangle \tag{I.11}$$

Other entangling multi-qubit gates are:

- the **controlled-Z (CZ) gate**:

$$\widehat{\text{CZ}}\,|x,y\rangle = (-1)^{x.y}\,|x,y\rangle = \begin{cases} -|1,1\rangle & \text{if } x=1 \text{ and } y=1 \\ |x,y\rangle & \text{else} \end{cases} \tag{I.12}$$

- the **Toffoli gate**:

$$\widehat{\text{Toffoli}}\,|x,y,z\rangle = \begin{cases} |x,y,z\rangle & \text{if } x=0 \text{ or } y=0 \\ |1,1,\overline{z}\rangle & \text{if } x=1 \text{ and } y=1 \end{cases} \tag{I.13}$$

In the following subsection, we examine the minimal set of gates required to operate a quantum computer.

I.1.3 - Universal gate sets

In classical computing, any Boolean function can be constructed using only NAND gates, where the NAND operation

$$f_{\text{NAND}}(x,y) = \begin{cases} (0,y) & \text{if } x=0 \\ (1,\overline{y}) & \text{if } x=1 \end{cases} \tag{I.14}$$

is the classical equivalent of the quantum CNOT gate. In other words, a universal classical computing machine, capable of performing any classical computation on bits, can be built using solely NAND gates (real computers use other gates as well to enhance efficiency).

In this spirit, we expect a quantum computer to universally implement any transformation on qubits, aligning with Feynman's original proposal for a "universal quantum simulator" [8]. In practice, a universal quantum computer must only be capable of approaching every unitary matrix with arbitrary precision by applying finite sequences of gates. The gate sequences may be assembled by drawing from a finite set of quantum gates called **universal gate sets**. The basic requirements for a universal set include the ability to create qubit superpositions and entangled states, as well as the inclusion of at least one gate with complex amplitudes. Additionally, the set must contain at least one gate that is not part of the **Clifford group** [46]. The Clifford group is the set of gates {CNOT, Hadamard, P}. Operations that use only Clifford group gates are efficiently classically simulable according to the Gottesman-Knill theorem [47] and, therefore, do not provide any quantum computational advantage from an algorithmic complexity point of view. Examples of universal sets of gates include:

- {CNOT, all single-qubit gates} [48]
- {CNOT, Hadamard, T} [49]
- {Toffoli, Hadamard, P} [50]

Thus, entangling gates like the CNOT and Toffoli gates are crucial for realizing a universal quantum computer and demonstrate quantum advantage.

In the next subsection, we explore the unique features of quantum mechanics that QI processing machines leverage to achieve a quantum computational advantage.

I.1.4 - Distinctive features of QI

From the significantly more sophisticated mathematical apparatus and formalism of QI emerge unique physical phenomena. Some distinctive features of QI, harnessed by quantum devices, are:

- the **no-cloning theorem**: the impossibility of exactly copying an arbitrary unknown quantum state [51]. If quantum cloning was possible, then superluminal communication would be as well [52]. In contrast, classical information can be copied.
- **Bohr's complementarity principle** [53]: certain properties of physical systems, such as the position and momentum of a particle cannot be measured simultaneously. This is a combined consequence of the existence of non-commuting observables in quantum mechanics and the quantum mechanical measurement postulate.

The following are commonly thought as distinctive features, but admit classical counterparts:

- **quantum superposition**: the vector space structure of quantum mechanics allows any linear combination of computational basis states to be also a valid state of the system (see Eq. I.1). Superposition states however also exist in classical optics, using polarization for instance [54].
- **quantum entanglement** (see Section I.1.2). So-called **classical entanglement** can also be realized with classical optics [55], for instance with a combination of polarization and path degrees of freedom.

The capital difference between superposition and entanglement in classical and quantum mechanics is the measurement formalism. Classical systems admit a joint probability distribution from which the probability of measuring each result derive, whereas quantum systems derive their measurement probability from a quantum probability theory, given by the Born rule [56, 54], coupled with the collapse of the measured wavefunction. Thus, classical entanglement does not violate Bell inequalities. On the contrary, quantum entanglement exhibits nonclassical behavior, also called **quantum nonlocality and contextuality**, as a consequence of Bohr's complementarity principle. We discuss these topics more in depth in Chapter III.

The following section lays the groundwork for photonic quantum computing by developing the formalism of quantum optics and the description of photons as qubits.

I.2 - From classical to quantum light

Classical light designates electromagnetic fields at optical frequencies described by classical electrodynamics [57, 58]. In classical electrodynamics, the electric field $\mathbf{E}(\vec{x},t)$ and the magnetic field $\mathbf{B}(\vec{x},t)$ obey Maxwell's equations

$$\nabla.\,\mathbf{E}(\vec{x},t)=\frac{\rho(\vec{x},t)}{\varepsilon_0} \qquad \nabla.\,\mathbf{B}(\vec{x},t)=0 \tag{I.15}$$

$$\nabla\wedge\mathbf{E}(\vec{x},t)=\mu_0\varepsilon_0\frac{\partial\mathbf{B}}{\partial t}(\vec{x},t)+\mu_0\mathbf{j}(\vec{x},t) \qquad \nabla\wedge\mathbf{B}(\vec{x},t)=-\frac{\partial\mathbf{E}}{\partial t}(\vec{x},t) \tag{I.16}$$

where bold characters represent 3-dimensional vectors, ε_0 is the vacuum permittivity, μ_0 is the vacuum permeability, ρ is the charge density and $\mathbf{j}$ is the current density vector. We use the notation $\nabla=\left(\frac{\partial}{\partial x},\frac{\partial}{\partial y},\frac{\partial}{\partial z}\right)$, . designates the dot product and $\wedge$ the cross product.

The purpose of this section is to briefly present the quantification procedure for Maxwell's equations in the case of free radiation in vacuum, following the procedure of [59], in order to introduce the quantum description of light. In Section I.2.1, we begin by expressing vacuum radiation

in terms of normal modes, establishing the basis for the quantization of the Maxwell's equations in Section I.2.2. This quantization leads us to the eigenstates of the vacuum Hamiltonian in Section I.2.3. We introduce the framework of linear optics in Section I.2.4 and conclude with a succinct overview of photonic qubit encodings Section I.2.5.

I.2.1 - Normal modes of Maxwell's equations

Consider a cubic volume of empty space of side L, i.e. $\rho = 0$ and $\mathbf{j} = \mathbf{0}$. The total energy of the electromagnetic field is given by

$$\mathscr{E} = \frac{\varepsilon_0}{2} \iiint_V \left[\mathbf{E}^2(\mathbf{x}, t) + c^2 \mathbf{B}^2(\mathbf{x}, t)\right] \tag{I.17}$$

with c the speed of light in vacuum. The electric and magnetic fields are decomposed in terms of polarized Fourier components, each indexed $\ell = (\mathbf{n}, s)$, with $\mathbf{n} \in \mathbb{N}^3$ an integer vector and a binary index $s \in \{1, 2\}$. Each polarized Fourier component ℓ is associated to a wavevector

$$\mathbf{k}_\ell = \frac{2\pi}{L}\mathbf{n} \tag{I.18}$$

and two polarization vectors $\mathbf{v}_{(\mathbf{n},s)}$, such that $(\mathbf{k}_\ell, \mathbf{v}_{(\mathbf{n},1)}, \mathbf{v}_{(\mathbf{n},2)})$ forms a direct triad. The electric and magnetic field are then

$$\mathbf{E}(\mathbf{x}, t) = \sum_\ell \tilde{E}_\ell(t) R\, e^{i\mathbf{k}_\ell.\mathbf{x}} \mathbf{v}_\ell \qquad \mathbf{B}(\mathbf{x}, t) = \sum_\ell \tilde{B}_\ell(t)\, e^{i\mathbf{k}_\ell.\mathbf{x}} \mathbf{v}_\ell \tag{I.19}$$

with $\tilde{E}_\ell(t)$ and $\tilde{B}_\ell(t)$ the Fourier components of the electric and magnetic fields. At this stage, the vector potential $\mathbf{A}$ defined by $\mathbf{B}(\mathbf{x}, t) = \nabla \wedge \mathbf{A}(\mathbf{x}, t)$ is introduced. The Coulomb gauge is used to fix the electromagnetic potentials:

$$\nabla . \mathbf{A}(\mathbf{x}, t) = 0. \tag{I.20}$$

Expanding the vector potential in terms of Fourier components gives

$$\mathbf{A}(\mathbf{x}, t) = \sum_\ell \tilde{A}_\ell(t)\, e^{i\mathbf{k}_\ell.\mathbf{x}} \mathbf{v}_\ell \tag{I.21}$$

with $\tilde{B}_\ell(t) = i k_\ell \tilde{A}_\ell(t)$. The electromagnetic energy can be rewritten

$$\mathscr{E} = \sum_\ell \hbar\omega_\ell |\alpha_\ell(t)|^2 \tag{I.22}$$

with $\hbar$ the reduced Planck constant, $\omega_\ell = c\|\mathbf{k}_\ell\|$ and

$$\tilde{\alpha}_\ell(t) = \sqrt{\frac{\varepsilon_0 L^3}{2\hbar\omega_\ell}} \left(\omega_\ell \tilde{A}_\ell(t) - i\tilde{E}_\ell(t)\right) \tag{I.23}$$

the decoupled normal modes of the electromagnetic field. We now proceed by quantizing the normal modes.

I.2.2 - Canonical quantization of the electromagnetic field

We set

$$\tilde{Q}_\ell = \sqrt{2\hbar}\,\mathrm{Re}(\tilde{\alpha}_\ell) \qquad \tilde{P}_\ell = \sqrt{2\hbar}\,\mathrm{Im}(\tilde{\alpha}_\ell) \tag{I.24}$$

and write the electromagnetic energy as a function of $\tilde{Q}_\ell$ and $\tilde{P}_\ell$:

$$\mathscr{E} \;=\; \mathscr{H}\left(\{\tilde{Q}\}, \{\tilde{P}\}\right) \;=\; \sum_\ell \frac{\omega_\ell}{2}\left(\tilde{Q}_\ell^2 + \tilde{P}_\ell^2\right). \tag{I.25}$$

From Maxwell's equations, α_ℓ obeys the differential equation

$$\frac{\mathrm{d}}{\mathrm{d}t}\mathrm{Re}(\tilde{\alpha}_\ell) = \omega_\ell \,\mathrm{Im}(\tilde{\alpha}_\ell) \qquad\qquad \frac{\mathrm{d}}{\mathrm{d}t}\mathrm{Im}(\tilde{\alpha}_\ell) = -\omega_\ell \,\mathrm{Re}(\tilde{\alpha}_\ell), \tag{I.26}$$

thus

$$\frac{\mathrm{d}\tilde{Q}_\ell}{\mathrm{d}t} = \frac{\partial \mathscr{H}}{\partial \tilde{P}_\ell} \qquad\qquad \frac{\mathrm{d}\tilde{P}_\ell}{\mathrm{d}t} = -\frac{\partial \mathscr{H}}{\partial \tilde{Q}_\ell}. \tag{I.27}$$

We recognize Hamilton's equations [60], with $\mathscr{H}$ the Hamiltonian of the system and $\{\tilde{Q}\},\{\tilde{P}\}$ the conjugate phase space variables. The canonical quantization procedure is applied, where conjugate variables are promoted to self-adjoint operators

$$\tilde{Q}_\ell \longrightarrow \hat{Q}_\ell \qquad\qquad \tilde{P}_\ell \longrightarrow \hat{P}_\ell \tag{I.28}$$

endowed with the canonical commutation relations

$$[\hat{Q}_\ell, \hat{P}_{\ell'}] = i\hbar\delta_{\ell,\ell'}\mathbb{1} \qquad\qquad [\hat{Q}_\ell, \hat{Q}_{\ell'}] = [\hat{P}_\ell, \hat{P}_{\ell'}] = 0 \tag{I.29}$$

where $\mathbb{1}$ is the identity operator. Similarly, the normal modes $\tilde{\alpha}_\ell$ are promoted to operators $\tilde{\alpha}_\ell \longrightarrow \hat{a}_\ell$ with commutation relations

$$[\hat{a}_\ell, \hat{a}^\dagger_{\ell'}] = \delta_{\ell,\ell'}\mathbb{1} \qquad\qquad [\hat{a}_\ell, \hat{a}_{\ell'}] = 0. \tag{I.30}$$

Finally, the Hamiltonian operator $\mathscr{H} \longrightarrow \hat{H}$ associated to the free radiation is expressed

$$\hat{H}_R = \sum_\ell \hbar\omega_\ell \left(\hat{a}^\dagger_\ell \hat{a}_\ell + \frac{1}{2}\right). \tag{I.31}$$

Following a similar procedure to quantize Maxwell's equations in the presence of charged particles, it is possible to show [59] that the quantum system consisting of the particles and the electromagnetic field is associated to a Hamiltonian operator

$$\hat{H} = \hat{H}_P + \hat{H}_R + \hat{H}_I \tag{I.32}$$

where $\hat{H}_P$ describes the charged particles and their Coulomb interaction, $\hat{H}_R$ is the free radiation Hamiltonian of Eq. I.31, and $\hat{H}_I$ accounts for light-matter interaction.

We continue by diagonalizing the free radiation Hamiltonian and introduce the formalism for the description of quantum states of light.

I.2.3 - Quantum states of light

In Section I.2.3.A, we introduce Fock states, from which single-photon states emerge. We then express single-mode coherent states in the Fock state formalism in Section I.2.3.B.

I.2.3.A - Fock states and single photons

We now index the polarization Fourier components by integers $\ell = 1, 2, \ldots$ for conciseness. The free radiation Hamiltonian $\hat{H}_R$ of Eq. I.31 can be understood as an infinite sum of harmonic oscillators. Each harmonic oscillator ℓ is described by the Hamiltonian

$$\hat{H}_\ell = \hbar\omega_\ell \left(\hat{a}^\dagger_\ell \hat{a}_\ell + \frac{1}{2}\right), \tag{I.33}$$

where $\hat{a}^\dagger_\ell$ and $\hat{a}_\ell$ are the associated **creation and annihilation** operators. The eigenvectors and eigenvalues of the harmonic oscillator Hamiltonian are

$$\hat{H}_j\,|n\rangle = \hbar\omega_\ell \left(n + \frac{1}{2}\right)|n\rangle \tag{I.34}$$

Consequently, every eigenvector of the free radiation Hamiltonian $\hat{H}_R$ is a so-called **Fock state** of the form

$$\hat{H}_R |n_1, n_2, ...\rangle = \left[\sum_{\ell=1}^{\infty} \left(n_\ell + \frac{1}{2} \right) \right] |n_1, n_2, ...\rangle \tag{I.35}$$

where $|n_1, n_2, ...\rangle = \bigotimes_{\ell=1}^{\infty} |n_\ell\rangle$. One special Fock state is the **vacuum state**

$$|\text{vac}\rangle = |0, 0, ...\rangle . \tag{I.36}$$

Every Fock state is obtained from the vacuum state by

$$|n_1, n_2, ...\rangle = \frac{(\hat{a}_1^\dagger)^{n_1} (\hat{a}_2^\dagger)^{n_2} ...}{\sqrt{n_1! n_2! ...}} |\text{vac}\rangle . \tag{I.37}$$

A **photon** is an elementary excitation of the quantum electromagnetic field, i.e. a Fock state of the form $|1, 0, 0, ...\rangle$ for instance. We will see in Section I.3.1.B that single photons exhibit highly non-classical behavior compared to quasi-classical states of light, which we introduce in the following section.

I.2.3.B - Single-mode coherent states

Consider a single optical mode j. The **coherent states** of the mode are defined as the eigenvectors of the mode annihilation operator [61]:

$$\hat{a}_j |\alpha\rangle = \alpha |\alpha\rangle \tag{I.38}$$

with $\alpha \in \mathbb{C}$. Every coherent state is expressed as a Fock state superposition

$$|\alpha\rangle = e^{-\frac{|\alpha|^2}{2}} \sum_{n=0}^{\infty} \frac{\alpha^n}{\sqrt{n!}} |n\rangle \tag{I.39}$$

where $|n\rangle$ are the Fock states of the mode j. Coherent states are electromagnetic field states that most closely resemble the behavior of a monochromatic electromagnetic wave, as described in [61]. However, coherent states do not have a well-defined photon number; instead, each photon number or intensity measurement can yield different results due to the quantum superposition of Fock states. This characteristic is not captured by classical electrodynamics, which is why coherent states are often referred to as **quasi-classical**. As the intensity of a coherent state increases ($|\alpha| \gg 1$), its behavior approaches that of a classical state because the ratio of the standard deviation in photon number, $|\alpha|$, to the average photon number, $|\alpha|^2$, tends to zero.

We have focused on photonic quantum states expressed as Fock state superpositions, which is at the core of the **discrete-variable** paradigm of quantum optics. The quantities of interest in discrete variables are finite or at most countable. It is also possible to manipulate the **quadratures** of the electric field (related to the operators $\hat{X}$ and $\hat{P}$ of Section I.2.2) which are defined on an infinite Hilbert space. The quadratures are thus fundamental in **continuous-variable** quantum optics.

In the following, we resume our usage of the discrete-variable formalism and introduce the framework of linear optics, which is central in the study of light manipulation.

I.2.4 - Linear optics

We consider optical systems with m input ports and m output ports (see Fig. I.1). Each input and output port supports a single spatial mode of light and two orthogonal polarizations. In the following, we focus for clarity and conciseness on optical systems that do not act on the polarization degree of freedom of light. This also reflects in principle the behavior of the integrated optical systems we use in this thesis to manipulate light. Each spatial mode is indexed $j \in [1, m]$.

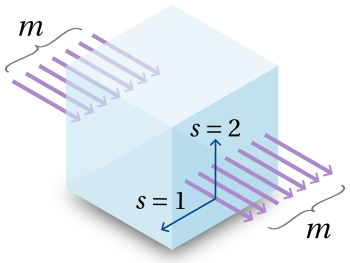

Figure I.1: Linear optical system with m input and output modes, supporting two polarizations $s = 1, 2$.

Linear optics refers to the set of photonic state transformations described by unitary matrices of the form [20]

$$\hat{U} = \exp\left(i \sum_{j,k} h_{jk} \hat{a}_j^\dagger \hat{a}_k\right). \tag{I.40}$$

where $\hat{a}_j$ is the creation operator associated to the spatial mode j. Note that we have omitted the free-radiation Hamiltonian term, because we work in the interaction picture. As a result from Eq. I.40, a linear optical transformation does not mix modes associated with different eigenvalues of the free radiation Hamiltonian. In other words, applying a linear optical transformation to monochromatic light results in monochromatic light at the same wavelength. Therefore, a linear optical transformation is fully defined by its action on the m position degrees of freedom at a fixed wavelength, and $\hat{U}$ can be represented as a $m \times m$ unitary matrix of elements $u_{jk} \in \mathbb{C}$. $\hat{U}$ looses its unitarity when the linear optical system is lossy. The columns of $\hat{U}$ encode the evolution of the creation operators, which transform according to [62]

$$\hat{a}_j^\dagger \quad \xrightarrow{\hat{U}} \quad \sum_{k=1}^{m} u_{kj} \hat{a}_k^\dagger. \tag{I.41}$$

In practice, linear optical transformations are constructed from optical components such as e.g. **phase shifters (PSs)** and **beamsplitters**. A PS acting on a spatial mode j is a component that implements the spatial transformation

$$\hat{a}_j^\dagger \quad \longrightarrow \quad e^{i\phi} \hat{a}_j^\dagger. \tag{I.42}$$

with $\phi \in \mathbb{R}$. The associated unitary matrix is

$$\begin{bmatrix} 1 & & & & \\ & \ddots & & & \\ & & e^{i\phi} & & \\ & & & \ddots & \\ & & & & 1 \end{bmatrix} \quad \begin{matrix} \\ \\ \leftarrow j \\ \\ \\ \end{matrix} \qquad (j \downarrow)$$

with zeros everywhere outside of the diagonal. A beamsplitter of reflectivity $R \in [0, 1]$ on spatial modes j and k is a two-mode spatial transformation of the form

$$\hat{a}_j^\dagger \longrightarrow \sqrt{R}\, \hat{a}_j^\dagger + i\sqrt{1-R}\, \hat{a}_k^\dagger \tag{I.43}$$

$$\hat{a}_k^\dagger \longrightarrow i\sqrt{1-R}\, \hat{a}_j^\dagger + \sqrt{R}\, \hat{a}_k^\dagger, \tag{I.44}$$

implementing the unitary matrix

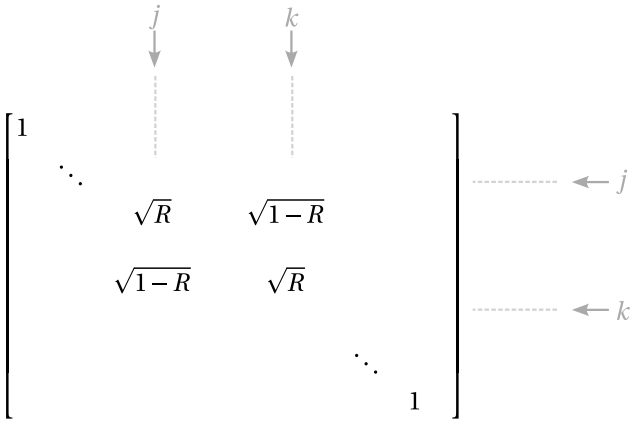

with zeros outside of the diagonal and indicated elements. A beamsplitter is **symmetric** when $R = 0.5$. We mention that general linear optical transformations can also act on the polarization degree of freedom using **quarter- and half-waveplates** for instance. Position and polarization degrees of freedom are interlinked using **polarizing beamsplitters**. The global unitary matrix $\hat{U}$ of a sequence of linear components is then computed by multiplying all the individual component matrices together in the corresponding order.

We conclude this subsection with the output state probability formula based on the matrix permanent, a key equation of linear optics. By Eq. I.41, the evolution of a multiphoton state $|\mathbf{n}\rangle = |n_1, n_2, \ldots, n_m\rangle$ through a unitary matrix $\hat{U}$ is expressed as

$$|\mathbf{n}\rangle = \prod_{j=1}^{m} \frac{(\hat{a}_j^\dagger)^{n_j}}{\sqrt{n_j!}} |\text{vac}\rangle \quad \xrightarrow{\hat{U}} \quad \prod_{j=1}^{2m} \frac{1}{\sqrt{n_j!}} \left(\sum_{k=1}^{m} u_{kj} \hat{a}_k^\dagger \right)^{n_k} |\text{vac}\rangle . \tag{I.45}$$

We are usually interested in computing the probability of measuring the state $|\mathbf{p}\rangle$ given an input state $|\mathbf{n}\rangle$, which is related to the quantity $\langle \mathbf{p}| \hat{U} |\mathbf{n}\rangle$. It has been shown that this can be expressed in an elegant form [63]:

$$\langle \mathbf{p}| \hat{U} |\mathbf{n}\rangle = \frac{1}{\sqrt{\prod_{j=1}^{2m} n_j!}\ \sqrt{\prod_{k=1}^{2m} p_k!}} \text{Per}\left[\hat{U}_{\mathbf{p}}^{\mathbf{n}}\right] \tag{I.46}$$

where

- Per is the matrix **permanent**, given by

$$\text{Per}\left[\hat{U}\right] = \sum_{\sigma \in \mathfrak{S}_m} u_{1,\sigma(1)} u_{2,\sigma(2)} \ldots u_{m,\sigma(m)} \tag{I.47}$$

  with $\mathfrak{S}_m$ the **symmetric group** of order m (set of permutations on m elements).

- $\hat{U}_{\mathbf{p}}^{\mathbf{n}}$ designates a matrix constructed from $\hat{U}$. An intermediate matrix is created by horizontally stacking n_1 times the first column of $\hat{U}$, n_2 times the second column and so on. Then the final matrix is obtained by vertically stacking p_1 times the first row of the intermediate matrix, p_2 the second row and so on. An example with $\mathbf{n} = (2,1,0)$ and $\mathbf{p} = (1,2,0)$ for an arbitrary matrix $\hat{U}$ is shown below:

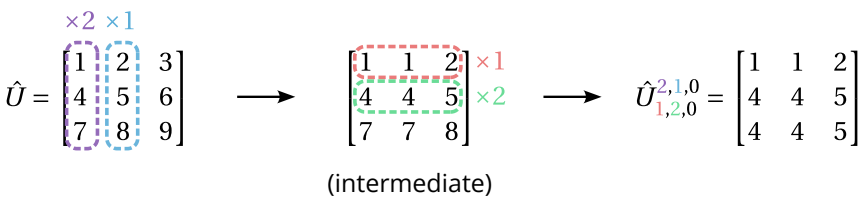

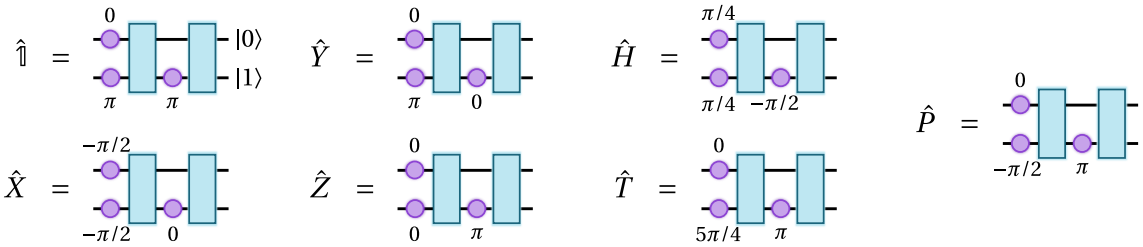

Figure I.3: Single-qubit gates in dual-rail encoding. All single-qubit gates of Section I.1.1 are implemented using the same arrangement of PSs and beamsplitters. Purple disks: PSs. Blue rectangles: symmetric beamsplitters ($R = 0.5$ in Eq. I.43).

Consequently, the probability of measuring $|\mathbf{p}\rangle$ given the input state $|\mathbf{n}\rangle$ is

$$\mathbb{P}(\mathbf{n} \longrightarrow \mathbf{p}) = \frac{1}{\prod_{j=1}^{2m} n_j! \;\; \prod_{j=k}^{2m} p_k!} \left|\mathrm{Per}\left[\hat{U}_{\mathbf{p}}^{\mathbf{n}}\right]\right|^2 \tag{I.48}$$

The *Perceval* Python package [1] developed by *Quandela* proposes a complete framework for studying linear optical systems, and features a state-of-the-art matrix permanent calculation engine. *Perceval* enables the simulation of photonic systems with up to 20 photons on a standard personal computer.

The framework of linear optics allows the formalization and manipulation of photonic qubits, as covered in the next subsection.

I.2.5 - Photonic qubits

Photons are versatile quantum information carriers, as they allow for a remarkable number of different encodings [12]. **Polarization encoding** for instance, assigns the logical $|0\rangle$ and $|1\rangle$ qubit states to the $s = 1$ and $s = 2$ mode polarization indices, which may refer to either of the following polarization bases (without normalization):

- (horizontal $|H\rangle$, vertical $|V\rangle$),
- (diagonal $|D\rangle = |H\rangle + |V\rangle$, antidiagonal $|A\rangle = |H\rangle - |V\rangle$),
- or (left-circular $|L\rangle = |H\rangle + i\,|V\rangle$, right-circular $|R\rangle = |H\rangle - i\,|V\rangle$).

Photons being massless spin-1 bosons, the polarization state is limited to a 2-dimensional Hilbert space and thus does not allow extensions to **qudit** encodings (generalization of qubit with $d \geq 2$ computational basis states).

Information on photons may also be imprinted using **path encoding**, specifically **dual-rail** path encoding. In dual-rail encoding, a pair of spatial modes forms a qubit and the logical state is given by the position of the photon as illustrated in Fig. I.2. Any single-qubit gate is easily and precisely implemented using a PS or an assembly of beamsplitters and PSs, as shown on Fig. I.3. Dual-rail encoding can be readily generalized to qudit encoding by allocating more spatial modes per qudit.

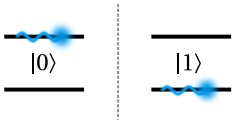

Figure I.2: Dual-rail path encoding.

Time-bin and **orbital angular momentum** encoding are particularly relevant for quantum communication. In time-bin encoding, the information is encoded in the photon time of arrival, which can be "early" ($|0\rangle$) or "late" ($|1\rangle$). Additionally, information can be encoded in the wavelength of the photon, known as **frequency-bin** encoding, which is a promising avenue for multiplexing quantum information. Multiple encodings may be combined for increased encoding capacity, resulting in **hyperencoded** qubits. **Photon-number** encoding uses the number of photons to represent logical states but is experimentally impractical due to photon losses and the difficulty in controlling exact photon numbers.

Photonic qubits are appealing for quantum communication due to their ability to be manipulated at room temperature and their natural integration with optical fiber networks. Photons interact mostly coherently with their environment, hence they are less exposed to decoherence than other QI processing platforms. However, photonic qubits can be lost to the environment by absorption or scattering, which limits the speed of computations in the discrete-variable framework. In addition, the inherent lack of interaction between photons complicates the implementation of entangling two-qubit gates necessary for quantum computation. This aspect is covered in Section I.5.2.

In the next section, we discuss the generation of photonic qubits using single-photon sources.

I.3 - Sources of quantum light

Common sources of light produce classical states of light, i.e. that do not or only partially exhibit quantum effects. Discharge lamps for instance produce thermal states, which are purely classical states. Lasers on the other hand create coherent states [64], which are quasi-classical due to their coherent photon number superposition. We will see in Section I.3.1 the defining characteristic that separates laser light from single-photon sources, that are capable of producing truly quantum light. Section I.3.1 also covers the specifications set on single-photon sources. Section I.3.2 discusses probabilistic single-photon sources. Section I.3.3 introduces the single-photon sources used in this thesis. We focus on **pulsed** photon sources, emitting photons with a fixed repetition rate $1/\tau$.

During this thesis, I developed a tool designed for the real-time characterization of pulsed single-photon sources, substantially reducing the time required for manual setup optimizations (see App. A).

I.3.1 - Single-photon source metrics and requirements

An **ideal single-photon source** is a system emitting on-demand a Fock state $|1\rangle$, i.e. a **single photon**, in a single optical mode (direction and polarization) at each emission trigger.

There are three key figures of merit for evaluating a single-photon source quantifying departure from ideality: **brightness** (Section I.3.1.A), **multiphoton emission** (Section I.3.1.B) and **photon indistinguishability** (Section I.3.1.C).

I.3.1.A - Brightness

The brightness B of a single-photon source is defined as

$$B = \frac{\text{number of detected photons}}{\text{number of emission triggers}}. \tag{I.49}$$

Brightness measurements need to be adjusted for detector imperfections in practice, as discussed in Section IV.2.1. As a result, accurate brightness measurements require well-calibrated photon detectors, and it is important to specify the stage of the optical setup at which the brightness is measured. For example, the **first-lens brightness** refers to the brightness measured immediately after the first light collection lens, while the **device brightness** is measured after any photon filtering stages. The device brightness hence represents the number of truly usable photons. It is also often important to measure the **polarized brightness** by placing a polarizer before the detectors, as an ideal photon source should emit photons with consistent polarization.

I.3.1.B - Multiphoton emissions and photon purity

Let p_k be the probability for a single-photon source to emit a Fock state $|k\rangle$ following an emission trigger. An ideal single-photon source has $p_1 = 1$. Imperfect single-photon sources have $p_1 < 1$, with $p_0 > 0$ due to limited brightness and $p_2, p_3, ... > 0$, representing multiphoton emissions. The multiphoton emission likelihood of a single-photon source is usually evaluated using the optical setup in Fig. I.4 consisting of a symmetric beamsplitter (BS), two single-photon detectors (indexed 1 and 2) and a correlator (&). For an ideal single-photon source, the two detectors will never click simultaneously, whereas we expect **two-photon coincidences** for an imperfect source. Thus, the figure of merit is here the normalized second-order quantum correlation function at zero delay

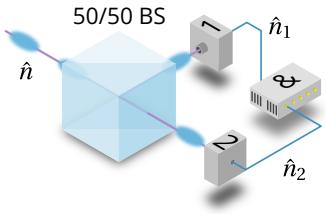

Figure I.4: Optical setup for measuring $g^{(2)}(0)$.

$$g^{(2)}(0) = \frac{\langle \hat{n}_1 \hat{n}_2 \rangle}{\langle \hat{n}_1 \rangle \langle \hat{n}_2 \rangle}. \tag{I.50}$$

where $\hat{n}_1$ and $\hat{n}_2$ are the operators associated to the photon number observables on detectors 1 and 2. It is shown that [61]

$$g^{(2)}(0) = 1 + \frac{\mathrm{Var}(\hat{n}) - \langle \hat{n} \rangle}{\langle \hat{n} \rangle^2}, \tag{I.51}$$

with $\hat{n}$ the photon number observable of the input state. We focus in the following on single-mode states (see [61] for the treatment of multi-mode states). Coherent states, for which $\mathrm{Var}(\hat{n}) = \langle \hat{n} \rangle$, yield $g^{(2)}(0) = 1$. For **thermal states**, classical photon-number distributions following Bose-Einstein statistics [65], we have $\mathrm{Var}(\hat{n}) = \langle \hat{n} \rangle^2 + \langle \hat{n} \rangle$, and thus $g^{(2)}(0) = 2$ [61]. In fact, using the classical version of the correlation function, it is straightforwardly shown that classical electrodynamics can only describe electromagnetic fields with $g^{(2)}(0) \geq 1$ [66]. In contrast, for single-photon sources with $p_1 \gg p_2$ and $p_3 = p_4 = ... = 0$, $g^{(2)}(0)$ measures the quantity

$$g^{(2)}(0) = \frac{2p_2}{(p_1 + 2p_2)^2} \approx \frac{2p_2}{p_1^2} < 1. \tag{I.52}$$

$g^{(2)}(0) < 1$ is thus a distinctive trait of nonclassical light, i.e. that cannot be described by classical electrodynamics. $g^{(2)}(0) < 1$ corresponds to the so-called **sub-Poissonian** statistics of arrival, which is a synonym for **temporal anti-bunching**. In other words, photons arrive separately one by one, as Fock states $|1\rangle$. The amount of multiphoton emissions is also referred to as **photon impurity**, not to be confounded with the purity of a quantum state (see Section I.1.1). Hence, an ideal single-photon source is expected to deliver **pure** single-photons.

For a pulsed single-photon source, the $g^{(2)}(0)$ is measured by acquiring the correlation histogram between the two detectors in Fig. I.4. An example is displayed on Fig. I.5. The correlation histogram consists of peaks, from which we deduce [32]

$$g^{(2)}(0) = \frac{\text{area of central peak}}{\text{average area of other peaks}}. \tag{I.53}$$

The formula is valid in the high-loss regime, where the adjacent peaks have a uniform height.

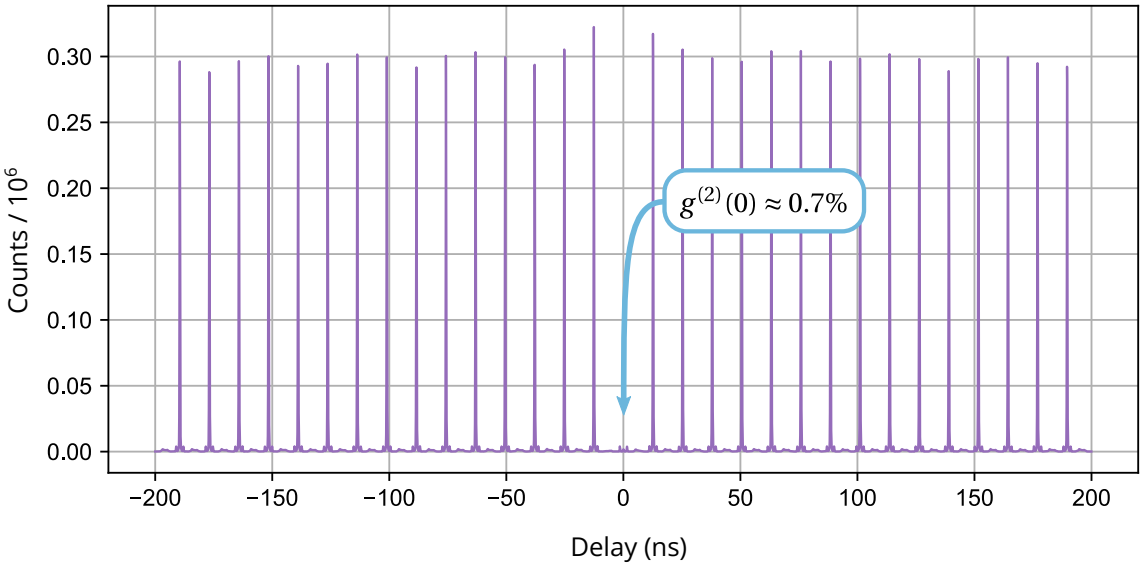

Figure I.5: $g^{(2)}(0)$ measurement with a pulsed single-photon source. Correlation histogram between the two $g^{(2)}(0)$ measurement detectors of Fig. I.4. The y-axis shows the number of combined detector clicks as a function of time elapsed between the two detections. The value at zero delay gives the number of two-photon coincidences recorded during the integration time of 2 seconds. Positive delays $\tau > 0$ are associated to events where detector 2 clicks after a time τ following a detector 1 click. Negative delays account for events where detector 1 clicks after detector 2. The peaks are here spaced by ≈ 12.5 ns, due to the repetition rate of ≈ 80 MHz of single-photon source excitations. For a peak area integration width of 1 ns, we measure $g^{(2)}(0) \approx 0.7$ %.

I.3.1.C - Photon indistinguishability

Consider an optical setup consisting of a symmetric beamsplitter followed by two beamsplitters and a correlator, as shown on Fig. I.6. The input and output modes of the beamsplitter are labelled $(1, s)$ and $(2, s)$ with $s = 1, 2$ the polarization index.

Single-photons sent both input modes are assumed to be perfectly indistinguishable in terms of wavelength, and overlap perfectly spatially and temporally inside the beamsplitter. The first input photon has a polarization $s = 1$, while the second photon has a polarization state

$$\alpha \left| n_{(2,s=1)} = 1 \right\rangle + \beta \left| n_{(2,s=2)} = 1 \right\rangle \quad \text{with} \quad |\alpha|^2 + |\beta^2| = 1. \tag{I.54}$$

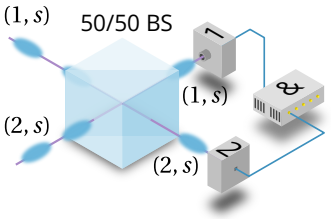

Figure I.6: Optical setup for measuring the HOM visibility V_{HOM}.

From the formalism for linear optics introduced in Section I.2.4, we compute the probability p_{coinc} of measuring a two-photon coincidence:

$$p_{\text{coinc}} = \frac{1 - |\alpha|^2}{2}. \tag{I.55}$$

Remarkably, if both photons are indistinguishable in all respects, i.e. $|\alpha| = 1$, then $p_{\text{coinc}} = 0$. This signifies that indistinguishable photons always exit the beamsplitter together. This is a signature of the bosonic nature of photons, as identical bosons in general exhibit a tendency to bunch [67]. The amount of indistinguishability $M_s = |\alpha|^2$ between the photons is directly given by the so-called **Hong-Ou-Mandel (HOM) visibility** [68]

$$V_{\text{HOM}} = M_s = 1 - 2p_{\text{coinc}}. \tag{I.56}$$

$V_{\text{HOM}} = 0$ corresponds to maximally distinguishable photons, whereas $V_{\text{HOM}} = 1$ signifies that the photons are fully indistinguishable. In practice, the measured HOM visibility must be corrected

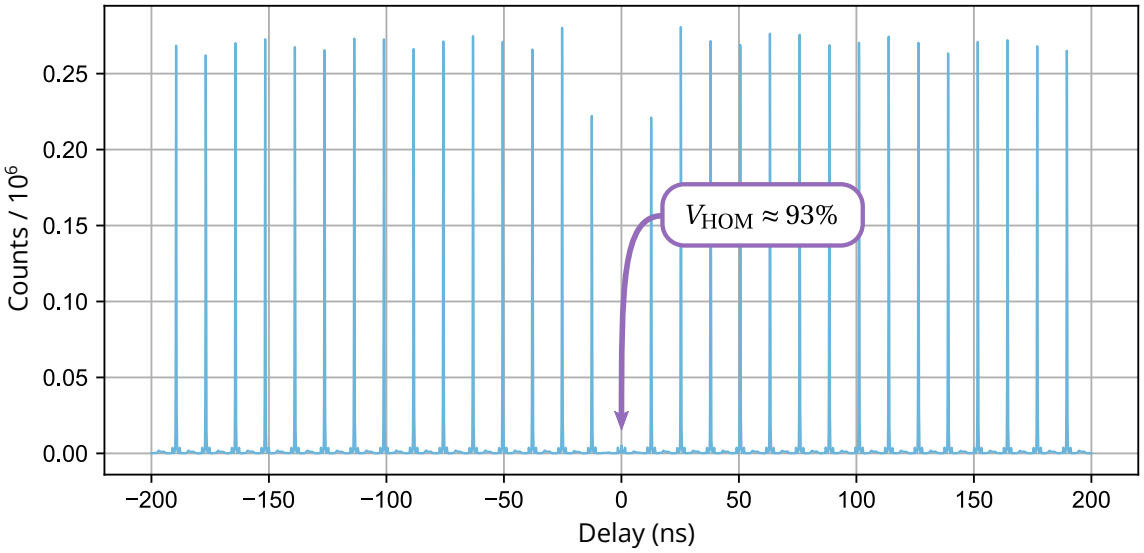

Figure I.7: V_{HOM} measurement with a pulsed single-photon source. Correlation histogram between the two V_{HOM} measurement detectors (see Fig. I.5). For an integration time of 5 s and a peak area integration width of 1 ns, we measure $V_{\mathrm{HOM}} \approx 93.0$ %.

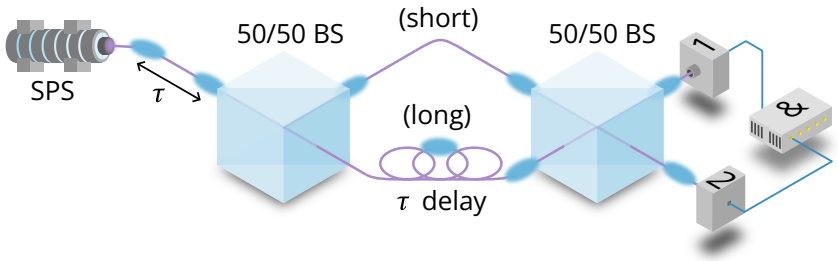

Figure I.8: V_{HOM} measurement for photons emitted from the same source. SPS: pulsed single-photon source emitting photons with a repetition rate $1/\tau$. 50/50 BS: symmetric beamsplitter. The first beamsplitter serves as a passive demultiplexer. One of its outputs connected to a τ delay line. The second beamsplitter is the HOM beamsplitter on which the photons interfere. Note that the demultiplexer delivers a valid photon interference only when a photon takes the long path and the following one takes the short path.

for multiphoton emissions introducing extra coincidences. The corrected formula is [69]

$$M_s = \frac{V_{\mathrm{HOM}} + g^{(2)}(0)}{1 - g^{(2)}(0)}, \tag{I.57}$$

assuming $g^{(2)}(0) \ll 1$ and that the emitted state is $|1\rangle$ (not a coherent superposition of $|0\rangle$ and $|1\rangle$).

From an experimental point of view, the HOM visibility V_{HOM} is measured similarly to $g^{(2)}(0)$ in Section I.3.1.B by acquiring the correlation histogram in the configuration depicted in Fig. I.6. Fig. I.7 displays an experimentally acquired histogram, from which the HOM visibility is computed in the high-loss regime via [32]

$$V_{\mathrm{HOM}} = 1 - 2\frac{\text{area of central peak}}{\text{average area of other peaks}}. \tag{I.58}$$

Notice that the peaks adjacent to the central one are smaller than the other peaks. This is due to the particular setup used to measure the indistinguishability of photons emitted from the same source (see Fig. I.8). The reduced adjacent peaks are not taken into account for the V_{HOM} estimation.

We mention that the partial distinguishability of a photon pair and its measurement via the HOM effect are well understood. However, the generalization of partial distinguishability to mul-

tiple photons is less trivial, and requires a specific interferometer and witnesses to be measured [70].

In the following subsection, we discuss a probabilistic method for generating single-photons.

I.3.2 - Probabilistic and heralded single-photon sources

One common approach for single-photon generation is through **parametric single-photon sources**, which rely on **spontaneous parametric downconversion (SPDC)**. SPDC is achieved by sending an intense light beam onto a crystal such as lithium niobate ($LiNbO_3$), lithium tantalate ($LiTaO_3$) or potassium titanyl phosphate (KTP), which have large second-order nonlinear susceptibility tensor $\chi^{(2)}$ elements. Using Maxwell's macroscopic equations in media from classical electrodynamics, it is shown [61] that an intense **pump** beam of angular frequency ω_{pump} and wavevector $\mathbf{k}_{\text{pump}}$ generates two **signal** and **idler** beams such that

$$\omega_{\text{pump}} = \omega_{\text{signal}} + \omega_{\text{idler}} \tag{I.59}$$

$$\mathbf{k}_{\text{pump}} = \mathbf{k}_{\text{signal}} + \mathbf{k}_{\text{idler}}. \tag{I.60}$$

The first equation expresses conservation of energy, while the second is called **phase-matching condition**. The phase-matching condition is determined by the physical properties of the crystal and the pump direction of propagation with respect to the crystal axis.

This result from classical electrodynamics implies that the system describing the pump light interacting with the crystal is associated to a Hamiltonian of the form

$$\hat{H} = \hat{H}_R + \hbar g \left(\hat{a}^\dagger_{\text{signal}} \hat{a}^\dagger_{\text{idler}} \hat{a}_{\text{pump}} + \hat{a}_{\text{signal}} \hat{a}_{\text{idler}} \hat{a}^\dagger_{\text{pump}} \right)$$

where g is the interaction strength and H_R is the free radiation Hamiltonian

$$\hat{H}_R = \hbar\omega_{\text{pump}} \left(\hat{a}^\dagger_{\text{pump}} \hat{a}_{\text{pump}} + \frac{1}{2} \right) + \hbar\omega_{\text{signal}} \left(\hat{a}^\dagger_{\text{signal}} \hat{a}_{\text{signal}} + \frac{1}{2} \right) + \hbar\omega_{\text{idler}} \left(\hat{a}^\dagger_{\text{idler}} \hat{a}_{\text{idler}} + \frac{1}{2} \right).$$

The first interaction term in $\hat{H}$ corresponds to the transformation of a pump photon into two signal and idler photons. The second term is associated to the inverse physical process and necessary to guarantee the self-adjointness of the Hamiltonian. The system Hamiltonian was here established heuristically following [59], but it can be derived more rigorously [61].

We now examine the evolution of the pump beam using the quantum formalism. Assume the pump beam contains $N \gg 1$ photons, the intensity of the beam being $\hbar\omega_{\text{pump}} N$. Schematically, the output state $|\psi_{\text{out}}\rangle$ is[1]

$$\begin{aligned} |\psi_{\text{out}}(t)\rangle &= \hat{U}(t) \, |n_{\text{pump}} = N\rangle \\ &= e^{-\frac{i}{\hbar}\hat{H}_{\text{int}} t} \, |n_{\text{pump}} = N\rangle \\ &= \sum_{k=0}^{\infty} \left(\frac{it}{\hbar} \right)^k \frac{\hat{H}^k_{\text{int}}}{k!} \, |n_{\text{pump}} = N\rangle \\ &\approx \sum_{k=0}^{\infty} \left(-itg\sqrt{N} \right)^k |n_{\text{pump}} = N, n_{\text{signal}} = k, n_{\text{idler}} = k\rangle. \end{aligned} \tag{I.61}$$

[1] Note that we have discarded the free radiation term in the Hamiltonian for this calculation, because we use the interaction picture formalism.

where t is the interaction time of the pump as it propagates through the crystal. In the weak pump regime and rejecting the pump at the output with a filter, we get

$$|\psi_{\text{out}}\rangle \approx |\text{vac}\rangle + \lambda\,|n_{\text{signal}}=1, n_{\text{idler}}=1\rangle + \lambda^2\,|n_{\text{signal}}=2, n_{\text{idler}}=2\rangle \tag{I.62}$$

where $|\lambda|^2 \ll 1$ is proportional to the pump intensity. Eq. I.62 indicates that the major contribution to the output state is vacuum and that attempting to increase the brightness by pushing the pump intensity will result in significant 2-photon emissions in both the signal and idler modes, reducing the quality of the single-photons.

SPDC sources fall under the category of **probabilistic** single-photon sources due to the fundamental photon-number coherence of the output state and random photon emission times. SPDC sources can however be used as **heralded** single-photon sources by detecting the signal or idler photon to announce the arrival of the other. By the expression of the output state Eq. I.62, there is a brightness / photon purity trade-off for parametric sources. Parametric sources are by nature limited to the low brightness regime ($B \approx 1-2\%$) if photon purity is to be kept with acceptable levels ($g^{(2)}(0) \approx 2-4\%$) [71, 72]. It is in theory possible to multiplex several heralded single-photon sources into a near-deterministic source, but the scaling of this process remains an open question [73].

We also mention that parametric sources can also be made using centrosymmetric materials that do not have a $\chi^{(2)}$ nonlinearity. In that case, the $\chi^{(3)}$ nonlinearity produces single-photons via **spontaneous four-wave mixing**, consuming two pump photons to produce two signal and idler photons at different wavelengths.

I.3.3 - On-demand single-photon sources

A second type of single-photon sources, such as neutral atoms [75], ions [76], molecules [77] or solid-state emitters [78], may operate by an on-demand process: pulsed excitation of two-level system and spontaneous emission of a photon following the decay to the ground state. In contrast to probabilistic single-photon sources, deterministic sources are in principle not bound to a brightness / photon purity trade-off. Fabricating and integrating on-demand sources generating pure and indistinguishable single photons with unit brightness, collected into a single optical mode without losses, is however a considerable challenge [79].

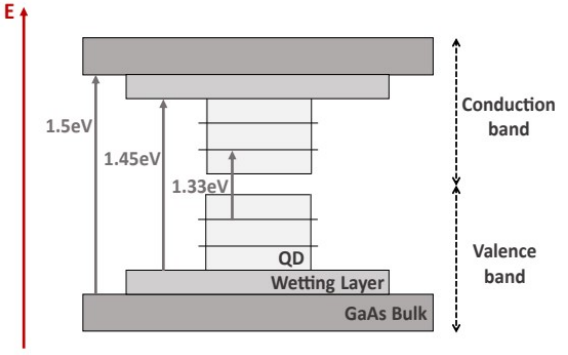

Figure I.9: From [74]. **Spatial band discontinuities induce discretization of the QD energy levels.** The wetting layer and QD are made of InGaAs (indium gallium arsenide). 1.33 eV = 930 nm.

Here we focus on **semiconductor quantum dots (QDs)** [80], that is quantum systems with discrete energy levels due to confinement in all three directions of space, where the confinement arises from spatial band gap discontinuity. The discreteness of the energy levels provides semiconductor QDs with an atom-like behavior. Hence, QDs act as so-called "artificial atoms".

Quandela single-photon sources In this thesis, we work with semiconductor QDs technology developed and investigated by the group of Pascale Senellart [81, 32] and now fabricated by *Quandela*. Droplets of InGaAs (indium gallium arsenide) are grown via molecular beam epitaxy on a substrate of GaAs (gallium arsenide) [74]. Fig. I.9 shows that this creates a quantum well structure in the electron bands, as required. Schematically, when the QD is excited by a pump pulse,

an electron-hole pair is created (**exciton**), which recombines spontaneously by emitting a photon around 930 nm (= 1.33 eV, see Fig. I.9). Other QD states can be excited such as biexcitons, with two electron-hole pairs, and trions, positively or negatively charged excitons [82].

QD formation by Stranski–Krastanov growth is non-deterministic [83]: the location of the QDs on the substrate is random. The geometry and environment of the QDs contributing to their photon emission properties is variable to some extent. A planar cavity is fabricated using molecular beam epitaxy (see Fig. I.10). The cavity features **distributed Bragg reflectors (DBRs)** below and above the QD. DBRs are mirrors composed periodical alternations of two materials "1" and "2" such that the layer thickness L_1 and L_2 of each material obeys

$$L_1 n_1 = L_2 n_2 = \frac{\lambda_{\text{QD}}}{4} \tag{I.63}$$

where n_1 and n_2 are the refractive index of each material. In the case of *Quandela* sources, the DBR materials are GaAs and AlGaAs (aluminum gallium arsenide). The top DBR is thinner than the bottom one, to favor emission towards the top.

After selecting the viable QDs on the sample, a cylindrical cavity is etched around the QD by in-situ lithography (see Fig. I.11), whose resonant wavelength λ_{cav} approximately matches the QD emission wavelength λ_{QD} [84]. The emission wavelength of the QD can be fine-tuned to match the pillar resonance by applying a voltage of the order of 1-2 V between the top and bottom extremities of the pillar. This leverages the Stark effect to shift the QD energy levels. For that purpose, the bottom (resp. top) DBR is n-doped (resp. p-doped), resulting in a diode structure with the QD in the central region.

The purpose of the cavity is to expedite the decay of the QD to its ground state, as well as guarantee photon emission into a single and well-defined optical mode. Indeed, a single-photon source with a very long decay time and omnidirectional photon emission is not suitable for our purposes. The cavity operates based on the Purcell effect [85], described by the Purcell factor

$$F_P = \frac{3}{4\pi}\left(\frac{\lambda_{\text{QD}}}{n}\right)^3 \frac{Q}{V} \tag{I.64}$$

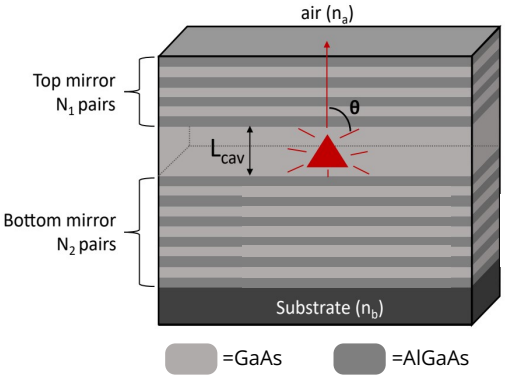

Figure I.10: From [74]. **QD in a planar cavity between two DBRs.** $N_1 \approx 15$, $N_2 \approx 36$. GaAs: gallium arsenide. AlGaAs: aluminum gallium arsenide.

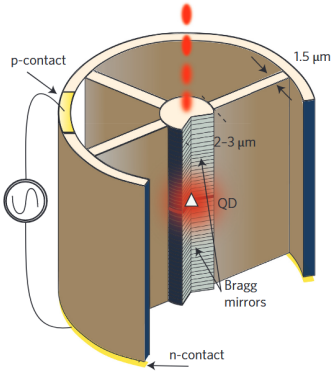

Figure I.11: From [32]. **Schematic of the single-photon source.** The structure features a QD between DBRs, and contacts to apply a static voltage.

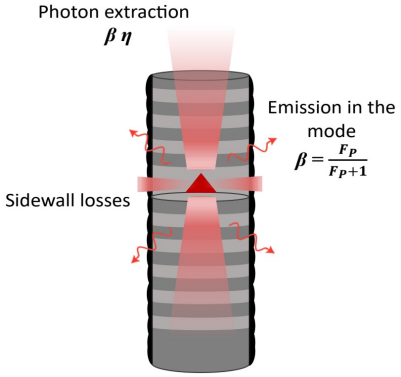

Figure I.12: From [74]. **Parameters affecting photon extraction.** η designates the extraction efficiency, which depends on absorption, sidewall and bottom losses.

with λ_{QD} the wavelength of the emitted photon, n the refractive index of the GaAs cavity, Q the cavity quality factor and V the mode volume. The preferential emission of a photon in the cavity mode instead of emitting in all directions is evaluated from

$$\beta = \frac{F_P}{1+F_P} \tag{I.65}$$

Increasing Q in Eq. I.64 to optimize the Purcell factor F_P is not an option, because emitted photons should to escape the cavity as fast as possible. The alternative is to reduce the size of the cavity, however this entails more photon losses on the side of the cavity (see Fig. I.12), which can however be mitigated at the fabrication level [74]. The engineering of the QD single-photon sources is beyond the scope of this work.

In the following, we focus on a few particular aspects of solid-state QD-based single-photon emitters and their influence on high-fidelity photonic QI processing. The two excitation schemes used in this thesis are compared in Section I.3.3.A. QD noise sources are discussed in Section I.3.3.B.

I.3.3.A - QD excitation schemes

Resonant excitation The QD acting in first approximation as an artificial atom can be addressed using resonant light, that is wavelength-tuned to the ground (g) → first excited state (e) transition. We can then apply the quantum optics formalism to treat the interaction of a two-level system with light [59]. This leads in particular to **Rabi oscillations** (see Fig. I.13). For an idealized square pulse of excitation laser, the probability of exciting the QD into the excited state is

$$\mathbb{P}(g \to e) = \frac{\Omega_1^2}{\Omega_1^2+\delta\omega^2} \sin^2\left(\frac{\sqrt{\Omega_1^2+\delta\omega^2}}{2}\Delta T\right) \tag{I.66}$$

where ΔT is the duration of the pulse, $\delta\omega$ is the detuning of the excitation angular frequency with respect to the QD resonance and

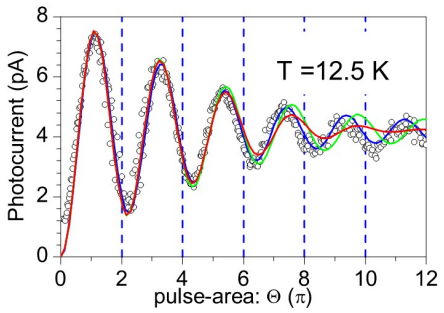

Figure I.13: From [86]. **Rabi oscillations of QD state.** Rabi oscillations in a resonantly driven InGaAs/GaAs QD. Continuous: theory. Markers: experimental data. The QD at 12.5 K is excited using 951 nm Gaussian pulses with a duration of 4 ps.

$$\Omega_1^2 = \frac{2d^2}{\hbar^2} I \tag{I.67}$$

is the **Rabi frequency** with d the dipole element associated to the $g \to e$ transition and I the intensity of the excitation beam at the QD's location. We define the **pulse area** Θ such that

$$\mathbb{P}(g \to e) \approx \sin^2(\Theta/2). \tag{I.68}$$

The QD is in the excited state when it receives a π**-pulse** with $\Theta = \pi$. The decay of the Rabi oscillations in Fig. I.13 are caused by the finite lifetime of the excited state, as well as interactions with the phonon bath [74].

It is important to note that resonant excitation of a perfectly circular QD cavity will always result in half of the photons being lost due to the polarization filtering [74]. This can however be improved using elliptical cavities [87].

There are other significant hurdles when operating experiments with resonant excitation on large time scales, i.e. more than 10 hours, which concerns the majority of the work in this manuscript. In resonant excitation, parasitic reflected excitation light is separated from the emitted single-photons using polarization filtering. Hence, any uncompensated polarization rotation in fibers

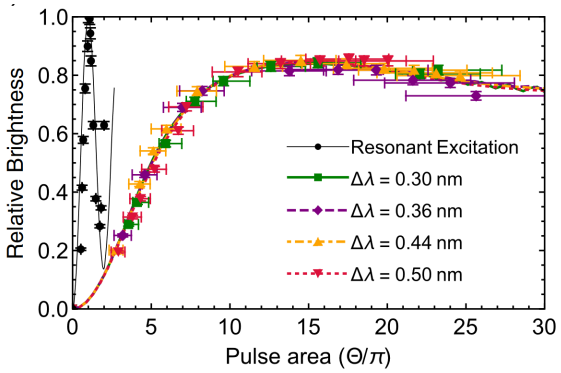

Figure I.14: From [88]. **Quasi-resonant excitation has a saturation behavior.** Brightness as a function of pulse area for different detunings of the excitation with respect to the resonance. The maximum brightness achieved in resonance normalizes the measured brightness to 1.

due to temperature fluctuations degrades significantly the quality of the photons by increasing $g^{(2)}(0)$. Second, the intensity of the excitation laser must be closely monitored to continuously provide π-pulses for optimal brightness and single-photon purity.

Both issues are solved by harnessing features specific to solid-state QDs: quasi-resonant excitation.

Quasi-resonant excitation **Longitudinal-acoustic (LA) phonon excitation** or **quasi-resonant excitation** [89, 90, 91] is achieved by sending blue-detuned excitation pulses, more energetic than the resonance. Schematically, this excites the cavity phonon bath, which then relaxes by bringing the QD into an excited state.

Because the excitation laser is detuned from the wavelength of the emitted photons by ≈ 1 meV (≈ 1 nm), parasitic pump light is efficiently rejected using optical filters. The photon emission rate has a saturating behavior at high excitation powers (see Fig. I.14). This saturation behavior provides a significantly enhanced stability during the operation of the single-photon source, adapted to the continuous operation of a single-photon source over long timescales, as discussed in Section II.4.3.D.

Quasi-resonant excitation has a few drawbacks. Note in Fig. I.14 that full population inversion is challenging to achieve using quasi-resonant excitation, thus the brightness achieved is lower than the theoretical maximum. The upper-bound on the achievable population inversion is related to the temperature of the phonon bath [91] and has a typical value of ≈85 % using our QDs at 4 K [88, 71]. Quasi-resonant excitation does not excite the QD coherently, that is the generated photonic state is a classical superposition of vacuum and $|1\rangle$. On the other hand, resonant excitation generates so-called **photon-number coherence**. Coherent superpositions of vacuum and $|1\rangle$ enable the exploration of rich physics [92]. Finally, quasi-resonant excitation require substantially more energetic excitation pulses (≈ 30 μW compared to $\ll 1$ μW fo resonant excitation), which may prevent reaching the optimal excitation power when using filtered broadband excitation pulses generated by a femtosecond laser for instance.

I.3.3.B - Charge and spin noise

We require indistinguishable photons to perform high-fidelity QI processing. A major source of indistinguishability is **charge noise** [93], which refers to the random fluctuations in the local electric field around the single-photon emitter, often caused by the movement of charges (such as electrons or holes) in the surrounding environment. These fluctuations lead to variations in the energy levels of the emitter via the Stark effect, resulting in spectral broadening of the emis-

sion line. In other words, due to charge noise, successively emitted photons may have differing wavelengths exceeding the natural emission line of the emitter. This results in the partial distinguishability of photons emitted from the same QD (see Fig. II.23).

QD noise sources are a key issue to address, as our current photonic quantum computing devices require photons emitted at substantially different times to interact (typically up to 1 μs). The success of the operation on the photons depends thus on the capability of these photons to be indistinguishable from each other, as demonstrated in our GHZ state experiment in Section II.6. The mitigation of charge noise is however outside of the scope of this thesis.

We have seen in this section the methods used in this thesis to generate single-photons and assess their quality. During this thesis, I routinely characterized single-photon sources, focusing on improving the stability and quality of the photon emission, in order to achieve the performance required for long high-fidelity experiments. We now cover in the following section the manipulation of light using photonic integrated circuits.

I.4 - Light manipulation in integrated circuits

Most optical laboratory experiments are performed with **free-space/bulk optics**, where the optical elements, such as lenses, mirrors and beamsplitter cubes, are massive components installed on an optical table. While this approach to optics enables the rapid setting up of experiments with off-the-shelf components, it is hardly scalable or compact. The simultaneous manipulation of hundreds of photons for large-scale QI processing can benefit from a different approach: **integrated photonics**. Integrated photonics is the study and application of photonic devices that integrate multiple optical components on a single chip, also called **photonic integrated circuit (PIC)**, to generate, manipulate and detect light. Every PIC can be seen in first approximation as a portion of material featuring waveguides, guiding light in the structure of the PIC. We call the **number of modes** of a PIC the number of parallel waveguides running through the PIC. The integration of optical circuits into single chips grants compactness as well as high phase stability, and opens the door to large-scale manufacturing.

We focus in this section, and in this thesis, on light manipulation with PICs. Section I.4.1 introduces the basic components features in the PICs, that are then assembled in Section I.4.2 into interferometers. We review various platforms for photonic integrated technologies in Section I.4.3.

I.4.1 - Integrated building blocks

At the core of any PIC lies the fundamental building block: the waveguide. A waveguide confines and directs light, guiding it along a predefined path with minimal loss. Typically, a waveguide consists of a high-refractive-index core surrounded by lower-refractive-index cladding. Fig. I.15 displays a simulation of a silicon nitride waveguide ($n_{\mathrm{SiN}} = 1.99$) of dimensions 800 × 150 nm, embedded in silica ($n_{\mathrm{SiO_2}} = 1.452$). The color scale indicates the electromagnetic field intensity. The mechanism ensuring that light remains confined within the core can be understood as total internal reflection, although a proper treatment with Maxwell's equations is more rigorous. The geometry and materials of the waveguide dictate its mode structure and propagation characteristics, playing a pivotal role in determining the overall performance of the PIC, as discussed in Section I.4.3.

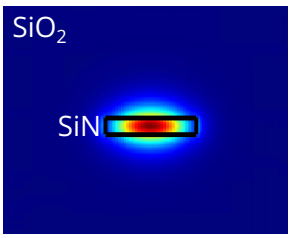

Figure I.15: Electromagnetic simulation of waveguide confinement via the finite-elements method.

Waveguides not only enable the transmission of light across a circuit but also serve as the foundation upon which more complex components like phase shifters (PSs) and beamsplitters are built. Most reconfigurable PICs for light manipulation embark these two types of components, and thus operate in the realm of linear optics (see Section I.2.4). PSs apply a phase shift on light while beamsplitters combine light on two spatial modes. A beamsplitter in a PIC is usually implemented as a **directional coupler**, which harnesses evanescent coupling between two waveguides to enable light to "leak" into the other waveguide as depicted on Fig. I.16. In the coupling region of the directional coupler, the guided electromagnetic modes overlap with the other waveguide. The reflectivity R of the implemented beamsplitter by a directional coupler is expressed as [94]

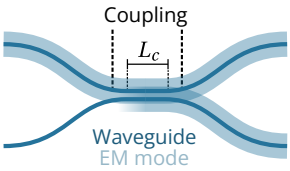

Figure I.16: Directional coupler

$$R = \cos^2\left(\frac{\pi}{2}\frac{L_c}{L_\pi} + \phi_0\right) \tag{I.69}$$

where L_c is the length of the straight coupling region, ϕ_0 is an offset introduced by the evanescent coupling occurring in the bends around the straight coupling region, and L_π is the length required to achieve a complete power transfer, which depends on the materials and geometry of the waveguides. Beamsplitters can also be implemented e.g. as 2 × 2 **multimode interferometers (MMIs)** [96]. MMIs are composed of a very large multimode waveguide, where the guided modes are free to propagate and interfere, leading to a controlled splitting and recombination of light. MMIs provide greater resilience to fabrication errors and a broader bandwidth, but they also introduce higher losses [97, 98], making them less suitable for quantum photonics.

On the other hand, PSs induce a phase shift on propagating light by modulating the effective refractive index of the waveguide. This can be achieved through various mechanisms, such as thermo-optic effects, where localized heating alters the refractive index, or electro-optic effects, where an applied electric field changes the refractive properties of the waveguide material. For a thermo-optic PSs, as illustrated in Fig. I.17, the induced phase shift $\Delta\phi$ is expressed as [99]

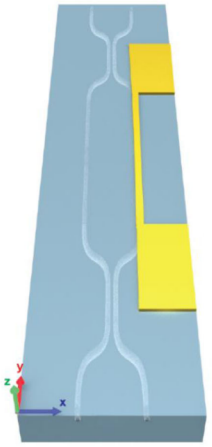

Figure I.17: from [95] **Thermo-optic PS** with Cr-Au heater.

$$\Delta\phi = \frac{2\pi L}{\lambda_0}\frac{\mathrm{d}n}{\mathrm{d}T}\Delta T \tag{I.70}$$

with L the PS heater length, λ_0 the vacuum wavelength, $\frac{\mathrm{d}n}{\mathrm{d}T}$ the **thermo-optic coefficient** and ΔT the temperature variation. We further discuss and compare PS technologies in Section I.4.3.

Symmetric beamsplitters and PSs can be combined to obtain another building block called **Mach-Zehnder interferometer (MZI)** (see Fig. I.18). The unitary matrix describing a **symmetric MZI** (featuring two internal PSs) is

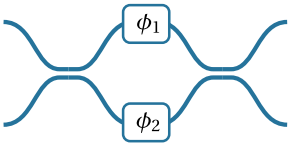

Figure I.18: Symmetric Mach-Zehnder interferometer

$$U_{\mathrm{MZI}}(\phi_1,\phi_2) = \frac{1}{\sqrt{2}}\begin{bmatrix}1 & i\\ i & 1\end{bmatrix}\cdot\begin{bmatrix}e^{i\phi_1} & 0\\ 0 & e^{i\phi_2}\end{bmatrix}\cdot\frac{1}{\sqrt{2}}\begin{bmatrix}1 & i\\ i & 1\end{bmatrix} \tag{I.71}$$

$$= ie^{i\frac{\phi_1+\phi_2}{2}}\begin{bmatrix}\sin\left(\frac{\phi_1-\phi_2}{2}\right) & \cos\left(\frac{\phi_1-\phi_2}{2}\right)\\ \cos\left(\frac{\phi_1-\phi_2}{2}\right) & -\sin\left(\frac{\phi_1-\phi_2}{2}\right)\end{bmatrix} \tag{I.72}$$

with ϕ_1 and ϕ_2 the phases implemented by the two phase shifters. An MZI thus implements a tunable beamsplitter of variable reflectivity

$$R = \sin^2\left(\frac{\phi_1-\phi_2}{2}\right). \tag{I.73}$$

Tunable beamsplitters can also be realized by mechanical [100] or thermal [101] action on a directional coupler.

It is also possible to integrate polarizing beamsplitters [102], as well as variable waveplates [103] to manipulate the polarization of light, but these components are still in the early development stage. Spectral filters have also been integrated on chips [104].

In the following subsection, MZIs and PSs are combined to form larger interferometer meshes, some endowed with remarkable properties.

I.4.2 - Interferometer meshes

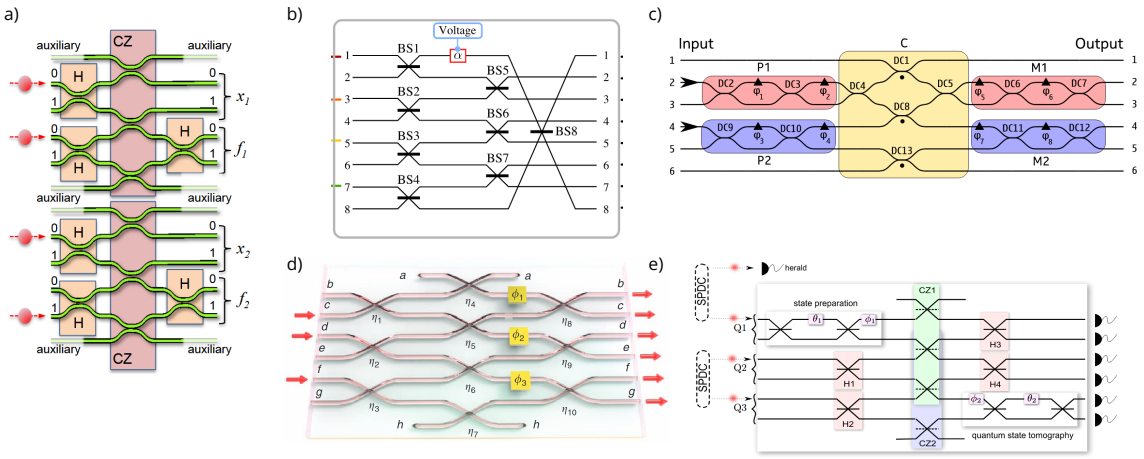

Figure I.19: Specialized PICs for precise QI tasks. a) From [105]. Silica-on-silicon static PIC for factorizing "15" using Shor's algorithm. **b)** From [70]. Silica PIC with femtosecond-laser-written waveguides and one phase shifter used to measure the global indistinguishability of four photons. **b)** From [106]. Silica-on-silicon PIC that generates an arbitrary postselected 2-photon Bell state and performs its tomography, using 8 phase shifters in total. **c)** From [107]. Silica-on-silicon PIC with three phase shifters for analyzing interference effects from three photons. **d)** From [108]. Silica-on-silicon PIC used to demonstrate postselected quantum teleportation using three photons and four phase shifters.

Most interferometers are assemblies of reconfigurable phase shifters and static directional couplers. It is possible to fabricate specialized interferometers dedicated to a specific purpose. Some examples from the litterature are

- [105], which factorized the number "15" using Shor's algorithm [109] with a static silica-on-silicon interferometer, i.e. consisting only of beamsplitters, to implement Hadamard and postselected CZ gates (Fig. I.19a).
- The authors in [70] designed a silica PIC with femtosecond-laser-written waveguides for measuring the global indistinguishability of four photons, requiring a single phase shifter (Fig. I.19b).
- The PICs of [110, 106, 111] features a static central part implementing a postselected CNOT gate, while MZIs upstream and downstream, for a total of 8 phase shifters, enable the generation of arbitrary Bell-states and their tomography (Fig. I.19c). The design was notably used by [111] for quantum chemistry (see Section I.5.1.B).
- [107] uses a silica-on-silicon PIC for investigating the quantum interference of three photons generated by a parametric source (Fig. I.19d).
- [108] demonstrated quantum teleportation on a silica-on-silicon PIC, which implements a postselected CZ gate and Hadamard gates (Fig. I.19e). MZIs are used to prepare arbitrary single-qubit state preparation and perform their tomography.

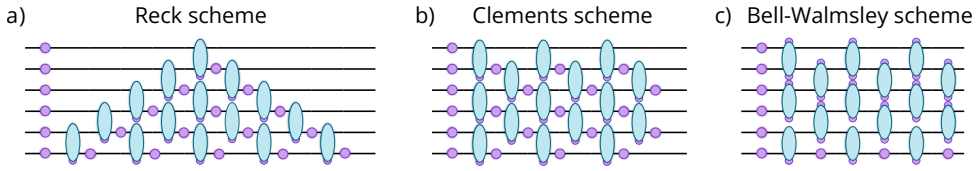

Figure I.20: **Universal-scheme PICs can implement any unitary matrix.** Comparison between 6-mode **a)** Reck, **b)** Clements and **c)** Bell-Walmsley interferometers. Blue ellipses: MZIs. Purple disks: PSs. Note that the Reck and Clements scheme feature only MZIs with an internal PS on the bottom mode, while the Bell-Walmsley scheme has mostly symmetric MZIs.

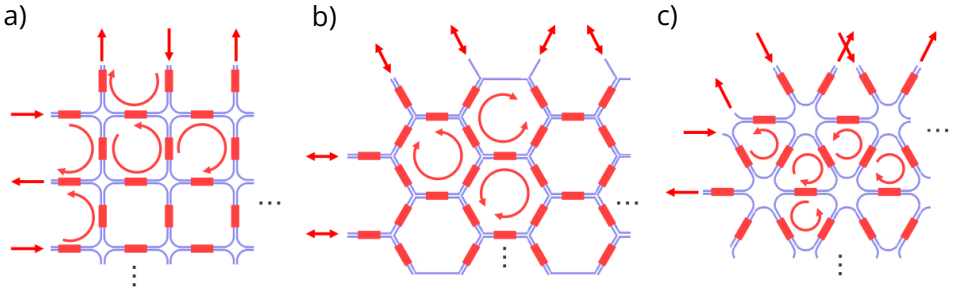

Figure I.21: **Recirculating waveguide meshes.** From [117]. Comparison between meshes with **a)** square, **b)** hexagonal and **c)** triangular unit cells.

- In Chapter II, we use two silica PICs with femtosecond-laser-written waveguides generating postselected entangled states and enabling to perform their tomography by implementing arbitrary single-qubit gates. In contrast to the other entries (except [70]), we use single-photons generated from a QD, instead of parametric sources.

Current demonstrations of near-term photonic quantum computing however mostly use interferometers capable of implementing a wide range of transformations on light. **Universal-scheme** PICs can implement any unitary matrix acting on the spatial input modes of the circuit (see Section I.2.4). The first proposal for such an interferometer was the triangular Reck scheme [36] (Fig. I.5.2a). A Reck interferometer with m modes is optimal in the number of m^2 reconfigurable phase shifters it features: an $m \times m$ unitary matrix is indeed parametrized by m^2 real parameters. The scheme was nevertheless superseded by the rectangular Clements scheme [37] (Fig. I.5.2b) which is more compact and allows a more homogeneous distribution of internal losses. The third generation of universal interferometers are built on the further improved Bell-Walmsley scheme [38] (Fig. I.5.2c), which maximally symmetrizes the internal losses by using symmetric MZIs. Thus all light paths undergo comparable losses in a Bell interferometer, which plays an important role in mitigating photon loss [112].

Other proposals for universal schemes designed for more resilience against hardware errors, but that have stayed to our knowledge at the simulation stage. are:

- [113], which replaces the MZIs in the Clements scheme by symmetric beamsplitters.
- the scheme of [114], alternating between layers of PSs and generalized beamsplitters on m modes.
- [115] and [116] that use more complex unit cells in a Clements scheme.

	Silica waveguides	Silicon-on-insulator	Silicon nitride	Lithium niobate on insulator	Gallium arsenide	Indium phosphide	Silicon oxynitride
Refractive index contrast	Low	High	Moderate	Moderate	Low	Low	Low, tunable
Losses	Ultralow	Moderate linear loss, High two-photon absorption	Low linear loss, low two-photon absorption	Moderate	Moderate	Moderate	Low linear loss, low two-photon absorption
Nonlinear index	Weak χ^3	Strong χ^3	Strong χ^3	Strong χ^2	Strong χ^2	Strong χ^2	Moderate χ^3
Laser	N/A	N/A	N/A	N/A	Yes	Yes	N/A
Modulator	Low speed	High speed	Low speed	High speed	High speed	High speed	Low speed
Detector	N/A	Ge, High speed	N/A	N/A	High speed	High speed	N/A
Mode matching with optical fibers	Excellent	Poor	Moderate	Moderate	Poor	Poor	Moderate
CMOS compatibility	N/A	Excellent	Good	N/A	N/A	N/A	Good

Figure I.23: From [120] (2023). **Comparison between material platforms for integrated photonics.** Green columns indicate material platforms used in this thesis.

The interferometer schemes discussed so far are so-called **forward-only meshes**, in which light can only propagate in a single direction. **Recirculating meshes** on the other hand are built with different unit cells (see Fig. I.21), allowing to program arbitrary paths for light. Recirculating meshes form the backbone of **programmable photonic circuits** [117]. Programmable circuit are too cumbersome to be used for the precise manipulation of quantum light, although the implementation of 3×3 and 4×4 unitary matrices has been recently demonstrated on programmable circuits [119]. Programmable photonic circuits are however relevant for optical and radio-frequency signal processing, providing versatility in the operations and tasks that can be performed with light such as signal routing and filtering (see Fig. I.22).

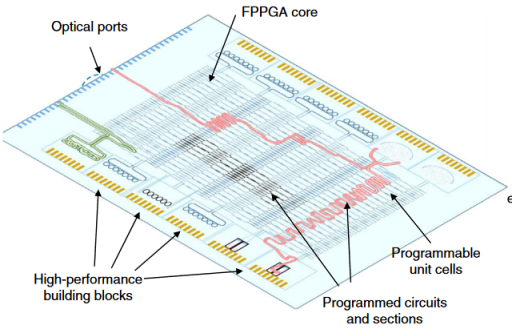

Figure I.22: **Programmable circuit** From [118].

In the next subsection, we review the different platforms for integrated photonics.

I.4.3 - Integrated platforms and technologies

The different material platforms available for the fabrication of photonic integrated technologies are summarized in Fig. I.23. The different criteria for evaluating the platforms are:

- **Refractive index contrast** (difference between waveguide core and cladding refractive indices): a high index contrast signifies that the guided mode is tightly confined by the waveguide, and a smaller mode is usually more sensitive to waveguide sidewalls imperfections that may scatter the guided light and induce additional optical losses. A high index contrast is beneficial however for compactness as waveguides can be sharply bent. On the opposite, material platforms with low refractive index contrast such as glass have lower losses in general but are less compact.

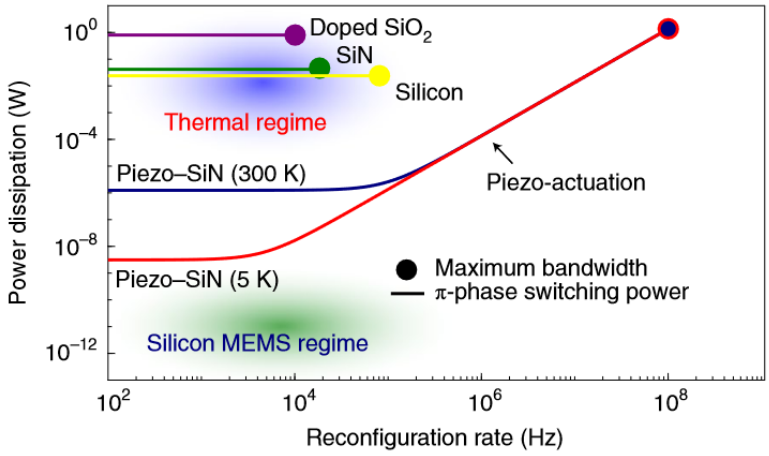

Figure I.24: From [124] (2022). **Reconfiguration speed and power consumption of thermo-optic and mechanical PSs.**

- **Losses**: the amount of optical losses during propagation in the waveguides, due to absorption and scattering. Typical figures for single-mode waveguides are 0.1 dB/cm for silicon nitride [121, 122], 0.15 dB/cm for glass [123] and 0.1 dB/cm for lithium niobate on insulator [25]. Experimentally measured values for losses are usually limited by the fabrication quality of the waveguides and not by the absorption coefficient of the material.
- **Nonlinear index**: A strong $\chi^{(2)}$ or $\chi^{(3)}$ nonlinearity can be harnessed to integrate parametric light sources and effects on a chip. A strong $\chi^{(2)}$ is also necessary to use fast electro-optic phase shifters, as discussed below.
- **Laser** and **Detector**: indicates if the platform allows the integration of lasers and detectors.
- **Modulator**: Phase shifter reconfiguration speed, discussed below.
- **Mode matching with optical fibers**: degree with which the guided light can be coupled to input and output optical fibers. This is related to the refractive index contrast, as a high refractive index contrast means that the guide mode size is substantially different from the fiber mode due to high guided confinement, and thus harder to couple.
- a **CMOS compatible** platform allows the integration of electronic components on a single monolithic chip.

One major aspect of the operation of PICs is the reconfiguration capabilities of the integrated PSs. PSs may harness the following physical effects to implement a phase shift:

- **Thermo-optic** [99]: the PS is physically implemented as a heater generating heat when a current or voltage is applied on it. The locally increased temperature modifies the refractive index of the waveguide, which then implements the targetted phase shift on light. Thermo-optic phase shifters are relatively slow with modulation bandwidths in the 100 kHz range, but easy to integrate on any platform.
- **Mechanical** [124]: using a piezo-actuator, it is possible to implement a phase shift via strain-induced birefringence and moving boundary effects. Mechanical PSs are substantially faster than thermo-optic ones, as can be seen in Fig. I.24, with modulation bandwidths in the MHz range.
- **Electro-optic** [125] PSs apply phase shifts via the Pockels effect for instance, which consists in the variation of the waveguide refractive index with respect to an applied electric field.

As a consequence, electro-optic phase shifters are immensely fast, with bandwidths in the tens of GHz range, with a caveat: the material platform must have a strong $\chi^{(2)}$ nonlinearity.

Silicon-based photonics has given the ability to fabricate large-scale and complex PICs, with a first demonstration of a 6-mode Reck interferometer [126]. This was then followed by a 12-mode Clements interferometers [122, 127] ($\approx$ 100 integrated PSs), followed by 20-mode Clements interferometers [18] ($\approx$ 400 integrated PSs). [128] uses a PIC to manipulate up to 8 squeezed modes. Silicon photonics is also widely used for creating PICs for optical multi-layer neural networks [129, 130]. Silica-glass with femtosecond-laser-written waveguides is another mature PIC platform, on which 4-mode [131], 6-mode [132, 133, 123] and 8-mode [134, 135] Clements interferometers were produced.

In this thesis, we use silica (Chapter II) and silicon nitride (Chapter III) PICs. The PICs are fitted with thermo-optic phase shifters, with single-PS reconfiguration times on the order of 100 ms (silica) to less than 5 ms (silicon nitride).

We conclude this chapter with the demonstration of QI processing merging single-photon sources with PICs.

I.5 - QI processing with integrated photonics

Photonic systems are particularly advantageous for quantum communication due to their ability to transmit quantum information over long distances with minimal loss, making them ideal for tasks like quantum key distribution and secure communication [9]. Recent demonstrations [136, 15, 16] also have shown that photonic systems can perform complex quantum computing tasks that have so far resisted classical spoofing attempts. Photons may in general offer an inspiring approach to QI processing because of their inherent mobility and the possibility of combining different qubit encodings (see Section I.2.5).

Integrated photonics plays a key role in the near-term development of QI processing because it allows quantum light to be manipulated with unparalleled compactness, stability, and scalability. In this thesis, we interface QD-based single-photon sources, PICs and single-photon detectors to perform quantum computation tasks. Consequently, our focus is on the use of integrated photonics for computing-oriented tasks in the discrete-variable framework. Nevertheless, we highlight that integrated photonics also supports quantum communication [120] and that continuous-variable photonic quantum computing is advancing rapidly [137].

We review recent developments in near-term photonic QI processing in Section I.5.1. We then discuss in Section I.5.2 the Knill-Laflamme-Millburn scheme, a proposal for photonic universal quantum computing based on linear optics. Finally, we briefly explore measurement-based quantum computing in Section I.5.3, in which computation is carried out through a sequence of adaptive measurements on an entangled resource state.

I.5.1 - Near-term photonic quantum computing

There is significant interest in leveraging current quantum technologies to achieve practical computational advantages before fully scalable, fault-tolerant quantum computers are realized. Unlike other quantum systems that require ultra-cold environments or complex electromagnetic control, photonic systems are naturally robust against decoherence, making them well-suited for implementing quantum algorithms in the **noisy intermediate-scale quantum (NISQ)** era.

Most applications demonstrated on current integrated photonic quantum computing machines boil down to a sampling task consisting of implementing unitary matrices on PICs, injecting indistinguishable single-photons or squeezed states at the input and collecting resulting output states

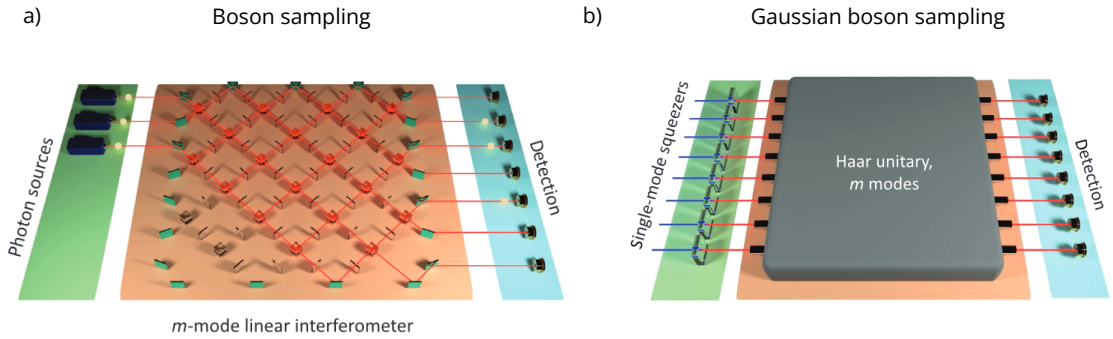

Figure I.25: Adapted from [142]. **Main boson sampling variants. a)** Initial proposal for boson sampling. n single-photon sources inject indistinguishable single photons into the m-mode interferometer, followed by single-photon detectors. **b)** Gaussian boson sampling uses single-mode squeezed states instead of single-photons.

[138, 71, 133, 139, 31]. This principle is used for instance to simulate bosonic quantum random walks using coupled integrated waveguides [140, 141].

We discuss in the following two specific sampling tasks: boson sampling in Section I.5.1.A and variational quantum algorithms in Section I.5.1.B.

I.5.1.A - Boson sampling

Boson sampling [142] was initially formulated as a problem specifically chosen to be hard for classical computers, but performed natively by photonic devices [14]: sampling from the output distribution of a linear interferometer injected with indistinguishable single-photons. On a photonic quantum device, this is straightforwardly performed by registering multi-photon coincidences at the output of an interferometer. Drawing output states from the full distribution is called **weak simulation**, as opposed to **strong simulation**, where the entire probability distribution is explicitly [143] computed. Weak simulation is hard for classical computers because computing the probability of obtaining a given multi-photon coincidence is related to the matrix permanent (see Section I.2.4) that is considered computationally expensive.

Gaussian boson sampling [144] is a variant of the original boson sampling model that uses **squeezed states of light** instead of single-photon states. Squeezed states for boson sampling are obtained from coherent states that have undergone interaction with a nonlinear medium in a cavity [145]. This variation allows for more flexible and practical experimental implementations while still providing computational tasks that are considered challenging for classical algorithms.

Boson sampling is deliberately designed as a computational problem that is tractable for photonic systems but lacks direct practical applications beyond being challenging for classical algorithms to solve. Despite its contrived nature, boson sampling serves as a prime example of near-term quantum advantage. Notably, all quantum advantage demonstrations to date that have resisted classical spoofing are exclusively Gaussian boson sampling tasks:

- [136] with 50 input squeezed states and a fixed 100-mode three-dimensional interferometer (see Fig. I.26a, 43-fold coincidence rate of $\approx$ 15 kHz, detection up to 76-fold coincidences). Most of the setup is free-space and fibered, and thus stabilized in phase. There is a caveat in using a fixed interferometer for boson sampling: in the original proposal [14], the interferometer is required to implement a Haar-random unitary matrix. Therefore, it is crucial to verify that the experimental interferometer does not implement a trivial unitary matrix, such as the identity or a permutation. Instead, it should approximate the statistical properties of Haar randomness to ensure the problem remains computationally hard for classical algorithms.

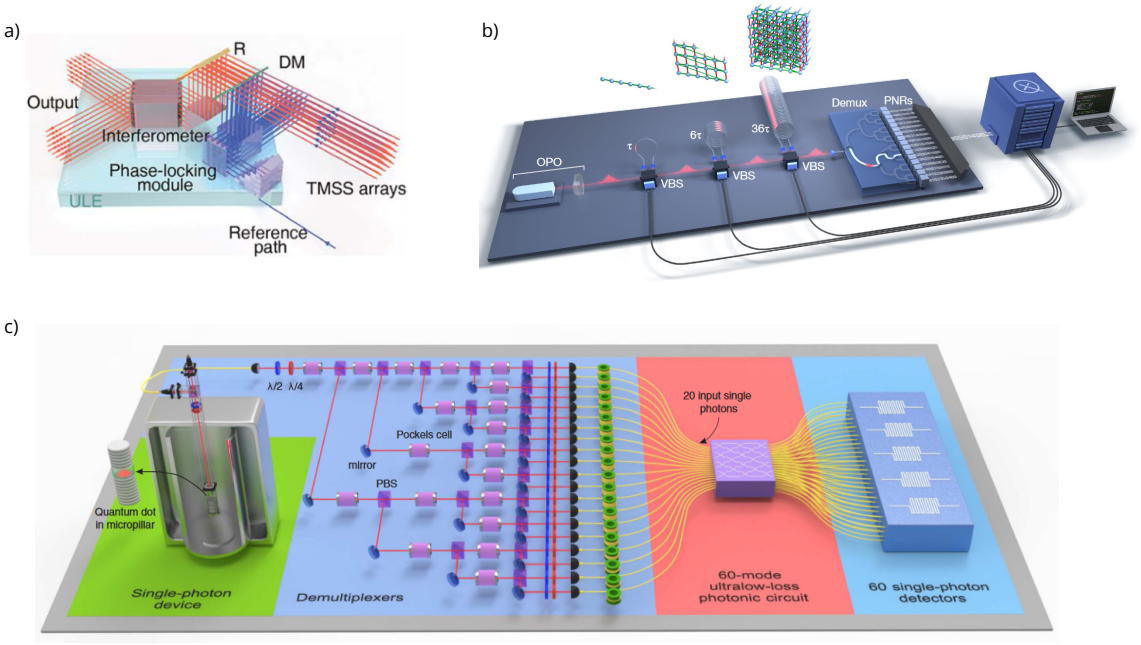

Figure I.26: Boson sampling experiments **a)** From [136]. three-dimensional interferometric network with 100 spatial and polarization modes for Gaussian boson sampling. **b)** From [16]. Gaussian boson sampling with a multipartite entangled Gaussian state generated using fiber delays. **c)** From [34]. Boson sampling with single-photons from a InAs/GaAs QD.

- [15] is an improvement to the previous experiment, with a larger interferometer on 144 modes and coincidences comprising up to 113 simultaneously detected photons. The interferometer remains fixed, but the experiment is reconfigured by changing the phases of the input squeezed states.
- The previous setup is further upgraded in [146] by adding photon-number resolving capabilities to the single-photon detectors. The experiment registered up to 255-fold coincidences.
- The experiment of Xanadu [16] (see Fig. I.26b) performs Gaussian boson sampling on 216 squeezed modes entangled in three dimensions. To do so, the setup cleverly implements reconfigurability of the interferometer from a single squeezed-state source by using free-space variable beamsplitters and fibered delay loops. The single interferometer output is actively demultiplexed to 16 photon-number-resolving detectors. On average, 125 photons are detected at a sampling rate of 10 kHz.

Single-photon-based boson sampling experiments are more challenging to realize, due to the stringent constraints set on the optical transmission of the setup and the brightness of the single-photon source [5]. For instance, [147] used a silicon chip to generate eight photons from SPDC and perform different boson sampling protocols. Note that because the parametric sources and the interferometer are optically integrated, active phase stabilization is not required. However, due to the low efficiency of parametric single-photon sources, the sampling rate is ≈ 1 mHz for 4 heralded and detected photons. Consequently, boson sampling with many indistinguishable single-photons requires a QD-based single-photon emitter. In this regard, we highlight the free-space boson sampling experiment of [34], performed with a static three-dimensional 60-mode interferometer and 20 indistinguishable input single-photons generated by a single QD (see Fig. I.26c). The experiment has following coincidence detection rates: 295 Hz (5 photons injected and detected), 0.01 Hz (10 photons injected and detected) and 1.7 mHz (20 photons injected and 14 detected).

I.5.1.B - Variational quantum algorithms

Another promising avenue for near-term photonic quantum computing is the implementation of **variational quantum algorithms (VQAs)** [148]. These hybrid algorithms combine the computational power of quantum processors with the optimization capabilities of classical computers. A popular example of a VQA is the **variational quantum eigensolver (VQE)**, which is used to find the ground state energy of a quantum system. In this approach, a quantum computer prepares a parameterized initial quantum state, and measurements are used to evaluate a cost function. A classical optimizer then adjusts the parameters to minimize the cost function iteratively, as schematized on Fig. I.27. VQAs are sampling-based algorithms, thus they are particularly well-suited for NISQ-era devices.

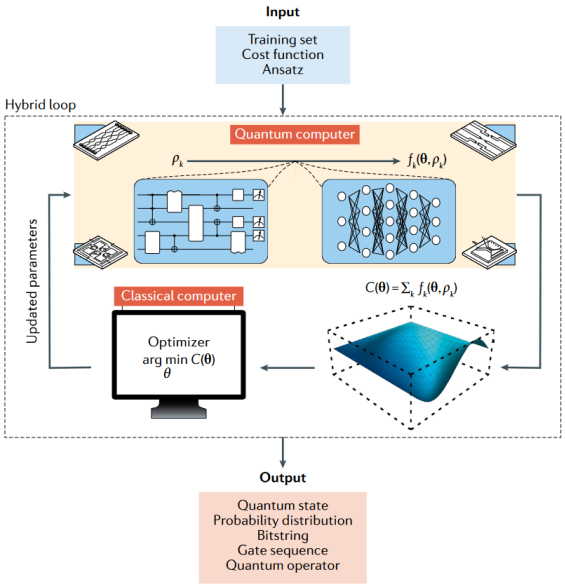

Figure I.27: From [148]. **Principle of VQA**

Photonic quantum systems using integrated photonics can naturally implement VQAs due to the fact that the parameters to optimize in the algorithms are encoded as phase shifts implemented by PSs. Thus, the optimizer only modifies a few voltages/electrical currents applied to the PIC, which otherwise remains static. VQE was first demonstrated in [111] on a photonic device.

Quantum machine learning (QML) [149] tasks, where quantum algorithms are designed to improve machine learning tasks such as classification, clustering, and optimization also fall under the category of VQAs. QML has been experimentally demonstrated on superconducting qubits [150] and with photonics [151].

Near-term quantum computing is interesting in its own right to generate traction and interest for quantum computing applications. This simultaneously allows technological processes to mature and valuable know-how to be gained, in anticipation of the requirements for universal quantum computing with linear optics, discussed in the following subsection. While this thesis primarily focuses on the near-term quantum computing regime, the challenges addressed here have broader relevance. Universal linear optical quantum computing shares many foundational elements and building blocks with near-term approaches, and stands to gain significantly from the advancements in integrated photonics developed in this work.

I.5.2 - Universal linear optical quantum computing

In this subsection, we use dual-rail path-encoded qubits (see Section I.2.5). We first show in Section I.5.2.A that it is not possible to implement a CNOT gate relying only on linear optics, and ways to circumvent this limitation. This provides the motivation for introducing the Knill-Laflamme-Millburn theory of universal quantum computing in Section I.5.2.B.

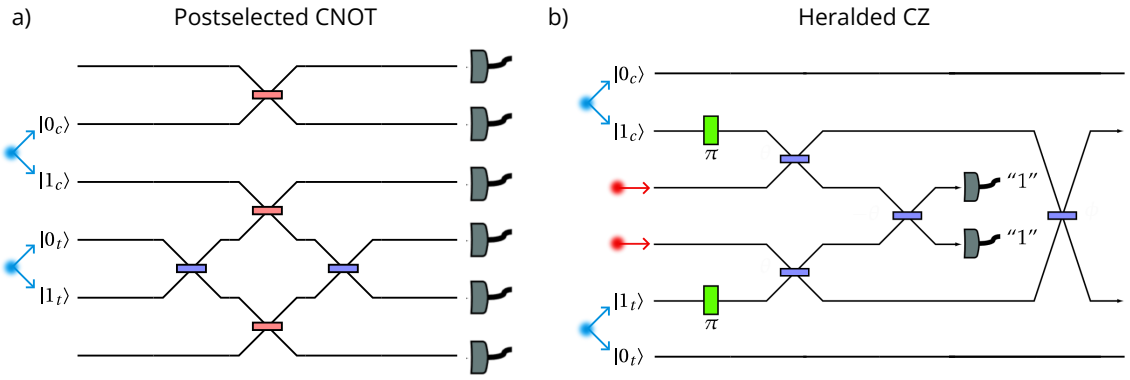

Figure I.29: Photonic entangling gates Blue input photons: control (c) and target (t) qubits. Red input photons: Ancillary photons. **a)** Postselected CNOT gate of [152]. Blue rectangles: symmetric beamsplitters. Red rectangles: beamsplitters of reflectivity 1/3. **b)** Adapted from [20]. Heralded CZ gate of [153]. Green rectangles: PSs. Blue rectangles: asymmetric beamsplitters.

I.5.2.A - Photonic CNOT gate

To prove that linear optics cannot implement a CNOT gate, it is equivalent to prove that it is not possible to create a Bell state using linear optics. Indeed, the Bell state $|\Phi^+\rangle$ is obtained from a CNOT gate, as shown in Section I.1.2. Consider a generic linear optical circuit on 4 modes implementing a unitary matrix $\hat{U}$ as depicted on Fig. I.28. Modes 1 and 2 (resp. 3 and 4) are associated to the dual-rail encoded qubit A (resp. B). The initial qubit state is $|0_A 0_B\rangle$. Applying the circuit on the initial state yields a linear transformation acting on the spatial mode creation operations of the form

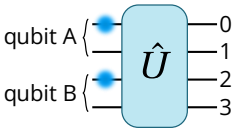

Figure I.28: 4-mode photonic circuit

$$|0_A 0_B\rangle = \hat{a}_1^\dagger \hat{a}_3^\dagger |\text{vac}\rangle \xrightarrow{\hat{U}} \sum_{k,l=1}^{4} u_{k1} u_{l3} \hat{a}_k^\dagger \hat{a}_l^\dagger |\text{vac}\rangle . \tag{I.74}$$

On the other hand, we want a Bell state creator that implements the transformation

$$\hat{a}_1^\dagger \hat{a}_3^\dagger |\text{vac}\rangle \xrightarrow{\text{Bell state creator}} \frac{1}{\sqrt{2}} (\hat{a}_1^\dagger \hat{a}_3^\dagger + \hat{a}_2^\dagger \hat{a}_4^\dagger) |\text{vac}\rangle . \tag{I.75}$$

If the Bell state creator is a linear optical linear implementing a unitary matrix $\hat{U}$, then the coefficients u_{k1} and u_{l3} of $\hat{U}$ are obey the following system of equations

$$\begin{cases} u_{11} u_{13} = 0 \\ u_{21} u_{23} = 0 \\ u_{31} u_{33} = 0 \\ u_{41} u_{43} = 0 \\ u_{11} u_{33} + u_{31} u_{13} = 1/\sqrt{2} \\ u_{21} u_{43} + u_{41} u_{23} = 1/\sqrt{2} \end{cases} \tag{I.76}$$

obtained by comparing Eq. I.74 and I.75. This system has no solution, thus linear optics cannot provide the necessary entanglement between photons to perform a CNOT gate, because there is no quadratic interaction term in the Hamiltonian of a linear optical circuit. The necessary nonlinearity can be provided to the optical circuit using nonlinear ingredients such as Kerr nonlinearities. The required nonlinearity strength is however several orders of magnitude higher than what is realistically achievable with current techniques [20].

Alternatively, quantum measurements can serve as a source of nonlinearity. [152] proposed a CNOT gate based on this principle with two caveats: it is a **probabilistic gate**, with success probability $1/9$, and it is **postselected**, meaning the output state is destroyed due to measurement upon application of the gate. It is also possible to design **heralded gates**, which consume additional **ancilla** photons to "announce" the success or failure of the gate. The output state can then be further used. A heralded CNOT with success probability $1/16$ was proposed in [154]. Similarly, a heralded CZ gate [153] with success probability $2/27$ exists.

From an experimental point of view, [110] and [106] implemented a postselected CNOT gate on specialized PICs, and used the PICs reconfigurability to perform the tomography of the generated Bell state. Similarly, [108] implemented the quantum teleportation protocol [155, 156, 157] with a postselected CNOT gate.

I.5.2.B - the Knill-Laflamme-Millburn paradigm

Knill-Laflamme-Milburn (KLM) theory represents a pivotal development in the field of photonic quantum computing [19]. The KLM scheme provides a constructive framework for achieving universal quantum computation using only linear optical elements, such as beam splitters and phase shifters, along with photon detectors and single-photon sources. KLM requires however photon-number resolving detectors and **feedforward** capabilities, which consist in adapting downstream elements of the circuit based on intermediate heralding measurements from the ancilla-assisted gates. Both requirements are currently technologically challenging.

The KLM protocol demonstrates that universal quantum computation is theoretically possible with linear optics, an essential insight for the development of photonic quantum computing. One of the primary advantages of the KLM protocol is its reliance on optical components that can all be integrated onto a PIC. However, the KLM scheme also comes with significant limitations. The probabilistic nature of the gate operations means that successful computation requires multiple trials, and the probability of success decreases with the complexity of the circuit. This issue necessitates the use of highly efficient photon sources and detectors, along with sophisticated error correction protocols to mitigate the inherent loss and noise. Furthermore, the need for large numbers of ancilla photons to boost success probabilities adds complexity and resource overhead to practical implementations.

For linear optical quantum computing to be viable, more efficient protocols are necessary. In response, several strategies have been proposed to enhance the scalability of the KLM scheme. The next subsection provides an overview of these approaches, which focus on reducing overhead by leveraging initial entanglement.

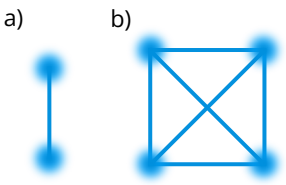

Figure I.30: **Graph states** **a)** and **b)** are respectively equivalent to a Bell state and a maximally entangled 4-qubit state $\frac{|0000\rangle+|1111\rangle}{\sqrt{2}}$ up to local single-qubit operations.

I.5.3 - Beyond KLM: measurement-based quantum computing

Measurement-based quantum computing (MBQC) [158, 159], also known as the "one-way" quantum computing model, represents a distinct approach to quantum computation that diverges from the traditional circuit model. MBQC leverages entangled quantum states to perform quantum computations through a series of adaptive single-qubit measurements. This model emphasizes the role of quantum measurements as the primary mechanism for computation, rather than the unitary evolution of quantum states, which is central to the circuit-based model of the KLM scheme.

In MBQC, the computation starts with the preparation of a highly entangled multi-qubit state, typically a **cluster state** [160]. A cluster state is usually represented as a **graph state**, that is a

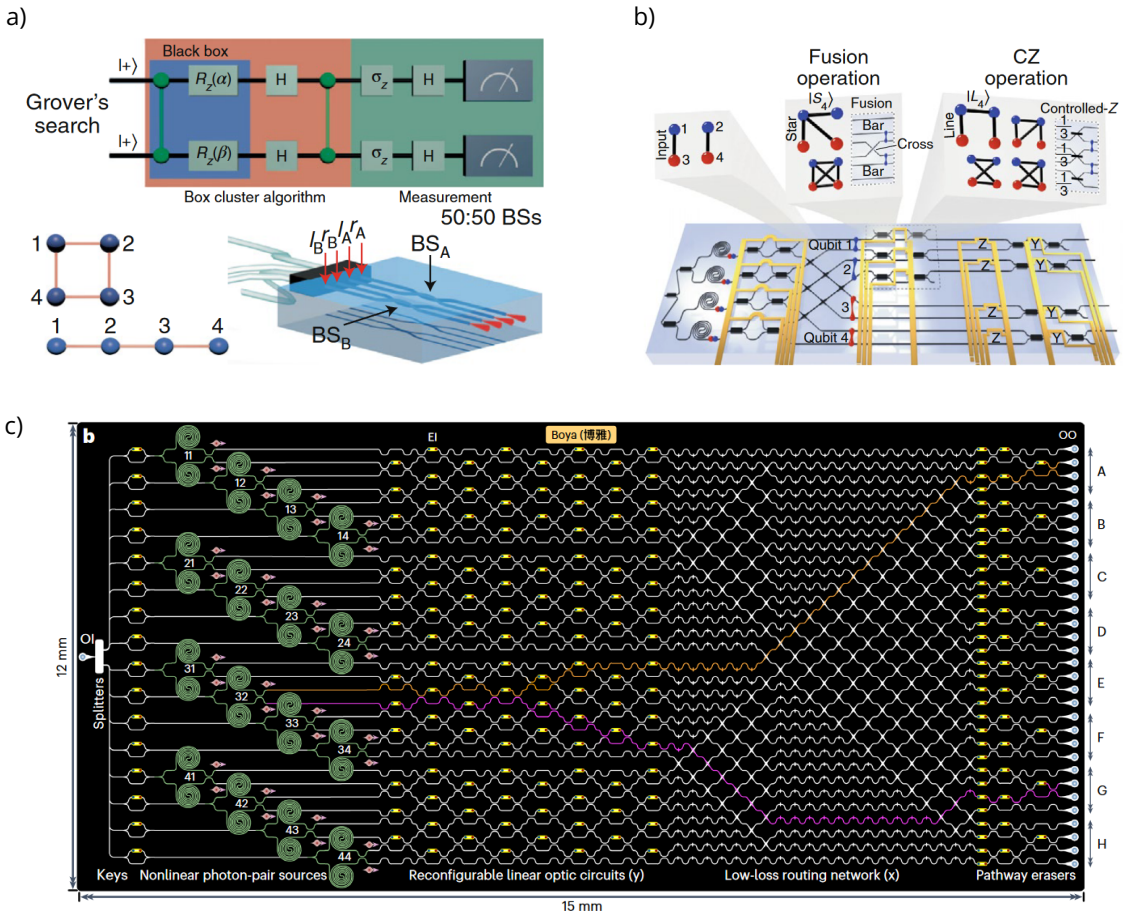

Figure I.31: Experimental demonstrations of MBQC. a) Adapted from [161] Implementation of Grover's search algorithm with MBQC and a static integrated circuit. **b)** (from [162]) and **c)** (from [30]): On-chip generation and manipulation of four-photon cluster states.

state entirely described by a graph where each vertex corresponds to a qubit, and each edge represents an entanglement link between the connected qubits. Graph states are created by preparing all qubits in the state $|+\rangle$ and then applying CZ gates between pairs of qubits according to the edges of the graph. Cluster state serves as a computational resource for MBQC and the desired quantum algorithm is then executed through a sequence of single-qubit measurements on this entangled state, where the choice of measurement bases depends on previous outcomes through feedforward, and on the specific algorithm. Each measurement induces a transformation on the remaining qubits, effectively performing a quantum gate operation.

Photons are ideal candidates for MBQC due to their robustness against decoherence, ease of manipulation in single-qubit gates using linear optics, and their robust detection process. The difficulty of photonic MBQC lies in the generation of the cluster state and the ability of error-correction codes to mitigate photon losses. Our QD single-photon sources can produce linear cluster states deterministically by leveraging the QD spin [163]. These linear cluster states, whose length is limited by the spin coherence time of the QD, can then be merged to form a two-dimensional cluster state using fusion gates [164]. [161] implemented Grover's search algorithm in a list with four elements, in the MBQC framework (see Fig. I.31a).

Current experimental demonstrations of MBQC use parametric single-photon sources integrated on-chip (see Fig. I.31b,c) and manipulate four-photon cluster states [162, 30, 165]. It is hence likely that photonic MBQC will, at least in the near-term, make use of integrated photonics and similar hardware as near-term photonic quantum computing demonstrations discussed in Sec-

tion I.5.1. Consequently, the challenges tackled in this thesis are equally relevant for the MQBC framework.

I.6 - Conclusion on integrated photonics for QI processing

In this chapter, we have laid the groundwork for quantum information (QI) processing, exploring the fundamental principles that underpin the promises of quantum advantage (Section I.1). We introduced the concept of **single photons** emerging from the quantization of the electromagnetic field (Section I.2.3), highlighting their role as **nonclassical quantum states of light and unique carriers of quantum information**. In this thesis, we use **bright quantum dot-based single-photon emitters, emitting pure and indistinguishable single-photons**, forming the basis of our approach to discrete-variable photonic quantum computing (Section I.3). **Integrated photonics** offers a compelling platform for manipulating quantum light with **unprecedented stability and compactness** in the linear optical framework (Section I.4). Photonic integrated circuits constitute the backbone of near-future photonic QI processing demonstrations, as the number of qubits and gates increases (Section I.5).

In Chapter II, we demonstrate the manipulation and operation of an integrated QI processing platform using few photons for **certified quantum random number generation** and the **tomography of a postselected four-photon maximally entangled state**. While most experimental demonstrations of photonic QI processing are limited to on-chip manipulation of fewer than four single photons with restricted control over circuit reconfigurability, this work aims to advance beyond these limitations: **We explore and address the experimental challenges associated with the control and universal manipulation of multiple photons**. In Chapter III, we develop circuit optimal control techniques using machine learning, focusing on the precise manipulation of photonic qubits. Further, in Chapter IV, we enhance these control methods, leading to a **deeper understanding of the behavior of crosstalk in integrated circuits**.

II - Small-scale dedicated circuits for QI processing: Certified randomness generation and entangled state tomography

> As an instrument for selecting at random, I have found nothing superior to dice.
>
> Francis Galton, *Dice for Statistical Experiments* ([166], 1890)

We begin by implementing photonic quantum information (QI) protocols on small-scale circuits. The experiments detailed in this chapter utilize specialized photonic integrated circuits (PICs) with a limited number of modes and few on-chip components, offering a manageable introduction to the technical aspects of the field.

Our first experiment focuses on certified randomness generation, which involves producing randomness with guarantees of security and privacy. This demonstrates that quantum computers already provide a quantum advantage in tasks such as certification in the near-term. Detailed information on certified randomness generation is provided in Section II.1. Sections II.2 and II.3 cover the theoretical foundations and the protocol of our experiment. Section II.4 reviews the experimental implementation, while Section II.5 offers a higher-level discussion on the state of the art, potential loopholes, and possible improvements.

The second experiment, using a similar PIC architecture, involves manipulating a photonic 4-GHZ (Greenberger-Horne-Zeilinger) state. The enhanced optical setup enables full tomography of the generated entangled state, with unprecedented generation rates. We then harness the 4-GHZ state for quantum secret sharing. This experiment is discussed in Section II.6.

II.1 - Motivation for on-chip certified quantum random number generation (C-QRNG)

Random numbers find crucial applications in Monte-Carlo simulations and cryptography, and are daily massively used in one-time passwords and CAPTCHAs [167]. The quality of a **random number generator (RNG)** is measured by its capability to deliver private and unpredictable randomness. In this context, "private" signifies that the generated random numbers are unknown to all parties except the one that generates it. "Unpredictability" refers to the property of a random value being impossible to predict from the previous ones.

Some applications require low-quality randomness at high rates, which is an adequate use case for **pseudo-RNGs**. Pseudo-RNGs (e.g. the Python package `random`) apply deterministic algorithms on a supplied input seed [168] to generate apparent randomness. For pseudo-RNGs, privacy is guaranteed as long as the seed remains private, whereas predictability can be compromised if the generated random number sequence exhibits patterns or biases due to a weak algorithm or seed.

On the other hand, **hardware-based RNGs** make use of dedicated hardware to produce randomness, via physical mechanisms such as coin flips, dice throws [166] or thermal fluctuations [169].

Among hardware-based RNGs, **quantum RNGs (QRNGs)** [170] are appealing as they harness the fundamental randomness of quantum mechanics. Indeed, by the postulates of quantum mechanics [39], the probability of a measurement outcome is deterministically computed, but the outcome itself is random. Hence, QRNGs are intrinsically unpredictable and a guarantee can be placed on the quality of the generated randomness. A paradigmatic QRNG is the so-called "optical branching path generator" [171] consisting as shown on Fig. II.1 of a stream of photons split by a symmetric beamsplitter. The detection probability on detectors "0" and "1" is $50\,\%$. The series of detections generates in principle an unbiased and unpredictable chain of random bits. QRNG implementations are already commercially available (e.g. Quantis QRNG chips by IDQ, Toshiba QRNG).

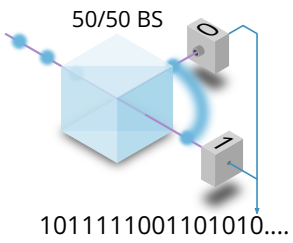

Figure II.1: Optical branching path QRNG

Standard hardware-based RNGs do have a common security flaw: the quality of the generated random numbers depends on the performance and security of the randomness generation device. As a result, the user is forced to blindly trust the device. Fortunately, quantum mechanics opens doors to higher standards of cryptographic security with so-called **certified QRNGs (C-QRNGs)**. C-QRNGs are devices that output a score along the generated random numbers. The score quantifies the amount of secure randomness collected during the experiment, allowing for **randomness certification**. Certification proves to the user that the device is fully functional and not being spied on. C-QRNG experiments are commonly based on the **(2, 2, 2) Bell scenario**, which also constitutes the basis for our implementation discussed in this chapter: 2 agents Alice and Bob, 2 measurement settings $x, y \in \{0, 1\}$ and 2 measurement outcomes $a, b \in \{0, 1\}$ as illustrated on Fig. II.2.a. For such experiments, the score is related to the measured Bell inequality violation on a given bipartite system, here a Bell state $|\psi_{\text{Bell}}\rangle$.

C-QRNGs based on the (2, 2, 2) Bell scenario require Alice and Bob to not be able to communicate with each other. Otherwise, Alice and Bob could mutually influence each other's measurements and fake a Bell inequality violation by "cheating". Absence of communication between the agents can only be rigorously achieved if Alice and Bob are **spacelike separated** in the sense of special relativity. Specifically, the spatial separation between the agents must be sufficiently large such that they cannot have the time to exchange their chosen measurement setting during a mea-

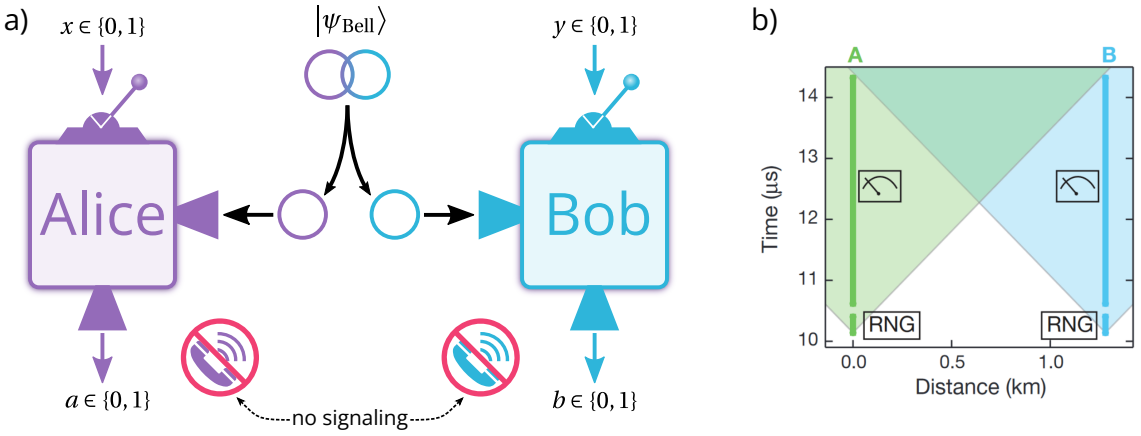

Figure II.2: (2, 2, 2) Bell scenario for device-independent randomness certification. **a)** The measurement device Alice (resp. Bob) has the choice between two measurement settings $x \in \{0,1\}$ (resp. $y \in \{0,1\}$) and outputs a binary result $a \in \{0,1\}$ (resp. $b \in \{0,1\}$). Alice and Bob perform measurements on their respective subsystem of a bigger system, usually a Bell state $|\psi_{\text{Bell}}\rangle$ as shown here. Communication between Alice and Bob must be prevented to validate the experiment. **b)** Space-time diagram of the experiment in [172] showing that Alice (green) and Bob (blue) are spacelike separated. Any light ray sent by Alice at the beginning of her measurement cannot reach Bob before the end of his measurement and vice-versa.

surement. The **nonlocality** of quantum mechanics may then be invoked to explain the violation of Bell inequalities, i.e. a **nonclassical** physical (2,2,2)-behavior that cannot be reproduced by local physical theories like classical and relativistic mechanics. This guarantees that the measurement outcomes of Alice and Bob are devoid of any deterministic origin and thus truly random. Such nonlocal C-QRNGs typically extend on hundreds of meters to spatially separate Alice and Bob [172, 173] (see Fig. II.2.b). Nonlocal C-QRNGs [173, 174, 175, 176, 177] are for this reason restricted to laboratory demonstrations of randomness certification. The state of the art in experimental certification of randomness is summarized in Table II.3 of Section II.5.2.

For compact and practical implementation of C-QRNGs, it is possible to abandon space-like separation and to shield the agents instead to prevent information flow [178, 179]. However, this means that the nonlocality of quantum mechanics is not a valid mean for certifying randomness anymore. Consequently, maximum compactness and theoretical rigor can only be reached with a theory based on **contextuality**, a generalization of nonlocality, and taking into account **signaling**, that is communication, between the agents Alice and Bob, as detailed in Section II.2. The randomness certification protocol (see Section II.3) then allows us to generate private randomness in a cryptographically secure way, even with signaling between Alice and Bob. Our experimental setup (see Section II.4) includes a compact **photonic integrated circuit (PIC)** generating a Bell state via postselection and selecting the measurement basis for Alice and Bob, which might communicate because of thermal crosstalk in the PIC. We reduce the signaling penalty in the randomness certification by exerting a precise control over the PIC phase shifters, with an accuracy in the milliradian range over 100 hours of experiment duration. The experiment is also made possible by the use of a bright single-photon source based on a semiconductor quantum dot delivering highly indistinguishable and pure single photons, producing large Bell inequality violations. In Section II.5, we discuss our experiment, in particular theoretical loopholes and proposed improvements. [3] is the associated article to the C-QRNG experiment. In Section II.6 we use a similar PIC architecture and control protocol to study and fully characterize highly-entangled 4-GHZ quantum states, as reported in [4].

II.2 - Theoretical foundations of our demonstration

The initial setting for this section is the (2, 2, 2) Bell scenario from Fig. II.2. Alice and Bob, assumed initially to be spacelike separated in the sense of special relativity, perform an experiment in which they measure properties of a quantum system using their respective measurement devices.

In Section II.2.1, we introduce a convenient representation for Alice's and Bob's experimental data called *(2,2,2)-behavior*. The (2,2,2)-behavior embodies a **device-independent** approach, in which an experiment is analyzed solely from its empirical statistics. This is in contrast with device-dependent approaches relying on a model or characterization of the experimental setup. The particular class of *no-signaling* (2,2,2)-behaviors to which Alice's and Bob's data conforms due to their spacelike separation is discussed in Section II.2.2. We describe in Section II.2.3 tools to probe nonclassicality in Alice's and Bob's experiment and generalize these tools subsequently in Section II.2.4, which is a short introduction to the framework of contextuality. Contextuality allows to detect nonclassicality without the requirement for spacelike separation of the agents. We define in Section II.2.5 the *signaling fraction*, which measures the amount of communication between Alice and Bob and that is compatible with the contextuality framework.

II.2.1 - (2,2,2)-Behaviors

Alice's and Bob's experiment consists in n_{test} rounds of measurements. At each round, Alice and Bob randomly choose a **measurement basis** (i.e. a setting for their measurement apparatus) and save the measurement outcome. As pictured in Fig. II.2, Alice's (resp. Bob's) measurement basis is denoted x (resp. y). A **measurement context** is a pair (x, y). In the (2, 2, 2) Bell scenario, there are thus four possible contexts:

$$(x, y) \in \{(0,0), (0,1), (1,0), (1,1)\} \tag{II.1}$$

After the n_{test} rounds of the experiment, Alice and Bob aggregate their data into a table called **(2,2,2)-behavior** (Def. II.2.1).

We define two operations that can be performed on (2,2,2)-behaviors:

- **Addition**: two (2,2,2)-behaviors may be added element-wise
- **Multiplication by a scalar** is performed also element-wise

As a result, every **convex combination** of (2,2,2)-behaviors results in a new well-defined (2,2,2)-behavior whose columns sum to 1. This statement is formalized in Prop. II.2.1.

Definition II.2.1: (2,2,2)-behavior

A **(2,2,2)-behavior** consists in the table featuring the empirical probabilities $\mathbb{P}(a,b|x,y)$ associated to Alice and Bob measuring jointly (a,b) in the measurement context (x,y).

		Measurement (x,y)			
		$(0,0)$	$(0,1)$	$(1,0)$	$(1,1)$
Result (a,b)	$(0,0)$	$\mathbb{P}(a,b\|x,y)$			
	$(0,1)$				
	$(1,0)$				
	$(1,1)$				

Notice that the values in a column necessarily sum to 1.

A (2,2,2)-behavior is **deterministic** when the results are entirely determined by the measurement contexts. For instance, the following (2,2,2)-behavior is deterministic:

(a,b) \ (x,y)	$(0,0)$	$(0,1)$	$(1,0)$	$(1,1)$
$(0,0)$	1	0	0	0
$(0,1)$	0	1	0	0
$(1,0)$	0	0	1	0
$(1,1)$	0	0	0	1

This is because each measurement choice (x,y) has a specific outcome (a,b) with probability 1.

Proposition II.2.1: Every convex combination of (2,2,2)-behaviors is a (2,2,2)-behavior

Let $\{e_1, e_2, ..., e_n\}$ be a set of (2,2,2)-behaviors and $a_1, ..., a_n$ be positive coefficients summing to 1.

Then $\sum_{k=1}^{n}(a_k \times e_k)$ is also a (2,2,2)-behavior.

II.2.2 - No-signaling condition

As Alice and Bob are spacelike separated during the experiment, the laws of special relativity guarantee that no information about Alice's state can reach Bob during a measurement and vice-versa. In other words, Alice cannot "signal" information to Bob while they are performing a joint measurement. Hence, Bob cannot extract Alice's measurement basis x from his measurement outcome b. As a consequence, their measured (2,2,2)-behavior falls into the class of **no-signaling (2,2,2)-behaviors** (Def. II.2.2). A no-signaling (2,2,2)-behavior represents a situation in which the way a measurement is performed on a subsystem of a bigger system does not affect the marginals of the measurements on another subsystem.

Definition II.2.2: No-signaling (2,2,2)-behavior

A (2,2,2)-behavior is **no-signaling** when Alice's probability of measuring the outcome $a = 0$ or $a = 1$ is not influenced by Bob's measurement basis choice. The associated mathematical statement is

$$\forall a, x, \quad \mathbb{P}(a|x, y = 0) = \mathbb{P}(a|x, y = 1) \tag{II.2}$$

where

$$\mathbb{P}(a|x, y) = \mathbb{P}(a, b = 0|x, y) + \mathbb{P}(a, b = 1|x, y) \tag{II.3}$$

is the **marginal distribution** of Alice. The equivalent must also hold for Bob.

Example:

The (2,2,2)-behavior e_1 shown below is signaling, because Alice measures deterministically $a = 0$ (resp. $a = 1$) when Bob measures chooses the basis $y = 0$ (resp. $y = 1$). Hence Alice is aware of Bob's basis choice. On the other hand, e_2 is no-signaling.

$e_1 =$

(a,b) \ (x,y)	(0, 0)	(0, 1)	(1, 0)	(1 ,1)
(0, 0)	1	0	0	0
(0, 1)	0	0	1	0
(1, 0)	0	1	0	0
(1 ,1)	0	0	0	1

$e_2 =$

(a,b) \ (x,y)	(0, 0)	(0, 1)	(1, 0)	(1 ,1)
(0, 0)	1	1	0	0
(0, 1)	0	0	0	0
(1, 0)	0	0	1	1
(1 ,1)	0	0	0	0

II.2.3 - Nonlocality and hidden-variable models in the spacelike separated case

Local physical theories, built on the **principle of locality**, prohibit instantaneous interactions between distant objects. For instance, Einstein's theory of general relativity is a local theory of gravity because gravitational field distortions cannot propagate faster than the speed of light in that theory. On the other hand, Newton's theory of gravity is **nonlocal** because it considers that gravitational interactions are immediate across all of space.

Alice and Bob investigate if their measured data can be explained by local theories, or if it is on the contrary the manifestation of a nonlocal theory like quantum mechanics. If their data was produced by a local theory, the outcomes of their measurements are the result of **hidden variables**, that is past common factors influencing both Alice's and Bob's measurements [180] (for instance the temperature of the lab in which the quantum state was generated). In fact, a central notion in the study of nonlocal correlations are **hidden variable models (HVMs)** (Def. II.2.3).

HVMs are used to express the existence of deeper underlying mechanisms giving rise to an observed (2,2,2)-behavior, as shown in the example of Def. II.2.3. In the spacelike separated experiment of Alice and Bob, it can be shown [180] that when performing the experiment with a Bell state, the obtained (2,2,2)-behavior cannot be realized by any hidden variable model composed of deterministic no-signaling (2,2,2)-behaviors. This is the signature of **quantum nonlocality**: entangled states can produce experimental outcomes that are not explainable by theories where Alice and Bob do not mutually influence their measurement outcomes and generate outcomes according to a deterministic process (or a probabilistic mixture of deterministic processes). Typically, the outcomes of Alice and Bob cannot be reproduced by non-quantum theories. Therefore, the randomness in Alice's and Bob's data is not **epistemological**, emerging from unknown deterministic causes. Instead it is **ontological**, in other words it is indeed an intrinsic feature quantum mechanics as stated by the axioms of the theory [39].

For instance, the example from Def. II.2.3 shows a local (2,2,2)-behavior e that is realized by a hidden variable model H consisting of such deterministic no-signaling (2,2,2)-behaviors. On the other hand, we show on Fig. II.3 examples of nonlocal (2,2,2)-behaviors.

a)

$e_{\text{PR}} =$

(a,b) \ (x,y)	$(0,0)$	$(0,1)$	$(1,0)$	$(1,1)$
$(0,0)$	0.5	0	0	0
$(0,1)$	0	0.5	0.5	0.5
$(1,0)$	0	0.5	0.5	0.5
$(1,1)$	0.5	0	0	0

b)

$e_{\text{Bell}} =$

(a,b) \ (x,y)	$(0,0)$	$(0,1)$	$(1,0)$	$(1,1)$
$(0,0)$	c_+	c_-	c_-	c_-
$(0,1)$	c_-	c_+	c_+	c_+
$(1,0)$	c_-	c_+	c_+	c_+
$(1,1)$	c_+	c_-	c_-	c_-

Figure II.3: Examples of nonlocal (2,2,2)-behaviors. a) Popescu-Rorhlich box. b) (2,2,2)-behavior obtained from Bell state $|\psi_{\text{Bell}}\rangle = (|0_A 1_B\rangle + |1_A 0_B\rangle)/\sqrt{2}$ with optimal measurement bases (see Section II.4.2.B), where $c_\pm = \frac{2\pm\sqrt{2}}{8}$.

Definition II.2.3: Hidden-variable model (HVM)

A **hidden variable model** is a set H of (2,2,2)-behaviors. A (2,2,2)-behavior e is realized by H when it is a convex combination of elements of H.

Example:

Let $H = \{h_1, h_2, h_3, h_4\}$ be a set of (2,2,2)-behaviors with elements defined as below:

$h_1 =$

(a,b) \ (x,y)	$(0,0)$	$(0,1)$	$(1,0)$	$(1,1)$
$(0,0)$	1	1	1	1
$(0,1)$	0	0	0	0
$(1,0)$	0	0	0	0
$(1,1)$	0	0	0	0

$h_2 =$

(a,b) \ (x,y)	$(0,0)$	$(0,1)$	$(1,0)$	$(1,1)$
$(0,0)$	0	0	0	0
$(0,1)$	1	1	1	1
$(1,0)$	0	0	0	0
$(1,1)$	0	0	0	0

$h_3 =$

(a,b) \ (x,y)	$(0,0)$	$(0,1)$	$(1,0)$	$(1,1)$
$(0,0)$	0	0	0	0
$(0,1)$	0	0	0	0
$(1,0)$	1	1	1	1
$(1,1)$	0	0	0	0

$h_4 =$

(a,b) \ (x,y)	$(0,0)$	$(0,1)$	$(1,0)$	$(1,1)$
$(0,0)$	0	0	0	0
$(0,1)$	0	0	0	0
$(1,0)$	0	0	0	0
$(1,1)$	1	1	1	1

Then, the (2,2,2)-behavior e defined as

$e =$

(a,b) \ (x,y)	$(0,0)$	$(0,1)$	$(1,0)$	$(1,1)$
$(0,0)$	0.25	0.25	0.25	0.25
$(0,1)$	0.25	0.25	0.25	0.25
$(1,0)$	0.25	0.25	0.25	0.25
$(1,1)$	0.25	0.25	0.25	0.25

$= \sum_{k=1}^{4} \frac{1}{4} \times h_k$

is realized by H. The emerging (2,2,2)-behavior e may be explained thus by an underlying hidden variable model where Alice and Bob agreed in advance to produce the outcome $(0,0)$ for the first quarter of experiment rounds, $(0,1)$ for the second quarter and so on. Thus, the resulting (2,2,2)-behavior e may be explained without even mentioning quantum mechanics or any source of randomness.

II.2.3.A - Measures of quantum nonlocality: the CHSH score and inequality value

It is possible to quantify the "amount of nonlocality" exhibited by a given (2,2,2)-behavior. In the particular case of the (2, 2, 2) Bell scenario, we can use the Clauser-Horne-Shimony-Holt (CHSH) inequality [181] to probe nonlocality. The **CHSH inequality value** of a (2,2,2)-behavior e is defined

as [1]

$$I_{\text{CHSH}}(e) = E_{(x=0,y=0)} - E_{(x=0,y=1)} - E_{(x=1,y=0)} - E_{(x=1,y=1)} \tag{II.4}$$

where

$$E_{(x,y)} = \mathbb{P}(0,0|x,y) + \mathbb{P}(1,1|x,y) - \mathbb{P}(0,1|x,y) - \mathbb{P}(1,0|x,y) \tag{II.5}$$

It can be shown [180] that in the spacelike-separated case:

- Local theories produces (2,2,2)-behaviors with $|I_{\text{CHSH}}| \leq 2$. This is the content of the CHSH inequality, a type of Bell inequality.
- Quantum mechanics produces (2,2,2)-behaviors with $|I_{\text{CHSH}}| \leq 2\sqrt{2}$ (**Tsirelson bound**), hence witnessing $I_{\text{CHSH}} \geq 2$ is sufficient for certifying nonlocal correlations. The (2,2,2)-behavior in Fig. II.3.b produces $I_{\text{CHSH}}(e_{\text{Bell}}) = 2\sqrt{2}$.
- From a mathematical point of view, $|I_{\text{CHSH}}| \leq 4$. The (2,2,2)-behavior in Fig. II.3.a yields $I_{\text{CHSH}}(e_{\text{PR}}) = 4$ and cannot be realized even by quantum mechanics.

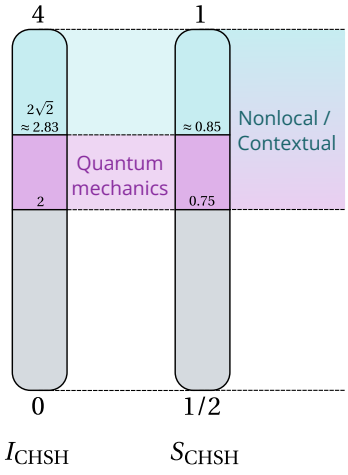

Figure II.4: Scale comparison of the CHSH metrics. Purple and blue areas indicate the scores certifying nonlocal correlations in the spacelike separated (2, 2, 2) Bell scenario (and contextual correlations in the no-signaling case).

For convenience, we also define the **CHSH score** S_{CHSH}, related to I_{CHSH} via (see Fig. II.4 for comparison)

$$S_{\text{CHSH}}(e) = \frac{|I_{\text{CHSH}}(e)| + 4}{8}. \tag{II.6}$$

Hence, $0.75 \leq S_{\text{CHSH}} \leq \cos^2(\pi/8) \approx 0.85$ certifies nonlocal correlations.

II.2.4 - Contextuality and hidden-variable models in the no-signaling case

Quantum nonlocality is a concept referring to a situation where Alice and Bob are spacelike separated. Quantum nonlocality admits a generalization that is valid even when Alice and Bob are not spacelike separated, as long as the no-signaling condition of Section II.2.2 holds. **Quantum contextuality** [182, 183] (see Def. II.2.4) is the mathematical formulation expressing that the observable properties of a quantum system are dependent on the context in which they are measured (measurement type, measurement apparatus, the other measurements being performed at the same time). The properties of a quantum system are not fixed and definite until they are measured, and the act of measurement itself can affect the outcome. This is in contrast to classical physics, where the properties of a system are independent of the context in which they are measured, a philosophical concept referred to as **realism**. We stress at this point that the no-signaling condition imposed on Alice and Bob, which does not allow them to deduce the context from their individual measurement outcomes, is not conflicting with the definition of quantum contextuality. The contextual nature of their experiment can only be brought to light when they construct the full joint probability distribution by aggregating their data in a (2,2,2)-behavior.

[1] As long as one of the E terms has a different sign than the others, it is a valid CHSH inequality value expression. We can permute Alice's basis and/or detector labels (and same for Bob) to switch expressions.

Definition II.2.4: Contextual (2,2,2)-behavior

A (2,2,2)-behavior is **contextual** when it does not admit an HVM consisting of deterministic no-signaling (2,2,2)-behaviors.

Remark:

It was stated earlier in Section II.2.3 that

$$\text{non-locality} \Rightarrow \text{absence of deterministic no-signaling HVMs} \tag{II.7}$$

thus

$$\text{non-locality} \Rightarrow \text{contextuality} \tag{II.8}$$

In that sense, contextuality generalizes non-locality. The contextual character of quantum mechanics is witnessed regardless of the distance between Alice and Bob when performing a Bell test (as long as there is no communication between them), but quantum nonlocality is the special case when there is spacelike separation between Alice and Bob.

The "amount of contextuality" in a (2,2,2)-behavior can be measured using the contextual fraction [184], but in a Bell test it is equivalent to use the CHSH inequality value I_{CHSH} and the CHSH score S_{CHSH} introduced in Section II.2.3.A.

II.2.5 - The signaling fraction

Contextuality and its measures have been defined for no-signaling (2,2,2)-behaviors. An essential component of our C-QRNG experiment are however on-chip Bell tests, in which Alice and Bob are located only centimeters apart from each other on the same integrated device. We are thus interested in certifying contextual behaviors, even when Alice and Bob are allowed to communicate.

It is possible to measure the amount of communication between Alice and Bob from their constructed (2,2,2)-behavior e by using the **signaling fraction** [185] denoted $\text{SF}(e)$. The signaling fraction quantifies departure from the ideal no-signaling setting.

For our randomness generation experiment, we need to relate malicious signaling between Alice and Bob that could occur at the hidden-variable level with a measurable and accessible quantity from their (2,2,2)-behavior e. Let H be the set of hidden-variable models of the experiment and

$$\sigma = \max_{h \in H} \{\text{SF}(h)\} \tag{II.9}$$

be the maximum signaling fraction of the hidden-variable models. Mathematically, it can be shown that $\sigma \geq \text{SF}(e)$. We assume that

$$\sigma = \text{SF}(e) \tag{II.10}$$

As discussed in [3], the assumption in itself is reasonable if the randomness generation device is built by a so-called "**honest provider**", otherwise it would be possible to construct a malicious device exhibiting a low value for $\text{SF}(e)$ with high σ, preventing detection of underlying communication between the agents Alice and Bob.

Given σ, it can be shown that the minimum CHSH score S_{CHSH} needed to certify contextual correlations increases from $\frac{3}{4}$ to $\frac{3+\sigma}{4}$. Thus, even supra-quantum contextual (2,2,2)-behaviors achieving $S_{\text{CHSH}} > 0.85$ like the Popescu-Rohrlich box ($S_{\text{CHSH}} = 1$, see Fig. II.3) are in fact experimentally measurable when signaling between Alice and Bob is allowed.

Definition II.2.5: Signaling fraction

The signaling fraction $\mathrm{SF}(e)$ of a (2,2,2)-behavior e is defined as

$$\mathrm{SF}(e) = \min\left\{\lambda \in [0,1] \quad \text{such that} \quad e = [1-\lambda] \times e^{\mathrm{NS}} + \lambda \times e'\right\} \tag{II.11}$$

where e^{NS} is a no-signaling (2,2,2)-behavior. This yields for e a decomposition of the type:

$$e = [1 - \mathrm{SF}(e)] \times e^{\mathrm{NS}} + \mathrm{SF}(e) \times e^{\mathrm{SS}} \tag{II.12}$$

where e^{SS} is strongly signaling, because it follows that its no-signaling component is empty, i.e. $\mathrm{SF}\left(e^{\mathrm{SS}}\right) = 0$.

Example:

a)

(a,b) \ (x,y)	$(0,0)$	$(0,1)$	$(1,0)$	$(1,1)$
$(0,0)$	0.25	0.25	0.25	0.25
$(0,1)$	0.25	0.25	0.25	0.25
$(1,0)$	0.25	0.25	0.25	0.25
$(1,1)$	0.25	0.25	0.25	0.25

b)

(a,b) \ (x,y)	$(0,0)$	$(0,1)$	$(1,0)$	$(1,1)$
$(0,0)$	0.25	0.25	0.25	0.25
$(0,1)$	0.2	0.25	0.25	0.25
$(1,0)$	0.25	0.25	0.25	0.25
$(1,1)$	0.3	0.25	0.25	0.25

The (2,2,2)-behavior a) has SF $= 0$, while b) has SF $= 0.05$. In b), Alice is able to extract the measurement basis of Bob from her individual measurement outcomes, because the probability of Alice getting the outcome "0" is 0.45 in context $(0,0)$, and 0.5 in context $(0,1)$.

In the following section, we use the introduced theoretical tools to establish the certified randomness generation protocol.

II.3 - Certified randomness generation protocol

Building on the theoretical tools introduced in the previous section, we now describe the protocol used in our randomness generation experiment. The theory supporting the experiment has been developed by the Quandela QI scientists Boris Bourdoncle, Pierre-Emmanuel Emeriau and Shane Mansfield. Section II.3.1 exposes the raw randomness generation stage of the protocol, while Section II.3.2 describes the certification process, which determines the quantity of private and unpredictable random bits that can be distilled in Section II.3.3.

II.3.1 - Raw randomness generation

The protocol used in our experiment extends on Miller and Shi's spot-checking randomness generation protocol [186]. The idea is to perform tests at random times during the experiment that will be used to compute the score of the experiment. The protocol takes as input

- N the number of rounds to carry out,
- q the test probability.

We explicit how these parameters are chosen in Section II.3.2. The following notations are consistent with the previous section and with Fig. II.2. Before the experiment, Alice and Bob each choose two **measurement bases**, that is two different settings for their respective measurement apparatus. Alice's bases are denoted $x \in \{0,1\}$ and Bob's bases $y \in \{0,1\}$. The **measurement contexts** are the four joint measurement settings (x,y). Alice's measurement outcomes are denoted $a \in \{0,1\}$

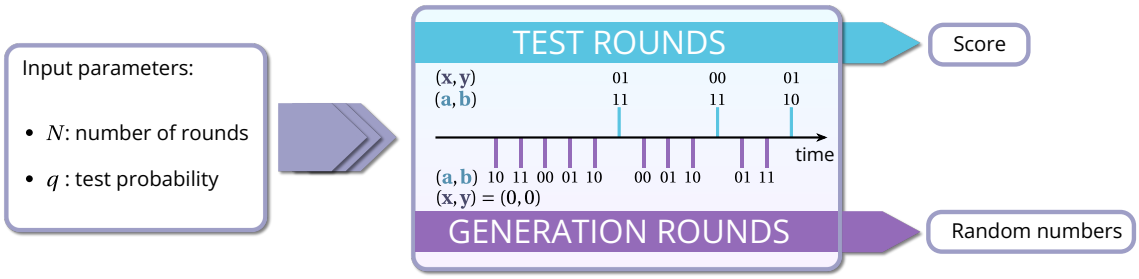

Figure II.5: Simplified flowchart of the C-QRNG experiment protocol. The protocol takes as input the number of rounds N to perform and the test probability q. The protocol then randomly alternates between test and generation rounds, according to q. The test rounds are used to compute the generation experiment score for randomness certification and the generation rounds yield the random numbers (after the randomness extraction step from Section II.3.3).

and Bob's ones $b \in \{0, 1\}$. Alice and Bob share a Bell state $|\psi_{\text{Bell}}\rangle$ and perform measurements on their respective qubit.

The protocol processes all N rounds sequentially and randomly determines at each new round if a **test round** is performed with probability q, otherwise it is a **generation round**.

- During a **test round**, Alice and Bob randomly choose their measurement basis x and y, and record their result a and b, all of which are saved.
- In a **generation round**, Alice and Bob set their measurement base to $x = 0$ and $y = 0$, and the results a and b are added to the generated random numbers.

This process is illustrated in the simplified flowchart of the experiment in Fig. II.5. We may use a public source of randomness for determining the round type.

II.3.2 - Randomness certification

Once all N generation and test rounds have been carried out, the data produced by the protocol consists of a chain of raw random bits from the generation rounds, along with the measurements contexts and results of the test rounds. The information provided by the $n_{\text{test}} \approx qN$ test rounds is aggregated into a (2,2,2)-behavior e_{XP} containing the empirical joint probability distribution relating Alice's and Bob's measurement choice (x, y) to the joint outcome (a, b).

In fact, Alice and Bob have performed a Bell test with the test rounds, and the score of the experiment is expressed with the CHSH score and signaling fraction as follows:

$$\text{score}(e_{\text{XP}}) = S_{\text{CHSH}}(e_{\text{XP}}) - \frac{\text{SF}(e_{\text{XP}})}{4} - 0.75. \tag{II.13}$$

As a consequence, performing the randomness generation experiment with a high-quality Bell state contributes to improving the score by increasing S_{CHSH}, but signaling SF between Alice and Bob reduces the final score. Signaling could be the result of an attack on the device or a dysfunction of the PIC, but in either case it does not go unnoticed thanks to the signaling fraction.

II.3.3 - Random number extraction

Raw random numbers are obtained by concatenating Alice's and Bob's $2n_{\text{gen}}$ results a and b from the $n_{\text{gen}} \approx (1 - q)N$ generation rounds. The raw randomness must undergo post-treatment because of two reasons:

- When performing the experiment following our implementation (specific Bell state and choice of measurement bases described in Section II.4.2.B), the generation result of Alice and Bob are correlated with probability ≈ 0.83 (see experimental (2,2,2)-behavior on Fig. II.17), i.e.

when Alice measures the outcome $a = 0$, it is more probable for Bob to measure $b = 0$ as well. As a result, the raw random numbers are correlated.

- The security proof of the experiment asserts that part of the generated numbers by Alice and Bob are "redundant". In fact, only a number $\kappa(\text{score}, N, q)$ of them are uniformly random and uncorrelated to the quantum side information accessible to an eavesdropper. Quantum side information is the amount of information that is recoverable by a third party using quantum mechanical attacks on the experiment (e.g. entanglement with single-photon source). The expression of $\kappa(\text{score}, N, q)$ is given in [3].

We use a randomness extractor to distill the $2n_{\text{gen}}$ raw random numbers into a sequence of perfectly unpredictable and private random bits of size $\kappa(\text{score}, N, q)$. A stringent requirement set on the randomness extractor is that it should preserve protection against quantum side information. The Toeplitz Hash Algorithm [187] and Trevisan's extractor [188] meet this condition [189, 190]. Both are in addition strong extractors, whose seed can be reused for other extractions.

We chose the Toeplitz extractor for our experiment for its ease of use and faster extraction rate [189]. The method relies on **Toeplitz matrices** (see Def. II.3.1).

Definition II.3.1: Toeplitz matrix

A **Toeplitz matrix** is a matrix of form

$$\text{Toep}_{n,m}(c_{-m}, \ldots, c_n) = \begin{bmatrix} c_0 & c_{-1} & c_{-2} & \ldots & c_{-m} \\ c_1 & c_0 & c_{-1} & c_{-2} & \ldots \\ c_2 & c_1 & c_0 & c_{-1} & c_{-2} \\ \ldots & c_2 & c_1 & c_0 & c_{-1} \\ c_n & \ldots & c_2 & c_1 & c_0 \end{bmatrix}. \tag{II.14}$$

Toeplitz matrices are straightforwardly generated in Python with `scipy.linalg.toeplitz`.

We succinctly describe Toeplitz extraction. Let $\vec{h}_{\text{in}}$ be the vector of length $n_{\text{in}} = 2n_{\text{gen}}$ containing all raw random numbers, and $\vec{h}_{\text{out}}$ be the vector of length $n_{\text{out}} = \kappa(\text{score}, N, q)$ containing the extracted certified random numbers. The latter is obtained by matrix multiplication of $\vec{h}_{\text{in}}$ with a Toeplitz matrix

$$\vec{h}_{\text{out}} = \text{Toep}_{n_{\text{out}}, n_{\text{in}}}(\vec{s}) \cdot \vec{h}_{\text{in}} \tag{II.15}$$

where $\mathbf{s}$ is a random seed of length $n_{\text{in}} + n_{\text{out}}$ and all additions are modulo 2. The downside of this method is evidently the input seed that is longer than the chain of initial raw random bits, whereas Trevisan's extractor works with relatively small seeds. We are allowed to use public randomness for the seed as long as it is not correlated with the experiment, so it is generated using `numpy.random` in practice. Because the Toeplitz matrix features billions of columns, it is divided into blocks of 20 million columns and the extraction is performed in multiple steps.

The next section presents the optical setup used for certifying randomness experimentally and implements the protocol introduced in this section to generate certified random numbers.

II.4 - Experimental implementation for C-QRNG

From the theoretical point of view, this is the first C-QRNG experiment taking into account signaling between Alice and Bob in a rigorous framework. The experimental implementation in itself also brings new ideas to the table. As exposed in Section II.4.1, this is the first C-QRNG experiment that uses a bright **single-photon source** based on a **quantum dot** (see Section I.3.3) and a **photonic integrated circuit (PIC)**. We detail in Section II.4.2 the purpose of the PIC. In Section

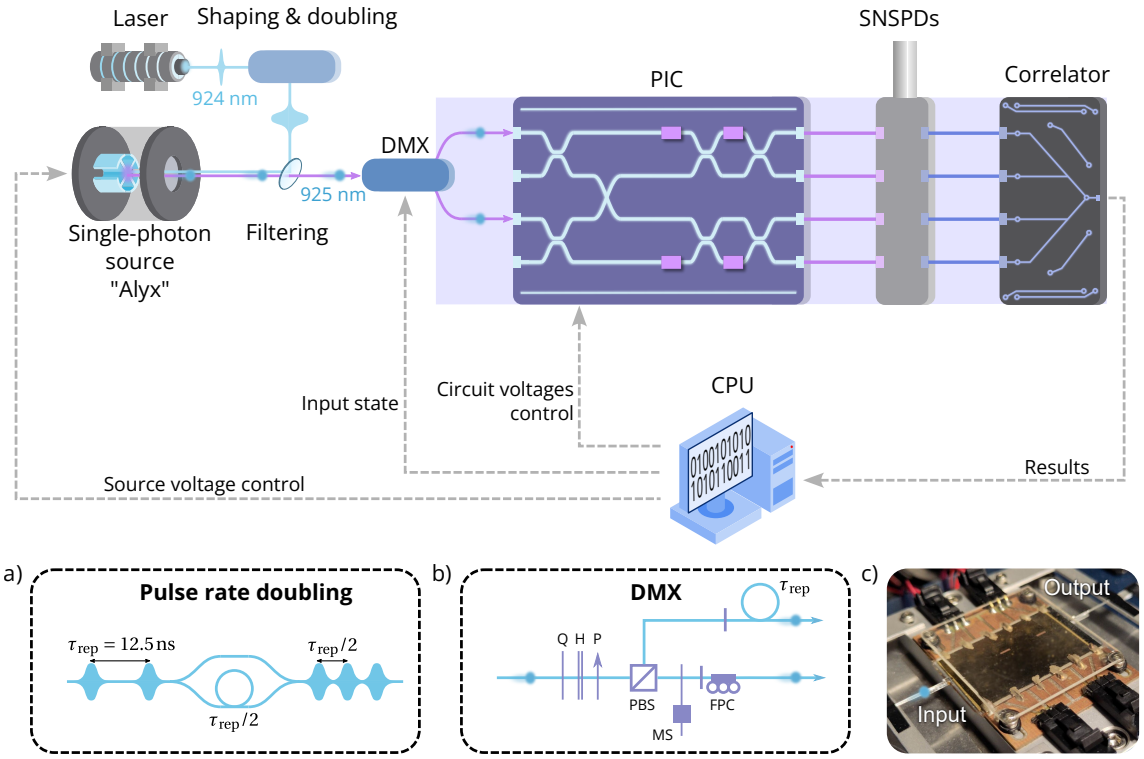

Figure II.6: Compact experimental C-QRNG setup with a quantum dot single-photon source and photonic circuit. The single-photon source "Alyx" generates photons at 925 nm via the quasi-resonant-excitation scheme (see Section I.3.3.A) from pump laser excitation pulses that have been shaped around 924 nm and doubled in rate (see inset a)). The generated single-photons are separated from parasitic reflected pump light in the filtering stage. A passive demultiplexer (DMX, see inset b)) splits the photon stream and allows to inject two photons simultaneously in the PIC. The photons are manipulated in the PIC, then detected by superconducting nanowire single-photon detectors (SNSPDs). Photon times of arrival are processed by a correlator. Dashed gray lines indicate that elements of the setup are automated to implement the randomness generation protocol. Blue area indicates the part of setup that is fibered or integrated. Numerical data on the setup such as the single-photon characteristics can be found in Table II.4. **a)** Pulse rate doubling is achieved by splitting the input pulses initially separated by a duration $\tau_{rep} \approx 12.5\,ns$ with a symmetric beamsplitter. One of its arms features a $\tau_{rep}/2$ delay line. The pulses are then recombined with a second beamsplitter, resulting in a sequence of pulses separated by $\tau_{rep}/2$. **b)** The passive demultiplexer consists of a polarizing beamsplitter (PBS). One of its arms is connected to a τ_{rep} delay line. The other arm can be blocked by a motorized shutter (MS). FPC: fibered polarization controller. Q, H: quarter- and half-wave plates. P: polarizer. **c)** Picture of PIC used for photon manipulation. The PIC has a length of 4 cm and width of 2 cm.

II.4.3, the stability of the experimental setup is discussed. We then use the certification protocol from Section II.3.2 in a slightly modified form (see Section II.4.4) and validate our randomness generation protocol with a 95-hour experimental run reported in Section II.4.5.

II.4.1 - Optical setup for C-QRNG

The setup is shown and described in brief on Fig. II.6. Details about the setup can be found in the associated article [3] and in Appendix B.1. The overall setup transmission of 2.7 %, defined as the probability of a photon being detected following a single-photon emitter excitation, is measured by summing the photon countrate on the detectors. The setup is remarkable by its large portion that is fibered or integrated (see lavender-colored area on Fig. II.6).

Single-photon source We use a single-photon source ("Alyx") based on a semiconductor quantum dot (QD, see Section I.3.3). The source emits photons at a wavelength of 925 nm with a trionic excited state and a polarized first-lens brightness of 38 ± 1 % (see Section I.3.1.A).

	"Alyx"	"Alyx" (with etalon)
Polarized device brightness	$14 \pm 1\,\%$	$8 \pm 1\,\%$
$g^{(2)}(0)$	$6.0 \pm 0.5\,\%$	$2.3 \pm 0.2\,\%$
V_{HOM}	$86 \pm 1\,\%$	$93 \pm 1\,\%$

Table II.1: **Characteristics summary of QD single-photon emitters used in this thesis** Polarized device brightness: see Section I.3.1.A. $g^{(2)}(0)$: quantifies multiphoton emission, see Section I.3.1.B. V_{HOM}: HOM visibility measured between successive photons, see Section I.3.1.C. The data was acquired with the quasi-resonant excitation scheme (see Section I.3.3.A). Error bars indicate the magnitude of typical day to day variations in the evaluated quantities, and account for measurement uncertainty.

An **etalon** (or Fabry-Perot cavity) is inserted into the filtering stage to act as an optical bandpass. The purpose of the etalon is to significantly improve the quality of the photons, as can be seen from Table II.1. For the quasi-resonant excitation scheme, in which the excitation pulses are spectrally distinct from the emitted photons, the etalon enhances pump rejection. The etalon also deals with QD re-excitation events, where two photons are successively emitted over the course of the same excitation pulse. The first photon of a re-excited pair indeed has a shorter temporal profile than the second which follows the natural linewidth of the emitter, in the 5 to 10 pm range (see Fig. 3.10 of [191]). As a consequence, the first photon is spectrally wider, and thus rejected by the etalon. Etalons are however double-edged swords, as they significantly reduce the overall transmission of the setup due to their tight bandwidth, here of 14 pm.

II.4.2 - QRNG PIC

The silica glass PIC for photon manipulation is schematized on Fig. II.7. The PIC features 6 symmetric directional couplers, 4 reconfigurable thermo-optic phase shifters and a waveguide crossing.

The PIC is used in dual-rail qubit encoding: the two input photons form a two-qubit system. Modes 0_A and 1_A correspond to Alice's qubit, modes 0_B and 1_B to Bob's qubit. Hence, Alice's outcome $a = 0$ (resp. $a = 1$) corresponds to her detector 0_a (resp. 1_a) clicking. The same applies for Bob. Joint measurements of Alice and Bob correspond to 2-photon coincidences between Alice and Bob.

II.4.2.A - Postselected Bell state generation

The two input photons initialize the quantum state in

$$\left|\psi_{\mathrm{in}}\right\rangle = |0_A, 0_B\rangle \tag{II.16}$$

$$= |1, 0, 1, 0\rangle \tag{II.17}$$

where the input state is written in qubit notation in Eq. II.16 and in Fock state notation in Eq. II.17. Applying a symmetric beamsplitter on each pair of modes and the waveguide crossing yields the following state in Fock state notation:

$$\left|\psi\right\rangle = \frac{|1,1,0,0\rangle + i\,|1,0,0,1\rangle + i\,|0,1,1,0\rangle - |0,0,1,1\rangle}{2} \tag{II.18}$$

Discarding the events where both of Alice's detectors click (and same for Bob), we are left with the postselected state yielding only 2-photon coincidences between Alice and Bob

$$\left|\psi_{\mathrm{Bell}}\right\rangle = i\frac{|1,0,0,1\rangle + |0,1,1,0\rangle}{\sqrt{2}} = i\frac{|0_A, 1_B\rangle + |1_A, 0_B\rangle}{\sqrt{2}} \tag{II.19}$$

which is the Bell state $\left|\Psi^+\right\rangle$ (see Section I.1.2) up to a global phase that can be discarded.

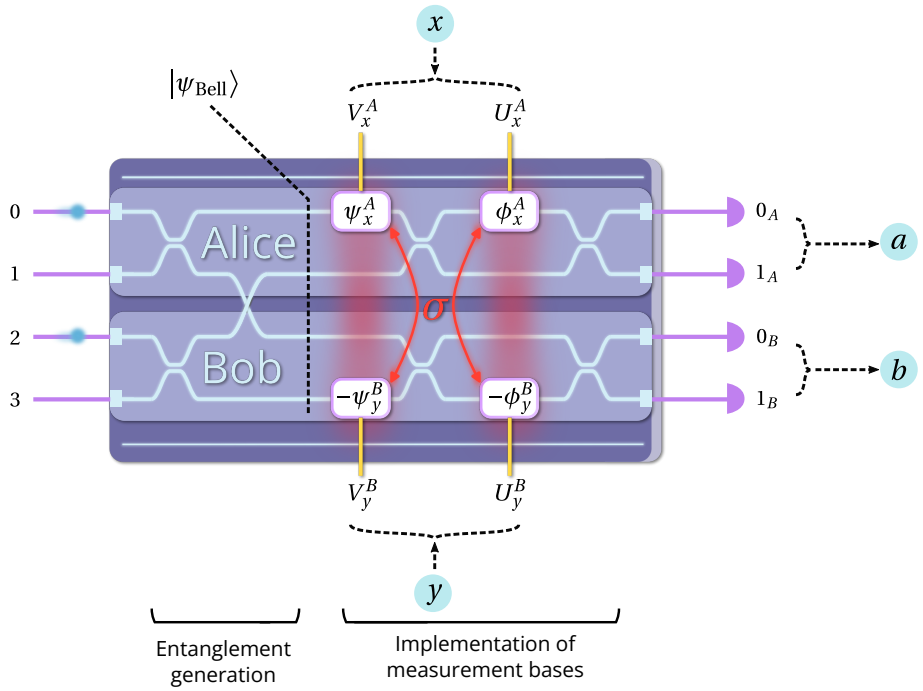

Figure II.7: C-QRNG on a 4-mode photonic integrated circuit. The PIC generates an entangled state from the two input photons and implements the measurement bases for Alice and Bob corresponding to the binary inputs x an y, which are to sets of voltages $V_x^A, U_x^A, V_y^B, U_y^B$ resulting in phase shifts $\psi_x^A, \phi_x^A, \psi_y^B, \phi_y^B$. The dotted line labeled $|\psi_{\text{Bell}}\rangle$ locates the generated Bell state in the circuit. Crosstalk between thermo-optic phase shifters is symbolized by σ. The measured binary outcome for Alice and Bob is labeled respectively a and b.

II.4.2.B - Implementation of measurement bases and on-chip CHSH inequality testing

In the randomness protocol, Alice chooses two measurements bases labeled $x = 0$ and $x = 1$. These correspond in practice to two sets of phase shifts (ψ_0^A, ϕ_0^A) and (ψ_1^A, ϕ_1^A) to implement on her two phase shifters. Same for Bob with $y = 0$ and $y = 1$. However, not all choices of phase shifts lead to a CHSH inequality violations. Hence, a "good" set of phase shifts is key to generating randomness. An optimal set of phase shifts is presented in Table II.2, with "optimal" in the sense that they achieve a maximal quantum violation of the CHSH inequality with $I_{\text{CHSH}} = 2\sqrt{2}$ as shown in Appendix C, without experimental imperfections.

Measurement context (x, y)	ψ_x^A	ϕ_x^A	ψ_y^B	ϕ_y^B
$(0,0)$	0	$-\pi/2$	0	$-\pi/4$
$(0,1)$	0	$-\pi/2$	0	$\pi/4$
$(1,0)$	0	0	0	$-\pi/4$
$(1,1)$	0	0	0	$\pi/4$

Table II.2: **Phase shift choices for maximal CHSH violations.**

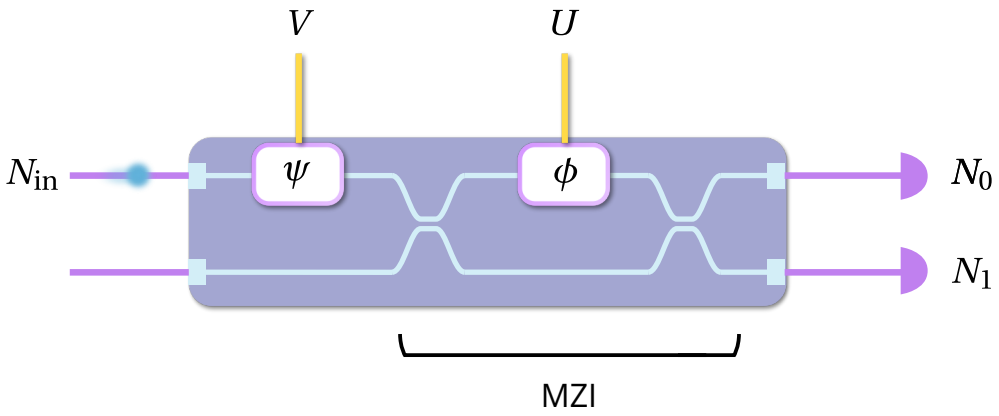

Figure II.8: Alice's and Bob's interferometer. The interferometer features two phases ψ and ϕ controlled by voltages V and U, and two symmetric beamsplitters, forming an MZI with the ϕ phase. N_{in} is the photon countrate entering the circuit, and N_0 and N_1 are the detected countrates at the outputs.

II.4.2.C - Phase shifter control

Alice's and Bob's phase shifts $\psi_{x/y}^{A/B}$ and $\psi_{x/y}^{A/B}$ are physically implemented by thermo-optic phase shifters. We denote the voltage applied on each phase shifter by

$$V_x^A \to \psi_x^A \tag{II.20}$$
$$U_x^A \to \phi_x^A \tag{II.21}$$
$$V_y^B \to \psi_y^B \tag{II.22}$$
$$U_y^B \to \phi_y^B \tag{II.23}$$

as shown on Fig. II.7. The PIC phase-voltage response, given by the manufacturer, is of the form

$$\begin{bmatrix} \psi_x^A \\ \phi_x^A \\ \psi_y^B \\ \phi_y^B \end{bmatrix} = \vec{c}_0 + C_2 \cdot \begin{bmatrix} V_x^A \\ U_x^A \\ V_y^B \\ U_y^B \end{bmatrix}^{\odot 2} + C_4 \cdot \begin{bmatrix} V_x^A \\ U_x^A \\ V_y^B \\ U_y^B \end{bmatrix}^{\odot 4} \tag{II.24}$$

where C_2 and C_4 are 4×4 matrices, $\vec{c}_0$ is a vector containing the 4 passives phases and $^{\odot}$ is component-wise exponentiation. The order 2 term represents Joule heating, and the order 4 term accounts for heater resistance changing with increasing temperature. Injecting a continuous diode laser in the chip and measuring the outputs with photodiodes reveals that there is measurable thermal crosstalk only between resistors belonging to the same column, as indicated in Fig. II.7. The same experiment also determines that the thermalization time is $250\,\text{ms}$ when switching to new voltages. The values of $\vec{c}_0, C_2$ and C_4 are provided and discussed in Appendix B.1.1. Appendix D.1 details how the phase-voltage equations are solved for this particular PIC.

II.4.3 - Setup monitoring and stabilization

A randomness generation experiment can take up to 100 hours of operation time. As a consequence, another key ingredient for efficient certification of randomness is a stable and accurate experimental setup.

II.4.3.A - Interferometer MZI phase ϕ measurement

We measure the MZI ϕ phases implemented by Alice and Bob by closing the motorized shutter on Fig. II.6, such that photons arrive only from the upper mode in their respective interferometer

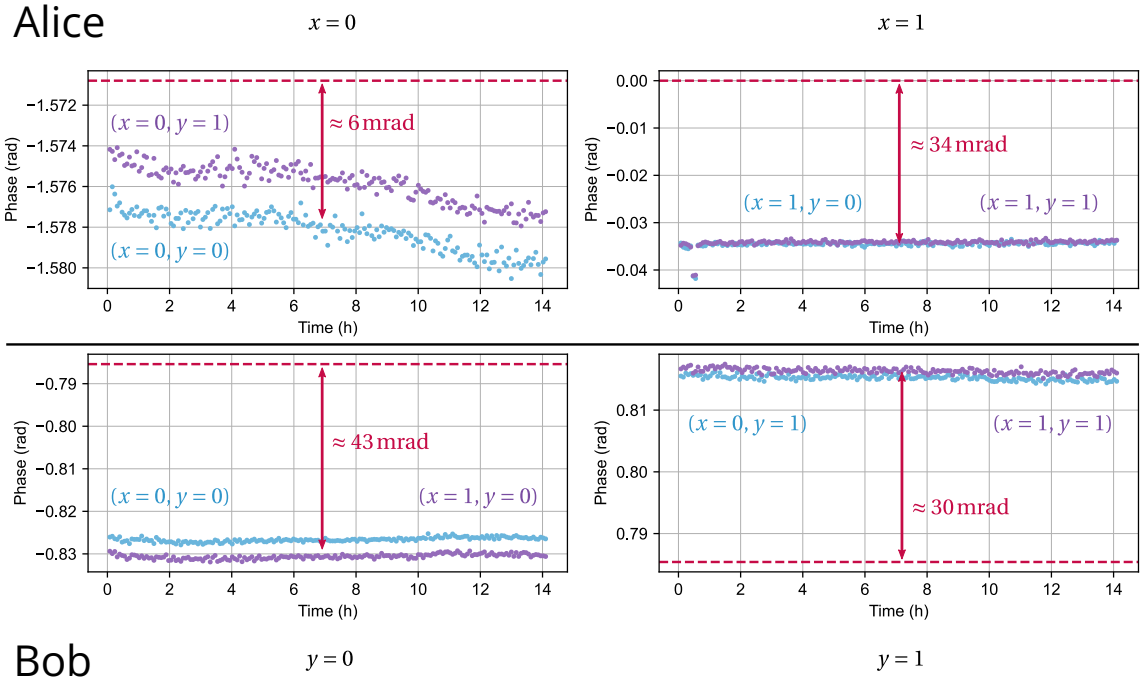

Figure II.9: Measured MZI ϕ phases of Alice and Bob over a period of 14 hours. Top: monitoring of Alice's measurement bases. Bottom: monitoring of Bob. Target phases for each measurement basis are indicated by red dashed lines. The blue and purple colors refer to different measurement contexts as indicated by the labels. The phase measurement of Alice's basis $x = 1$ is limited by dark counts.

as depicted in Fig. II.8. We then simultaneously measure Alice's and Bob's interferometer splitting defined by

$$s_0^{A/B} = \frac{N_0^{A/B}}{N_0^{A/B} + N_1^{A/B}} \tag{II.25}$$

where $N_0^{A/B}$ and $N_1^{A/B}$ are the photon countrates detected at the output of the upper and lower mode respectively of Alice's / Bob's interferometer. The measured splitting is related to the interferometer phase ϕ via

$$s_0^{A/B} = \sin^2\left(\frac{\phi}{2}\right) \quad \Longleftrightarrow \quad \phi = (-1)^k \times 2\arcsin\left(\sqrt{s_0^{A/B}}\right) + 2k\pi \tag{II.26}$$

where $k = \left\lfloor \frac{\phi}{2\pi} + \frac{1}{2} \right\rfloor$. This yields the phases ϕ^A and ϕ^B of Alice and Bob[2], assuming equal losses on both outputs. Inhomogeneous output losses may be caused by inconsistencies in the fiber-to-PIC couplings and in the single-photon detector efficiencies. Compensating the output transmissions would require a second motorized shutter in the optical setup to block Alice's photon when needed.

Using our MZI ϕ phase estimation method, we measure Alice's and Bob's phases in the four chosen measurement contexts from Table II.2 for several hours as shown on Fig. II.9 with voltages computed from the phase-voltage relation Eq. II.24. Some phase configurations exhibit a noticeable offset from the target phase value. In general, we estimate that the phase-voltage relation Eq. II.24 implements the target phases with an average error of the order of $50\,\mathrm{mrad}$. This is because the PIC is thermalized to $30\,^\circ\mathrm{C}$ in our setup, while it was left at ambient temperature during its characterization by the manufacturer. We measure the PIC to be sensitive to temperature, as we show on Fig. II.10 where we study the measured signaling fraction between Alice and Bob as a

[2] If the MZI beamsplitters are not symmetric, then we will measure the phase that an ideal MZI would need to implement to produce the same splitting. This does not induce errors in what follows.

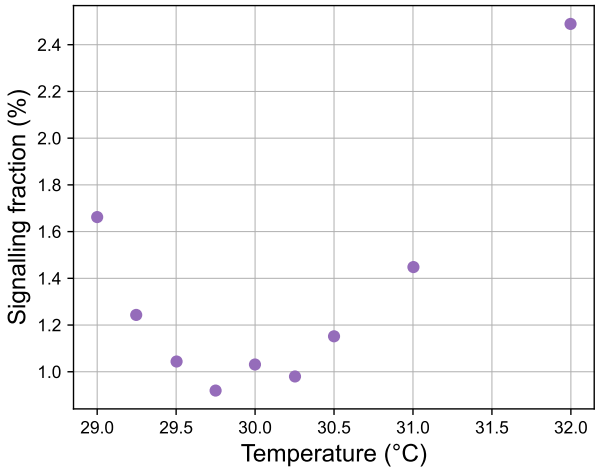

Figure II.10: signaling fraction as a function of PIC temperature The dependence of the signaling fraction with the temperature indicates that the implemented phase shifts, and by extension the PIC phase-voltage calibration, depend on the temperature.

function of temperature. There may also be electric crosstalk because of a shared ground in our voltage supply (see Appendix B of [6]).

In addition, we observe that the measured phases drift over time, with typical values of the order of $0.25\,\mathrm{mrad/h}$. The drifts may be caused by internal component fluctuations in the voltage supply and by polarization instabilities in the fibers linking the PIC outputs to the detectors, which are polarization-sensitive. Output transmission fluctuations should in principle not be compensated with the MZI phase, otherwise leading to a reduced CHSH inequality value, but it is equally important that Alice and Bob keep a precise interferometer setting to limit signaling.

II.4.3.B - Phase calibrations

We choose to recalibrate the voltages every 6 protocol hours such that the measured interferometer ϕ phase matches the target phase. The ϕ phases are calibrated optically for each of the 4 measurement contexts using the interferometer splittings following Protocol B.2.1 detailed in Appendix B.2. Optical phase calibration with data fitting as described in our protocols is robust and fast compared to other methods based on optimization algorithms such as Nelder-Mead, where the measurement noise can critically undermine its attempts to converge to the target phases.

Alice's ψ phase (pre-MZI phase, see Fig. II.8) also require calibration. We do not calibrate Bob's ψ phase, as only the difference $\psi^A - \psi^B$ is physically measurable. Alice's ψ phase is used to compensate errors in the Bell state preparation. Indeed, the generated entangled state has in reality the general form

$$\left|\psi_{\text{entangled}}\right\rangle = \frac{|0,1\rangle + e^{i\theta}\,|1,0\rangle}{\sqrt{2}} \tag{II.27}$$

where $\theta = 0$ corresponds to the ideal Bell state $\left|\Psi^+\right\rangle$. $\theta \neq 0$ reduces the measured CHSH inequality value I_{CHSH} because the measurement bases have been chosen with respect to the expected $\left|\Psi^+\right\rangle$ Bell state. The calibration of the ψ phase is less straightforward than the ϕ phases, because ψ does not affect single-photon countrates. Instead, ψ induces variations in the 2-photon coincidence rates. We calibrate Alice's ψ phase to maximize the measured I_{CHSH} following Protocol B.2.2 from Appendix B.2.

We calibrate the ψ phase only once. On the other hand, the MZI ϕ phases are calibrated at the beginning of a C-QRNG acquisition and then every 6 hours of operation. The measured phase then stays confined in an interval of $3\,\mathrm{mrad}$ around the target phases (see Fig. II.11). Notice that the target

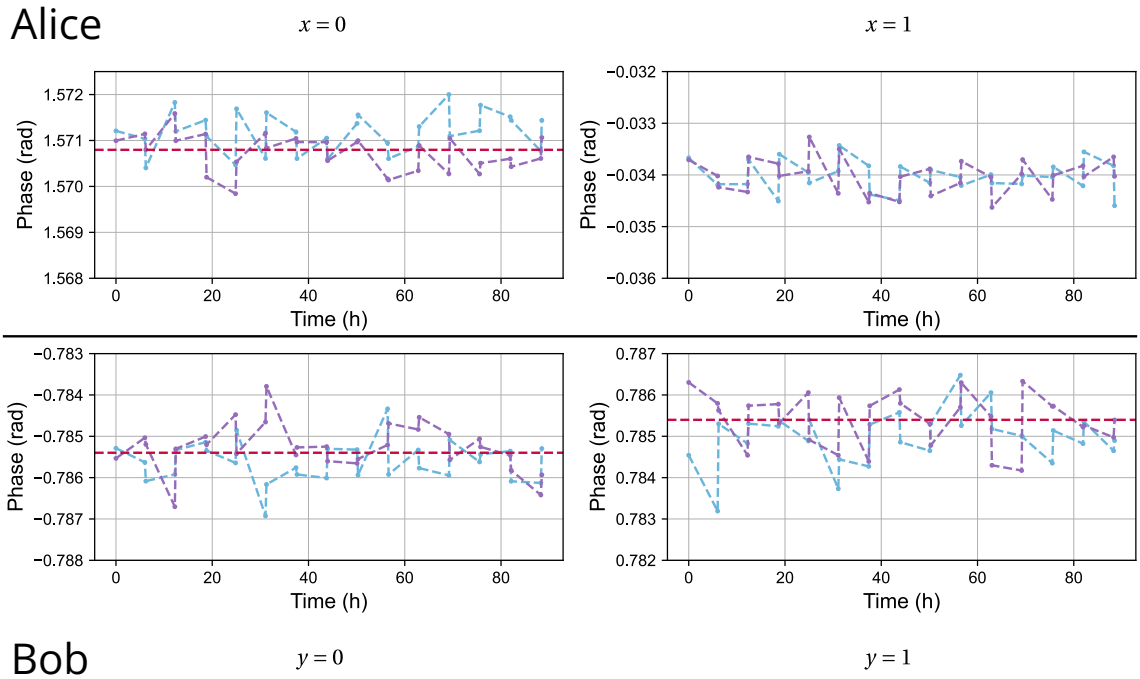

Figure II.11: Measured phases over 94 hours with periodic phase calibrations. Red dashed lines indicate target phases. The phase is measured every 6 hours before and after a phase calibration.

phase in Alice's $x = 1$ basis is $0\,\mathrm{rad}$, but dark counts on the detectors prevent from approaching that value. Hence, even if the measured phase of Alice is $\approx -30\,\mathrm{mrad}$, it is in truth much closer to $0\,\mathrm{rad}$. In addition, given the dark counts rate $\approx 300\,\mathrm{Hz}$ which are not temporally correlated to the signal photons and the chosen coincidence window of $1\,\mathrm{ns}$, the probability of recording a coincidence between a signal and a noise photon is of the order of 10^{-7}.

II.4.3.C - Single-photon characteristics monitoring

In addition to measuring the total countrate on the detectors, we follow the HOM visibility of the single-photons, quantifying photon indistinguishability (see Section I.3.1.C), in realtime during the protocol. Indeed, from the phase shift choices in Table II.2, Alice's MZI phase is $\pi/2$ during the generation rounds. As a result, Alice's MZI acts like a symmetric beamsplitter during the generation rounds, which directly yields the HOM visibility value from the coincidence statistics on her detector pair.

Before and after the periodical phase calibrations, we also measure the photon purity via $g^{(2)}(0)$ (see Section I.3.1.B) by setting again Alice's MZI to $\pi/2$ and blocking Bob's input photon using the motorized shutter shown on Fig. II.6b. Hence, we are able to keep track of all relevant single-photon characteristics during the random number acquisition.

II.4.3.D - Feedback loops for setup stabilization

A significant part of our contribution to the experiment consisted in identifying sources of instability in the setup and the implementation of feedback loops to mitigate them. During the initial phases of the experiment, we used resonant excitation to address the QD single-photon source (see Section I.3.3.A). Resonant excitation is challenging to use for long experiments, as the emitted photons are separated from the reflected excitation pulses via polarization filtering. Our lab being measurably unstable in temperature, we implemented a feedback loop on the total number of detected photons acting on motorized quarter- and half-wave plates in the filtering stage. This greatly improved stability, but the setup remains very sensitive to external perturbations, as can

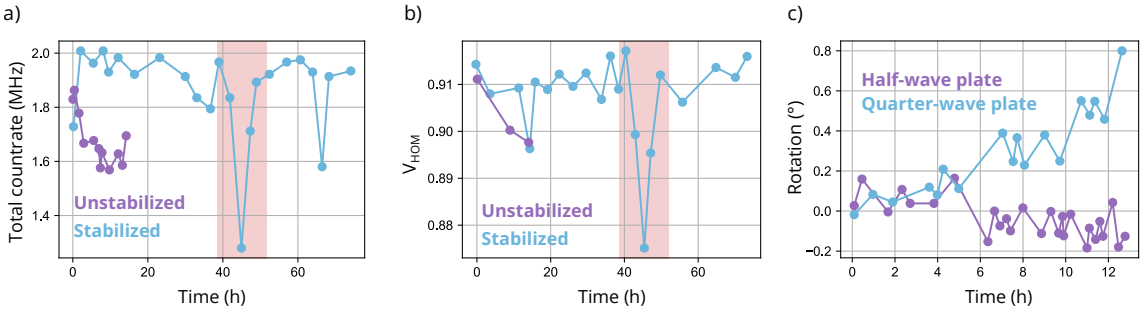

Figure II.12: Setup stabilization in resonant excitation. **a)** Total countrate and **b)** HOM visibility as a function of time. In the stabilized setting, motorized quarter- and half-waveplates compensate polarization drifts affecting the polarization-based filtering stage. The red area indicates for the stabilized run a time period with increased activity in the lab. **c)** Typical drift of the wave plate rotations during experimental stabilization.

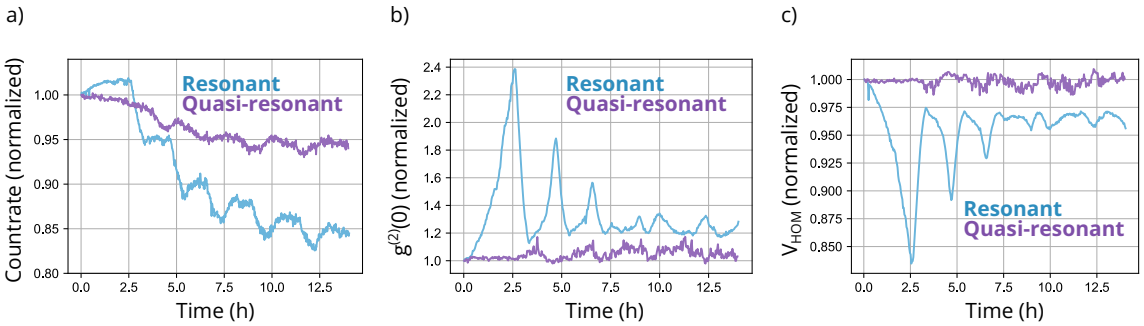

Figure II.13: Quasi-resonant excitation improves the stability of the QD single-photon emitter. **a)** Brightness, **b)** $g^{(2)}(0)$ (see Section I.3.1.B) and **c)** V_{HOM} (see Section I.3.1.C) as a function of time for resonant and quasi-resonant excitation. The measured data is normalized such that the first value is 1.

be seen from the red area in Fig. II.12.

We then transitioned to the single-photon source "Alyx" used for our main experimental C-QRNG acquisition, and decided to use the quasi-resonant excitation scheme (see Section I.3.3.A). Fig. II.13 shows that quasi-resonant excitation grants more stability compared to resonant excitation, due to its saturating behavior. We use in addition an etalon for improved photon filtering (see Section II.4.1), thus the QD emission wavelength requires stabilization such that the wavelength of the emitted photons stays in line with the etalon. The issue is addressed by adding a feedback loop on the QD voltage control maximizing the total countrate on the detectors.

We show on Fig. II.14 the monitored characteristics of the single-photon source during our main 95-hour experiment, with a fully stabilized optical system. The setup is remarkably stable on long operations without requiring exterior intervention. We attribute the oscillations in the countrate to the air conditioning cycles of the lab, which affect the polarization of the single photons arriving on the polarization-sensitive detectors.

II.4.4 - Practical considerations for the protocol

While setting up the experiment, we realized that some aspects of the QRNG protocol of Section II.3 needed to be modified to conform to a more practical reality. We discuss in Section II.4.4.A a modification for the signaling fraction and in II.4.4.B how generation rounds are be processed in batches instead of individually.

II.4.4.A - Revisiting the signaling fraction

We introduced in Section II.2.5 the signaling fraction, a measure of the amount of communication between Alice and Bob during a Bell test. We argue in this section that the signaling fraction

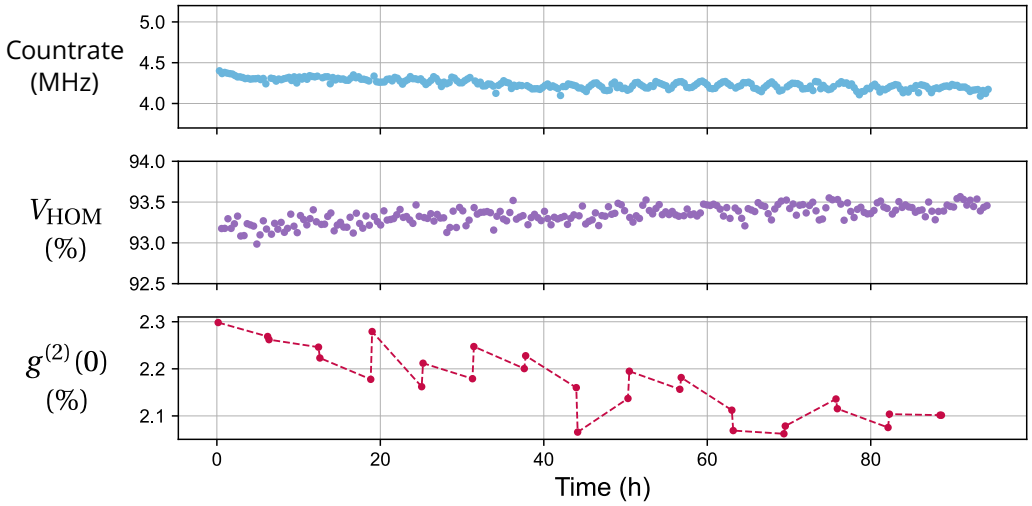

Figure II.14: Stability of the experimental setup and single-photon source. Total countrate on all detectors, HOM visibility V_{HOM} and $g^{(2)}(0)$ measured over 95 hours in our main experimental run.

is not sufficient by itself to detect deviations from an ideal Bell test and must be redefined.

We conduct the following simulated experiment: Instead of calibrating Alice's and Bob's MZI ϕ phases using optical measurement as described in Section II.4.3.B, we instruct the setup to find MZI ϕ phases that maximize the CHSH score S_{CHSH}. The initial CHSH score is $S_{\mathrm{CHSH}} \approx 0.83$ given our single-photon source characteristics. After optimization, we then observe that the the resulting choice of phases lead to $S_{\mathrm{CHSH}} \approx 0.98$, largely exceeding the Tsirelson bound (≈ 0.85). Investigating the measurement contexts shows that the (2, 2, 2) Bell scenario structure where Alice and Bob each have two measurement bases x and y has been abandoned, as can be seen on Fig. II.15. Indeed, now Alice and Bob each have 4 measurement bases, one for each measurement context. This experiment was also reproduced on the experimental setup, achieving $S_{\mathrm{CHSH}} \approx 0.92$.

Remarkably, the signaling fraction $\mathrm{SF} \approx 6 \times 10^{-11}$ fails to detect this anomaly in the measurement contexts, which an adversary might exploit to fake a very high randomness generation score. The above simulation and experiment demonstrate that the respect of the (2, 2, 2) Bell scenario must additionally be enforced. This led us to use in practice a modified version of the signaling fraction that we call the **quantum fraction**, denoted SF_ℓ with $\ell \in \mathbb{N}$ (see Def. II.4.1).

Definition II.4.1: Quantum fraction

The **quantum fraction** $\mathrm{SF}_\ell(e)$ of a (2,2,2) behavior is defined as

$$\mathrm{SF}_\ell(e) = \min\left\{\lambda \in [0,1] \quad \text{such that} \quad e = [1-\lambda] \times e^{\text{NS-NPA}} + \lambda \times e'\right\} \tag{II.28}$$

where $e^{\text{NS-NPA}} \in \mathrm{NPA}_\ell$, the ℓ-th level of the Navascués–Pironio-Acín hierarchy [192]. This yields for e a decomposition of the type:

$$e = (1 - \mathrm{SF}_\ell) \times e^{\text{NS-NPA}} + \mathrm{SF}_\ell \times e' \tag{II.29}$$

We have the following property:

$$\mathrm{SF}_\ell \geq \mathrm{SF}_{\ell-1} \geq \ldots \geq \mathrm{SF}_0 = \mathrm{SF} \tag{II.30}$$

SF_ℓ approximates the distance between the measured (2,2,2)-behavior e and the space of no-signaling (2,2,2)-behaviors that can be reached with a formalism of the type:

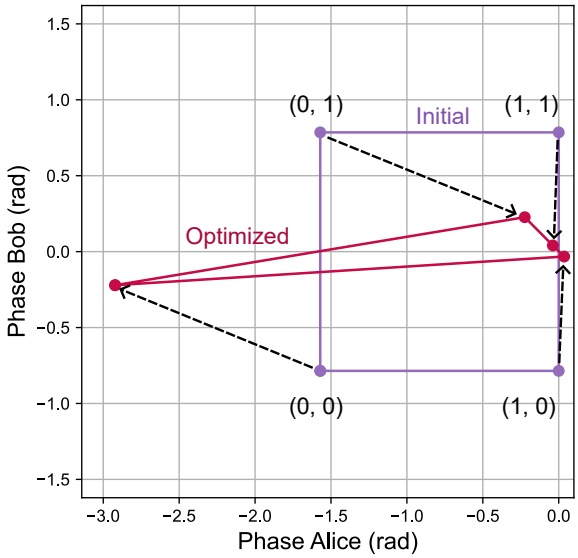

Figure II.15: Example of measurement contexts exceeding the Tsirelson bound. Purple: Alice's and Bob's phases for optimal quantum no-signaling violation of the CHSH inequality in the (2, 2, 2) Bell scenario, as presented in Table II.2. Notice that this forms a square of side $\pi/2$. (x, y) labels indicate the measurement context. Red: phases after optimization for maximal CHSH violations without constraints, resulting in a Tsirelson bound violation. The arrows indicate how the measurement contexts evolved.

$$\mathbb{P}(a, b|x, y) = \mathrm{Tr}\left(\hat{\rho}_{x,y}\hat{M}_x \otimes \hat{M}_y\right) \tag{II.31}$$

Consequently, the quantum fraction SF_ℓ measures the departure from (2,2,2)-behaviors realized by quantum mechanics with separable measurements where Alice and Bob each have two measurement bases. In other words, SF_ℓ measures the amount of communication between Alice and Bob and if Alice and Bob respect the (2, 2, 2) Bell scenario. Any deviation from this scenario may be the result of uncorrected thermal crosstalk or malicious attacks. We choose[3] $\ell = 2$ and set the new following relation for the hidden-variable signaling bound σ (previously $\sigma = \mathrm{SF}$ in Section II.2.5):

$$\sigma = \mathrm{SF}_2. \tag{II.32}$$

As a result, the new score of the experiment (see Section II.3.2) given an experimental (2,2,2)-behavior e_{XP} is

$$\mathrm{score}(e_{\mathrm{XP}}) = S_{\mathrm{CHSH}}(e_{\mathrm{XP}}) - \frac{\mathrm{SF}_2(e_{\mathrm{XP}})}{4} - 0.75 \tag{II.33}$$

SF_ℓ imposes stronger constraints than simply the departure from no-signaling, quantified by the original signaling fraction SF. Repeating the CHSH maximization simulation yields a quantum fraction $\mathrm{SF}_2 \approx 0.84$ which detects the imperfections in the measurements and penalizes accordingly the score of the experiment.

II.4.4.B - Batch processing of generation rounds

In principle the protocol rounds should be processed one by one as described in Section II.3.1, but in practice this slows down the experiment by a large amount (10 protocol rounds processed

[3]The choice $\ell = 2$ is motivated by the fact that Bell inequality violations in the (2, 2, 2) Bell scenario are computed from order 2 correlations between Alice and Bob (e.g. $\langle A_x B_y \rangle$ where A_x is Alice's observable in her measurement basis x and similar for B_y), hence taking into account order 3 correlations with SF_3 would not add anything.

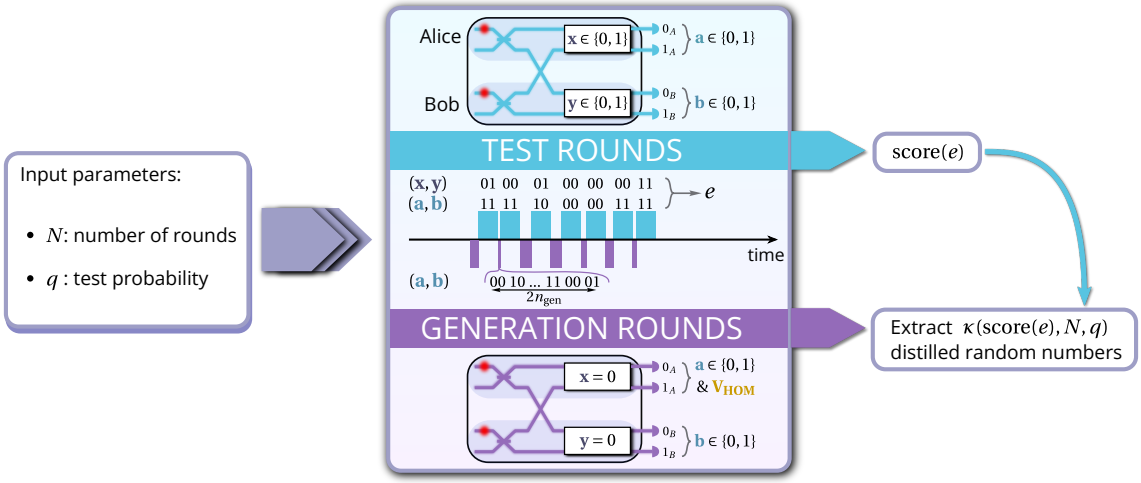

Figure II.16: Flowchart of our C-QRNG experiment. The inputs of the protocol are N the number of protocol rounds to process and q the test probability. The experiment is a succession of batches of n_{gen} generation rounds in the context $(0,0)$ followed by a test round in a randomly chosen context. Alice records the HOM visibility V_{HOM} in realtime with her interferometer during the generation rounds. The test rounds are used to construct the (2,2,2)-behavior e of the experiment, whose properties give the number of random bits to extract from the generation rounds data.

per second against >1000 per second in theory, see Section II.5.5.A). To alleviate the latencies imposed by the Python implementation and communication with the hardware, we process the generation rounds in batches. The question is, how many generation rounds should be processed per batch?

In the round-per-round case, the probability to do a test round is q, otherwise it is a generation round. This is mathematically equivalent to drawing a number of generation rounds n_{gen} according to a **geometric distribution** $\text{Geo}(q)$ (see Def. II.4.2), processing the n_{gen} in a single run, and then doing a test round. The average value of n_{gen} remains $1/q$ as expected. Processing the generation rounds in batches allowed to us to meet the expected rounds processing rate (see Section II.5.5.A).

From a cryptographic point of view, batch processing the generation rounds is not a problem as the exact number of generation rounds carried out per batch is not known to the adversary and the timing of the test rounds remains unpredictable.

Definition II.4.2: Geometric distribution

Let X be a discrete random variable. X follows a geometric distribution $\text{Geo}(p)$ of parameter p when

$$\mathbb{P}(X = k) = (1-p)^{k-1}p \tag{II.34}$$

The geometric distribution is the "law of first success" and is implemented in Python via `numpy.random.geometric`.

II.4.5 - Main experimental run and results

Before running the experiment, we separately measure a CHSH inequality violation of $I_{\text{CHSH}} = 2.68$, which we use to fix the optimal parameters for the protocol. The total number of rounds $N = 2.4 \times 10^9$ was determined by the desired duration of the acquisition of $\approx 100\,\text{h}$ together with the rounds processing rate of $\approx 7300\,\text{s}^{-1}$ of our experimental setup. We choose a test probability $q = 1.34 \times 10^{-4}$ to maximize the amount of extractable random numbers $\kappa(\text{score}, N, q)$ given the measured I_{CHSH} and targeted N. We carry out the experiment following the flowchart shown on

a) Experiment

(a,b) \ (x,y)	$(0,0)$	$(0,1)$	$(1,0)$	$(1,1)$
$(0,0)$	0.424	0.090	0.085	0.077
$(0,1)$	0.087	0.416	0.418	0.429
$(1,0)$	0.084	0.410	0.418	0.423
$(1,1)$	0.405	0.084	0.079	0.071

b) Simulation

(a,b) \ (x,y)	$(0,0)$	$(0,1)$	$(1,0)$	$(1,1)$
$(0,0)$	0.415	0.085	0.081	0.081
$(0,1)$	0.085	0.415	0.419	0.419
$(1,0)$	0.085	0.415	0.419	0.419
$(1,1)$	0.415	0.085	0.081	0.081

Figure II.17: **a)** Experimental (2,2,2)-behavior from test rounds **b)** Expected (2,2,2)-behavior simulation with single-photon source parameters $g^{(2)}(0) = 2.3\%$ and $M_s = 97\%$ (mean-wave packet overlap, equal to V_{HOM} when $g^{(2)}(0) = 0$), similar to our experiment. The transmission of the optical setup is set to 2.7%. The simulation was performed with `Perceval`.

on Fig. II.16.

The 3.2×10^5 test rounds are used to construct the (2,2,2)-behavior e_{XP} of our experiment. We show e_{XP} on Fig. II.17 and compare it to the expected one given our single-photon source characteristics. We obtain $I_{\text{CHSH}}(e_{\text{XP}}) = 2.685$ and $\text{SF}_2(e_{\text{XP}}) = 0.005$ on the test rounds. The measured quantum fraction is compatible with the uncertainty due to a finite number of test rounds (discussed in Section II.5.4). We extract 7.21×10^6 random bits with the Toeplitz matrix hashing randomness extractor. For this proof of principle experiment, we achieved a generation rate of 21.2 bits/s. Below are the first 100 generated private and unpredictable random bits against quantum side information:

0 1 0 1 1 1 1 1 0 0 0 0 1 0 1 1 0 0 0 1 0 1 0 1 1 1 0 1 1 1 0 0 1 0 0 0 1 0 0 0 0 1
0 1 1 1 1 0 1 1 0 1 0 0 1 0 1 1 0 1 1 1 0 1 1 1 1 0 1 1 1 1 1 1 0 1 1 1 0 1 1 1 1 1
0 1 1 1 1 1 0 1 1 1 0 0 0 1 1 0.

In the next section, we discuss our experimental implementation, considering potential loopholes, the current state of the art, and possible improvements.

II.5 - Discussion of our certification: loopholes, state of the art and perspectives

Randomness certification protocols are built on theoretical assumptions. Experimental implementations of randomness certification may be invalidated because of the existence of Bell test loopholes, as discussed in Section II.5.1. We then review the state of the art in randomness certification experiments (Section II.5.2) and the novelty of our experiment in this regard. Subsequently, we discuss imperfections (Section II.5.3), the impact of finite statistics (Section II.5.4) and potential near-term improvements for the experimental implementation (Section II.5.5).

II.5.1 - Bell test loopholes

A **loophole** is a mechanism that may be exploited by theoretical models or cryptographic adversaries to reproduce the experimental data using a local model, hence faking the contextuality in the observed data. In other words, it is possible to abuse certain weaknesses of the optical setup to counterfeit high Bell inequality violations. In our C-QRNG experiment, this would lead to a vanishing of the privacy and unpredictability of the generated random bits. We present the three main discussed loopholes in Bell tests and discuss how they are accounted for in our experiment.

II.5.1.A - The time-coincidence loophole

The time-coincidence loophole [193, 194] refers to an exploit of the detection timings of the experiment. In our experiment, we can argue that the loophole is partially closed because the co-

incidence window ($1\,\mathrm{ns}$) is significantly smaller than the time of arrival between successive photon pairs ($= 2\tau_{\mathrm{rep}} \approx 24\,\mathrm{ns}$ in the best case). Consequently, the probability of mixing up two photon pairs is quasi-nonexistent. We could however more convincingly close the loophole by synchronizing Alice's and Bob's detection window with the pump laser clock signal.

II.5.1.B - The detection loophole

In a realistic setting, there is always some amount of photons lost in the setup due to absorption for instance. As a consequence, we never implement the (2, 2, 2) Bell scenario. In reality, Alice and Bob have three outcomes instead of two: they can measure 0, 1 or $\perp$ (inconclusive measurement). A measurement is inconclusive when one of the agents measures a click but the other does not[4]. If the detection efficiency is not high enough, local models can reproduce the experimental data [180].

We check if the detection loophole can be opened in our version of the experiment. We denote by T the overall optical setup transmission. We assume that the stream of single-photons is evenly split between Alice and Bob by the demultiplexer and neglect multi-photon emissions and dark counts. When our single-photon source generates two consecutive single-photons, they lead to a valid outcome when the pair is correctly demultiplexed, not rejected by Bell state postselection and both photons are detected. Thus, the probability that the photon pair leads to a valid measurement is

$$\mathbb{P}_{\mathrm{valid}} = \frac{T^2}{4}. \tag{II.35}$$

Hence, for our experiment $\mathbb{P}_{\mathrm{valid}} \approx 0.02\,\%$. On the other hand, the litterature relates $\mathbb{P}_{\mathrm{valid}}$ to a "detection efficiency" η via

$$\mathbb{P}_{\mathrm{valid}} = \eta^2 \tag{II.36}$$

which is tailored for parametric single-photon sources providing natively entangled photons. We relate our setup transmission to the η parameter:

$$\eta = \frac{T}{2} \approx 1.4\,\% \tag{II.37}$$

The detection loophole is closed when $\eta > \eta^* = 2/3$ which is not realized by our experiment. In fact, even with a perfect setup transmissions $T = 1$ corresponding to $\eta = 1/2$, we still do not close the loophole because of Bell state postselection and passive demultiplexing. Going to active photon demultiplexing multiplies the valid outcome rate by 2, and would allow for a perfect setup to reach $\eta \approx 71\,\%$, eventually closing the detection loophole.

II.5.1.C - The locality/compatibility loophole

The **locality loophole** applies when Alice and Bob are not spacelike separated. In that case, the agents might communicate during a measurement and "cheat" the Bell test. The locality loophole is closed by separating Alice and Bob spatially and invoking special relativity to assert that communication between the agents is prevented. In our experiment, we do not rely on locality to certify randomness but on contextuality. This replaces the locality loophole by the more general **compatibility loophole**, referring to the fact that Alice's and Bob's measured observables A_x and B_y need to be **compatible** in the sense:

$$A_x \cdot B_y = B_y \cdot A_x \tag{II.38}$$

Failing to satisfy this condition amounts to signaling between the agents. We do not close the loophole, but quantify it via the signaling fraction.

[4] Inconclusive measurements may be also used to take into account the cases where one of the agents measures a click on both of their detectors due to multi-photon emission or dark counts.

II.5.1.D - On the importance of closing loopholes

All three mentioned loopholes are not closed in our experiment. In particular, closing the detection loophole is challenging when relying on post-selection to entangle the photons due to the very limited room for optical losses. Our setup may not be adapted for detection loophole-free experiments, but we argue that while it is of utmost importance to design loophole-free Bell tests when probing the fundamental aspects of nature [172, 195], they may be tolerable for cryptographic purposes like random number generation on a machine that is closely monitored in a dedicated server room, assuming

- an **honest provider** setting: the measured signaling fraction is correct and representative of the signaling fraction at the hidden-variable level (implying $\sigma = \mathrm{SF}$ in Section II.4.2.B)
- **fair sampling** to address the detection loophole: the joint detections by Alice and Bob are representative of the outcomes that would have been measured without optical losses.

II.5.2 - Comparison with state of the art in experimental randomness certification

		Source	Bitrate	On-chip	Side information	Detection loophole	Locality loophole
2010	[178]	Trapped ion	$\approx 16\,\mu$bits/s	No	Classical	Closed	Shielding
2018	[196]	SPDC-P	114 bits/s	No	Quantum	Closed	Open
	[174]	SPDC-P	≈ 2.3 bits/s	No	Classical	Closed	Closed
	[197]	SPDC-C	240 bits/s	No	Quantum	Closed	Open
	[173]	SPDC-P	181 bits/s	No	Quantum	Closed	Closed
2020	[175]	SPDC-P	≈ 1.7 bits/s	No	Quantum	Closed	Closed
	[198]	Trapped ion	270 bits/s	No	Quantum	Closed	Bounded disturbance
2021	[176]	SPDC-P	2.3 kbits/s	No	Quantum	Closed	Closed
	[177]	SPDC-P	3.6 kbits/s	No	Classical	Closed	Closed
	[179]	SPDC-P	13.5 kbits/s	No	Quantum	Closed	Shielding
2023	**This work**	**QD**	**21 bits/s**	**Yes**	**Quantum**	**Open**	**Bounded signaling**

Table II.3: **State of the art of certified QRNG experiments** SPDC-P (resp. SPDC-C): pulsed (resp. continuous) spontaneous parametric downconversion. . QD: quantum dot.

We show the state of the art of C-QRNG experiments in Table II.3. Our experiment constitutes the first C-QRNG demonstration on a PIC with a security proof against quantum side information while addressing the locality loophole in an elegant and satisfying manner, with room for improvement regarding the bitrate.

II.5.3 - Impact of imperfections

II.5.3.A - Single-photon characteristics

Single-photon and optical setup imperfections decrease the maximum achievable CHSH inequality violation. This places requirements on the purity and indistinguishability of the emitted photons. In our case, the main causes of photon distinguishability arise from polarization fluctuations in the optical fibers and charge noise around the quantum dot single-photon emitter. For the ideal case of a source emitting only pure photons in a lossless optical circuit, we derive in Appendix C the relation

$$I_{\mathrm{CHSH}} = \sqrt{2}(V_{\mathrm{HOM}} + 1) \tag{II.39}$$

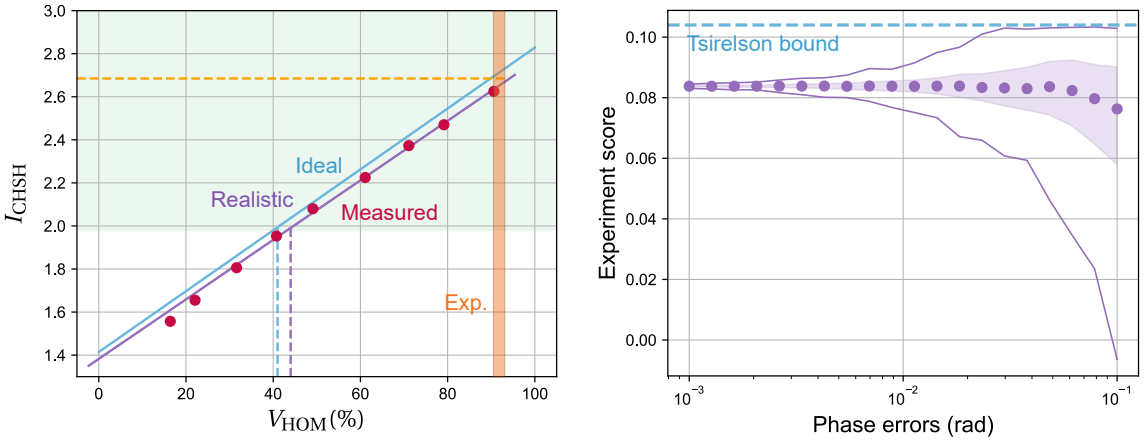

Figure II.18: **Impact of imperfections on measured CHSH inequality value and bitrate of the experiment** **a)** CHSH inequality value I_{CHSH} as a function of HOM visibility V_{HOM}. Blue : analytical dependence derived for a photon source emitting only pure single photons $g^{(2)}(0) = 0$ in a lossless circuit. Purple: realistic curve simulated with `Perceval` for $g^{(2)}(0) = 0.023$ and an optical circuit transmission of $T = 2.7\,\%$ (experimental values). The blue and purple dotted lines indicate the minimum HOM visibility required to certify quantum correlations for the ideal and realistic case respectively. The minimum values are respectively $\approx 41.4\,\%$ and $\approx 44.5\,\%$. Red points: experimental measurements by changing the polarization of one of the two photons entering the photonic chip. The error bars are contained in the plot markers. Light green area indicates CHSH violations certifying contextual correlations. Orange vertical bar indicates the range of HOM visibility values measured during our 94.5 hours main experiment, which the horizontal one represents the measured I_{CHSH} value. **b)** Simulation of impact on experiment score of random phase errors in Alice's and Bob's Mach-Zehnder interferometer (only the ϕ phases, the ψ phases are kept constant and exact). Errors are chosen according to a Gaussian distribution of given standard deviation. All other parameter values are taken equal to those of our experiment. Each point corresponds to 200 repetition of the simulation with different errors. The purple area indicates the standard deviation and continuous lines correspond to the minimum and maximum simulated values.

where V_{HOM} is the HOM visibility of the photons. We also simulate the relationship between I_{CHSH} and V_{HOM} taking additionally into account photon impurity and circuit losses with `Perceval`. We compare on Fig. II.18.a our theoretical predictions with measurements performed with the experimental setup by manually misaligning the polarization of one of the input photons. The close agreement between the simulated and acquired data points validates our theory and our experimental setup.

II.5.3.B - Phase errors

Phase errors, in particular in Alice's and Bob's MZI phase ϕ due to an imperfect calibration or spurious crosstalk, will also affect the performance of the experiment. Random phase errors will affect both the CHSH score S_{CHSH} and the measured quantum fraction SF_2. We perform simulations to evaluate the impact of phase errors on the measured experiment score and plot the results in Fig. II.18.b. We note that the score can be better or worse than the value without phase errors. However the Tsirelson bound cannot be exceeded due to the quantum fraction SF_2 penalty in the score.

The fact that the score can be enhanced by phase errors is in fact a weakness of the setup that can be exploited by an adversary to artificially increase the level of trust in the experiment. The weakness is addressed when the single-photon sources behaves ideally, because then the score can only be equal to or worse than the Tsirelson bound. Because we assume a honest provider scenario, we are not allowed to exploit this weakness to introduce controlled phase errors that enhance the final bitrate. Our milliradian precision on the phase is sufficient to be considered "honest provider" as the experiment score is weakly affected by potential phase errors in this range.

II.5.4 - Impact of finite statistics

The score of an acquisition is computed from a finite amount of test rounds n_{test}, which affects the score of an experimental run. We take in our finite statistics study as reference the theoretical (2,2,2)-behavior computed from our single-photon source characteristics (see Fig. II.17b). Notice that this (2,2,2)-behavior has $\text{SF}_2 = 0$. We then sample from the expected (2,2,2)-behavior a given number of test rounds and use these to recompute the CHSH score S_{CHSH} and the quantum fraction SF_2, which are the two quantities intervening in the C-QRNG score (see Eq. II.13). We are interested in the **standard error** of these quantities, that is the average deviation from the ideal value due to a finite sample size [199]. Mathematically, the standard error of these quantities must exhibit proportionality with respect to $n_{\text{test}}^{-1/2}$, which we verify on Fig. II.19(a,b). For the number of test rounds in main experimental run (see Section II.4.5):

$$\text{ste}(S_{\text{CHSH}}) \approx 5 \times 10^{-6} \ll \text{ste}(\text{SF}_2) \approx 3 \times 10^{-3} \tag{II.40}$$

Thus, the main contribution in the statistical error of the measured score comes from the quantum fraction SF_2. As seen on Fig. II.19.c, the measured signaling fraction is significantly affected due to finite statistics. Notably, the experimental value of 0.5% in our main run is compatible with the distribution of simulated values. Hence, it is likely that a major contribution in the obtained signaling fraction in our main experimental run stems from statistical errors.

II.5.5 - Improving the experiment

Our experiment generates private randomness with the highest standard of cryptographic security. As mentioned in Section II.5.2, a major aspect that must be improved for practical applications is evidently the bitrate. The different parameters that may be optimized in our experiment are the optical setup transmission, the PIC thermalization waiting time for a measurement context switch and the photon indistinguishability. We simulate the impact of each individual parameter

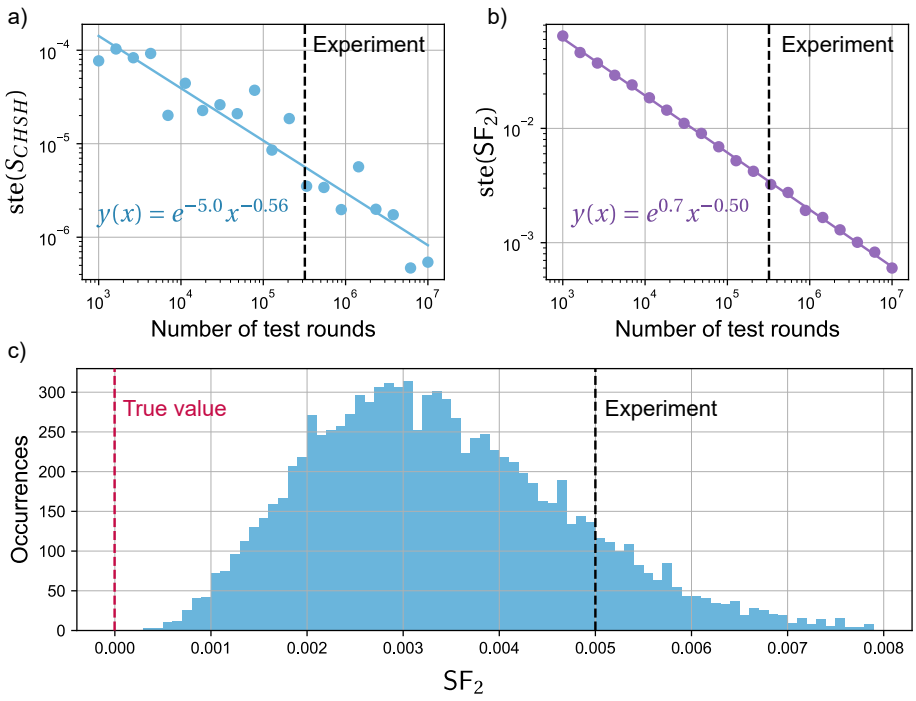

Figure II.19: Impact of finite statistics on measured CHSH score and signaling fraction.. a) (resp. b)) Standard error of S_{CHSH} (resp. SF) versus the the number of test rounds when sampling from the expected (2,2,2)-behavior given our experimental parameters (see Fig. II.17). Each point corresponds to 10 000 (resp. 100) repetitions of the sampling experiment. The black dashed line indicates the value of our main experimental run from Section II.4.5. The continuous line is a fit whose expression is displayed. **c)** Histogram of signaling fraction values when sampling n_{XP} rounds. The red dashed line indicates the signaling fraction of the reference (2,2,2)-behavior from which we sample. The black dashed line indicates the signaling fraction we obtained experimentally.

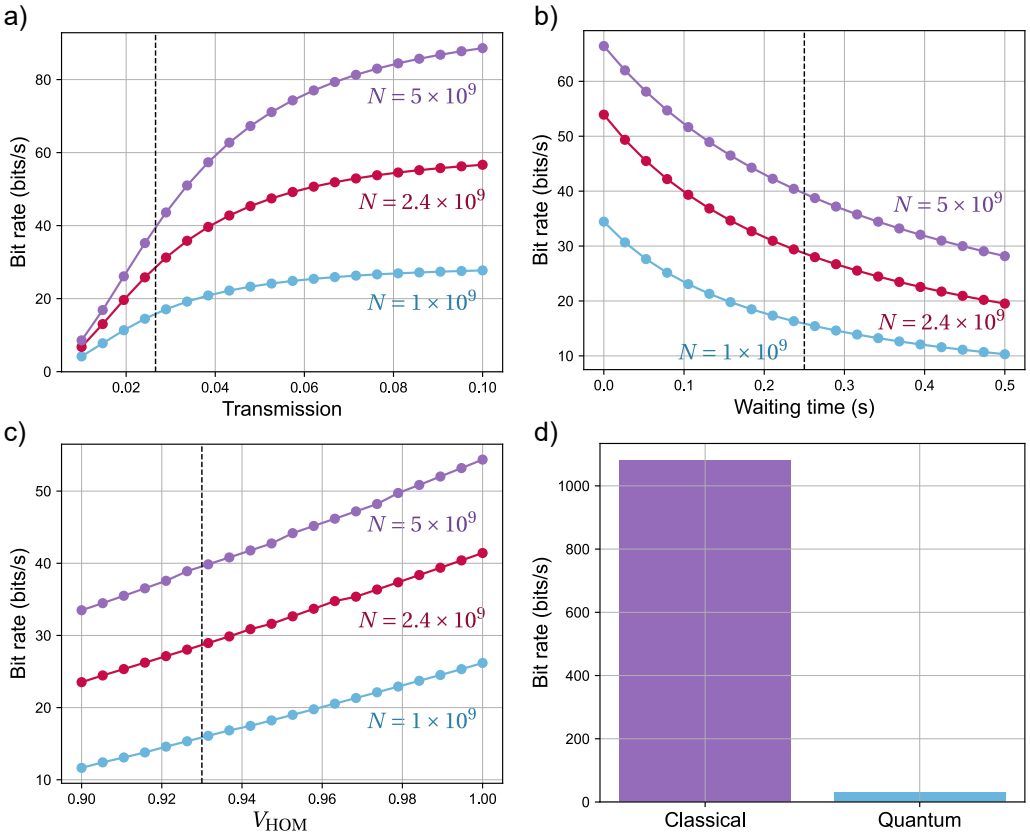

Figure II.20: Bitrate dependence of the experiment For each plot, we vary only a single parameter at a time with respect to the parameters of our main experimental run. We run the simulation for different number of protocol rounds N to process ($N = 2.4 \times 10^9$ in our experiment, red curve). Black dashed line indicates the experimental value. **a)** Impact of setup transmission. **b)** Impact of PIC thermalization time for measurement context switch. **c)** Impact of photon indistinguishability. **d)** Bitrate improvement when lowering down the security to classical side information.

and plot the results on Fig. II.20(a,b,c). The simulations neglect the impact of multi-photon emissions, but take into account the impact of finite statistics on the measured signaling fraction.

II.5.5.A - Setup transmission and waiting time

To make an educated guess on how the bitrate may be improved in the short-term, we break down the optical setup transmission:

$$\begin{aligned} T =& 0.39 \pm 0.03 && \text{(photon source brightness)} \\ & \times 0.75 \pm 0.05 && \text{(coupling to fiber)} \\ & \times 0.935 \pm 0.015 && \text{(losses between source and fiber)} \\ & \times 0.72 \pm 0.01 && \text{(filtering stage)} \\ & \times 0.59 \pm 0.01 && \text{(etalon)} \\ & \times 0.71 \pm 0.01 && \text{(photon polarisation)} \\ & \times 0.80 \pm 0.01 && \text{(demultiplexing)} \\ & \times 0.58 \pm 0.01 && \text{(chip insertion losses)} \\ & \times 0.70 \pm 0.01 && \text{(detectors efficiency)} \\ & = 0.027 \pm 0.003 && \text{(overall setup transmission)} \end{aligned} \tag{II.41}$$

The predicted coincidence rate between Alice and Bob is thus computed as follows:

$$\begin{aligned} R_{\text{coinc}} =& 158 \times 10^6 && \text{(pump laser pulse rate)} \\ & \times T^2 && \text{(overall photon transmission)} \\ & \times 1/4 && \text{(passive demultiplexing)} \\ & \times 1/2 && \text{(state post-selection)} \\ & = 14\,000 \pm 3000\,\text{s}^{-1} \end{aligned} \tag{II.42}$$

Factoring in the waiting time that is required for the PIC to thermalize when switching the measurement context gives the following formula for the amount of protocol rounds that are processed per second:

$$R_{\text{rounds}} = \frac{(1+q)R_{\text{coinc}}}{1+q+\frac{3}{2}wqR_{\text{coinc}}} \tag{II.43}$$

where w is the waiting time and q the test probability. For our experiment the predicted rounds processing rate is $R_{\text{rounds}} = 8300\,\text{s}^{-1}$, whereas the real rate is $7300\,\text{s}^{-1}$ (periodical phase calibrations subtracted from the protocol run time). This shows that there is already room for improvement in the software implementation of the experiment.

II.5.5.B - Short-term improvements

We list plausible and achievable improvements for the experiment:

- a single-photon source with polarized brightness $50\,\%$ and $V_{\text{HOM}} = 94\,\%$ without etalon.
- single-photon detectors with $90\,\%$ efficiency.
- active demultiplexing with similar insertion losses

As a result, the setup transmission would increase to $T = 10\,\%$. The active demultiplexer would also double the coincidence rate. Keeping the duration of the experiment constant at 90 hours, this would allow to reach bitrates in the $110\,\text{bits/s}$ range.

On the longer term, switching to a PIC with fast electro-optic phase shifters, would even allow to reach a bitrate of $3\,\mathrm{kbits/s}$ (again keeping the run duration constant), competing with state-of-the-art bitrates (see Table II.3).

II.5.5.C - Classical side information

Another way to efficiently increase the bitrate is to reduce the level of security. Instead of generating private randomness against quantum adversaries that may be entangled with our single-photon source for instance, we can consider a more relaxed setting in which the adversaries only have access to classical attacks. From Fig. II.20.d, we note that doing so, keeping all other parameters constant, increases the bitrate by a factor of 50.

The PIC we used to generate certified randomness can also be used to generate and study Bell states. In the same spirit, we use in the next section a similar PIC design and experimental setup to generate a 4-photon entangled state and perform its tomography.

II.6 - Building on on-chip photon manipulation: high-fidelity 4-GHZ state generation

The photonic integrated platform provided a compact and stable framework for conducting our C-QRNG experiment. We used a similar PIC design and optical setup to study and fully characterize a 4-photon **Greenberger–Horne–Zeilinger (GHZ) state**, that is a maximally entangled 4-qubit state of the form

$$|4\text{-GHZ}\rangle = \frac{|0,0,0,0\rangle + |1,1,1,1\rangle}{\sqrt{2}}. \tag{II.44}$$

The experiment was realized in a collaboration with Mathias Pont and the groups of Roberto Osellame and Fabio Sciarrino, and is thoroughly discussed in Mathias Pont's PhD thesis [71]. We will give an overview of the main points of interest and focus on our personal contributions to the project.

II.6.1 - Experimental setup

The experimental setup is an upgrade of the C-QRNG setup described in Section II.4.1. For an overview of the improvements and differences, see Table II.4. We detail the main points of the table:

- The pump laser **pulse rate doubling** has been removed to conserve pump power to optimally excite the single-photon source in the LA-excitation scheme. In addition to **new band-pass filters** in the photon filtering stage, the characteristics of the single-photon sources were substantially improved.
- the passive 2-photon demultiplexer has been replaced by an **active 4-photon demultiplexer**. The new demultiplexer drives an acousto-optic modulator to deflect photons into 4 different paths sequentially. To synchronize the deflected photons, the demultiplexer is followed by fibered delays (see Fig. II.21.a) of length $36\,\mathrm{m}$, $72\,\mathrm{m}$ and $108\,\mathrm{m}$.
- The 4-photons must enter the PIC while sharing the same polarization to maximize indistinguishability. For that purpose, we installed **motorized polarization controllers**, that allow to automatize the process of polarization optimization.
- The PIC for photon manipulation, shown on Fig. II.21, features 8 modes and 8 thermo-optic phase shifters. It bears the same structure as the QRNG PIC from Section II.4.2: a postselected entanglement stage and measurement basis implementation stage. This 4-GHZ PIC

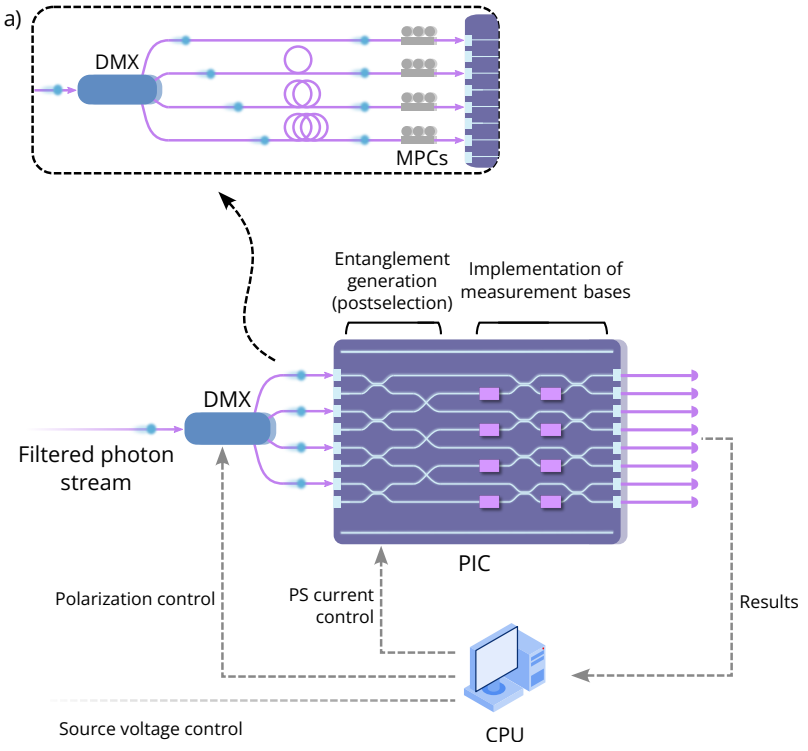

Figure II.21: **Upgraded setup for postselected 4-GHZ state generation and tomography.** Elements of the setup that have been upgraded from the C-QRNG experiment shown on Fig. II.6 are the demultiplexer (DMX) and the PIC for photon manipulation. The active demultiplexer deflects light sequentially in four directions. The photons are then synchronized in time by adding fiber delays of different length on each DMX output port (see inset **a)**). Motorized polarization controllers (MPCs) are used to automatically optimize the photon polarization. The PIC for photon manipulation features 8 modes and 8 thermo-optic phase shifters. The PIC generates the entangled state via postselection and selects the measurement bases, similarly to the C-QRNG PIC of Fig. II.7.

	C-QRNG	4-GHZ
Single-photon source	"Alyx"	"Alyx" (better excitation and filtering)
Pump pulse rate	158 MHz	79 MHz
Polarized brightness first lens	28 %	35 %
$g^{(2)}(0)$	2.3 %	0.5 %
V_{HOM}	93 %	95 %
Overall setup transmission	2.7 %	5.3 %
Demultiplexing	Passive	Active
Entangled state	Bell-state	4-GHZ
Post-selected coincidence rate	14 kHz (2-photon)	0.5 Hz (4-photon)
Number of photons in PIC	2	4
Number of modes in PIC	4	8
Number of on-chip phase shifters	4	8
PIC reconfiguration time	250 ms	1.1 s
Polarization stabilization	Manual	Automated

Table II.4: **Comparison between the C-QRNG and the 4-GHZ experiments.** The polarized brightness, $g^{(2)}(0)$ and V_{HOM} (see Section I.3.1) are measured with a filtering etalon (see Section II.4.1) also used during the experiment. The single-photon source emits photons following the quasi-resonant-excitation scheme (see Section I.3.3.A).

may be viewed as four agents: Alice, Bob, Charlie and Diane (see Fig. II.22a). The 4-GHZ state is generated via postselection on the outcomes where each agent detects exactly one photon. The postselected coincidence rate is 0.5 Hz.

II.6.2 - PIC control

The 4-GHZ PIC was provided by the same manufacturer as the QRNG PIC. The phase shifts are implemented like previously by thermo-optic phase shifters exhibiting crosstalk, with phase-electric current matrix relations similar to Eq. II.24. Controlling the PIC in electric current advantageously does not entail electric crosstalk. In addition, the heater technology has been improved such that the order 4 dependence of the phases in the electric current is not measurable, leading to far simpler matrix equations to solve.

Because the PIC structure is the same, we transposed directly our phase calibration procedure from Section II.4.3.B to the 4-GHZ PIC. The phase shifter thermalization time is here chosen to be 1 s (instead of 250 ms for the QRNG PIC). Our strategy for solving the phase-current equations is described in Appendix D.2.

II.6.3 - Photon indistinguishability stabilization

Photon indistinguishability is a key element for a successful quantum information experiment. The four injected photons need to share the same polarization when entering the PIC. There is however no direct way of measuring the polarization of each individual photon, because the PIC is polarization insensitive. In addition, each motorized polarization controller (see Fig. II.21.b) has three tiltable paddles, resulting in a total of 12 parameters left to optimize.

We program simultaneous optimizations of the polarization of the four photons using the Nelder-Mead optimization algorithm. We chose the latter because it is quite resilient to noise and does not require the gradient of the function to optimize. Our procedure sets the MZI phase of the four agents to $\pi/2$, such that the MZIs act as symmetric beamsplitters. We can then measure at the

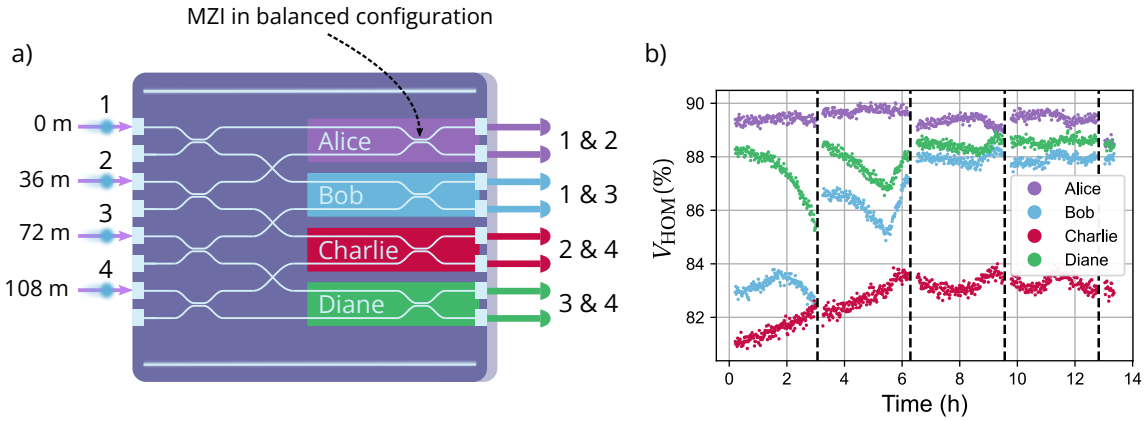

Figure II.22: **Simultaneous HOM optimization and stabilization.** **a)** Configuration for simultaneous measurement of four HOM visibility values between different pairs of photons, as written next to the detectors. The fiber delay length of each input is written next to the input fibers. During the measurement, all the MZIs are set to the balanced configuration, hence they have been replaced by symmetric beamsplitters in the drawing of the PIC. **b)** Continuous HOM measurement for 14 hours. Black dashed lines indicate automated HOM optimizations.

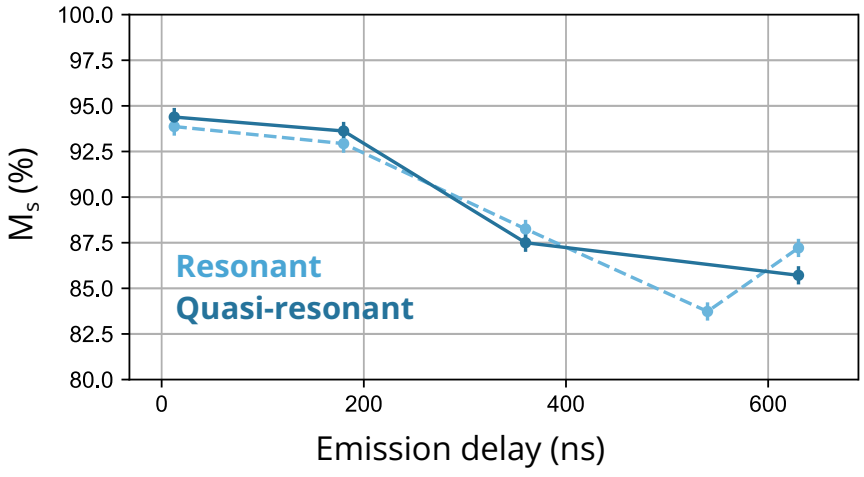

Figure II.23: **Effect of charge noise on photon indistinguishability.** Photon indistinguishability M_s (see Section I.3.1.C) as a function of emission delay between the two photons interfering. The data has been acquired in resonant and quasi-resonant excitation, without using an etalon for enhanced photon filtering.

	Single-photon source	Platform	$\mathbb{P}_4$	Fidelity of n-photon entangled state
[200], 2018	SPDC	Free-space	5.1×10^{-4}	$57.6\,\%$ $(n = 12)$
[201], 2020	QD	Free-space	3.0×10^{-6}	$79.0\,\%$ $(n = 4)$
[29], 2021	SFWM	Silicon PIC	3.6×10^{-10}	$72\,\%$ $(n = 4)$
[4], 2022 This work	**QD**	**Glass PIC**	1.1×10^{-6}	$86.0\,\%$ **$(n = 4)$**

Table II.5: **State of the art in the photonic entangled stage generation.** SPDC: spontaneous parametric downconversion. QD: quantum dot. SFWM: spontaneous four-wave mixing. $\mathbb{P}_4$ denotes the probability of detecting a 4-photon entangled state, detector efficiency not taken into account.

same time the HOM visibility of all 4 photon pairs received by the agents as shown on Fig. II.22.a. The optimization algorithm is instructed to maximize the sum of the four HOM values, by moving all 12 paddles simultaneously.

Fig. II.22.b shows a continuous acquisition of all four HOM values with optimizations about every three hours (dashed vertical lines). The automated operation of the polarization controllers enables the precise stabilization of the photon indistinguishability. A few comments on the HOM values:

- The experiment was done without etalon in the filtering stage, thus the measured HOM values cannot be higher than $93\,\%$.
- The shortest delay between two interfering photons ($36\,\mathrm{m}$ difference for Alice and Diane) is already much longer than the usual delay ($2.5\,\mathrm{m}$) between two consecutive photons when measuring the source characteristics. The highest measurable HOM value is affected by charge noise around the QD (see Section I.3.3.B). This explains why Alice's and Diane's HOM value does not exceed $90\,\%$.
- Charlie measures the HOM between a pair of photons with $72\,\mathrm{m}$ delay difference. Increased impact of charge noise further reduces the measured HOM value, as can be seen on Fig. II.22.b.
- It is unclear why there is such a strong discrepancy between Bob's and Charlie's HOM value, as they should be equivalent.

The automated HOM optimization allowed to us to carry out continuous 4-photon experiments spanning on more than 80 hours in an unstable environment.

II.6.4 - 4-GHZ state results and conclusion

With our upgraded and stabilized setup, we carried out the following experiments reported in [4]:

- Violation of a Bell-like inequality certifying non-classical correlations between the four agents. Signaling (see II.2.5) was not taken into account in this experiment.
- Full tomography of the 4-GHZ state in only 50 hours consisting of 81 measurements to reconstruct its 16×16 density matrix. We achieved a fidelity of $86\,\%$ and a state purity of $76\,\%$. The matrix is displayed in Fig. II.24.
- Quantum secret sharing [202], a protocol in which one of the agents shares a key with the other agents in a cryptographically secure way, harnessing quantum correlations. The measured quantum bit error rate of $10.87\,\%$ is just below the secure communication threshold of $11\,\%$ and the raw bit generation rate is $0.5\,\mathrm{Hz}$.

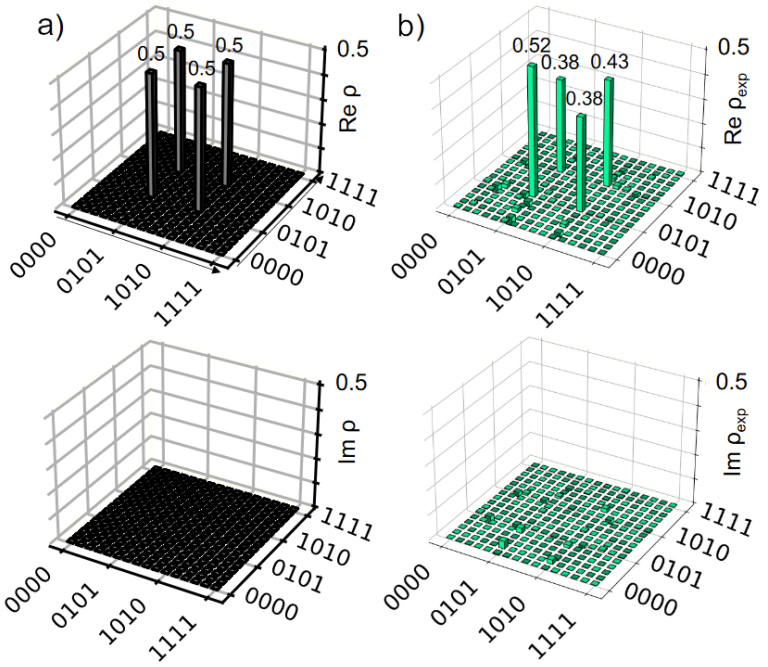

Figure II.24: (from [4]) **Full reconstruction of 4-GHZ density matrix.** **a)** Theoretical density matrix of GHZ state. **b)** Measured density matrix.

Table II.5 summarizes the state of the art in experimental photonic entangled state generation. Our 4-GHZ state demonstrates remarkable measured fidelity. However, the state generation rate could be significantly improved with better fabrication quality of the single-photon source. In fact, this experiment underscores the critical need for extremely bright and clean single-photon sources. Enhanced sources would enable high-rate multi-photon coincidences and prevent photon indistinguishability degradation caused by charge noise with delay length, a major challenge for scaling beyond few-photon experiments. On the integrated platform, our quantum-dot-based single-photon source already achieves impressive rates, with potential for further improvements, whereas parametric sources are operating at their maximum capacity.

II.7 - Conclusion on small-scale dedicated circuit QI processing demonstrations

Starting with small-scale, specialized PICs, this chapter has laid the foundation for photonic QI processing demonstrations that scale up the number of single photons, modes, and on-chip components.

We experimentally implemented a **practical certified random number generator**, including a quantum dot-based single-photon source and a compact photonic integrated circuit. The circuit entangles 2 path-encoded photonic qubits via postselection and selects the qubit measurement bases. We set up the experiment and demonstrated its remarkable stability, thanks to the use of fibered and integrated optics, in addition to periodic optical phase calibrations. The bright single-photon source delivers a steady stream of indistinguishable photons via the quasi-resonant-excitation scheme, allowing us to carry out 100-hour experimental runs. **During our main run of 94 hours, we generated and distilled more than 7×10^6 certified random bits, corresponding to a bitrate of 21 bits/s, with a signaling fraction of 0.5 % attributed to finite**

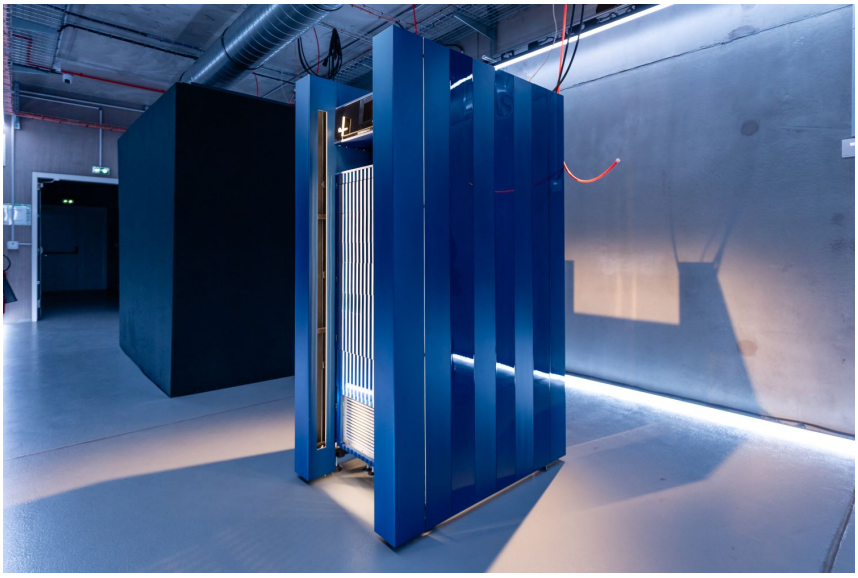

Figure II.25: ***MosaiQ* in the OVH Cloud server room.** The device generates certified randomness based on a protocol similar to the one introduced in this chapter.

statistics. We then analyzed and discussed our experiment in light of the state of the art, Bell test loopholes, main sources of imperfections and possible near-term improvements. Our results on C-QRNG were published in [3].

The architecture of the PIC used for randomness generation comprised post-selected entanglement and qubit basis selection stages. We used a similar PIC to generate 4-GHZ states and perform their tomography, carrying over our experience on PIC control and qubit manipulation. The optical setup was extended to work with four photons, requiring further motorization of the setup and new approaches to stabilize single-photon experiments. **The dedicated PIC was used for the precise and stable generation and characterization of a 4-photon entangled state, while the upgraded optical setup allowed us to carry the experiment in a record time of ≈ 50 hours. We measured a state fidelity of 86 % and purity of 76 %, surpassing the state of the art.** The generated 4-GHZ states were then harnessed to perform quantum secret key sharing, which we reported in [4].

The C-QRNG and 4-GHZ experiments enabled us to become well-acquainted with the essential components of a modular photonic device architecture, as well as foster and nourish interactions with the Quandela quantum information theory team. The certified randomness generation experiment evolved into *MosaiQ*, a full-fledged machine installed in an OVH Cloud server room (see Fig. II.25), generating certified randomness following a protocol similar to the one introduced in Section II.3. Other elements from our small-scale experiments, such as the realtime performance monitoring system and the motorized photon polarization stabilization have been fleshed out and are now integrated into Quandela's cloud-accessible quantum devices.

A particularly striking aspect is the challenge of achieving precise control over PICs. Although we proposed a phase calibration procedure based on optical measurements, these procedures assumed homogeneity in PIC output transmissions and detection efficiencies, which is likely not the case. In addition, working with specialized PICs has been a major asset in the C-QRNG and 4-GHZ experiments, but with the consequence that our phase calibration is tailored to these specific PICs. Ideally, we would have at our disposal a reliable method to control PICs that does not require a case-by-case approach and allows direct dialing of the phase configurations without preliminary calibration. We tackle this issue in the next chapter.

III - Towards high-fidelity photonic QI processing: circuit characterization and control using machine learning

Start focusing on the things you can control.

Any website giving life advice.

One of the fundamental divergences in the operation of classical and quantum computers resides in the error rates. The error rate refers to the probability that a bit or qubit state is altered incorrectly during computation, such as a bit flipping from 0 to 1 or a qubit flipping between quantum states. In classical computers, bit errors due to clock jitters and background radiation are practically non-existent with error rates of the order of $10^{-13} - 10^{-18}$ [203]. On the contrary, qubit error rates of current quantum devices are in the 1 % to 0.1 % range [204], which is insufficient for practical applications. Quantum error correction [205] will be an essential ingredient of full-fledged quantum computers to suppress qubit errors, along with reliable hardware providing high qubit gate fidelities: **higher qubit gate fidelities reduces the number of physical qubits needed to form a fault-tolerant logical qubit**.

For quantum computing platforms like superconducting qubits, trapped ions or neutral atoms, qubit errors arise from environmental perturbations such as cosmic rays or stray electromagnetic fields, qubit decoherence and gate imprecision [10, 11]. For these platforms, qubit gates are performed by sending microwave or optical pulses onto the qubits. Thus, engineering pulse sequences and shapes using machine learning is increasingly used to mitigate qubit errors [206].

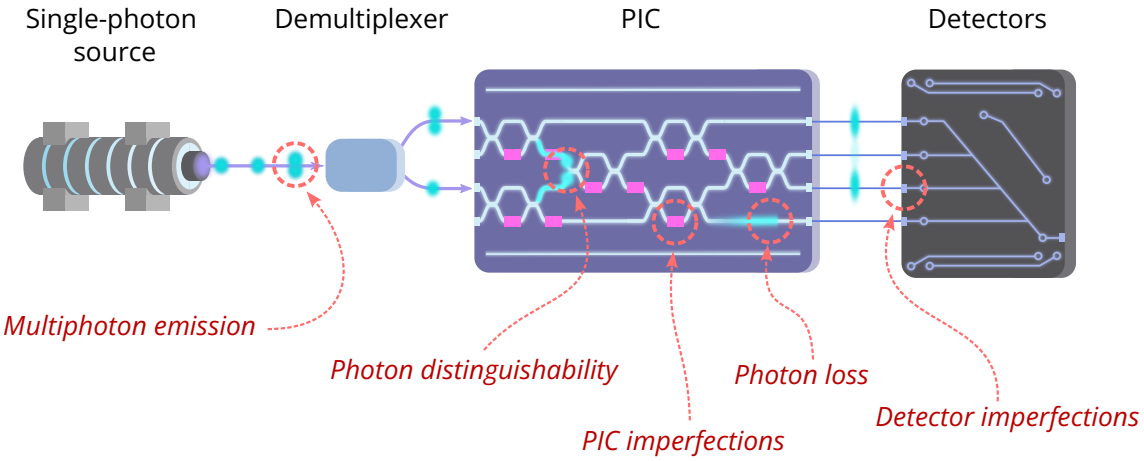

Figure III.1: Qubit error sources in single-photon- and circuit-based photonic quantum computers. Schematic of a modular near-term photonic quantum computer. The single-photon source emits photons that are demultiplexed into different paths. Light is then manipulated in the PIC and subsequently detected, yielding the results of the quantum calculation.

Photonic quantum computer error rates are affected by other detrimental mechanisms: **photon loss, multi-photon emissions, photon distinguishability, detector imperfections and interferometer imprecision**, as depicted in Fig. III.1. The **optimal control** of PICs, meaning the precise management of implemented phase and mitigation of imperfections, is consequently a major concern for the operation of near-term and future fault-tolerant photonic quantum computers.

During the development of *Ascella*, Quandela's first photonic quantum device accessible on the cloud, we faced significant challenges in characterizing and controlling the PIC used for photon manipulation. The *Ascella* PIC is a 12-mode Clements universal interferometer ([37], see Section I.4.2). Universal interferometers are designed to implement any desired unitary matrix acting on the photons, enabling *Ascella* to perform a wide range computations, as reported in [5], at the cost of a substantially increased interferometer complexity compared to the PICs of Chapter II.

Section III.1 provides an overview of the field of PIC optimal control. We then present our approach to tackle PIC optimal control in Section III.2 by using machine learning for characterization. Section III.3 discusses the mitigation of PIC imperfections. Section III.4 reviews the different PICs that have been experimentally characterized and controlled using our method, while Section III.5 covers in-depth details on the operation of the cloud-accessible quantum computer *Ascella*.

Our results on PIC optimal control are reported in a dedicated article [6] and as part of [5], showcasing the capabilities of *Ascella*. [2] discusses the online availability of *Ascella*.

Contents

III.1 - Optimal control of PICs

A PIC is accurately controlled when it faithfully implements targeted transformations on light. In other words, for linear optics, the unitary matrix U_{XP} implemented by the PIC acting on the photons (see Section I.2.4) must be close to the target matrix U_{target}. The control accuracy of current PICs is affected by imperfections stemming from fabrication constraints, tolerances or operation wavelength, which we examine in Section III.1.1. Section III.1.2 mentions self-configuration protocols that configure PICs without relying on a precise description of the internal workings and imperfections of the device. We argue that self-configuration protocols impose severe limitations on the purposes of PICs and prevent taking full advantage of PIC reconfigurability. These limitations are lifted when using model-based control as introduced in Section III.1.3, which utilizes a virtual replica of the physical device. We define measures of control accuracy in Section III.1.4, and review the state of the art in PIC control accuracy in Section III.1.5.

III.1.1 - Overview of PIC imperfections

III.1.1.A - Beamsplitter reflectivity errors

Each on-chip beamsplitter has a **reflectivity**

$$R = R^* + \varepsilon + \varepsilon' \ \in [0,1] \tag{III.1}$$

with R^* the target value, ε a random error and ε' the systematic error. E.g. a **symmetric beamsplitter** dividing light into two equal parts has $R = 0.5$. Fabrication introduces random errors in the reflectivity of beamsplitters, with correlations between closely lying beamsplitters arising from the thickness and width properties of the wafer [207]. Systematic reflectivity errors result from differences between the operational and fabrication wavelength [208].

The unitary matrix associated to a beamsplitter of reflectivity R is

$$U_{BS}(R) = \begin{bmatrix} \sqrt{R} & i\sqrt{1-R} \\ i\sqrt{1-R} & \sqrt{R} \end{bmatrix} = \begin{bmatrix} \cos\left(\frac{\pi}{4}+\alpha\right) & i\sin\left(\frac{\pi}{4}+\alpha\right) \\ i\sin\left(\frac{\pi}{4}+\alpha\right) & \cos\left(\frac{\pi}{4}+\alpha\right) \end{bmatrix}. \tag{III.2}$$

where α is the **reflectivity angle**, related to the reflectivity via

$$\alpha = \arccos\left(\sqrt{R}\right) - \frac{\pi}{4}. \tag{III.3}$$

For $R = 0.5$ (i.e. $\alpha = 0$), the beamsplitter matrix reduces to the familiar symmetric beamsplitter matrix

$$U_{BS}(R = 0.5) = \frac{1}{\sqrt{2}} \begin{bmatrix} 1 & i \\ i & 1 \end{bmatrix}. \tag{III.4}$$

An ideal **Mach-Zehnder interferometer (MZI)** is an optical building block composed of symmetric beamsplitter + **phase shifter (PS)** + symmetric beamsplitter. A PS is a component that dephases light by some, usually variable, amount. An MZI with internal phase shift ϕ essentially acts as a tunable beamsplitter of **effective reflectivity** $R(\phi)$ ranging from 0 to 1 given by

$$R(\phi) = \sin^2(\phi/2) \tag{III.5}$$

An MZI is said to be in the **cross configuration** when $R = 0$, corresponding to $\phi = 0$. Similarly, the **bar configuration** is associated to $R = 1$ and $\phi = \pi$. An MZI in the cross configuration thus permutes light between its two modes, while an MZI in the bar configuration does not alter the input state of light.

Actual integrated devices however feature imperfect MZIs with asymmetric beamsplitters. The effective reflectivity of an imperfect MZI is limited in range, i.e. a generic imperfect MZI cannot implement the cross, nor the bar configuration (see Fig. III.2a). As a consequence, beamsplitter reflectivity errors reduce the **unitary space coverage** of PICs, that is the number of unitary matrices

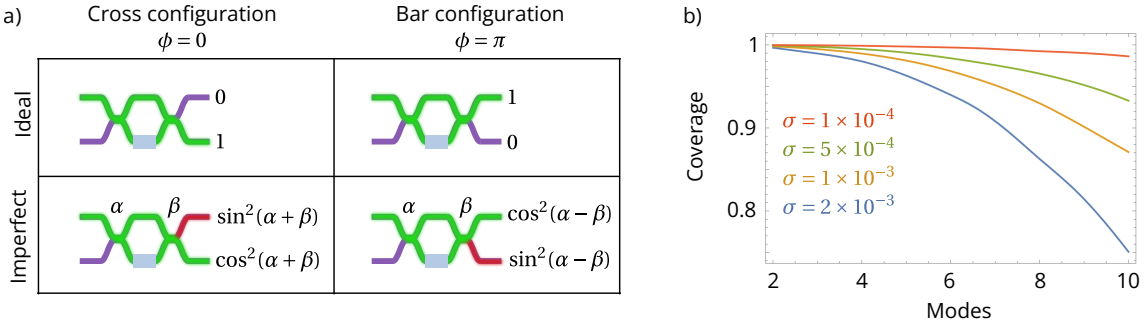

Figure III.2: Impact of beamsplitter reflectivity errors on unitary space coverage. a) We consider a single Mach-Zehnder interferometer (MZI) with an internal phase shifter implementing a phase ϕ and beamsplitters of reflectivity angles α and β. We compare the behavior in the cross ($\phi = 0$) and bar ($\phi = \pi$) configurations between an ideal ($\alpha = \beta = 0$) and imperfect MZI ($\alpha \neq 0$ and $\beta \neq 0$). Light propagates from left to right. The fraction of light exiting from each port is indicated as a function of the beamsplitter errors. Notice that a generic imperfect MZI cannot achieve the bar, nor the cross configurations. **b)** Adapted from [209]. Simulation of unitary space coverage of Clements interferometers up to interferometers on 10 modes. Beamsplitter reflectivity errors for each MZI are indirectly introduced by choosing $\varepsilon = \sin^2(\alpha+\beta) = \sin^2(\alpha-\beta)$ according to a normal distribution of standard deviation σ.

that can be implemented on a given PIC [209] (see Fig. III.2b). The full unitary space coverage can be recovered to some extent by adding supplementary layers of MZIs [210], or replace the MZIs in the circuit by more elaborate components [115].

Because of fabrication error correlations and the systematic error caused by the light wavelength, beamsplitters belonging to the same MZI tend to have approximately the same reflectivity.

III.1.1.B - Other imperfections

We list here other major PIC imperfections:

- **Passive phases**: Differences in waveguide lengths and refractive index inhomogeneities cause PSs to assume nonzero phases at rest (no voltage / electric current applied) [211].
- **Crosstalk from reconfigurable components**: Thermo-optic PSs generate heat that can affect other PSs nearby [22]. Crosstalk is also expected to occur with PSs harnessing strain-induced birefringence or electro-optic effects, due to their tight integration. Electric crosstalk is present for voltage-controlled PSs that share a common electric ground (see Appendix B of [6]).
- **Inhomogeneous optical transmissions**: Variations in optical fiber-to-PIC coupling and light detection efficiency causes uneven optical transmissions across all input and output modes. This also causes the matrices implemented by PICs to be non-unitary in practice. Internal circuit losses can occur as well due to waveguide bending and absorption losses. If all losses are uniform, then they can be accurately mitigated in a post-processing stage [112].

In the following we will focus on PICs with voltage-controlled thermo-optic PSs without loss of generality. Our conclusions remain the same for other PS technologies.

III.1.2 - Self-configuration protocols for PICs

We categorize as **self-configuration** protocol any technique that configures a PIC without storing information about the physical device. Each PIC reconfiguration is then performed without prior assumptions about the device. In general, self-configuration protocols can be summarized as a flowchart similar to the one displayed in Fig. III.3. An optimizer seeks to minimize the difference between the implemented matrix U_{XP} by the PIC and the target U_{target} matrix by acting on the voltages $\vec{V}$ applied to the PIC. The optimizer can consist of a gradient-descent algorithm [212] or a derivative-free algorithm (e.g. Nelder-Mead method [213], evolutionary algorithms [214], Bayesian optimization [215]). Derivative-free algorithms may offer more resilience to measurement noise and to complex optimization landscapes. Because the optimizer does not learn the behavior of the device, **the optimization routine is performed from scratch at every new reconfiguration**. The upside is that self-configuration tries to compensates all the imperfections of the circuit by default.

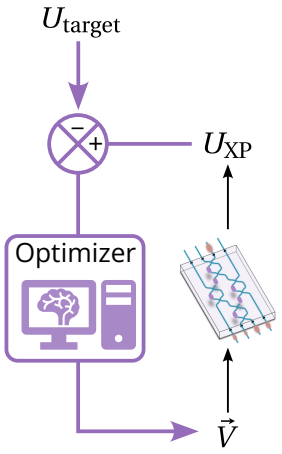

Figure III.3: Flowchart of self-configuration protocols

The efficacy of self-configuration protocols hinges on the measurement of the implemented matrix U_{XP} that describes the action of the PIC on light. The modulus of the elements of U_{XP} are straightforwardly accessed: $|u_{i,j}|^2$ is the probability that a photon entering in port j exits through port i. Measuring the angles of the complex entries of U_{XP} is more involved and requires measuring 2-photon coincidences by injecting two single photons simultaneously in the PIC [216, 217, 218] or recording interference fringes produced by two input coherent states [219]. Measuring the entire unitary matrix U_{XP} is experimentally cumbersome and this procedure has to our knowledge not been implemented for self-configuration of PICs. We argue in Section III.1.4.B that it may however be sufficient to measure only the modulus of the elements of U_{XP}.

Self-configuration has been successfully implemented experimentally on PICs [131, 134] and on programmable photonic processors [118] for simpler tasks like routing light from one input port to a chosen output port. These tasks do not require the measurement of the entire target matrix U_{target}, but only the amplitudes of specific matrix elements. For specific interferometer meshes like the Reck or Clements mesh, there exists a deterministic self-configuration protocol [220], although vulnerable to crosstalk and optical transmission inhomogeneities.

III.1.3 - Model-based control of PICs and model opacity

As the number of on-chip PSs increases above ≈ 10, self-configuration becomes unusable for practical purposes. This is especially true when the PIC must be frequently reconfigured to implement different unitary matrices. In that case, it is preferable to compute numerically in advance the voltages to apply on the PIC to achieve a given target matrix. This allows to reconfigure the PIC by **direct-dialing** the desired target matrices, that is by correctly configuring the PIC on the first try.

In this spirit, **model-based control** uses a **virtual replica** of the PIC. The virtual replica is a software emulation of the physical PIC, which ideally should reproduce the "behavior of the hardware" i.e. what happens to light when we apply a set of voltages on the PSs of the PIC. One of the main aspects of model-based control is the **opacity of the model** as shown on Fig. III.4:

- A **black-box approach** represents a situation where nothing is assumed on the inner workings of the PIC. In this paradigm, the PIC is an unknown function that converts the applied voltages into detection probabilities. In the virtual replica, black-boxes are usually embodied by neural networks, that is universal function approximators [221].

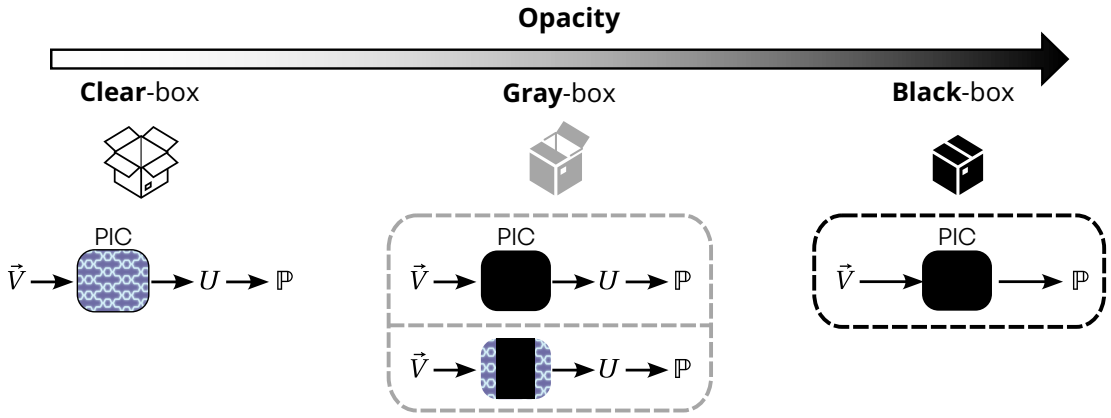

Figure III.4: Model-based control for different model opacities. $\vec{V}$: voltages applied on PSs. U: matrix implemented by the PIC. $\mathbb{P}$: light detection probabilities. In the black-box approach, the PIC is considered as a black-box. In intermediate gray-box approaches, the PIC itself may remain a black-box, or be a partial black-box. The clear-box approach harnesses a physical model of the PIC.

- On the opposite side of the spectrum, a **clear-box approach** builds on a fully modeled virtual replica of the hardware PIC, with a physical model for instance.
- A **gray-box approach** is an intermediate viewpoint where parts of the physical device are modeled, while other parts remain black-boxes. The top gray-box model of Fig. III.4 shows a gray-box model in which the PIC produces a unitary matrix according to some unknown mechanism and where the detection probabilities are then computed according to the laws of quantum mechanics. Alternatively, some gray-box model [222, 223] consider that only parts of the PIC are unknown.

Considering parts of the PIC as black-boxes may be a deliberate choice to adopt a more general approach rather than just related to the knowledge of the system at hand.

From an experimental point of view, these three different approaches have been explored for PIC optimal control, with and without machine learning. Before comparing the methods, we introduce measures of PIC control accuracy in the next subsection.

III.1.4 - Control accuracy metrics

III.1.4.A - Fidelity

We summarize in Table III.1 metrics for PIC control accuracy. The similarity between two unitary matrices U and V is quantified by the Frobenius inner product [224]

$$\langle U, V \rangle_F = \mathrm{Tr}(U^\dagger \cdot V) \tag{III.6}$$

which is in general a complex quantity. The **fidelity** $\mathscr{F}(U,V)$ between U and V is obtained by taking the modulus and normalizing the obtained quantity by the number of input modes in which light is injected. Methods for experimentally measuring the unitary matrix U_{XP} implemented by a PIC were mentioned in Section III.1.2.

To evaluate the control accuracy of a PIC, we select random target unitary matrices U_{target} that are uniformly distributed according to the Haar measure. The target matrices are then said to be **Haar-random**, and are "good representatives" of the set of unitary matrices [225]. In fact, sampling Haar-random unitary matrices can be understood as the multi-dimensional equivalent of sampling uniformly points from a circle. The generated target Haar-random matrices are implemented on the PIC and the resulting matrices are measured. The average fidelity between target and implemented matrices is computed, yielding the **Haar-random fidelity**.

	Fidelity $\mathscr{F}$	**Amplitude fidelity** $\mathscr{F}_a$	**Total variation distance** TVD
Compares	Unitary matrices	Modulus matrices	Probability vectors
Formula	$\mathscr{F}(U,V)=\frac{\lvert\mathrm{Tr}(U^\dagger\cdot V)\rvert}{m_{\text{in}}}$	$\mathscr{F}_a(P,Q)=\frac{\mathrm{Tr}(P^T\cdot Q)}{m_{\text{in}}}$	$\mathrm{TVD}(\vec{p},\vec{q})=\frac{1}{2}\sum_i\lvert p_i-q_i\rvert$
Bounds	$0\leq\mathscr{F}(U,V)\leq 1$	$0\leq\mathscr{F}_a(P,Q)\leq 1$	$0\leq\mathrm{TVD}(\vec{p},\vec{q})\leq 1$
Upper bound reached means...	$U=V$ (up to a global phase)	$P=Q$	/
Lower bound reached means...	/	/	$\vec{p}=\vec{q}$

Table III.1: **Measures of PIC control accuracy** Modulus matrices are real matrices with non-negative elements and whose columns sum to 1 when the elements are squared. Probability vectors are vectors summing to 1. m_{in} is the number of input modes in which light is injected, which also corresponds to the number of non-zero columns in the matrices.

III.1.4.B - Amplitude fidelity: an experiment-friendly metric

Measuring experimentally the fidelity between the target matrix U_{target} and the implemented matrix U_{XP} is cumbersome and time-consuming as mentioned in Section III.1.2. Hence, the control accuracy is usually quantified in the litterature by the **amplitude fidelity**, which is the fidelity between $|U_{\text{target}}|$ and $|U_{\text{XP}}|$ where the modulus applied element-wise. The modulus of a unitary matrix yields a matrix with non-negative entries and whose columns sum to 1 when the elements are squared. We call matrices with such properties **modulus matrices**. Each element of $|U_{\text{target}}|$ is related to a single-photon detection probability, thus easy to measure. In Table III.2 summarizing the state of the art in PIC optimal control, we compare the **amplitude infidelities** $1-\mathscr{F}_a$ (the lower, the better).

One could argue that the amplitude fidelity measurement is unreliable as it is possible to find unitary matrices with high amplitude fidelity, but low fidelity. For instance:

$$U=\frac{1}{\sqrt{2}}\begin{bmatrix}1 & 1\\ 1 & -1\end{bmatrix},\qquad V=\frac{1}{\sqrt{2}}\begin{bmatrix}1 & -1\\ 1 & 1\end{bmatrix}, \tag{III.7}$$

give $\mathscr{F}(U,V)=0$ and $\mathscr{F}_a(U,V)=1$. For PICs, the angles of the complex elements of the implemented unitary matrix are however related to the element amplitudes. It was demonstrated that a high amplitude fidelity correlates with a high fidelity [123].

III.1.4.C - Comparing output light intensity distributions

The **light intensity distribution** $\vec{p}(i,\vec{V})$ is the collection of detector readings, normalized to sum to 1 (**probability vector**), with light injected into the i-th input and voltages $\vec{V}$ applied. **We will restrict to light intensity distributions resulting from light injected into a single input at a time** as illustrated in Fig. III.5. When using powermeters, $\vec{p}$ is determined by the powermeter readings. For single-photon detectors, $\vec{p}$ is obtained from the countrate on each detector.

To compare light intensity distributions, we use the **total variation distance (TVD)**. TVD is the half sum of absolute differences between two probability vectors (see Table III.1). TVD has an accessible interpretation: for instance $\mathrm{TVD}(\vec{p},\vec{q})=0.05$ can be understood as "there is a 5

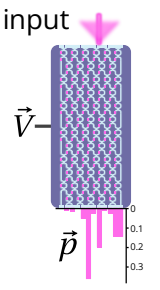

Figure III.5: Example of light intensity distribution $\vec{p}$

					Characterization metrics			Control metrics
	Approach	ML	Imperfections taken into account	PIC	Circuit $1-\mathcal{F}_a$	Sample cost	Parameter cost	Unitary $1-\mathcal{F}_a$
[138], 2020	Black-box	NN	all	3 modes 2 PSs	-	2400 (exponential)	20750	-
[226], 2023	Gray-box	NN	all	3 modes 4 PSs	-	1300	450	0.26 % [a]
[122], 2020	Clear-box	No	passive phases	12-mode CI 126 PSs	-	-	-	9.6 % (Haar-random)
[130], 2022	Clear-box	GD	passive phases, thermal crosstalk, BS reflectivity, output losses	6-mode CI 36 PSs	3.1 %	≥ 23 [b]	-	1.3 % (Haar-random)
[18], 2023	Clear-box	-	-	20-mode CI 380 PSs	-	-	-	2.6 % (Haar-random)
[6], 2023 This work	**Clear-box**	**GD**	**passive phases, thermal crosstalk, BS reflectivity, input/output losses**	**12-mode CI 126 PSs**	**0.08 %**	**1.4**	**1**	**0.23 % / 0.15 % [c] (Haar-random)**
[123], 2023	Clear-box	No	passive phases, thermal crosstalk	6-mode CI 27 PSs	-	-	-	2.1 % (Haar-random)
[135], 2024	Clear-box	GD	passives phases, thermal crosstalk, BS reflectivity	8-mode CI 52 PSs	-	≥ 18	-	0.9 % (Haar-random)
[227], 2024	Clear-box	GD	passives phases, BS reflectivity output losses	2 input modes 24 output modes 66 PSs	0.14 %	0.3	-	-

[a] Distribution of unitary matrices is not specified

[b] Voltage sweeps of PSs not included

[c] Raw value / value with output losses compensation

Table III.2: **State of the art in experimental demonstrations PIC optimal control.** -: data not available. The demonstrations are grouped by approach and then listed in chronological order of release on arXiv. **Approach)** Black-box: no model for the relation between observed probabilities and applied voltages/electric currents. Gray-box: partial model, where the PIC is not modelled and the measurement obeys the laws of quantum mechanics. Clear-box: full model of the PIC and its imperfections. **ML)** If machine-learning has been used. NN: neural network. GD: model fit by gradient descent. **Imperfections taken into account)** List of considered PIC imperfections. Black- and gray-box approaches take by definition all types of imperfections into account, including imperfections that can be hard to model like nonlinear effects on light. BS: Beam-splitter. **PIC)** Photonic chip used for experimental validation. CI: Clements interferometer, PS: thermo-optic phase shifter. **Circuit $1-\mathcal{F}_a$)** Amplitude infidelity between measured output light intensity distributions and corresponding model predictions. Quantifies accuracy of the characterization. The lower, the better. **Sample cost and Parameter cost)** Estimation of sample and computational efficiency. The lower the better. **Unitary $1-\mathcal{F}_a$)** Amplitude infidelity between target unitary matrix and implemented unitary matrix. The lower, the better. Haar-random: target unitary matrices are Haar-randomly chosen.

% difference between $\vec{p}$ and $\vec{q}$".

III.1.5 - State of the art in PIC control accuracy

The state of the art in experimental PIC optimal control is reviewed and summarized in Table III.2. Black-box [138] and grey-box [228, 226] PIC control with neural networks were investigated on very small PICs with only a few modes and phase shifters. In the clear-box paradigm, [123] achieves a remarkable fidelity without machine-learning, owing to a particular property of the used PIC: thermal crosstalk does not affect PSs between different columns, due to the large spacing between successive PSs. [130] and [135] train a clear-box model to fit the experimental data via gradient-descent. [227] proceeds in a similar manner on a PIC that does not exhibit thermal crosstalk, significantly diminishing the complexity of the virtual replica. The largest PIC characterized to this date is [18], without details on the procedure. Metrics for comparison are:

- **Circuit fidelity**. This metric applies for machine learning-based methods. In such methods, the virtual replica learns from a training dataset and its prediction accuracy is evaluated on

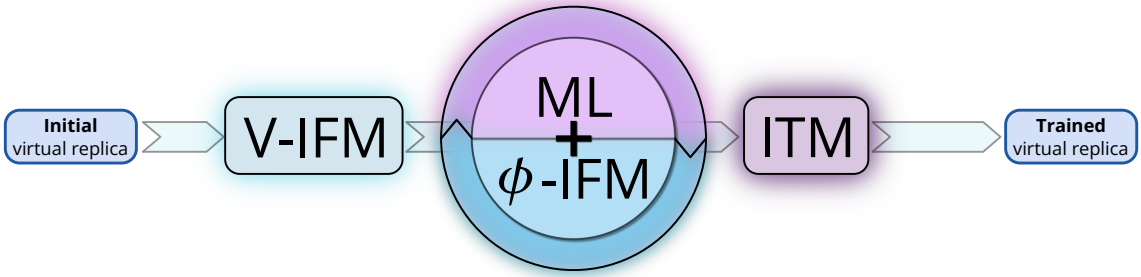

Figure III.6: Machine-learning assisted characterization of PICs. The initial virtual replica is coarsely trained in an initial voltage-interference fringe measurement (V-IFM). The training process then iteratively finetunes the virtual replica by repetitions of machine learning stages (ML) and phase-interference fringe measurements (ϕ-IFM). A fully trained virtual replica is returned by the process after the input transmission measurement (ITM).

a test dataset it has never seen. This point is further discussed in Section III.2.3. The circuit fidelity is the average amplitude fidelity between the test dataset and corresponding virtual replica predictions. The circuit fidelity quantifies the quality of the virtual replica.

- **Sample efficiency**, i.e. the amount of samples required to train the model, estimated by

$$\text{sample cost} = \frac{\text{number of training samples}}{n_{\text{PS}}^2} \tag{III.8}$$

  where a training sample is a light intensity distribution measurement, and n_{PS} is the number of PSs in the PIC. We choose n_{PS}^2 as an indicator of PIC complexity because the dominant imperfection in terms of number of parameters is PS crosstalk, which scales like n_{PS}^2 in the worst case where every PS influences every other PS.

- Similarly, we assess **computational efficiency** using

$$\text{parameter cost} = \frac{\text{number of model parameters}}{n_{\text{PS}}^2}. \tag{III.9}$$

  A virtual replica with a high parameter cost has a large number of parameters, making it cumbersome and computationally expensive to train and manipulate.

- the **Haar-random fidelity** introduced in Section III.1.4.A, measured here with the amplitude infidelity. The Haar-random fidelity quantifies the overall accuracy of the PIC and its ability to faithfully implement targeted operations on light.

Having established the context and challenges of PIC optimal control, the following section presents our approach to addressing this issue through a model-based, clear-box solution and iterative virtual replica training.

III.2 - Our clear-box approach to PIC characterization

We expect from a PIC characterization and control method to meet the following specifications: the ability to measure thermal crosstalk, the capability to characterize large PICs with hundreds of components, and an experimentally friendly process that is compatible with cloud-operated machines frequently reconfigured on the fly. Following these guidelines, we use machine learning to handle the substantial number of parameters in the problem. We adopt a clear-box perspective for the method to work with complex interferometers such as the Clements mesh,

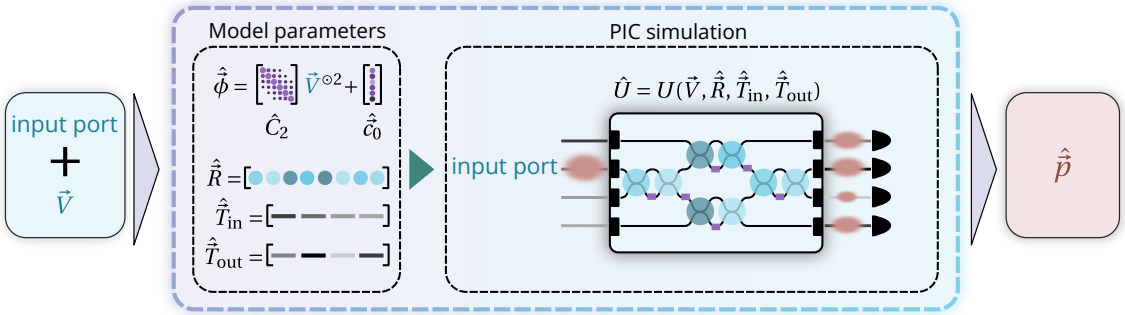

Figure III.7: Virtual replica for PIC characterization and control. The model parameters store the estimated phase-voltage relation (crosstalk matrix $\hat{C}_2$ and passive phases vector $\hat{\vec{c}}_0$), beamsplitter reflectivity values $\hat{\vec{R}}$ and input/output transmissions $\hat{\vec{T}}_{\text{in/out}}$. When given an input port and a list of voltages $\vec{V}$, the model estimates the phases $\hat{\vec{\phi}}$ implemented on the PIC and predicts the output light intensity distribution $\hat{\vec{p}}$ from the resulting PIC matrix $\hat{U}$. When fully trained, the prediction $\hat{\vec{p}}$ should match to a high degree the output light intensity distribution $\vec{p}$ measured on the physical device in the same conditions.

ruling out neural networks from the scope of our solution. This choice is further justified by the relative ease to build a physical PIC model for our virtual replica. The incentive for model-based control is to control PICs by direct-dialing of unitary matrices, as argued in Section III.1.3.

In this section, we focus on the virtual replica used for characterizing PICs and the training process. Imperfection mitigation for PIC optimal control, harnessing the data acquired by the virtual replica, is addressed in Section III.3.

Section III.2.1 introduces the clear-box structure of our virtual replica. The virtual replica is subsequently trained following our training protocol, summarized on Fig. III.6. The individual stages of the process are discussed in their respective section:

- **voltage-interference fringe measurement (V-IFM)** in Section III.2.2
- **machine learning stages (ML)** in Section III.2.3
- **phase-interference fringe measurement (ϕ-IFM)** and **input transmission measurement** in Section III.2.4.

We close the section by evaluating our characterization method in simulations in Section III.2.5.

III.2.1 - Model of the physical device

We break down in this section the physical model behind our virtual replica. This section thus illustrates the essence of the clear-box approach introduced in Section III.1.3 by building a model of the physical device from intuition. The following features are included in the virtual replica schematized on Fig. III.7:

- **Components** The interferometer mesh of the virtual replica includes discrete PSs and beamsplitters. MZIs are represented by a dedicated component to expedite computations by aggregating multiple components into a single one.
- **Crosstalk model**

  Given a PIC, let n_{PS} be the number of on-chip PSs. We express the implemented phase shifts $\vec{\phi}$ as a function of the applied voltages $\vec{V}$ via a matrix relation of the form

$$\vec{\phi}(\vec{V}) = \sum_{k \neq 1} C_k \cdot \vec{V}^{\odot k} + \vec{c}_0 \tag{III.10}$$

where the C_k are $n_{PS} \times n_{PS}$ matrices, which we call **crosstalk matrices**, $^{\odot}$ is element-wise exponentiation and $\vec{c}_0$ is a vector containing the n_{PS} passive phases. The diagonal elements of the crosstalk matrices C_k are called **self-heating coefficients** and quantify the efficiency of the PS to produce a phase shift on its assigned waveguide. **Off-diagonal elements account for crosstalk between PSs**.

In practice, the phase-voltage relation of a PIC is of one of the two following forms:

$$\vec{\phi} = C_2 \cdot \vec{V}^{\odot 2} + \vec{c}_0 \tag{III.11}$$

$$\vec{\phi} = C_4 \cdot \vec{V}^{\odot 4} + C_2 \cdot \vec{V}^{\odot 2} + \vec{c}_0 \tag{III.12}$$

The V^2 dependence is physically linked to Joule heating and the V^4 term takes into account the dependence with temperature of the PS heater ohmic resistance. We will focus on PICs described by a relation only with V^2 dependence, except in Section III.4.2 presenting the experimental characterization of a PIC with a V^4 term.

- **Component matrices** Each on-chip component is represented by a unitary matrix encoding its action on light (see Section I.2.4). This formalism is valid for both classical and quantum linear optics. The unitary matrix $U(\vec{V}, \vec{R})$ encapsulating the action of the PIC as a whole on light is the matrix product of its individual components, where PSs have phases $\vec{\phi}(\vec{V})$ and beamsplitters have reflectivity values $\vec{R}$.

- **Input and output optical transmissions**

  Let $\vec{T}_{in}$ and $\vec{T}_{out}$ be the vectors containing the input and output optical transmissions of the PIC. The rows and columns of the unitary matrix $U(\vec{V}, \vec{R})$ are scaled by appropriate factors:

$$U(\vec{V}, \vec{R}) = \begin{bmatrix} u_{1,1} & \cdots & u_{1,m} \\ \vdots & \ddots & \vdots \\ u_{m,1} & \cdots & u_{m,m} \end{bmatrix} \begin{matrix} \leftarrow \times \sqrt{T_{out}^{(1)}} \\ \\ \leftarrow \times \sqrt{T_{out}^{(m)}} \end{matrix}$$

$$\uparrow \times \sqrt{T_{in}^{(1)}} \qquad \uparrow \times \sqrt{T_{in}^{(m)}}$$

  Note that the resulting matrix $U(\vec{V}, \vec{R}, \vec{T}_{in}, \vec{T}_{out})$ is in general not unitary.

- **Model parameter storage**

  The virtual replica stores the physical model parameters, providing its best estimated description of the characterized PIC at a given time. Given a PIC, let n_{PS} be the number of PSs, n_{BS} the number of beamsplitters and m the number of modes. The physical parameters that are optimized to agree with experimental data are, as shown on Fig. III.7,

  - the crosstalk matrix $\hat{C}_2$ (n_{PS}^2 parameters)
  - the passive phases $\hat{\vec{c}}_0$ (n_{PS} parameters)
  - the beamsplitter reflectivity values $\hat{\vec{R}}$ (n_{BS} parameters)
  - the input and output transmissions $\hat{\vec{T}}_{in/out}$ ($2m$ parameters)

  where **quantities with hats indicate model predictions**. Thus, the number of virtual replica parameters scales like $n_{PS}^2 + n_{BS} + 2m$. For Clements interferometers, which have $n_{PS}, n_{BS} \approx m^2$, the scaling is m^4.

- **Output light intensity distribution prediction**

  Let $\vec{p}(i, \vec{V})$ be the output light intensity distribution resulting from light injected in the i-th input of the PIC and voltages $\vec{V}$ applied. From its stored estimated parameters, the virtual replica predicts the value of $\vec{p}(i, \vec{V})$ as illustrated in Fig. III.7 by

1. computing the predicted phase shifts $\hat{\vec{\phi}}(\vec{V}, \hat{\vec{c}}_0, \hat{C}_2)$ from the voltages applied, the estimated passive phases $\hat{\vec{c}}_0$ and the estimated crosstalk matrix $\hat{C}_2$,
2. then calculating the predicted PIC matrix $\hat{U} = U(\vec{V}, \hat{\vec{R}}, \hat{\vec{T}}_{\text{in}}, \hat{\vec{T}}_{\text{out}})$ encoding the action of the PIC on light. $\hat{U}$ takes into account the estimated beamsplitter reflectivity values $\hat{\vec{R}}$ and the estimated input/output port transmissions $\hat{\vec{T}}_{\text{in/out}}$.
3. The intensity distribution prediction $\hat{\vec{p}}(i, \vec{V})$ is obtained by taking the element-wise modulus square of the i-th column of $\hat{U}$.

The objective of the training process detailed in the next subsections is to tune the parameters of the virtual replica such that its predictions agree with the actual behavior of the physical PIC. In other words, the training process seeks to minimize the average TVD (see Section III.1.4.C and Table III.1) between experimentally measured output light intensity distributions $\vec{p}(i, \vec{V})$ and corresponding virtual replica predictions $\hat{\vec{p}}(i, \vec{V})$.

III.2.2 - Coarse model estimations: voltage interference fringe measurements (V-IFM)

The virtual replica is initialized in the following state:

- a blank phase-voltage relation. All coefficients of the estimated crosstalk matrix $\hat{C}_2$ and the passive phases vector $\hat{\vec{c}}_0$ are set to 0.
- the reflectivity of each beamsplitter assumes its target value, i.e. usually $R = 0.5$.
- the input and output port of the PIC are assumed to be perfectly transmissive, i.e. all values of $\hat{\vec{T}}_{\text{in/out}}$ are set to 1.

This section details the first stage of the characterization process (see Fig. III.6) in which the virtual replica undergoes coarse training. This stage, which we call **voltage interference fringe measurement (V-IFM)**, aims to recover

- the diagonal elements of the crosstalk matrix $\hat{C}_2$
- the passive phases $\hat{\vec{c}}_0$.

Consider a PS indexed i. The principle is to sweep the voltage of PS i to produce an interference fringe, that is monitored and fitted to recover the self-heating coefficient $(C_2)_{ii}$ and the passive phase $(c_0)_i$. We then say that PS i has been **characterized**.

The V-IFM stage has two sub-stages: first, all the internal PSs of MZIs are characterized (see Section III.2.2.A) and then all the remaining PSs, called **external PSs** (see Section III.2.2.B).

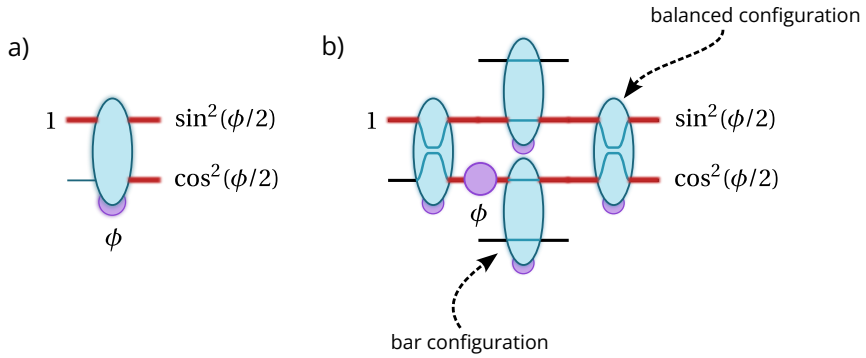

Figure III.8: Mach-Zehnder interferometer (MZI) and example of meta-MZI used for PS characterization Blue ellipses represent MZIs, purple disks are phase shifters (PS). **a)** An MZI with internal phase ϕ splits light into intensity fractions $\sin^2(\phi/2)$ and $\cos^2(\phi/2)$. **b)** The displayed meta-MZI is composed of two MZIs in the balanced configuration ($\pi/2$ internal phase, acting as symmetric beamsplitter), and two MZIs in the bar configuration. The internal PS of the meta-MZI, here implementing a phase ϕ, determines the light intensity splitting ratio $\sin^2(\phi/2)/\cos^2(\phi/2)$, similarly to a).

III.2.2.A - Characterization of MZI PSs

Section III.1.1 mentioned that MZIs act as tunable beamsplitters: an MZI with internal phase ϕ and light injected into a single mode splits the light intensity into fractions $\sin^2(\phi/2)$ and $\cos^2(\phi/2)$, as shown on Fig. III.8. Hence, the oscillatory response of an MZI PS indexed i as a function of applied voltage V has the general form

$$f(V) = a_i \cos^2\left(\frac{(C_2)_{ii}V^2 + (c_0)_i - \theta_i}{2}\right) + b_i \qquad \text{(III.13)}$$

where θ_i an optional phase offset determined in advance, and a_i and b_i are additional fit parameters. See Fig. III.9 for an example of an interference fringe. The curve fit recovers the self-heating coefficient $(C_2)_{ii}$ and the passive phase $(c_0)_i$. PS i is then labeled as characterized.

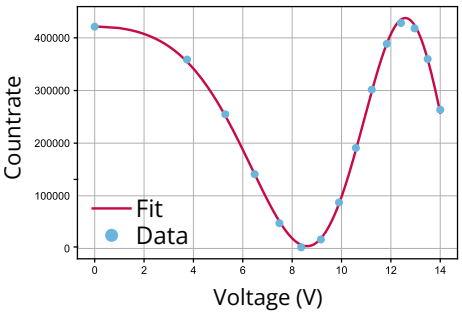

Figure III.9: Interference fringe when sweeping the voltage applied to a PS. Experimental data from a 12-mode Clements interferometer. The phase offset is here 0 rad. The measured passive phase is 0.38 rad and the self-heating coefficient is 0.037 mrad/V^2.

To characterize MZI PS with index i, light must be routed to the corresponding MZI using already characterized MZIs, while avoiding interference with stray light in the PIC. This is illustrated in Fig. III.10. Parasitic interferences offset the recorded interference fringe, which in turn induces errors in the estimation of the passive phase $(c_0)_i$.

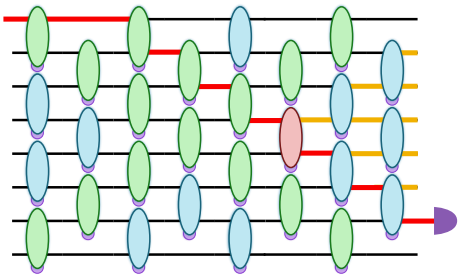

Figure III.10: Light routing example Ellipses: MZIs. Green: characterized MZI. Red: MZI to characterize. Red light: routing. Orange light: stray light.

The **V-IFM protocol** is the list of instructions to perform the V-IFM on a given PIC. The V-IFM protocol notably encodes the sequence in which the MZIs are characterized, the instructions for routing light for each PS and the precomputed phase offsets θ_i in Eq. III.13. [229, 23] give an example of such a protocol for Clements interferometers. It is relatively straightforward to establish the V-IFM protocol for PICs with up to 6 modes, but the task rapidly becomes tedious and prone to errors for higher numbers of modes.

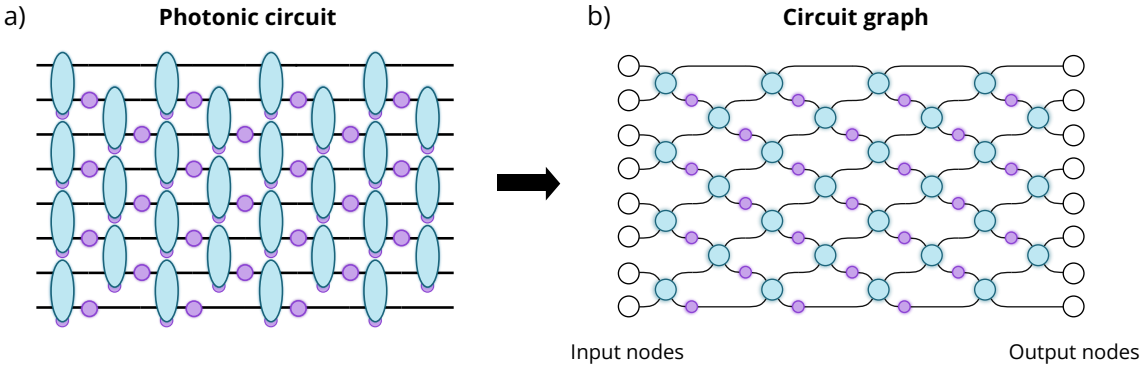

Figure III.11: Circuit graph of an 8-mode Clements interferometer. **a)** 8-mode Clements interferometer. Ellipses: Mach-Zehnder interferometers (MZIs). Disks: phase shifters (PSs). **b)** Corresponding circuit graph. Every node represents here an MZI or a PS. The edges reproduce the waveguide connections in a).

We have devised an algorithm that generates a suitable V-IFM protocol given a generic interferometer mesh. The main ideas of the algorithm are sketched here. Details can be found in [6].

The V-IFM protocol generation algorithm converts the PIC into a mathematical graph, which we call **circuit graph**. Fig. III.11 displays the circuit graph of an 8-mode Clements interferometer as an example. Nodes in the circuit graph represent on-chip components such as PSs, beamsplitters and input/output ports. The circuit graph nodes are interconnected by edges replicating the waveguides in the circuit.

To characterize the MZIs of a circuit, the algorithm identifies the **direct paths** of light. These are paths in the circuit graph on which light cannot interfere with itself. Notice in Fig. III.12 that direct paths are the only paths connecting specific inputs and outputs. We recall that in our protocol light is injected into a single input at a time. Each direct light path provides a sequence of MZIs that can be characterized without relying on previously characterized ones. The algorithm subsequently characterizes the children nodes of direct path nodes, leveraging characterized nodes to route light to MZIs lying deeper in the circuit. The final set of MZIs to be characterized are the parents nodes of direct path nodes. See Fig. III.13 for an illustration of children and parent nodes. Doing so, all MZI nodes are characterized, provided the circuit has a sufficient number of direct paths.

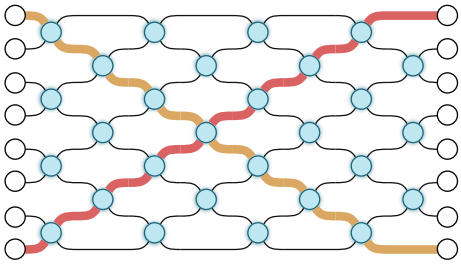

Figure III.12: Direct paths in a Clements interferometer. Orange and red edge paths indicate direct light paths

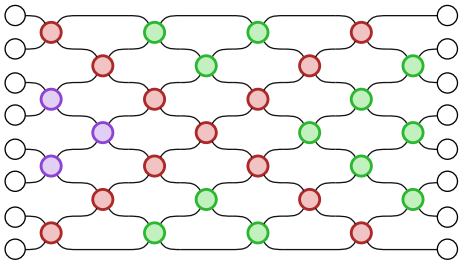

Figure III.13: Illustration of node filiation Red: direct path nodes. Green: children nodes. Purple: parent nodes.

III.2.2.B - Characterization of external PSs

External PSs are characterized by enclosing the PS in a **meta-MZI**, a structure acting like an MZI but in which the beamsplitters are replaced by MZIs. An example is shown on Fig. III.8b. As can be observed on Fig. III.14b, meta-MZIs in the photonic circuit are cycles in the circuit graph. Thus, the problem for the V-IFM protocol generation algorithm to find suitable meta-MZIs for characterization reduces to finding smallest cycles in a graph.

Similarly to the case of MZIs, the sequence in which external PSs are characterized is also

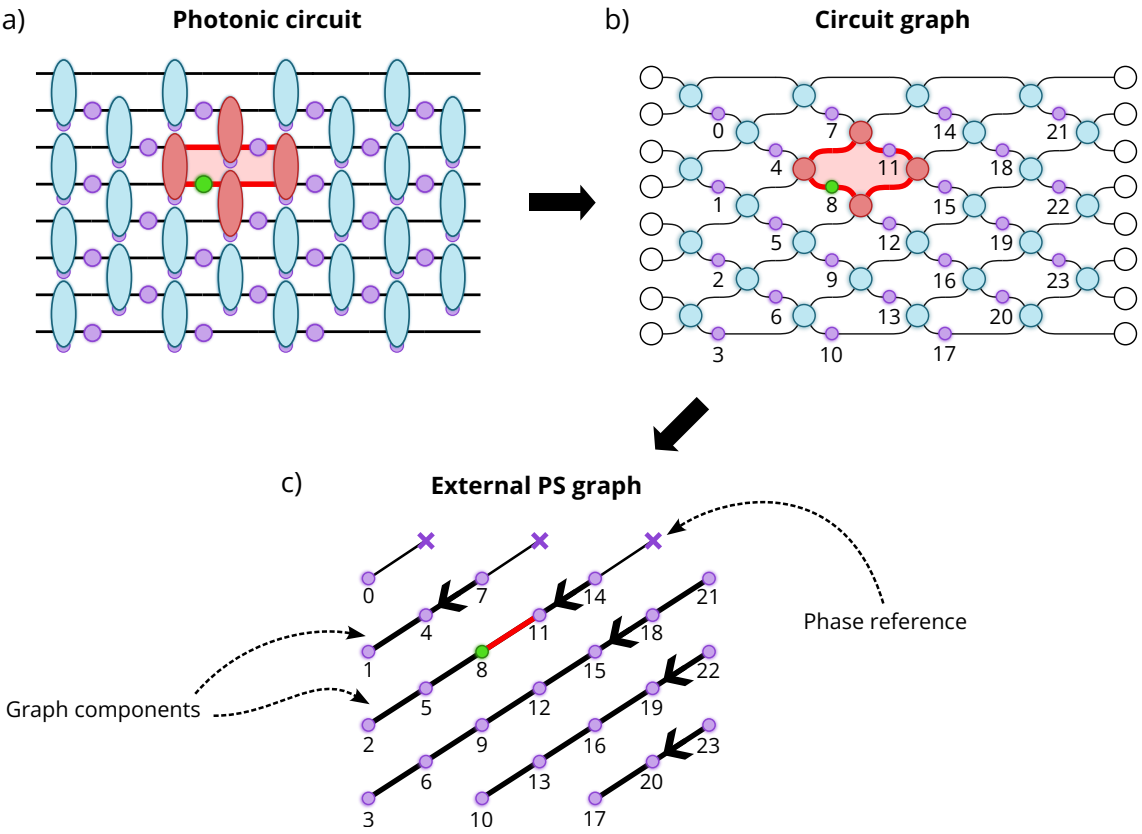

Figure III.14: Characterization of external PSs using graph theory. **a)** Blue ellipses represent MZIs, purple disks are phase shifters (PS). The green PS represents the external PS to characterize. The group of MZIs highlighted in red indicates a suitable meta-MZI for characterization. **b)** The meta-MZI forms a cycle in the circuit graph. **c)** External PS graph constructed by enumerating all meta-MZIs in the circuit. The nodes represent external PSs. Two nodes are linked if they can be enclosed in the same meta-MZI (e.g. red link associated to meta-MZI highlighted in a) and b)). The external PS graph displayed here is composed of multiple linear chains. If an external PS admits a meta-MZI in which it is alone (here nodes 0, 7 and 14), then the external PS is linked to a phase reference. The arrows indicate the sequence in which every chain of external PSs is characterized.

of prime importance. This is because the passive phase of each external PS must be measured with respect to a well-defined phase reference, consistent across all external PSs. The algorithm labels two external PSs as **linked** when they can be enclosed in the same meta-MZI. Physically, this means that the relevant quantity between two linked external PSs is the phase difference between the two PSs. Thus, two linked external PSs need to share a common phase reference for consistency. Our algorithm enumerates the cycles in the circuit graph containing external PSs, and construct a second graph, the **external PS graph** (see Fig. III.14c) synthesizing the links between the external PSs. The external PS graph is broken down into individual graph components, and the algorithm determines the characterization sequence by stepping through the components starting from a reference node. If a graph component does not include a reference node to begin with, an arbitrary node is designated as the starting point.

In the resulting characterization sequence, each external PS is characterized in a meta-MZI featuring only characterized and properly phase-referenced external PSs, ensuring consistency and stability of the measured PS characteristics.

III.2.2.C - Impact of imperfections on V-IFM measurements

V-IFM measurements are affected by crosstalk. MZI PSs that need to be actuated to route light offset the interference fringe through crosstalk. Similarly, beamsplitter reflectivity errors shift the interference fringe of meta-MZIs, which has a severe impact on the measured passive phase of external PSs. We performed simulations in the supplementary information of [6] estimating for a 12-mode Clements interferometer that crosstalk induces random errors on the order of 100 mrad on the passive phases, while beamsplitter reflectivity errors shift systematically the measured passive phases of external PSs by $\approx$ 250 mrad (for an average reflectivity $R = 0.56$, matching our hardware).

The V-IFM stage yields an initial guess for the parameters of the virtual replica, constituting a convenient starting point for the machine learning stage described in the following section.

III.2.3 - Model tuning via machine learning (ML) stages

In our characterization protocol, the V-IFM stage is followed by a **machine learning (ML) stage**, supplementing the initial V-IFM stage. We use the ML stage to tune the parameters of the virtual replica that are difficult to access and measure in practice: crosstalk matrix $\hat{C}_2$, beamsplitter reflectivity values $\hat{\vec{R}}$ and output transmissions $\hat{\vec{T}}_{\text{out}}$.

III.2.3.A - Training and test datasets

The ML stage requires training and test datasets, acquired before carrying out the characterization protocol. The training dataset is used specifically to update the model parameters. Each learning step, also called **epoch**, consists in

1. a **training step**, during which a virtual replica parameter update is performed to minimize the difference between the training dataset and corresponding virtual replica predictions. The step is illustrated on Fig. III.15.
2. An **evaluation step** then evaluates the virtual replica prediction accuracy on the test dataset. Thus, the test dataset consists of data the virtual replica has never seen during training. The evaluation step gauges the ability of the virtual replica to generalize the extrapolated information from the training dataset. As such, the evaluation step is a good indicator for prediction accuracy and overfitting.

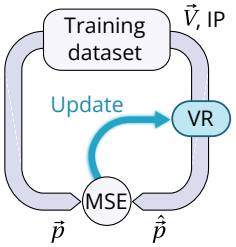

Figure III.15: Virtual replica (VR) training step. $\vec{V}$: dataset voltages. IP: input port. MSE: mean square error between training dataset light intensity distributions $\vec{p}$ and corresponding prediction $\hat{\vec{p}}$.

The training and test datasets consist of **ML samples**. An ML sample is acquired on the physical PIC by injecting light into a random input port i, applying a random list of voltages $\vec{V}$ and recording the associated output light intensity distribution $\vec{p}$ (see Sec. III.1.4.C). This results in a sample $(\vec{V}, i, \vec{p})$. Thus, the training and test datasets are representative of the behavior as a whole of the physical PIC. We use a training/test dataset ratio of 80/20, which is common practice in machine learning.

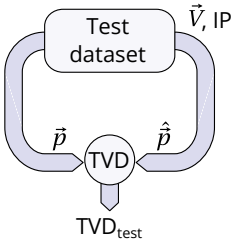

Figure III.16: Virtual replica (VR) evaluation step. $\vec{V}$: dataset voltages. IP: input port. TVD: total variation distance between test dataset light intensity distributions $\vec{p}$ and corresponding prediction $\hat{\vec{p}}$.

III.2.3.B - Virtual replica prediction accuracy TVD_{test}

The prediction accuracy of the virtual replica is quantified by the **test dataset TVD** denoted TVD_{test}. The test dataset TVD is the average TVD between the test dataset and the corresponding virtual replica predictions. TVD_{test} is computed at each evaluation step (see Fig. III.16). The lower the TVD_{test}, the better the virtual replica reproduces the behavior of the physical PIC, the better the resulting control accuracy of the PIC.

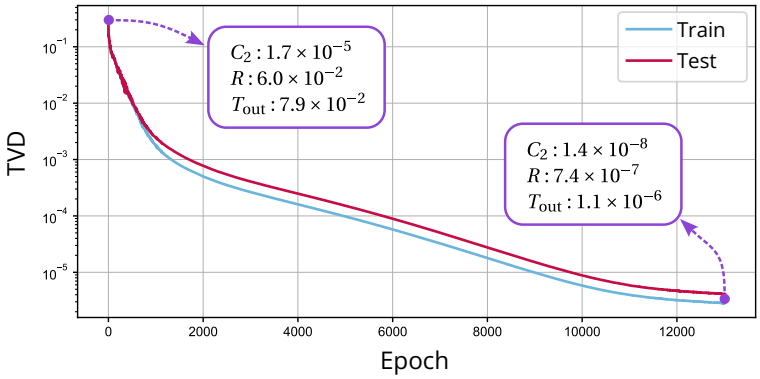

Figure III.17: Evolution of the TVD evaluated on the training and test datasets during virtual replica training in an ML stage. The PIC to characterize is here a simulated 8-mode Clements interferometer with a simulated crosstalk matrix according to the distance between components, beamsplitter reflectivity values of 0.56 ± 0.01 and output transmissions uniformly between 0.7 and 1. All of the passive phases are set here to 0, which is equivalent to a situation where the passive phases are perfectly known. The number of training samples is equal to the number of parameters to learn. The boxes indicate the average error between the estimated and actual parameters for the crosstalk matrix (C_2), beamsplitter reflectivity values (R) and output transmissions (T_{out}).

III.2.3.C - Optimization by gradient descent

The virtual replica parameters are updated in the training steps by a gradient descent algorithm. The algorithm seeks to minimize the mean square error between the the measured output light intensity distributions $\vec{p}$ and the corresponding predictions $\hat{\vec{p}}$. More specifically, we chose the `Adam` optimizer to perform the gradient descent [230]. Standard gradient descent algorithms follow the direction of steepest descent to update parameters. The `Adam` optimizer is more evolved in that it adds "momentum" to the gradient descent, by adjusting the step size according to past cost function evaluations. This allows for instance our virtual replica to "jump" over shallow obstacles and bumps in the optimization landscape. We use the `PyTorch` machine learning package for `Python` to build our virtual replica and machine learning framework. We show in Fig. III.17 that the ML stage allows the virtual replica to retrieve the values of the physical parameters with high accuracy.

III.2.3.D - Circuit fidelity

The **circuit fidelity** measures the degradation of the PIC control accuracy attributable to an imperfect characterization. The circuit fidelity is measured by generating target random phase configurations. For each target phase configuration $\vec{\phi}$:

1. the expected PIC matrix $U(\vec{\phi}, \hat{\vec{R}}, \hat{\vec{T}}_{\text{out}})$ is computed taking into account the estimated beamsplitter reflectivity values $\hat{\vec{R}}$ and output transmissions $\hat{\vec{T}}_{\text{out}}$.

2. In parallel, the phase configuration $\vec{\phi}$ is converted into voltages $\vec{V}$ using the estimated phase-voltage relation. $\vec{V}$ is applied to the PIC.

3. The amplitude fidelity $\mathcal{F}_a$ is measured between the expected and implemented matrices on the PIC.

The circuit fidelity is then the average amplitude fidelity over all tested phase configurations. Empirically, we observe that the circuit fidelity is related to the virtual replica prediction accuracy TVD_{test} by

$$1 - \mathcal{F}_a \approx \text{TVD}_{\text{test}}^2. \tag{III.14}$$

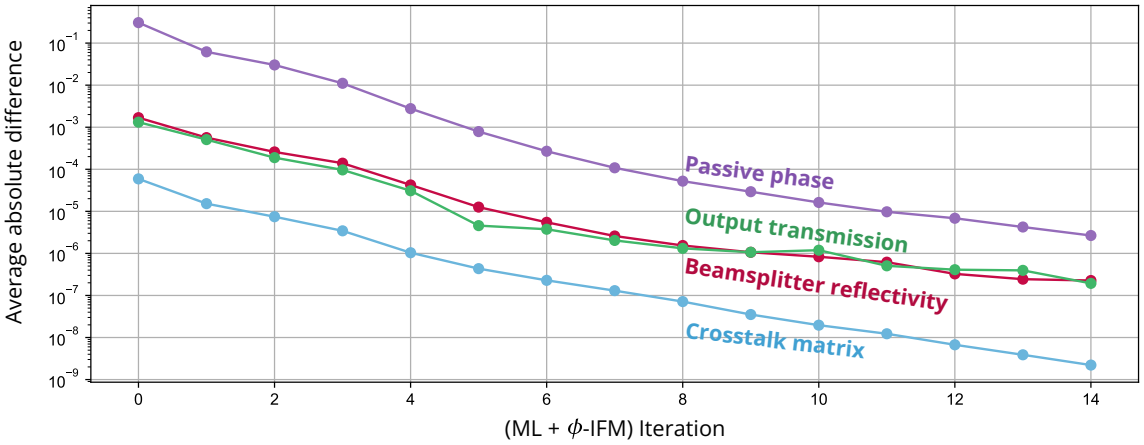

Figure III.19: The virtual replica parameters converge arbitrarily close to the actual values. The curves show the average absolute difference between the estimated virtual replica parameters and the actual value as a function of the number of performed (ML + ϕ-IFM) iterations. Notice that the virtual replica is able to approach the actual passive phases with sub-milliradian precision in only a few iterations.

From this formula, we see that a well-trained virtual replica, associated to low values of TVD_{test}, indeed reduce the impact attributable to characterization errors on the overall PIC control accuracy.

III.2.4 - Further adjusting the virtual replica with (ML+ ϕ-IFM) iterations

The estimated passive phases $\hat{\vec{c}}_0$ of the virtual replica are held fixed during the ML stages. This is because the optimization landscape for the passive phases is highly complex, and usually results in the estimated passive phases getting trapped in a local minimum. A wrong estimation of the passive phases places a limit on prediction accuracy of the model.

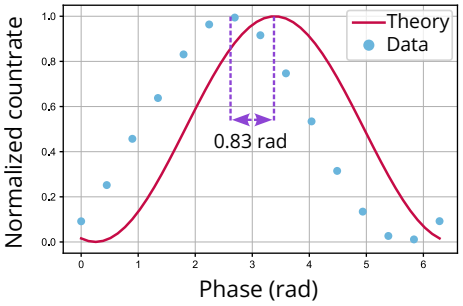

Figure III.18: Interference fringe when sweeping the phase of a PS. Experimental data from a 12-mode Clements interferometer

We address residual passive phase errors by introducing a new stage in the characterization protocol: the **phase interference fringe measurement (ϕ-IFM)**. In this stage, every PS is swept in phase from 0 to 2π. Doing so uses the estimated crosstalk matrix $\hat{C}_2$ that was previously updated during the ML stage. Using the crosstalk matrix also controls the PSs collectively, thus canceling crosstalk and leading to more accurate passive phase measurements. The recorded interference fringe is compared to the expected fringe, computed from the estimated beamsplitter reflectivity values $\hat{\vec{R}}$ and output transmissions $\hat{\vec{T}}_{\text{out}}$. The offset between the recorded and expected fringes updates the passive phase of the swept PS accordingly, as shown on see Fig. III.18. To our knowledge, passive phase correction via ϕ-IFMs is a novel procedure implemented for the first time in this work (and reported in [6]).

The protocol performs several (ML+ ϕ-IFM) iterations. Every new ML stage benefits from more accurate passive phase estimations $\hat{\vec{c}}_0$, while the ϕ-IFM stages are performed with increasing accuracy thanks to updated virtual replica parameters. We demonstrate in simulations that this process recovers the PIC parameters with arbitrary precision (see Fig. III.19). In practice, the iteration loop stops when the virtual replica prediction accuracy TVD_{test} stagnates compared to the previous iteration.

A last stage in the characterization process, called **input transmission measurement** mea-

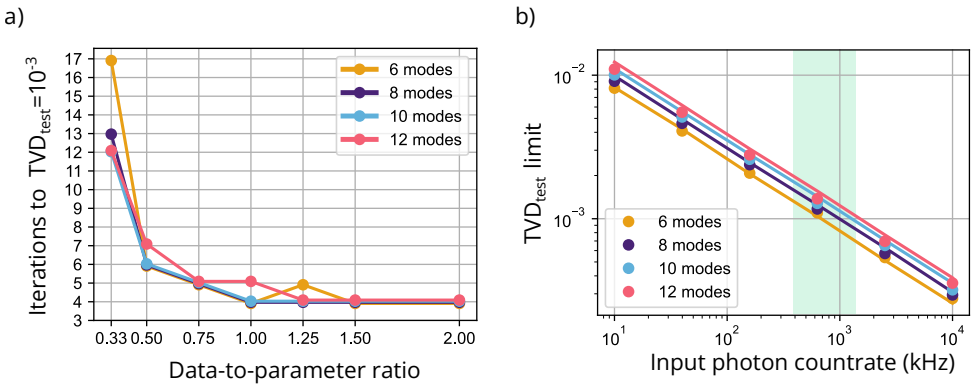

Figure III.20: Virtual replica training dependence on number of training samples and detector noise. Adapted from [6]. **a)** Number of (ML + ϕ-IFM) iterations required to reach $\text{TVD}_{\text{test}} = 10^{-3}$ as a function of the data-to-parameter ratio (number of training samples / number of virtual replica parameters). **b)** Simulated lowest reachable TVD_{test} value as a function of input photon countrate. The green area indicates typical experimental values in our optical setup. The continuous lines correspond to the noise floor, computed from the average $\text{TVD}(\vec{p}, \vec{q})$, where $\vec{p}$ is a generic probability vector and $\vec{q}$ is $\vec{p}$ with Poisson noise added.

sures the optical input transmissions $\vec{T}_{\text{in}}$. This is achieved by correcting total intensity measurements based on the estimated output transmissions $\hat{\vec{T}}_{\text{out}}$.

In the next subsection, we study the behavior of our characterization protocol in different scenarios related to experimental considerations.

III.2.5 - Evaluation of our characterization protocol in simulations

We assess the dependence of our machine learning-assisted characterization protocol on the number of training samples and detector noise. We use simulated Clements interferometers for that purpose (see Section I.4.2). In simulations without detector noise, we consider that a PIC is characterized when the prediction accuracy of the virtual replica reaches $\text{TVD}_{\text{test}} = 10^{-3}$. We will argue later in this subsection that TVD_{test} values below this threshold are experimentally challenging to observe.

III.2.5.A - Sample efficiency

The data-to-parameter ratio is defined as the number of training samples over the number of virtual replica parameters. A smaller data-to-parameter ratio indicates greater sample efficiency. This efficiency is crucial experimentally, as collecting training and test data samples consumes the majority of the characterization time: for the 12-mode Clements interferometer of Section III.4.1, acquiring the samples takes 16 hours, against 1 hour of protocol execution time. We show in Fig. III.20a that a data-to-parameter of 1 suffices to characterize a PIC in a reasonable number of (ML+ϕ-IFM iterations). In fact, even a data-to-parameter ratio of 0.5 may be chosen, at the cost of slightly higher number of iterations. We choose in the following to work with a data-to-parameter ratio equal to 1.

III.2.5.B - Detector noise

Detector noise manifests as a variation in the measured light intensities between successive measurements even when nothing in the optical setup is being altered. We focus on the case of a pulsed single-photon source and single-photon detectors. For every emitted photon, each photon detector has a fixed probability of detecting the photon determined by the optical setup losses and the matrix implemented by the PIC. Nevertheless, the measured countrate varies from one measurement to the other because of the finite integration time. In this context, the observed detector noise is thus mostly **photon counting noise**. We assume that the single-photon detectors are op-

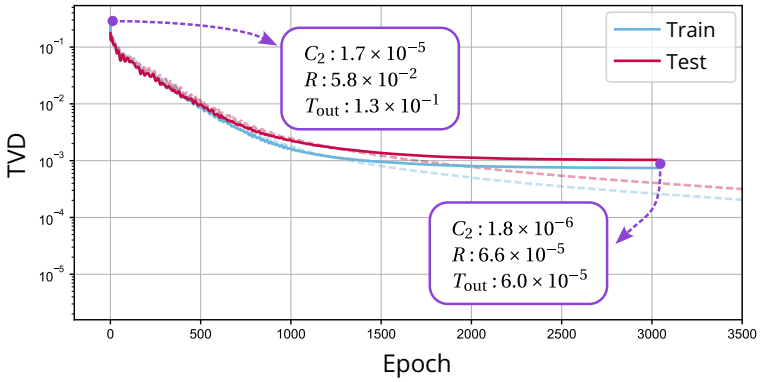

Figure III.21: Impact of detector noise on gradient descent Same as Fig. III.17 with Poisson noise in the data samples. The noise is computed for an input photon countrate of 1 MHz. Dashed curves correspond to the noiseless case of Fig. III.17. Note that in comparison with Fig. III.17, the TVD is stuck at 10^{-3} and the error on the estimated physical parameters is higher by 1 to 2 orders of magnitude.

erated in the linear regime and that the photon detections are independent. As a consequence, photon detection is a **Poisson process**. The detector noise is then **Poisson noise**, characterized by a statistical variance equal to the average. We simulate photon counting noise on the detectors by applying Poisson noise on the training and test samples. Fig. III.21 shows that detector noise prevents the virtual replica from fully converging. We demonstrate that the virtual replica prediction accuracy reaches the noise floor in any case (see Fig. III.20b). In particular, the minimally achievable TVD_{test} is of the order of 10^{-3} in an experimental setting, given the characteristics of our setup.

When performing the characterization with a continuous-wave laser and powermeters, the detector noise is usually Gaussian due to the internal electrical components of the detector. Empirically, we observe that the detector noise with powermeters is greater than with single-photon detectors.

III.2.5.C - Generalization to other material platforms

The machine learning-assisted characterization protocol was developed with generality in mind but its implementation is tailored to the specific material platform used for experimental validation, namely silicon nitride. In particular, the silicon nitride platform has very weak isotropic crosstalk between neighboring components. The crosstalk strength is defined as the ratio between nearest-neighbor crosstalk and self-heating coefficients and is indeed on the order of 1 % in the silicon nitride platform.

On the other hand, the crosstalk in silica glass circuits is significantly more intense, with crosstalk strengths on the order of 20 %, but restricted to the vertical direction thanks to the substantial horizontal separation (i.e. along the light propagation direction) between phase shifters. Simulations have shown that our method breaks down in this setting, but adding a coarse manual crosstalk measurement stage to initialize the crosstalk matrix before the machine learning stage solves the issue.

These findings support the conclusion that, while the specific implementation details of the characterization stages (V-IFM, ML, ϕ-IFM, ITM), as illustrated in Fig. III.6, may vary depending on circuit fabrication platforms, the overall procedure remains applicable.

With the physical PIC characterized, we now have access to the physical parameters of the device. These parameters are subsequently harnessed in the following section by an imperfection mitigation to perform operations on light with high fidelity.

III.3 - PIC Imperfection mitigation

In our context, imperfection mitigation is a collection of algorithms compensating device imperfections to implement target unitary matrices with high-fidelity on a PIC. Most imperfection mitigation techniques assume that the physical parameters of the PIC such as the beamsplitter reflectivities are known [21, 22, 23, 24]. We use our machine learning-assisted characterization described in Section III.2 to recover the values of these physical parameters, that are otherwise difficult to access in generic interferometer meshes. For imperfection mitigation, we assume that the estimated virtual replica parameters match the actual values:

$$\hat{\vec{c}}_0 = \vec{c}_0, \qquad \hat{C}_2 = C_2, \qquad \hat{\vec{R}} = \vec{R}, \qquad \hat{\vec{T}}_{\text{in/out}} = \vec{T}_{\text{in/out}}. \tag{III.15}$$

Hence, the overall quality of the control accuracy of a given PIC depends on both a reliable imperfection mitigation process and an accurate characterization of the PIC.

We discuss mitigation of beamsplitter reflectivity errors in Section III.3.1, optical loss inhomogeneities in Section III.3.2 and crosstalk in Section III.3.3.

III.3.1 - Mitigation of beamsplitter reflectivity errors

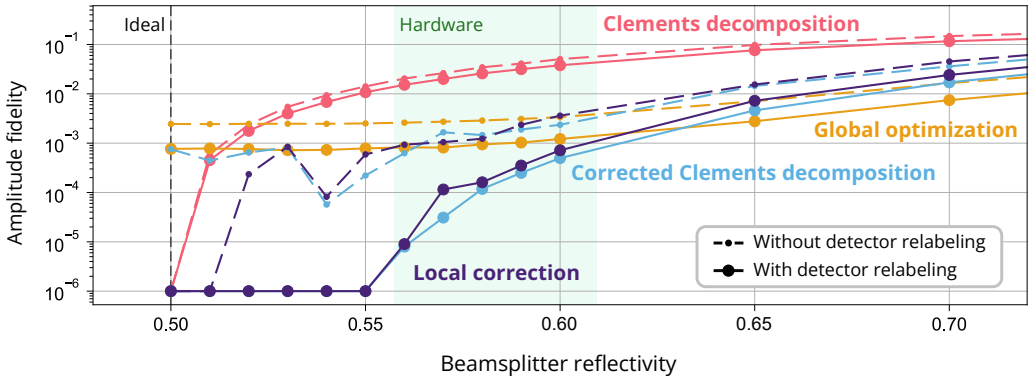

Figure III.22: Simulated comparison of beamsplitter reflectivity mitigation algorithms Adapted from [6]. The simulations are performed on a 12-mode Clements interferometer with uniform beamsplitter reflectivity. The black dotted line indicates the ideal reflectivity value of 0.5 for Clements interferometers. The green area indicates typical experimental values. Value zero is clipped to 10^{-6}.

Beamsplitter reflectivity errors can be addressed by optimization-based and deterministic algorithms. Optimization-based algorithms find suitable phases $\vec{\phi}$ to implement on the PIC by minimizing a specified cost function [21]. We implement an optimization-based algorithm called ***global optimization*** (see flowchart on Fig. III.23) that tunes the phase shifts $\vec{\phi}$ via gradient descent. The minimized cost function is the fidelity $\mathscr{F}$ between the target unitary matrix U_{target} and $U(\vec{\phi})$, the matrix computed from $\vec{\phi}$ and the known beamsplitter reflectivities. Our implementation of *global optimization* can be customized to include for instance a penalty for power consumption. In addition, *global optimization* adapts straightforwardly to any interferometer mesh, reinforcing the versatility and flexibility of the method.

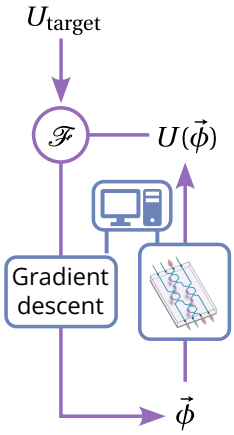

Figure III.23: Flowchart of *global optimization*

On the other hand, deterministic methods are computationally more efficient than *global optimization*, but generally tied to a specific interferometer mesh. Usual deterministic methods are built on the canonical decompositions of Reck [36], Clements [37] or Bell-Walmsley [38] interferometers. These canonical decompositions deterministically compute the phase shifts

$\vec{\phi}$ from the target unitary matrix U to implement assuming every beamsplitter has a reflectivity $R = 0.5$ (i.e. no beamsplitter reflectivity errors). Two deterministic reflectivity error correction methods have been devised for Clements interferometers:

- the ***local correction*** algorithm [23] computes an initial guess $\vec{\phi}$ on the phases with the Clements decomposition and subsequently finetunes each PS such that beamsplitter errors are locally corrected.
- the ***Clements corrected*** decomposition [24] performs a modified Clements decomposition that takes into account the beamsplitter reflectivity errors.

We compare *global optimization*, *local correction* and *Clements corrected* against the standard Clements decomposition in Fig. III.22. We observe that the flexibility of *global optimization* comes at the cost of a less qualitative compilation, compared to *local correction* and *Clements corrected*.

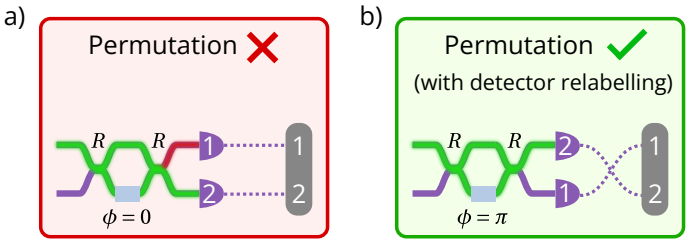

Figure III.24: **Implementation of a high-fidelity permutation with an imperfect MZI** Consider an MZI with uniform beamsplitter reflectivity $R \neq 0.5$. **a)** To implement a permutation on the two MZI modes, it is possible to set the MZI to the cross configuration by setting the internal phase shift ϕ to 0. Because of the beamsplitter reflectivity errors, the permutation is not implemented with unit fidelity. **b)** Alternatively, we can set the MZI to the bar configuration with $\phi = \pi$. This configuration is achievable despite the beamsplitter reflectivity errors as long as the two beamsplitters have the same reflectivity. We then swap the two detector links, which yields at the logical level a perfect permutation.

Reflectivity error correction can be improved by introducing **detector relabeling**, which consists in permuting the labels on the detectors e.g. if the labels of detectors "1" and "2" are permuted, then a click on the physical detector "2" is processed as a detector "1" click. We suggest that detector relabeling extends the unitary space coverage of a given PIC (see Section III.1.1). The intuition is that an ideal MZI followed by detectors can implement a permutation between its two modes when the internal phase shift is $\phi = 0$. An MZI with uniform beamsplitter reflectivity errors (most frequent case, see Section III.1.1) cannot perform the permutation as is with $\phi = 0$, but if the two detector labels are permuted and the internal phase set to $\phi = \pi$, then the permutation is perfect from a logical point of view. The process is illustrated on Fig. III.24.

Fig. III.22 shows that detector relabeling improves the accuracy of all the reflectivity error mitigations. For every target unitary matrix, 16 random detector relabeling are tested and the best (relabeling + phases) pair in terms of fidelity is kept. The question of whether it is possible to efficiently choose a detector relabeling yielding a significant fidelity improvement remains open. [24] used detector relabeling to decrease the power consumption of PICs, and proposed an optimized search of detector labels.

For the PIC optimal control demonstration of [6], we used the *local correction algorithm* paired with detector relabeling, to target the highest fidelity value.

III.3.2 - Mitigation of optical loss inhomogeneities

A first approach to the mitigation of inhomogeneities in optical input and output transmissions $\vec{T}_{\text{in/out}}$ could be to optimize the implemented phase shifts $\vec{\phi}$ to maximize the fidelity of the implemented matrix, similarly to the *global optimization* beamsplitter error mitigation of Section III.3.1. Recent preliminary works seem however to indicate that this approach is ineffective. A simple

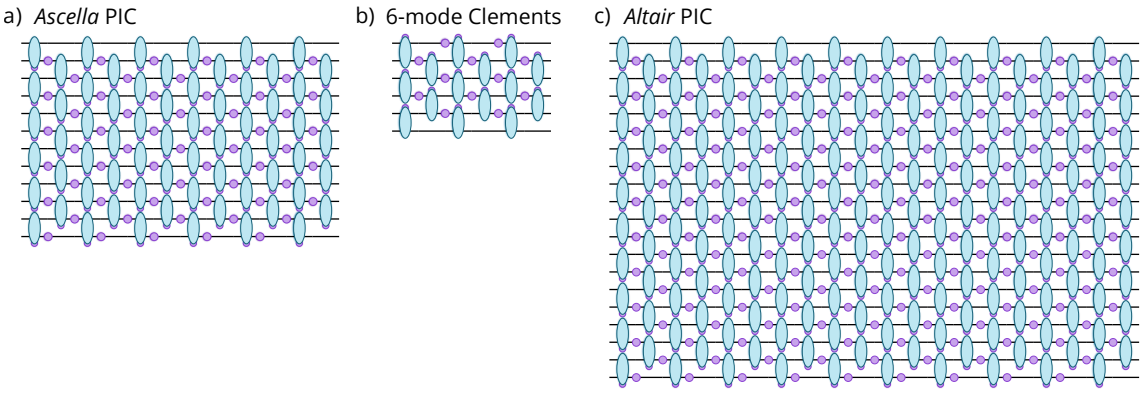

Figure III.25: PICs for the experimental validation. Schematics of tested Clements interferometers. Blue ellipses: MZIs. Purple disks: PSs. **a)** and **c)** respectively have 12 and 20 modes, following exactly the same design. **b)** has 6 modes with phase shifters located in different positions.

argument already excludes a unit fidelity recovery: target unitary matrices lie in the set of unitary matrices, while PICs with transmission inhomogeneities produces matrices outside of the unitary set.

In certain cases, such as when the target unitary matrix has a smaller dimension than the number of PIC modes, then we can choose to inject (resp. detect) photons in input (resp. output) ports with similar optical transmissions to attenuate the inhomogeneity. The procedure is described in [6] and works only for universal interferometers. Indeed, universal interferometers can implement the desired target unitary matrix U and additional input and output permutations P_{in} and P_{out}, because the resulting matrix $U' = P_{\text{out}} \cdot U \cdot P_{\text{in}}$ is also unitary.

III.3.3 - Cancelling thermal crosstalk

Thermal crosstalk is described by the phase-voltage equation Eq. III.10. Given a list of target phases $\vec{\phi}$, solving the phase-voltage equation for $\vec{V}$ readily cancels crosstalk. The phase-voltage relation of a PIC is a nonlinear matrix equation, which are notoriously challenging to solve. This is exacerbated by the constraints on the voltages which must be positive and below a safe operation bound. In [6], we presented a general step-based solver with an $O(n_{\text{PS}}^3)$ complexity with n_{PS} the number of on-chip PSs (see App. D.3). The solver was subsequently improved to be matrix-based, reducing significantly the runtime of the algorithm and its scaling to $O(n_{\text{PS}}^2)$ (see App. D.4). In the general case, our solver delivers an approximation of the voltage solution implementing the target phases with an arbitrary precision threshold set to 0.1 mrad.

In the following section, we showcase our PIC characterization and imperfection mitigation on multiple physical devices.

III.4 - Experimental validation of our characterization process and imperfection mitigation

We provide a survey of the different PICs that were used to develop and validate our machine learning-assisted characterization (see Section III.2) and imperfection mitigation (see Section III.3). All the PICs are fabricated in the silicon nitride platform (see Section I.4.3). Table III.3 summarizes the key figures of the different experimental validations.

III.4.1 - The *Ascella* PIC

The *Ascella* PIC drawn on Fig. III.25a is a 12-mode Clements interferometer that served as a the main validation platform for our processes. Fig. III.26 shows the estimated physical parameters.

PIC	m	n_{PS}	$n_{samples}$	Duration	TVD_{test}
Ascella	12	126	≈ 16000	17 hours	2.9 %
6-mode Clements interferometers	6	27	≈ 700	1 hour	2.4 ± 0.9 % ($n = 4$)
Altair	20	370	≈ 54000	3-4 days	9.0 %

Table III.3: **Experimental validations of our PIC characterization method** m: number of modes. n_{PS}: number of PSs. $n_{samples}$: number of training samples. Duration: characterization time, including the dataset acquisition. TVD_{test}: average TVD evaluated on the test dataset. The error bar for the 6-mode Clements interferometers refers to the standard deviation on the four characterized PICs. *Altair* was characterized with a data-to-parameter ratio of 40 % due to time constraints.

Most noticeably, the beamsplitter reflectivity errors are consistently far off from the ideal 0.5 value, because the PIC was fabricated for a light operation wavelength of 941 nm, while our single-photon sources emit between 925 and 928 nm (see Section I.3.3). Using our imperfection mitigation from Section III.3, we demonstrated unprecedented control accuracy with the *Ascella* PIC in [6]. To the best of our knowledge, this remains to this date the most accurate operation of a PIC, with one of the biggest available PICs (see state of the art in Table III.2).

III.4.2 - Four 6-mode Clements interferometers

We then used our method to characterize a set of four 6-mode Clements interferometer fabricated in the same foundry. The flexibility and generality of our method allowed each PIC to be characterized in a record time of one hour, despite the differences in the interferometer mesh with *Ascella* (see Fig.III.25b). Interestingly, the PSs exhibit here a marked V^4 dependence. This allowed to test the characterization of a more complex phase-voltage relation, with both V^2 and V^4 terms. Fig. III.27 displays the estimated physical parameters of one of the four PICs. Notice that our characterization protocol detected fabrication anomalies in the beamsplitter reflectivities: depending on the direction of light propagation (the circuit is bent to reduce the footprint of the integrated device), the reflectivity is either 0.6 or 0.4.

III.4.3 - The *Altair* PIC

The *Altair* PIC is a 20-mode Clements interferometer and constitutes currently the largest PIC characterized using our method. The estimated parameters are shown on III.28.

We have demonstrated that our machine learning-assisted characterization process is adapted to an experimental setting. After their characterization and testing, the *Ascella*, 6-mode Clements and *Altair* PICs were built into photonic quantum devices accessible at a distance, where reliability on the implemented operations on light is key. We focus in Section III.5 on the setting up and operation of *Ascella*.

III.5 - Application: A quantum computer on the cloud

Our PIC characterization protocol and imperfection mitigation are essential building blocks of photonic quantum computing platforms relying on integrated photonics, such as *Ascella*, Quandela's first quantum computer accessible on the cloud. Owing to the achieved level of control accuracy with the *Ascella* PIC, *Ascella* demonstrated state-of-art results for quantum information protocols with a remarkable precision reported in [5]. The range of demonstrated protocols covers heralded 3-GHZ state generation and variational quantum algorithms such as variational quantum eigensolvers and quantum machine learning. *Ascella* was the first quantum computer to demonstrate on-cloud availability rates above 90 %, as reported in [2]. This marks a significant milestone

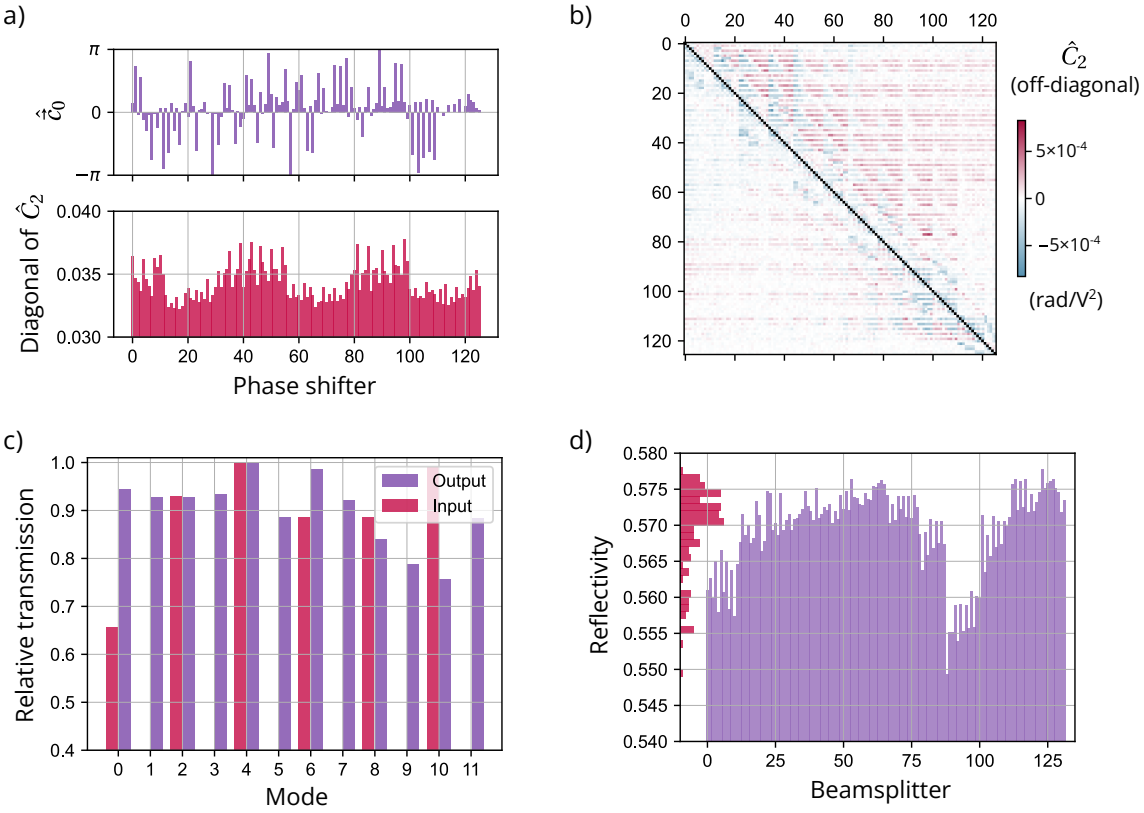

Figure III.26: Estimated physical parameters of *Ascella* **a)** Passive phases and self-heating coefficients (diagonal coefficients of the crosstalk matrix). **b)** Crosstalk matrix. Dominant diagonal coefficients have been masked. **c)** Input and output transmissions, normalized such that the maximum value is 1. **d)** Beamsplitter reflectivities. Histogram of values in red.

for photonic quantum computing.

We describe in Section III.5.1 the hardware architecture of *Ascella*. Section III.5.2 discusses the characteristics of *Ascella* focusing on stability and autonomy. We illustrate the operation of *Ascella* with our contribution to an academic project in Section III.5.3.

III.5.1 - System architecture

The optical setup behind *Ascella* shown on Fig. III.29 is an upgrade of the experimental setup used for the 4-GHZ experiment (see Section II.6). Notable improvements are the transition to a 6-photon architecture, the universal 12-mode Clements interferometer (*Ascella* PIC) able to manipulate up to 6 dual-rail encoded photonic qubits simultaneously and 12 high-efficiency (>90 %) single-photon detectors. *Ascella* is also powered by the single-photon source "Faith", which has significantly better characteristics than the source used in Chapter II ("Alyx", see Table III.4 for a comparison). Fig. III.30 shows in particular that "Faith" is substantially less sensitive to charge noise compared to "Alyx" (see Section I.3.3.B), with a stable photon indistinguishability across all explored photon emission delays.

To allow for a variable number of photons to enter the PIC simultaneously, it is possible to reconfigure the active demultiplexer to distribute the stream of incoming photons only into the desired input modes. This proved however to introduce substantial polarization instabilities, leading to highly fluctuating countrates on the detectors (the *Ascella* PIC waveguides are polarization-selective). It is assumed that these instabilities are caused by the varying amounts of heat generated in the demultiplexer acousto-optic crystal from one input state configuration to the other. Instead, the demultiplexer is operated in a static regime and a system of mechanical shutters in

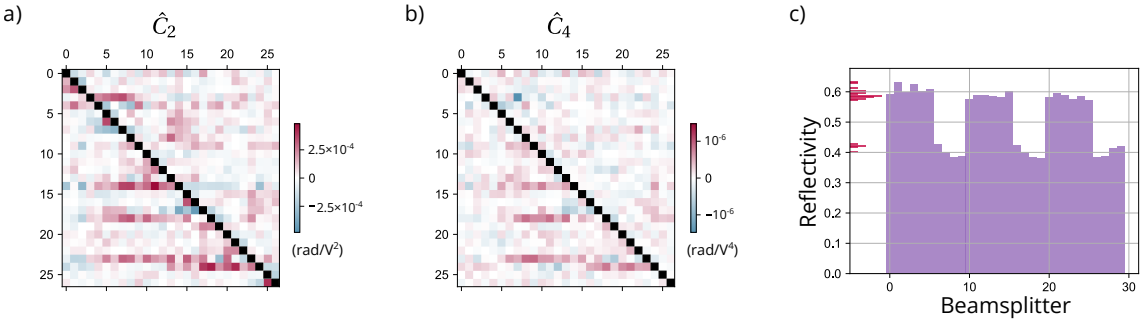

Figure III.27: Estimated physical parameters of one of the four 6-mode Clements interferometers **a)** (resp. **b)**) Crosstalk matrix associated to V^2 (resp. V^4). Dominant diagonal coefficients have been masked. **c)** Beamsplitter reflectivities. Histogram of values in red.

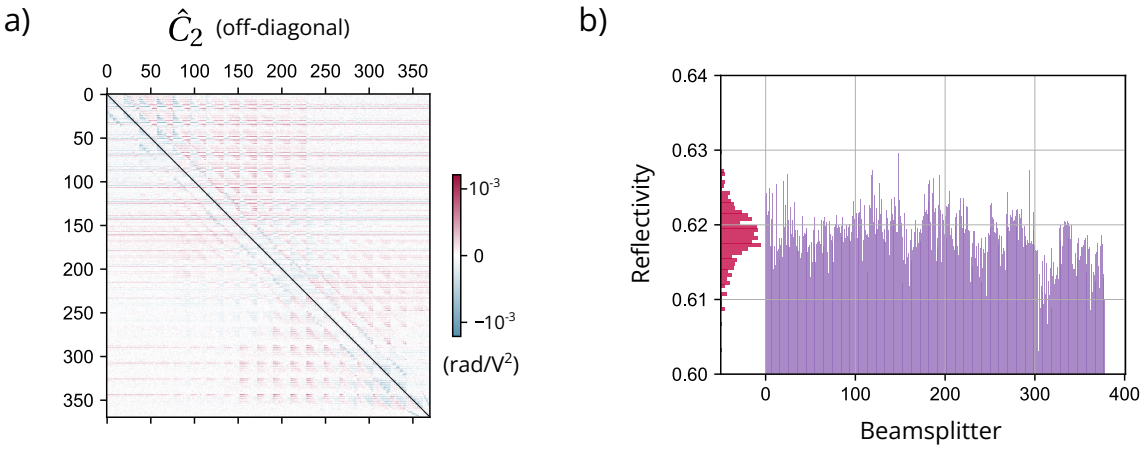

Figure III.28: Estimated physical parameters of *Altair* **a)** Crosstalk matrix. Dominant diagonal coefficients have been masked. **b)** Beamsplitter reflectivities. Histogram of values in red.

the demultiplexer blocks the unnecessary photons.

As a result, the photonic input state is of the form

$$|\alpha_0, 0, \alpha_1, 0, \alpha_2, 0, \alpha_3, 0, \alpha_4, 0, \alpha_5, 0\rangle \tag{III.16}$$

where each α_i is either 0 or 1. It is possible to work with more complicated input states such as $|\psi_{\text{in}}\rangle = |1,1,1,1,1,1,0,0,0,0,0,0\rangle$ by letting the input photons evolve in the PIC first through a permutation matrix P_{in}. The implemented matrix on the PIC is then $U' = U \cdot P_{\text{in}}$, where U is the unitary matrix to apply on $|\psi_{\text{in}}\rangle$. U' can always be implemented on the PIC thanks to its universality. This procedure is similar to the optical transmission mitigation of Section III.3.2.

Certain quantum information protocols such as variational quantum algorithms require frequent, but localized PIC updates affecting only a few PSs. We implement a quick update option in the PIC control software. This option bypasses the full reconfiguration of the PIC taking 2 seconds, and only updates individual PSs whose voltage changes significantly compared to the previous voltage configuration. In comparison, updating a single PS takes less than 5 ms. The voltage update threshold is set to 0.1 mV, corresponding to phase displacement of 1 mrad in the worst case.

Carrying over from our experience with the QRNG and 4-GHZ experiments (see Chapter II), *Ascella* benefits from highly stable optical components and a comprehensive monitoring solution discussed in the following section.

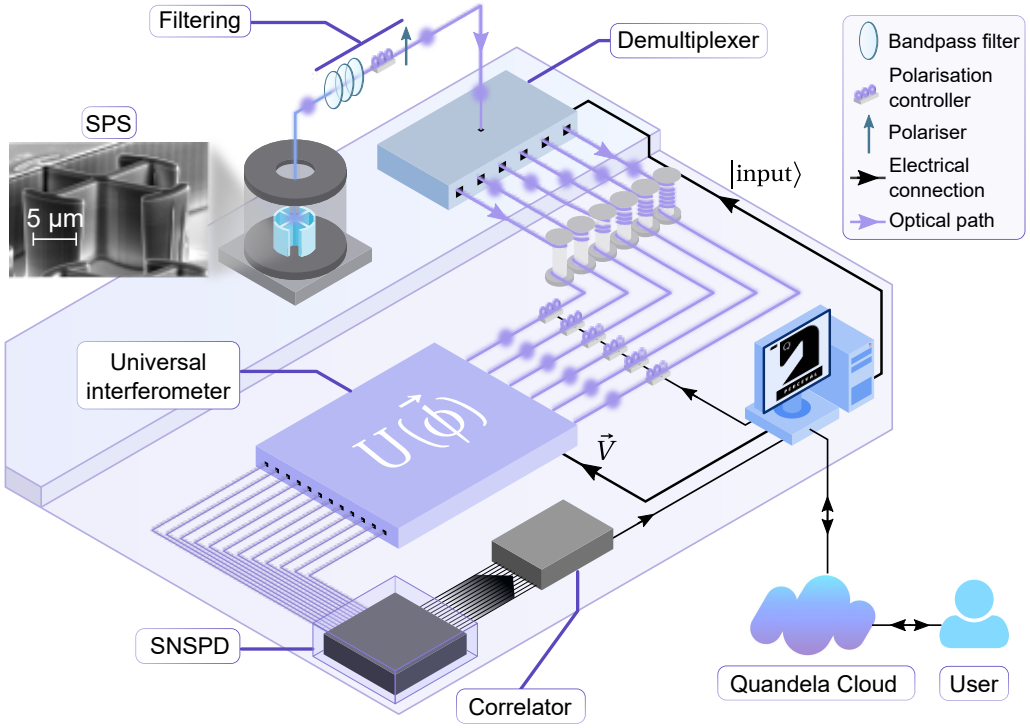

Figure III.29: Optical setup of *Ascella* Adapted from [5]. The stream of emitted single photons is actively demultiplexed into 6 spatial modes. Fiber delays guarantee that all the photons arrive at the same time in the universal interferometer (*Ascella PIC*). The experiment is controlled by a CPU setting PIC voltages and input states, as well as gathering measurement results.

III.5.2 - Stability, self-characterization and availability

Ascella's optical setup is mostly fibered or integrated. Consequently, the optical setup is particularly stable on the long-term. The major sources of instability come from the free space optics in the demultiplexer and at the level of the single-photon source. In addition, temperature fluctuations and vibrations affect the fiber delays after the demultiplexer, which in turn have an impact on photon polarization and indistinguishability.

We use a monitoring system coupled with periodical self-characterizations to assess the stability of the setup. Each hour, the single-photon countrate, photon coincidence rates, dark counts, multi-photon emissions and photon indistinguishability are measured, among others (see Fig. III.31). In particular, the high degree of reconfigurability of the PIC allows to measure the HOM visibility between all pairs of photons. The monitoring system also tests the implementation of simple matrices such as the identity matrix.

Degradation of single-photon countrates due to polarization shifts in the fibers is compensated with 6 motorized polarization controllers (see Fig. III.29). Occasionally, significant decreases in photon distinguishability caused by substantial temperature fluctuations require to finetune the free-space delay stages in the demultiplexer to recover the initial values. A 4-hour maintenance period each week is generally sufficient to diagnose and realign common setup elements, yielding an online availability beyond 90 %.

Thanks to its remarkable stability, availability and accuracy of control, *Ascella* was used for several experimental demonstrations of quantum information protocols reported in [5]. The implemented protocols include

- single-photon-based boson sampling with a sampling rate (6 photons injected and detected) of 0.16 Hz (see Section I.5.1.A for a comparison with other boson sampling experiments),

	"Alyx"	"Faith"
Emission wavelength	925 nm	928 nm
Excited state	trion	exciton
Polarized first-lens brightness	$38 \pm 1\,\%$	$55 \pm 1\,\%$
Polarized device brightness	$18 \pm 1\,\%$	$26 \pm 1\,\%$
$g^{(2)}(0)$	$2.0 \pm 0.1\,\%$	$0.7 \pm 0.1\,\%$
V_{HOM}	$90 \pm 1\,\%$	$93 \pm 1\,\%$
M_s	$94 \pm 1\,\%$	$94 \pm 1\,\%$
M_s with 600 ns delay	$86 \pm 1\,\%$	$94 \pm 1\,\%$

Table III.4: **Comparison between single-photon sources "Alyx" and "Faith"**. Polarized first-lens / device brightness: see Section I.3.1.A. $g^{(2)}(0)$: quantifies multiphoton emission, see Section I.3.1.B. V_{HOM} and M_s: photon indistinguishability measured between successive photons, see Section I.3.1.C. The M_s value is given as well for photons emitted with a time interval of $\approx$ 600 ns. The decrease for Alyx is attributed to charge noise (see Section I.3.3.B). The data was acquired with the quasi-resonant excitation scheme, without etalon. Error bars indicate the magnitude of typical day to day variations in the evaluated quantities, and account for measurement uncertainty.

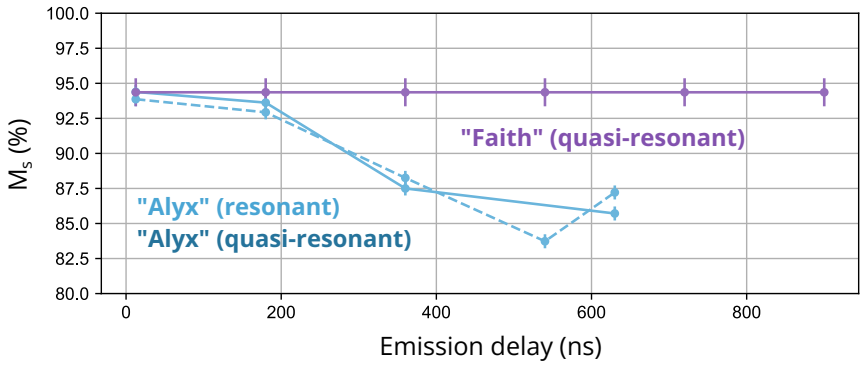

Figure III.30: **Effect of charge noise on photon indistinguishability.** Photon indistinguishability M_s as a function of emission delay between the two photons interfering. The blue curves have been acquired for "Alyx" in resonant and quasi-resonant excitation. The purple curve is associated to "Faith" in quasi-resonant excitation. The data was acquired without using an etalon for enhanced photon filtering.

Figure III.31: Monitoring system of *Ascella*. The monitored parameters are grouped into section "optical systems", "single photons" and "quantum information". The arrows in the cycle indicate that the quality of the quantum information protocols run on *Ascella* depend on the characteristics of the single-photons, which themselves depend on the state of the optical systems. In the quantum information section, the CNOT fidelity is the fidelity of a single CNOT gate evaluated in the computational basis, whereas RB36 tests the CNOT gate with randomized input states (see [5]). Dual CNOT implements two CNOT gates in parallel.

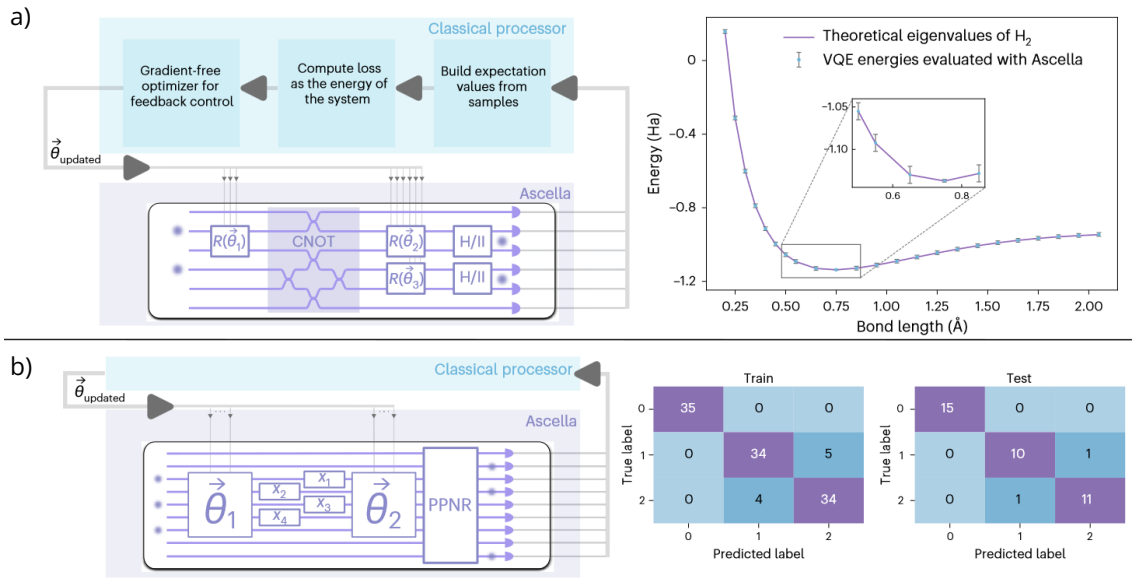

Figure III.32: From [5]. **Experimental demonstration of photonic variational quantum algorithms (see Section I.5.1.B) on *Ascella*.** **a)** Variational quantum eigensolver algorithm for determining the ground state energy of the dihydrogen molecule using two photons and a postselected CNOT gate. **b)** Quantum machine learning for classification on Fisher's Iris data set using three photons and pseudo-photon-number resolving detectors (PPNR).

- a variational quantum eigensolver for finding the ground state energy of the dihydrogen molecule (see Fig. III.32a) with a faster convergence and better precision then previous demonstrations thanks to the quality of the single photons and accuracy of the PIC control,
- the first single-photon-based realization of a classification algorithm using a quantum neural network (see Fig. III.32b),
- the generation of heralded 3-GHZ states with a fidelity of 82 %, as a resource state for fault-tolerant universal quantum computation.

In the following section, we use *Ascella* to investigate the impact of partial photon distinguishability on the fidelity of a postselected CNOT gate.

III.5.3 - CNOT gate with distinguishable photons

We participated in an international project involving students from Polytechnique Montréal. The project consisted in implementing a CNOT gate with *Ascella* and study the gate fidelity as a function of photon distinguishability. The goal of the work was to explore partial indistinguishability models for `Perceval` based on Schmidt decompositions. We took over the experimental work and provided support in the data analysis.

We implement a postselected CNOT gate on *Ascella* ([152], see Section I.5.2.A). Let U_{CNOT} be the unitary matrix of the linear optical circuit implementing the CNOT gate. The fidelity of the gate is estimated by measuring the coincidence counts between the two qubits in the computational basis

$$\{|0,0\rangle, |0,1\rangle, |1,0\rangle, |1,1\rangle\}. \tag{III.17}$$

where we use dual-rail qubit path-encoding. Physically, the two photons always enter the PIC from the same input ports. Thus, the input photons must be routed inside the PIC to generate the adequate basis state, which is then transferred to the CNOT gate. Hence, there are four unitary

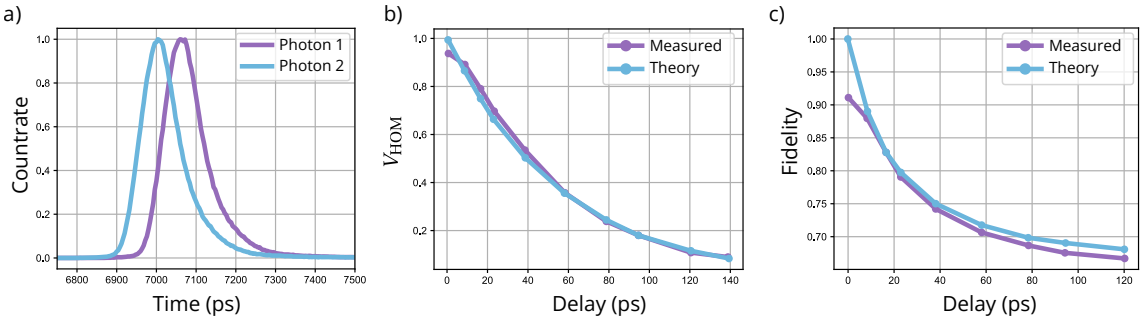

Figure III.33: **Implementing a CNOT gate with distinguishable photons on *Ascella*** **a)** Envelope of the photons, here delayed by 58 ps. Time is measured with respect to the pump pulse trigger. The associated photon indistinguishability is measured to be $V_{\text{HOM}} = 35.6\%$. **b)** HOM visibility as a function of delay between photons. Measured values have been acquired by setting the PIC to implement a symmetric beamsplitter, thus yielding the HOM value experimentally. The theoretical value is computed from the photon envelopes, after deconvolution with a Gaussian. **c)** CNOT gate fidelity as a function of delay between photons. Measured values correspond to the fidelity of the implemented gate on the hardware. The theoretical values are computed from the photon envelopes.

matrices to implement of the form

$$U'_{xy} = U_{\text{CNOT}} \cdot P_{xy} \tag{III.18}$$

where P_{xy} is a permutation matrix that initializes the two qubits in the state $|x, y\rangle$. We compile each U'_{xy} using the *global optimization* algorithm of Section III.3.1 into phase shifts.

The distinguishability between the two photons is changed by manually moving a free-space translation stage in the demultiplexer. This yields photon envelopes that do not arrive at the same time in the PIC (see Fig. III.33a). We show on Fig. III.33b the HOM visibility of the photons as a function of the delay between the envelopes, along the predicted HOM visibility from the envelope overlap. For each delay, we measure the resulting fidelity of the CNOT gate. The measured fidelity agrees with the theoretical model for partial indistinguishability, as can be seen on Fig. III.33c. Interestingly, the point at zero delay deviates strongly from the model. We attribute this to the predominance of spectral distinguishability in the synchronized photon regime, due to charge noise around the quantum dot emitter (see Section I.3.3.B).

III.6 - Conclusion on optimal control of PICs using machine learning

Fabrication of photonic integrated devices is progressing at a rapid pace, yet current devices are riddled with imperfections. Typical imperfections in PICs include **thermal crosstalk between PSs, beamsplitter reflectivity errors and input/output port optical losses** (see Section III.1.1). Given the challenges of controlling large-scale PICs at the heart of near-term photonic quantum computing platforms such as Quandela's *Ascella*, we have tackled the problem of optimal control of PICs.

We use machine learning to handle the complexity of linear interferometer meshes and adopt a **model-based clear-box approach** (see Section III.1.3). This involves constructing a virtual replica of the hardware PIC **based on a physical model** (see Section III.2.1), instead of e.g. neural networks acting as black-boxes. The virtual replica acts as a software emulation of the hardware.

Given a physical PIC to control, the virtual replica gathers and stores information about the PIC throughout a training process. By design, each parameter of the virtual replica corresponds to a physical parameter of the PIC. The virtual replica training process is an **iterative process alternating between machine learning stages and interference fringe measurements** (see Section III.2.4).

Our **patented** machine learning-assisted characterization method has been validated both in simulations (see Section III.2.5) and experimental demonstrations (see Section III.4). We have demonstrated the capabilities of our method to **scale and adapt to different interferometer meshes.**

The estimated physical parameters by the virtual replica are then transferred to an imperfection mitigation (see Section III.3). Given a target unitary matrix to implement, the imperfection mitigation returns the voltages to apply on the PIC in order to implement the target matrix with high fidelity. We tackle beamsplitter reflectivity errors, thermal crosstalk and discuss mitigation of optical loss inhomogeneities. As a result, **our experimental demonstration on a 12-mode Clements interferometer reported in [6] remains the most accurate demonstration of PIC optimal control, carried out on one of the largest available PICs.** From a broader perspective, our work suggests that clear-box models for optimal control of physical devices are significantly more **sample efficient** than neural network-based approaches, and yield **lighter machine learning models** in terms of number of parameters. Our protocol and machine learning model can thus run on standard lab computers, up to 16-mode universal interferometers, beyond which a dedicated graphics card is recommended.

The control accuracy achieved by our characterization protocol and imperfection mitigation has enabled state-of-the-art results on *Ascella*, Quandela's first quantum device accessible on the cloud (see Section III.5). Evaluated qubit gate fidelities on our photonic platform are comparable to those of superconducting and trapped ion qubits, as reported in [5].

Our virtual replica is able to measure physical parameters of PICs that are difficult to access and isolate in the general case. As such, our method recovers valuable properties of the device that may be used to provide feedback to fabrication processes on large integrated structures.

The prediction accuracy of the virtual replica in our experimental demonstrations does however not yet meet the level expected from photon counting noise on the detectors (see Section III.2.5). Specifically, **the prediction accuracy of the virtual replica could be improved by an order of magnitude** in terms of $\mathrm{TVD}_{\mathrm{test}}$. For instance, we achieve $\mathrm{TVD}_{\mathrm{test}} = 2.9\,\%$ on a 12-mode Clements interferometer (see Section III.4.1), but detector noise places the lower bound at $\approx 10^{-3}$. We attribute this shortfall to physical effects not captured by our current PIC model, thus limiting the prediction accuracy of the virtual replica. In the next chapter, we will extend our clear-box approach to probe these physical effects in PICs, aiming to improve the prediction accuracy of our

model and, consequently, the control accuracy of our PICs.

IV - Targeting noise-limited circuit control with physical model extensions

To boldly go where no [hu]man has gone before.

James T. Kirk, *Star Trek*

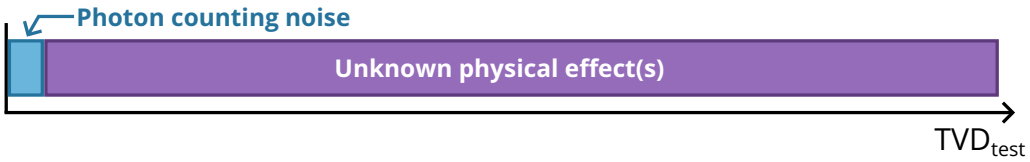

Figure IV.1: Factors assumed to limit the virtual replica prediction accuracy. The figure is to scale, based on the results from Section III.4.1.

In Chapter III, we use a machine-learning assisted characterization to estimate the physical parameters of PICs. To achieve this, a virtual replica is trained during a characterization process to copy the behavior of the hardware PIC to control. The virtual replica stores the estimated parameters, and uses these to perform predictions on the behavior of the hardware PIC. The accuracy of the predictions is quantified by the **total variation distance evaluated on the test dataset (TVD_{test})** introduced in Section III.1.4. In our experimental validation on a 12-mode Clements interferometer (see Section III.4.1), the measured prediction accuracy after characterization is $TVD_{test} \approx 2.9\%$. This result, however, exceeds the estimated lower limit of $TVD_{test} \approx 0.1\%$ set by detector noise. The consistent presence of this discrepancy in all experimental characterizations conducted so far suggests the existence of an elusive physical effect that our virtual replica does not currently capture.

The control accuracy of a given PIC is contingent on both the precision of its characterization and the effectiveness of subsequent imperfection mitigation strategies. Therefore, refining the virtual replica to improve prediction accuracy down to the fundamental noise limit is crucial for ensuring the high-fidelity operation of PICs.

In this chapter, we use our virtual replica and machine-learning assisted characterization as a tool for exploring and probing physical effects in PICs that are otherwise difficult to measure. In Section IV.1, we extend the crosstalk model of Section III.2.1 to take into account crosstalk effects on bare waveguide sections and cover the mitigation of this physical mechanism. We reported our results in [7] (in preparation, included in App. E). Section IV.2 investigates the presence of detector nonlinearities, beamsplitter reflectivity variations due to crosstalk and internal losses.

Contents

IV.1 - Induced phase shifters

A **controlled PS** is a PS corresponding to a dedicated on-chip component implementing a phase shift on light traveling in its associated waveguide following the application of a voltage. We call **restricted crosstalk model** a model that describes crosstalk as an influence between controlled PSs. In Chapter III, the virtual replicas used for characterization were all equipped with restricted crosstalk models. Similar approaches are followed in [22, 231, 130, 123, 135].

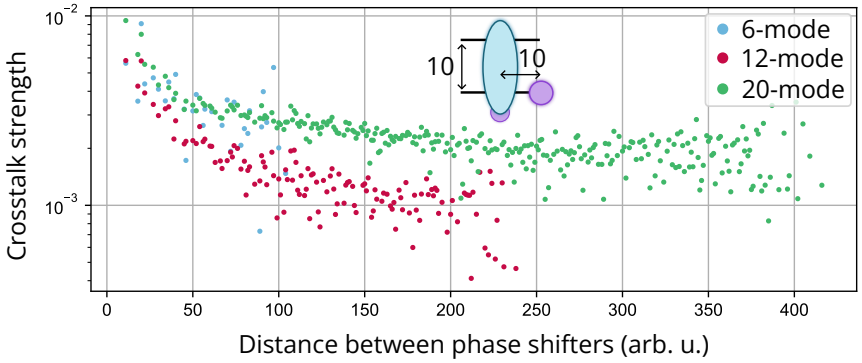

Figure IV.2: Crosstalk as a function of distance between components. Estimated crosstalk strength (off-diagonal coefficient magnitude / average diagonal value) as a function of distance between phase shifters. Crosstalk strength is computed from the experimentally acquired matrices on a 6-mode (see Section III.4.2), 12-mode (see Section III.4.1) and 20-mode (see Section III.4.3) Clements interferometers. The distance is estimated from a 2D layout of the PIC with arbitrary units displayed above the plot: 10 units of distance between two waveguides and 10 units of separation between MZIs (blue ellipse) and PSs (purple disk).

The experimentally estimated crosstalk matrices displayed in Fig. III.26, Fig. III.27 and Fig. III.28 all exhibit long-range crosstalk defying physical intuition (see Fig. IV.2). Intuitively, crosstalk should be a localized effect. This questions the validity of physical parameters estimated by the virtual replica and hints towards a missing ingredient in our description of crosstalk.

Indeed, in addition to locality, physical intuition dictates that we should also expect crosstalk to affect any waveguide section, not only those featuring a controlled PS. In other words, crosstalk should shift the phase of light traveling in any waveguide subject to heating. To account for this effect, we introduce an additional category of PSs: the **induced PS** component. The phase shift implemented by an induced PSs is not controlled by voltage, but is caused by crosstalk.

In Section IV.1.1, we build induced PSs into the crosstalk model of the virtual replica, yielding the **extended crosstalk model**. The virtual replica equipped with an extended crosstalk model is evaluated in simulations in Section IV.1.2 for characterization. Section IV.1.3 discusses the mitigation of crosstalk in the extended model and Section IV.1.4 gives a graphical criterion for certifying the resilience to crosstalk of a given PIC. In Section IV.1.5, we demonstrate that the extended crosstalk model enables the capture of a more realistic picture of crosstalk in experimental PICs.

IV.1.1 - Crosstalk model extension

Let n_{CPS} be the **number of controlled PSs** on a given PIC. In the restricted crosstalk model introduced in Section III.2.1, the phases $\vec{\phi}^{(\text{res})}$ implemented by the controlled PSs are related to the n_{CPS} applied voltages $\vec{V}$ via the **restricted phase-voltage relation**

$$\vec{\phi}^{(\text{res})} = \sum_{k\neq 0} C_k^{(\text{res})} \cdot \vec{V}^{\odot k} + \vec{c}_0^{(\text{res})} \tag{IV.1}$$

where $C_k^{(\text{res})}$ are the **restricted crosstalk matrices** of size $n_{\text{CPS}} \times n_{\text{CPS}}$, $^{\odot k}$ is element-wise exponentiation and $\vec{c}_0^{(\text{res})}$ is the **restricted passive phases vector**.

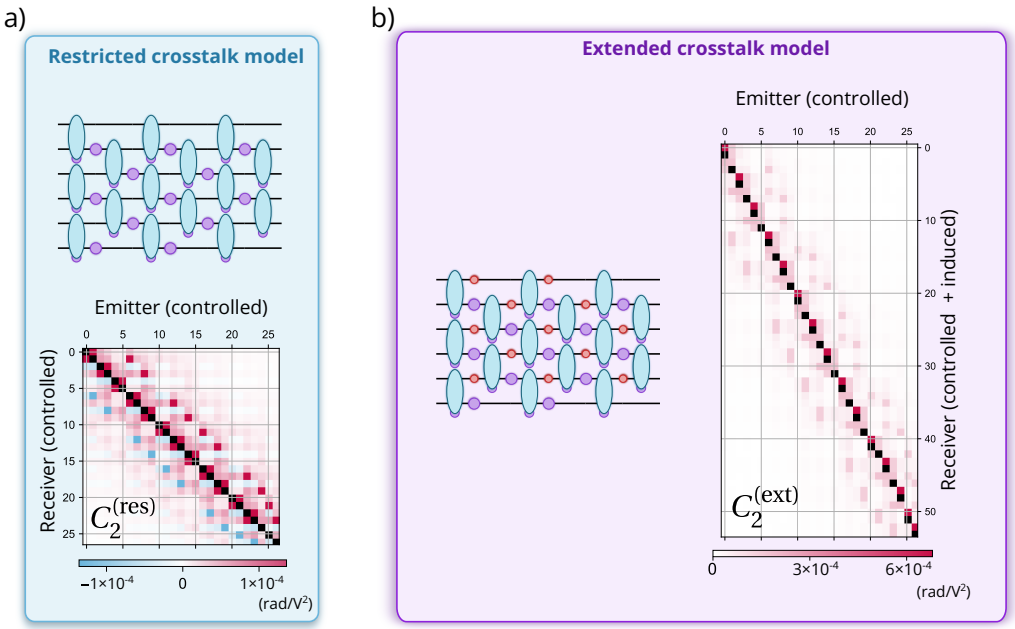

Figure IV.3: Transition from restricted to extended crosstalk model. Circuit layout and crosstalk matrix for **a)** restricted and **b)** extended crosstalk models. The circuit shown here is a 6-mode Clements interferometer. Blue ellipses: Mach-Zehnder interferometers. Purple disks: external PSs. Red disks: induced PSs. Matrices are generated in simulation, with distances computed as in Fig. IV.2.

We now transition to the extended crosstalk model. Induced PSs are represented by dedicated components in the PIC. An induced PS is placed on every waveguide section that does not feature a controlled PS. After the procedure, every PIC waveguide either has an induced or a controlled PS (see Fig. IV.3). The **total number of PSs** (controlled + induced) is denoted n_{PS}. The number of voltages applied to the PIC remains n_{CPS}, but the number of implemented phase shifts grows from n_{CPS} to n_{PS}. The **extended phase vector** $\vec{\phi}^{(\mathrm{ext})}$ has n_{PS} components, consisting of the controlled and induced phase shifts. The **extended phase-voltage relation** relates the extended phase vector $\vec{\phi}^{(\mathrm{ext})}$ to the applied voltages $\vec{V}$:

$$\vec{\phi}^{(\mathrm{ext})} = \sum_{k\neq 0} C_k^{(\mathrm{ext})} \cdot \vec{V}^{\odot k} + \vec{c}_0^{(\mathrm{ext})} \tag{IV.2}$$

where $C_k^{(\mathrm{ext})}$ are the **extended crosstalk matrices** of size $n_{\mathrm{PS}} \times n_{\mathrm{CPS}}$ and $\vec{c}_0^{(\mathrm{ext})}$ is the **extended passive phases vector** with n_{PS} components. Notice than extended crosstalk matrices have more rows than columns, as shown on Fig. IV.3. Similarly to Chapter III, we will restrict for clarity our study to phase-voltage relations Eq. IV.1 and Eq. IV.2 containing only the passive phases vector and a V^2 ($k = 2$) contribution.

In the following section, we adapt the virtual replica of Section III.2.1 to the extended model and evaluate the machine learning-assisted characterization in simulations.

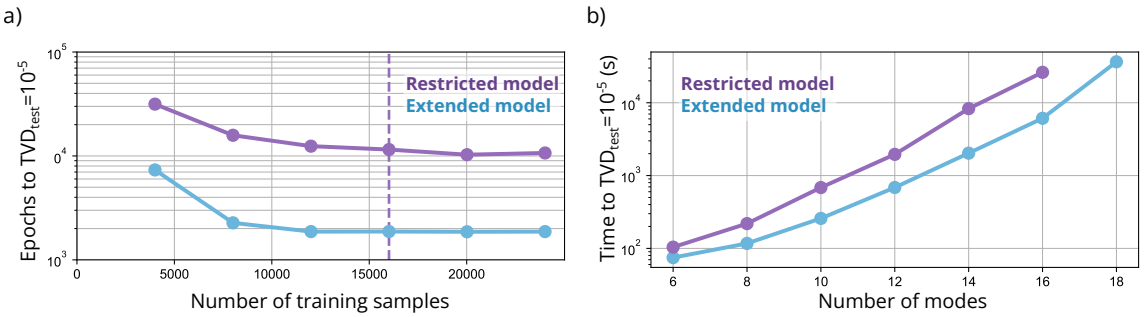

Figure IV.4: Sample efficiency assessment and characterization duration for restricted and extended virtual replicas. Adapted from [7] (in preparation, included in App. E). **a)** Number of epochs to reach a prediction accuracy $\text{TVD}_{\text{test}} = 10^{-5}$ as a function of the number of training samples for the restricted and extended virtual replicas. The purple dashed line indicates the number of training samples corresponding to a data-to-parameter ratio of 1 for the restricted model. The simulation is performed for a 12-mode Clements interferometer. **b)** Training duration to reach a prediction accuracy $\text{TVD}_{\text{test}} = 10^{-5}$ as a function of the number of modes of the Clements interferometer, for restricted and extended virtual replicas.

IV.1.2 - Characterization of induced phase shifters

The virtual replica of Chapter III used for characterizing PIC with machine learning is equipped with a restricted crosstalk model, i.e. the model features a square crosstalk matrix $\hat{C}_2^{(\text{res})}$ (**hats on quantities indicate parameters estimated by a virtual replica**). The virtual replica is here promoted to an extended crosstalk model, replacing the square crosstalk matrix by a rectangular $\hat{C}_2^{(\text{ext})}$ of size $n_{\text{PS}} \times n_{\text{CPS}}$. We denote **restricted (resp. extended) virtual replica** a virtual replica equipped with a restricted (resp. extended) crosstalk model.

We compare the behavior of the restricted and extended virtual replica during the training process in simulations. The virtual replicas are instructed to update their respective crosstalk matrix to characterize an idealized PIC. The idealized PIC does not have passive phases, beamsplitter reflectivity errors nor output losses, only crosstalk with induced PSs as an imperfection. The virtual replicas are trained by gradient descent, as in the ML stages (see Section III.2.3) of the characterization process of Chapter III.

Fig. IV.4a shows that the number of training samples required to train the restricted and extended virtual replicas is the same. We also observe that the extended virtual replica is trained in a significantly shorter number of epochs. The duration of an epoch for the extended virtual replica is longer than for the restricted one, because the number of partial derivatives to compute is greater. Fig. IV.4b confirms however that the extended virtual replica is trained in a substantially shorter amount of time compared to the restricted one.

Fig. IV.5a displays the evolution of the prediction accuracy of the virtual replica as training progresses when characterizing a 12-mode Clements interferometer. Both virtual replicas converge to a similar TVD_{test} value and manage to accurately replicate the behavior of the simulated PIC after training. The restricted virtual replica is however not able to converge with arbitrary MZI meshes, as can be observed in Fig. IV.5b. We explain in Section IV.1.4 that the restricted model can only converge if the circuit is robust to crosstalk. Consequently, the extended virtual replica can retrieve the extended crosstalk matrix $C_2^{(\text{ext})}$ of a larger class of interferometers featuring induced PSs.

After the training process, as in Chapter III, the physical parameters estimated by the virtual replica are harnessed to perform imperfection mitigation (see Section III.3). The next section covers crosstalk cancellation in the extended paradigm.

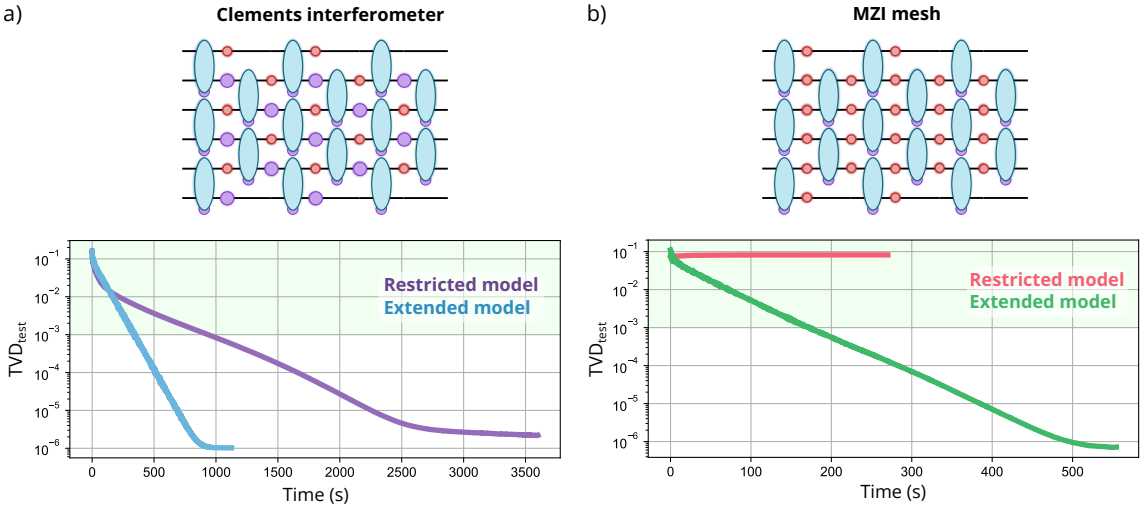

Figure IV.5: Convergence comparison between restricted and extended virtual replicas. Adapted from [7] (in preparation, included in App. E). Prediction accuracy $\mathrm{TVD}_{\mathrm{test}}$ as a function of training time for restricted and extended virtual replicas. The characterization is performed with a 12-mode Clements interferometer for **a)** and on a 12-mode MZI mesh for **b)**. 6-mode versions of the circuits are displayed on top of the plots. Blue ellipses: MZIs. Purple disks: external PSs. Red disks: induced PSs. The MZI mesh is obtained by replacing the external PSs of a Clements interferometer by induced PSs.

IV.1.3 - Mitigation of induced phase shifters

In this section, we modify the imperfection mitigation of Section III.3 to handle extended crosstalk matrices $\hat{C}_2^{(\mathrm{ext})}$. As for Section III.3, we assume that the estimated parameters by the virtual replica match the actual values, i.e. $\hat{C}_2^{(\mathrm{ext})} = C_2^{(\mathrm{ext})}$.

Extended crosstalk matrices $C_2^{(\mathrm{ext})}$ describing crosstalk with induced PSs are rectangular (see Fig. IV.3), thus the algebraic inverse is not defined. In other words, the phase-voltage relation is an underdetermined system of equations. Our phase-voltage equation solver (see App. D.4) relies however on the inverse of the crosstalk matrix to mitigate crosstalk. The **Moore-Penrose pseudo-inverse** can be used instead, with a considerable caveat. The Moore-Penrose pseudo-inverse returns the least-squares approximate solution of a system of equations. Consequently, the returned voltage solution is inaccurate. With realistic crosstalk parameters for a 12-mode Clements interferometer, we estimate in that the average amplitude fidelity with respect to target unitary matrices decreases to 97.7 % because of the approximate matrix inversion. For square crosstalk matrices, we achieve 100 % amplitude fidelity.

As a result, cancelling induced PS crosstalk requires a more sophisticated procedure. The intuition behind our extended crosstalk mitigation lies in the fact that induced PSs can be propagated in the circuit by modifying adjacent phase shifts, following the ϕ-remove rule displayed in Fig. IV.6. The ϕ-remove rule is also used in [38, 70, 232, 233]. By repeated application of the ϕ-remove rule, an induced PS can be entirely moved out of the circuit, as shown in Fig. IV.7.

We mathematically prove in [7] (in preparation, included in App. E) that the procedure for removing induced PSs from the circuit can be imprinted onto the crosstalk matrix. For each removed induced PS, it is sufficient to apply a specific linear transformation on the crosstalk matrix and delete one of its rows. The procedure is illustrated on Fig. IV.8.

We assume in the following that all the input and output ports of the PIC are **phase-invariant**, i.e. the measurable outcomes (light intensity, photon countrates and coincidences...) are not affected by phase shifts before and after the entire circuit. For instance, a PIC connected to single-photon detectors has phase-invariant output ports, because single-photon detectors are not sensitive to phase. Similarly, a PIC operated with single-photon Fock states (such as in [3, 4, 5] has

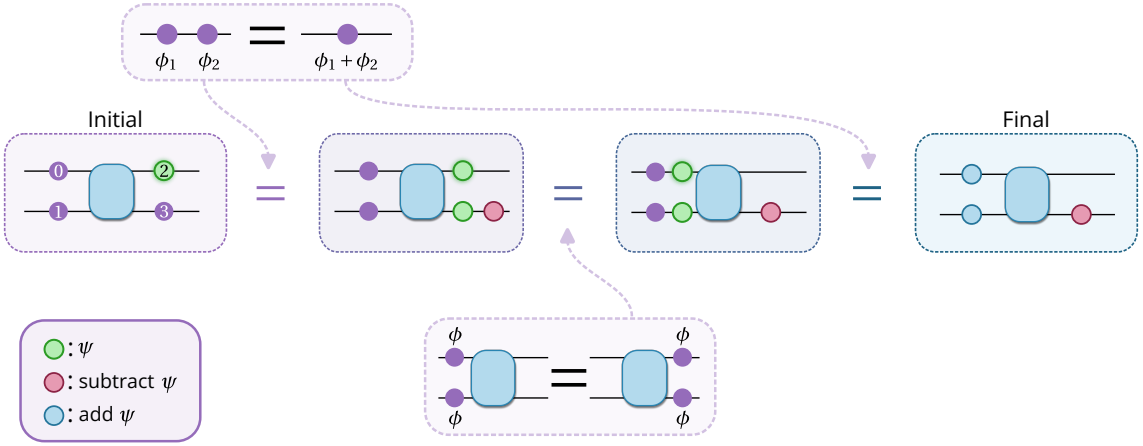

Figure IV.6: Derivation of the ϕ-remove rule. The ϕ-remove rule states that the depicted initial and final linear photonic circuits are equivalent. Disks represent PSs. Blue rectangles represents any linear on-chip component on two modes such as a beamsplitter or an MZI. Equality between two circuits means that both implement the same unitary matrix. The green disk represents a phase shift to remove from the initial state, by subtracting or adding the phase shift from or to adjacent phase shifts in the final state.

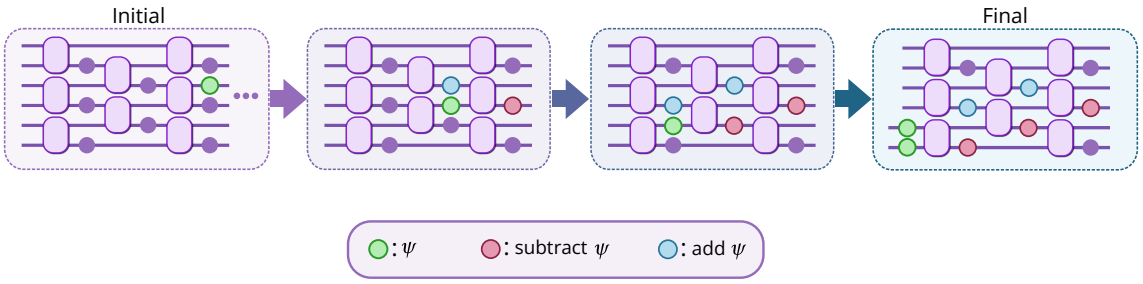

Figure IV.7: Removing an induced PS from a circuit using circuit rewriting. In the initial circuit, the green disk is an induced PS with a phase ψ in a 6-mode Clements interferometer. Purple rectangles are MZIs. Purple disks are controlled PSs. The three dots on the right indicate that the circuit has been truncated for readability. The induced phase shift is moved across the circuit by repeatedly applying the rule ϕ-remove from Fig. IV.6. The rule ϕ-remove is applied to cross an MZI. In the intermediate and final circuits, blue (resp. red) disks represent PSs whose phase has been increased (resp. decreased) by ψ.

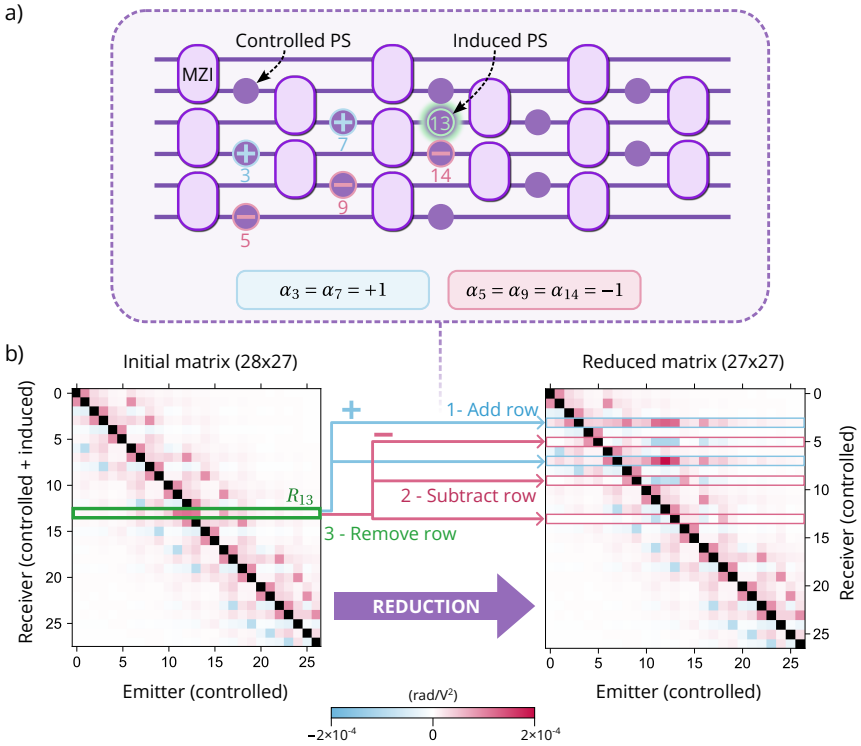

Figure IV.8: Matrix reduction by removing induced PSs. We consider a 6-mode Clements interferometer featuring a single induced PS. The circuit features $n_{\mathrm{PS}} = 28$ PSs, among which $n_{\mathrm{CPS}} = 27$ are controlled. **a)** Schematic of the circuit. The purple squares represent Mach-Zehnder interferometers (MZIs, each featuring one controlled PS), and the purple disks depict controlled PSs. The induced PS (green disk) indexed as PS 13 implements a phase shift ϕ_{13}. PSs 3, 5, 7, 9 and 14 are modified following $\phi_i \to \phi_i + \alpha_i \phi_{13}$, as derived from Fig. IV.7. **b)** Illustration of the matrix reduction process. The initial matrix is generated from the circuit layout, as in Fig. IV.3. We select the 13-th row (green frame), denoted R_{13} of the initial rectangular crosstalk matrix of size $n_{\mathrm{PS}} \times n_{\mathrm{CPS}}$. The dominant diagonal coefficients with approximate value $0.034\,\mathrm{rad/V^2}$ are masked for readability. According to the coefficients α_i, R_{13} is added ($\alpha_i = 1$, blue frames) to or subtracted ($\alpha_i = -1$, red frames) from the rows of the initial matrix. The process yields a square reduced matrix of size $n_{\mathrm{CPS}} \times n_{\mathrm{CPS}}$ after deletion of R_{13}.

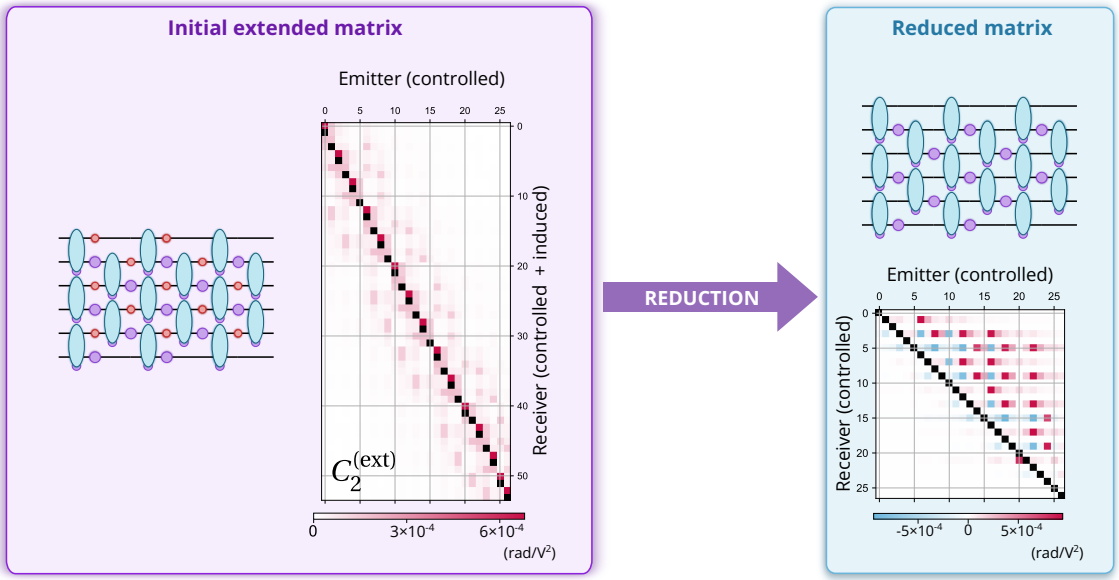

Figure IV.9: Full matrix reduction. The initial extended matrix of a 6-mode Clements interferometer is transformed into a square matrix using our reduction procedure.

phase-invariant inputs.

Certain interferometers allow all induced PSs to be removed from the circuit. Consequently, the fully reduced matrix is square and observed to be invertible. This is the case for Clements interferometers (see Fig.IV.9). Notice that the reduction process introduces long-range crosstalk between controlled PSs to account for the removal of induced PSs. Because the reduced matrix is invertible, the phase-voltage equations solver recovers a perfect control accuracy over the PIC (see upper half of Fig. IV.10).

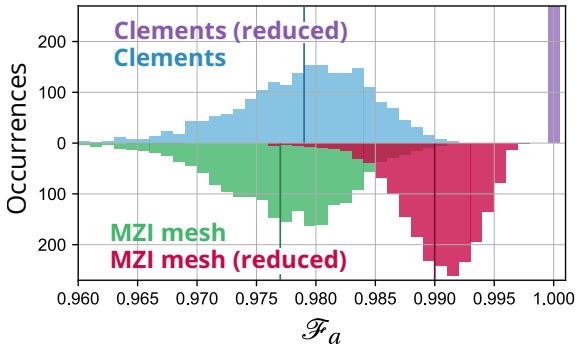

Figure IV.10: Reduction improves control accuracy Histogram of amplitude fidelities between targeted and implemented matrices. Simulations performed on 12-mode circuits.

On the other had, some interferometer meshes do not allow every induced PS from being propagated out of the circuit, due to the gradual removal of induced PSs during the reduction process. Then, the extended matrix cannot be fully reduced to a square matrix. Consequently, the control accuracy is improved after matrix reduction but optimal control is not recovered. This is illustrated in the lower half of Fig. IV.10 with the MZI mesh of Fig.IV.5.

We say that a PIC is **crosstalk-robust** when its extended crosstalk matrix can be reduced to a square matrix. On the contrary, a non-crosstalk-robust interferometer, whose matrix cannot be fully reduced to square, is fundamentally flawed and vulnerable to crosstalk. The design of crosstalk-resilient interferometers is crucial for providing reliable and accurate experimental platforms. In the next section, we introduce a graphical criterion for straightforwardly certifying the resilience of a PIC to crosstalk.

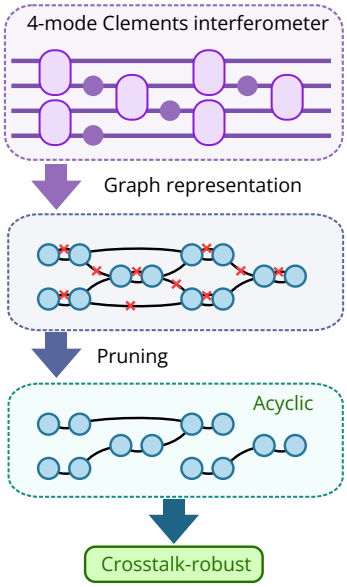

Figure IV.11: Certifying that Clements interferometers are crosstalk-robust.

IV.1.4 - Criterion for crosstalk robustness

The PIC is converted into a mathematical graph called **circuit graph** to analyze its structure. Every node in the graph is associated to a beamsplitter in the circuit, and the edges represent the waveguides interconnecting the components. A similar approach is followed in Section III.2.2 to algorithmically generate the interference fringe measurement protocol used for PIC characterization.

Every edge featuring a controlled PS in the circuit is then marked with a cross. The graph is pruned by removing every edge marked with a cross, yielding a **pruned circuit graph**. The crosstalk resilience criterion proved in [7] (in preparation, included in App. E) is then[1]:

A PIC is crosstalk-robust if and only if its pruned graph is acyclic.

A graph is **acyclic** when none of its edges form a cycle. The criterion is illustrated in Fig. IV.11. The criterion proves that known universal schemes such as the Reck [36], Clements [37] and Bell-

[1]We present here a simplified version of the criterion for clarity, valid when all PIC input and output ports arr phase-invariant. The general case is treated in [7] (in preparation, included in App. E).

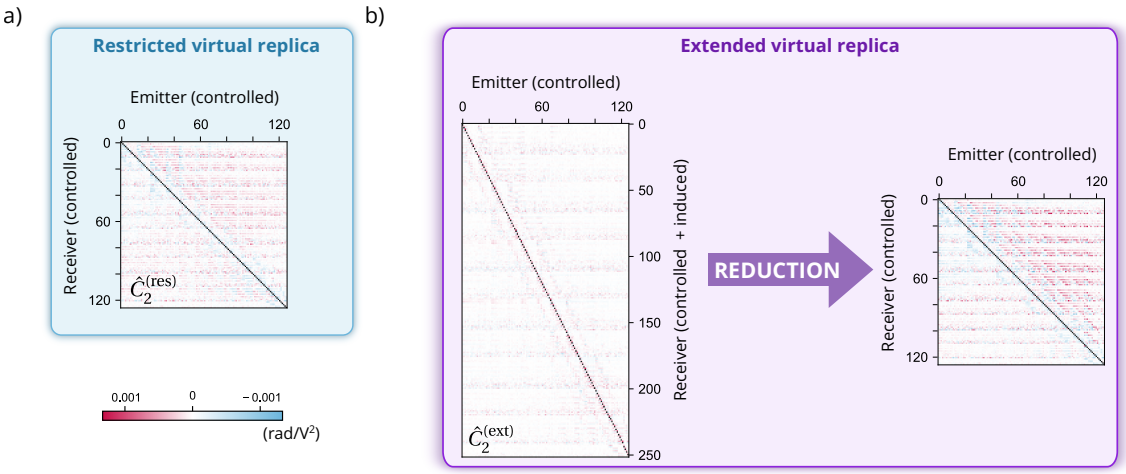

Figure IV.12: Estimated crosstalk matrices by restricted and extended virtual replicas. Dominant diagonal of average value 0.034 is masked. The estimated extended crosstalk matrix $\hat{C}_2^{(ext)}$ is reduced following our matrix reduction procedure introduced in Section IV.1.3.

Walmsley [38] schemes are crosstalk resilient. On the contrary, it is possible to show that the specialized interferometers of [110, 106, 108, 111] are not crosstalk-robust.

Robustness to crosstalk gives an explanation for our observations in Section IV.1.2 regarding the ability of the restricted virtual replica to converge or not on given interferometers. If a PIC is crosstalk-robust, then its extended crosstalk matrix reduces to a square matrix. In other words, the behavior of its crosstalk can be encapsulated into a square matrix acting on the controlled PSs. Thus, a virtual replica equipped with a restricted crosstalk model is able to converge on crosstalk-robust PICs such as Clements interferometers by directly learning a reduced crosstalk matrix. This explains the long-range crosstalk observed in Fig. IV.2. For non-crosstalk-robust interferometers, the restricted virtual replica is not able to converge (see Fig. IV.5) because a rectangular crosstalk matrix is necessary to describe the behavior of the PIC.

In the following section, we compare in an experimental setting restricted and extended virtual replicas used for PIC characterization.

IV.1.5 - Experimental validation

We characterize a 12-mode Clements interferometer (*Ascella* PIC from Sections III.4.1 and III.5) using our machine learning-assisted characterization introduced in Chapter III. After training, restricted and extended virtual replicas achieve similar prediction accuracies of $\text{TVD}_{\text{test}}^{(res)} = 7.5\,\%$ and $\text{TVD}_{\text{test}}^{(ext)} = 7.6\,\%$ respectively. This is expected from the simulations of Section IV.1.2: Clements interferometers are crosstalk-robust, thus the restricted virtual replica can converge and learn the behavior of the hardware PIC. Notice that $\text{TVD}_{\text{test}}^{(res)}$ is significantly higher than the value $\text{TVD}_{\text{test}} = 2.9\,\%$ reported in Section III.4.1, because we use here an attenuated continuous-wave laser with single-photon detectors to perform the characterization, instead of using a true single-photon source.

The estimated restricted $\hat{C}_2^{(res)}$ and extended $\hat{C}_2^{(ext)}$ crosstalk matrices are displayed in Fig. IV.12. The restricted matrix clearly exhibits the expected long-range crosstalk accounting for induced PSs, which is absent in the extended matrix. Using the crosstalk matrix reduction procedure of Section IV.1.3, the extended crosstalk matrix $\hat{C}_2^{(ext)}$ is reduced to a square matrix bearing a noticeable resemblance with the restricted matrix $\hat{C}_2^{(res)}$.

Interestingly, the extended matrix $\hat{C}_2^{(ext)}$ is substantially sparser than the restricted matrix $\hat{C}_2^{(res)}$. This can be seen in Fig. IV.13a, where the noise floor of the average off-diagonal magnitude is significantly lower in the extended matrix $\hat{C}_2^{(ext)}$ compared to the restricted matrix $\hat{C}_2^{(res)}$.

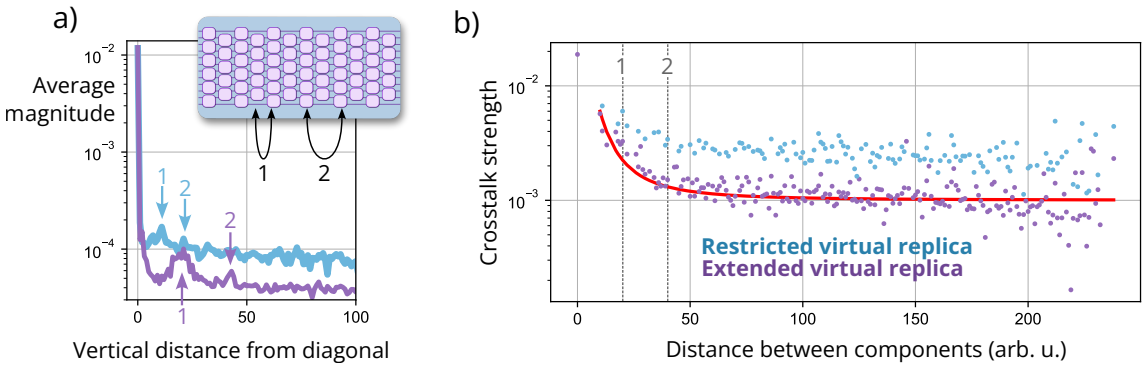

Figure IV.13: The extended virtual replica captures a more realistic picture of crosstalk. **a)** Average magnitude of crosstalk matrix elements as a function of vertical distance from diagonal. Arrows labeled "1" and "2" indicate distances from the diagonal corresponding to unit cell column jumps as indicated in the inset. **b)** Crosstalk strength (off-diagonal coefficients / average diagonal coefficient) as a function of distance between components. The distance is estimated from a 2D layout of the circuit as in Fig. IV.2. The red continuous curve shows the crosstalk-versus-distance function used for the simulations (dependence in $1/d^2$ with d the distance), with an additional offset of 1e-3 for clarity due to the log scale. Zero distance is by convention the distance between the two internal PSs of an MZI. The vertical gray lines labeled "1" and "2" indicate the distance between consecutive unit cell columns (see inset of a)).

As a consequence, it is possible to isolate crosstalk between columns (see Fig. IV.13a). In addition, the retrieved crosstalk-versus-distance behavior is more localized, reflecting the fact that the extended virtual replica is able to capture a more realistic picture of crosstalk (see Fig. IV.13b).

The resulting control accuracy of the PIC is similar when using the restricted and extended virtual replicas. The average amplitude fidelity between targeted and implemented unitary matrices is $\mathcal{F}_a^{(\text{res})}$=98.7 % and $\mathcal{F}_a^{(\text{res})}$=98.6 % respectively. The fact that $\mathcal{F}_a^{(\text{res})} \approx \mathcal{F}_a^{(\text{ext})}$ is a consequence of the similar prediction accuracies achieved by the restricted and extended virtual replicas ($\text{TVD}_{\text{test}}^{(\text{res})} \approx \text{TVD}_{\text{test}}^{(\text{ext})}$) and the empirical relation $\mathcal{F}_a \approx 1 - \text{TVD}_{\text{test}}^2$.

To summarize, using extended virtual replicas to characterize PICS enables shorter machine learning stage durations and the recovery of a more realistic crosstalk matrix.

In this section, we have improved the virtual replica used for the machine learning-assisted characterization of PICs based on the observation of long-range crosstalk in the estimated crosstalk matrix. Taking into account induced PSs in the physical model of the virtual replica did however not improve the prediction accuracy over the virtual replica of Chapter III. In the next section, we investigate other physical effects that can be taken into account into our physical model.

IV.2 - Additional PIC imperfections considered

The physical model of the virtual replica of Chapter III accounts for crosstalk between controlled PSs, beamsplitter reflectivity errors and optical losses on the output ports. In Section IV.1, we have improved the physical model by introducing the concept of induced PS.

In Section IV.2.1, we investigate the relevance of taking detector nonlinearity into account in the physical model. We then examine the case of beamsplitter crosstalk in Section IV.2.2 and internal losses in Section IV.2.3. The physical model improvements are then tested experimentally in Section IV.2.4.

IV.2.1 - Detector nonlinearity

So far, we have assumed that the light intensity detectors used to characterize the PIC are linear, i.e. each detector reading is related to the impinging light intensity by a proportionality coef-

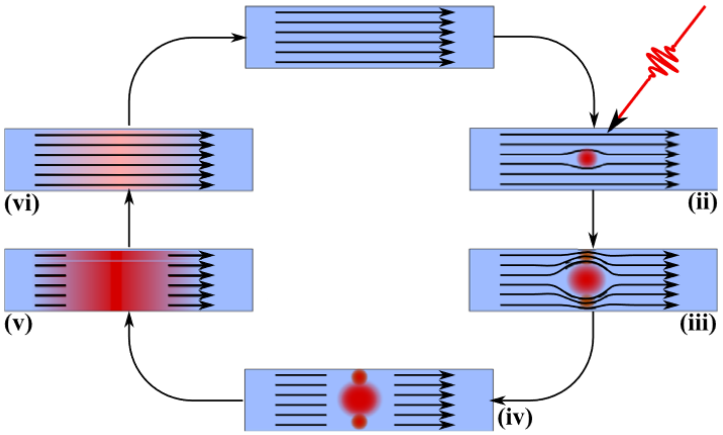

Figure IV.14: From [234]. **Principle of superconducting nanowire single-photon detection (SNSPD) operation. i)** The main component of an SNSPDs is a nanowire cooled down below its superconducting critical temperature. A bias current is applied on the wire. The current experiences no resistance due to superconductivity. **ii)** A photon is absorbed by the nanowire. The energy carried by the photon causes the creation of a so-called **hotspot** on the nanowire, a region of non-superconducting metal. **iii)** The hotspot of nonzero ohmic resistance deflects the bias current around it. **iv)** The current density of the regions around the hotspot exceed the superconducting critical current. Consequently, the entire nanowire section acquires an ohmic resistance. **v)** An electric circuit detects the rise in resistance of the nanowire and sets the bias current to zero. **vi)** The hotspot is resorbed by the ambient cooling and the nanowire returns to its nominal superconducting state.

ficient η called **detector efficiency**. The detector efficiencies are taken into account by the virtual replica as contributing to output port losses. In reality, single-photon detectors and powermeters exhibit a nonlinear behavior. We focus in this section on the case of single-photon detectors. The detector characteristics of interest in this section are [27]:

- the detector efficiency,
- the **dark count rate**, a constant rate of detector clicks, present even when the incoming rate of photons is zero,
- and the **deadtime**, the minimal duration between two successive photon detections that can be performed by the detector.

In particular, we will cover **superconducting nanowire single-photon detectors (SNSPDs)**, which constitute our lab equipment. SNSPDs are state of the art photon detection systems based on the principle displayed in Fig. IV.14. Compared to previous single-photon detector models such as avalanche photodiodes [235], commercially available SNSPDs have low dark count rates ($\approx$ 10 Hz), short dead times ($\approx$ 20 ns) and high detection efficiencies (>90 %).

We are interested in the nonlinear response function of SNSPDs. Many efforts in the litterature are devoted to understanding the underlying physical mechanisms allowing SNSPDs to detect photons [234, 236, 237]. It would be possible to harness these works to derive response functions.

The essence of our approach however in Chapter III is to construct physical models following a top-bottom logic. We choose to describe the nonlinearity of SNSPDs as an offset due to dark counts and a saturation effect caused by the deadtime. Consequently, the most general detector response function is

$$f(x) = \sum_{k\in\mathbb{N}} \eta_k x^k, \tag{IV.3}$$

where x is the input photon countrate, $f(x)$ is the measured countrate and the η_k are real coefficients. We argue that keeping the $k = 0, 1, 2$ terms is sufficient in our case with two simple models,

considering the following assumptions:

- dark counts do not affect the detection of signal photons. This assumption is realistic as the dark count rate is weak (≈ 100 Hz) and uncorrelated to the signal photons.
- The detectors recover their baseline detection efficiency immediately after the deadtime. In other words, we set the detector recovery time to zero [27].
- Each absorbed photon by the detector resets the deadtime. This behavior is expected for SNSPDs for reasonable countrates, as each photon detection occurs at a different location on the nanowire.

We investigate two models, one for pulsed single-photon sources (Section IV.2.1.A) and a second one more adapted to continuous sources of light such as attenuated continuous-wave lasers (Section IV.2.1.B). Both models are relevant in our case, as our machine learning-assisted characterization is usually carried out either with pulsed single-photon sources or attenuated continuous-wave laser light.

IV.2.1.A - Model 1: pulsed single-photon sources

In this model, we consider a single-photon source emitting photons at a fixed repetition rate R. A time window t_{sim} is subdivided into temporal sites spaced by a duration $1/R$. Before arriving on the detector, each site is occupied by a photon with a probability x/R, where x is the true countrate impinging on the detector. Due to the detector efficiency η, the probability that a temporal site is occupied with a photon detection is

$$p_{\text{occ}} = \frac{\eta x}{R}. \tag{IV.4}$$

Thus, without deadtime, the ideal number of detections N_0 during the time window is the site occupation probability multiplied by the number of sites:

$$N_0 = p_{\text{occ}} \times (R t_{\text{sim}}) = \eta x t_{\text{sim}} \tag{IV.5}$$

We now introduce deadtime effects. Assume that the detector deadtime spans over k successive photon emissions, and that each photon reaching the detector resets the deadtime. A photon detection is valid when the k preceding sites are empty. The probability of this event is $(1-p_{\text{occ}})^k$. The number of detections N_k with a deadtime spanning k sites is the ideal number of detections N_0 that also have k empty preceding sites:

$$N_k = N_0 \times (1-p_{\text{occ}})^k = \eta x t_{\text{sim}} \left(1 - \frac{\eta x}{R}\right)^k. \tag{IV.6}$$

This yields a detector response function

$$f_k(x) = \text{dc} + \eta x \left(1 - \frac{\eta x}{R}\right)^k \tag{IV.7}$$

where dc is the dark count rate.

In the case $k = 1$ corresponding to our experimental specifications (deadtime of ≈ 20 ns, separation between single-photon of 12.5 ns), the expected detector response function is

$$f(x) = \text{dc} + \eta x(1 - \eta x) \tag{IV.8}$$

$$= \text{dc} + \eta x - \frac{(\eta x)^2}{R}, \tag{IV.9}$$

which is exactly of the form Eq. IV.3.

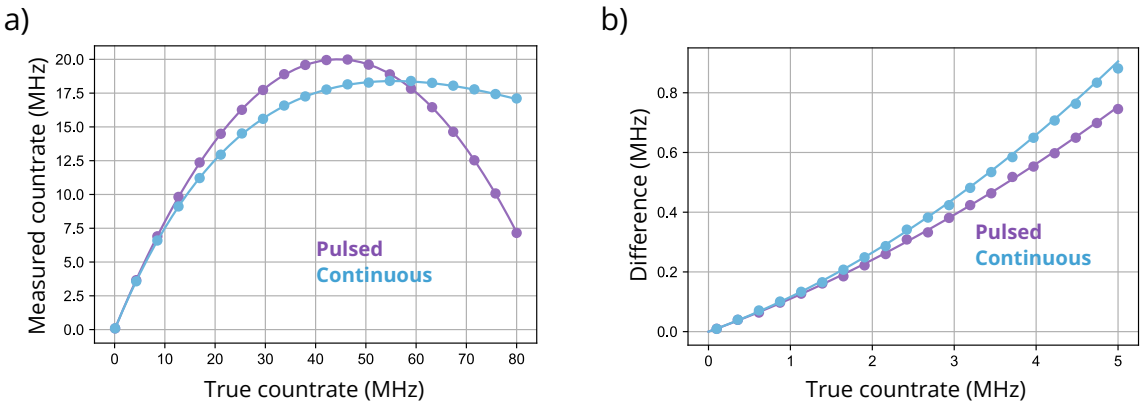

Figure IV.15: Comparison between pulsed and continuous detector models. Simulation parameters: detector efficiency $\eta = 0.9$, pulse rate R =80 MHz, deadtime τ=20 ns. **a)** Measured countrate as a function of true countrate. Dots are simulated values. Continuous lines are computed using the full expression of the respective model (Eq. IV.8 and IV.13). **b)** Difference between true and measured countrate as a function of true countrate. Dots are simulated values. Continuous lines are computed from the detector responses expanded to second order (Eq. IV.8 and IV.14).

IV.2.1.B - Model 2: continuous single-photon source (e.g. attenuated laser)

Consider a continuous source of single-photons emitting photons at a fixed rate x with random independent times of emission. The derivation of the response function follows the same approach as the previous model. Choose a time window t_{sim}. Without deadtime, the ideal number of detected photons is

$$N_0 = \eta x t_{\text{sim}} \tag{IV.10}$$

with η the detector efficiency.

We now assume that the detector has a deadtime τ. We compute the probability $p_\varnothing$ of having zero detected photons during a time interval τ. Because the photon emissions are independent, the number of photons detected during a given time interval follows a Poisson law (see Section III.2.5). Thus,

$$p_\varnothing = e^{-\tau\eta x}. \tag{IV.11}$$

The number of valid detections N_τ is the ideal number of detected photons multiplied by the probability of not being affected by deadtime:

$$N_\tau = N_0 p_\varnothing = \eta x t_{\text{sim}} e^{-\tau\eta x}. \tag{IV.12}$$

The corresponding detector response function is

$$f(x) = \eta x e^{-\tau\eta x}, \tag{IV.13}$$

which was also derived in [238]. Experimentally, $\eta \approx 0.9$, $\tau \approx 20\,\text{ns}$ and $x \approx 100\,\text{kHz}$, resulting in $\eta\tau x \approx 1.8 \times 10^{-3}$. We can thus Taylor expand the detector response:

$$f(x) = \text{dc} + \eta x - \eta^2 \tau x^2, \tag{IV.14}$$

The approximated response function is of the form Eq. IV.3.

The detector response models are validated in simulations in Fig. IV.15. From the results of the two models, we build detector nonlinearity into the virtual replica as a response function of the form

$$f(x) = \eta_0 + \eta_1 x + \eta_2 x^2 \tag{IV.15}$$

where the η_i are free parameters left to optimize. Each detector has its own set of parameters.

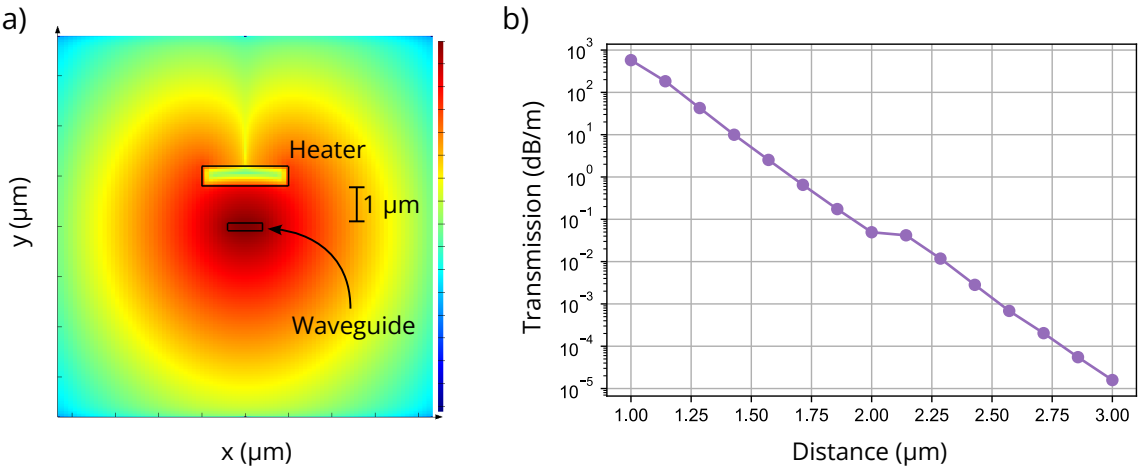

Figure IV.16: Estimation of optical losses due to PS heaters. a) Simulation of the electromagnetic field in a transverse section of the waveguide. The heater used to induce phase shifts on the light traveling in the waveguide disturbs the optical mode. log scale. intensity of E field **b)** Optical transmission of PS as a function of distance between heater and waveguide.

IV.2.2 - Beamsplitter crosstalk

Let n_{BS} be the number of beamsplitters in a given PIC and n_{CPS} the number of controlled PSs. **Beamsplitter crosstalk** designates the change of beamsplitter reflectivities due to the actuation of neighboring controlled PSs. Indeed the emitted heat raises the temperature of the directional coupler implementing the beamsplitter, affecting the refractive index of the waveguides and substrate. Beamsplitter crosstalk is nontrivial to predict physically, as the reflectivity variation depends on the geometry of the temperature gradient across the directional coupler. Beamsplitter crosstalk is harnessed on purpose in [101] to create tunable integrated beamsplitters. Beamsplitter crosstalk has to our knowledge however neither been simulated nor experimentally investigated on our PIC fabrication platforms.

We consider a simplified model in which the reflectivity $\vec{R}$ of the beamsplitters is related to the applied voltages $\vec{V}$ via the relation

$$\vec{R} = D_2 \cdot \vec{V}^{\odot 2} + \vec{r}_0 \tag{IV.16}$$

where D_2 is an arbitrary matrix of size $n_{BS} \times n_{CPS}$, $^{\odot 2}$ is element-wise squaring and $\vec{r}_0$ contains the beamsplitter reflectivities at rest.

IV.2.3 - Internal losses

A third effect we wish to investigate is the presence of internal losses in the PIC. Sources of internal losses may be absorption losses or waveguide bending losses [239]. These contribute however to homogeneous losses in the PIC, i.e. every path of light in the PIC has the same optical transmission.

We are interested in losses created by the presence of PSs in the PIC. The metallic heater element located in close proximity of the waveguide disturbs the optical mode propagating in the waveguide, causing stronger light absorption in the vicinity of PS heaters (see Fig. IV.16). Consequently, the optical transmission of light depends strongly on the traveled path. The distance between heaters and waveguides is a compromise between optical loss and efficiency of the PSs.

We adapt the model to take into account lossy PSs. A PS implementing a phase ϕ with trans-

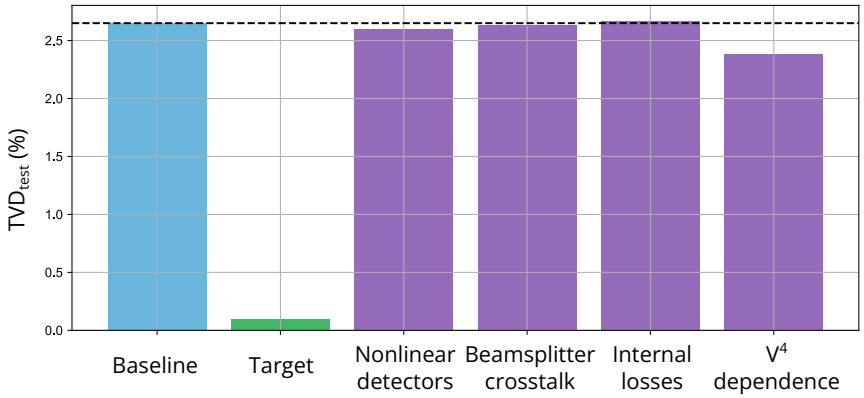

Figure IV.17: Probing PIC and circuit imperfections using our machine learning-assisted characterization Virtual replica prediction accuracy TVD_{test} as a function of included imperfections in the physical model. Baseline: virtual replica from Chapter III accounting for PS crosstalk, beamsplitter reflectivities and output port losses. Target: theoretical limit estimated from detector counting noise (see Section III.2.5). Each bar represents an experiment in which the virtual replica is equipped with the designated additional imperfection model.

mission $\lambda \in [0, 1]$ applies the diagonal non-unitary matrix

$$\begin{bmatrix} 1 & & & & & & \\ & \ddots & & & & & \\ & & 1 & & & & \\ & & & \lambda e^{i\phi} & & & \\ & & & & 1 & & \\ & & & & & \ddots & \\ & & & & & & 1 \end{bmatrix} \tag{IV.17}$$

on the state of light. This model for internal losses is valid because the data samples used to train the virtual replica are acquired by injecting light into a single input at a time.

In the next section, we implement detector nonlinearities, beamsplitter crosstalk and PS losses into the virtual replica used for characterization. We then assess improvements in the prediction accuracy of the virtual replica.

IV.2.4 - Experimental investigation

We probe for detector nonlinearities, beamsplitter crosstalk and internal losses using a hardware 12-mode interferometer (*Ascella* PIC, see Section III.5). We do not follow the full and iterative characterization protocol introduced in Section III.2. The virtual replica is here trained in an "offline" manner by gradient descent using the training and test datasets from Section III.4.1. The virtual replica is initialized before the gradient descent with the self-heating coefficients and passive phases of the trained virtual replica of Section III.4.1.

Fig. IV.17 summarizes our results. Neither detector nonlinearities, beamsplitter crosstalk nor internal losses significantly enhance the prediction accuracy of the virtual replica. This suggests that these physical effects are not preponderant sources of imperfections in current devices. For comparison, instructing the virtual replica to learn a phase-voltage relation featuring a V^2 and V^4 dependence increases the prediction accuracy by 10 %.

As a final experiment, we add all imperfections mentioned in this manuscript into a single virtual replica:

- PS crosstalk with V^2 and V^4 dependence,

- beamsplitter reflectivity errors and crosstalk,
- internal and output losses.

The full virtual replica is then trained. The prediction accuracy does not improve and worse, the virtual replica starts to noticeably overfit the training samples. Defining the overfit indicator as

$$\text{overfit indicator} = \frac{\text{TVD}_{\text{train}}}{\text{TVD}_{\text{test}}}, \tag{IV.18}$$

with $\text{TVD}_{\text{train/test}}$ the prediction accuracy on the training/test dataset, the full virtual replica has an overfit indicator of 1.8 after training. In comparison, the virtual replica of Chapter III has an overfit indicator of 1.3. Adding more degrees of freedom enables the virtual replica to better reproduce the training samples, here at the cost of generality.

The physical or numerical effect limiting the virtual replica prediction accuracy one order of magnitude above the expected value remains elusive. Improving the prediction accuracy and unraveling the current limitations is an active research subject.

IV.3 - Conclusion on noise-limited circuit control

In this chapter, we target noise-limited circuit control by improving the physical basis of our virtual replica introduced in Chapter III used for PIC characterization. This allows our machine learning also to be used as a tool for probing additional physical effects.

We successfully **explain unphysical long-range crosstalk observed** in the crosstalk matrices displayed in Chapter III with the presence of induced PSs. While controlled PSs implement phase shifts by applying a voltage on a dedicated on-chip component, induced PSs arise from crosstalk affecting also bare waveguide sections. Our extended crosstalk model featuring induced PSs thus reflects a **more realistic description of crosstalk**. We demonstrate that a machine learning model for characterization equipped with an extended crosstalk model **converges faster during the training process** and that the recovered crosstalk matrix exhibits **short-range crosstalk**. This boost generated by induced PSs in the execution time of gradient-descent based algorithms is currently being explored as an improvement for the *global optimization* algorithm used to mitigate beamsplitter reflectivity errors in Section III.3.1.

We established a framework for mitigating crosstalk in the extended model featuring induced PSs. Our framework reduces rectangular crosstalk matrices, describing crosstalk between controlled and induced PSs, into **invertible square matrices** mapping the applied voltages solely to controlled PSs. To do so, the reduction process **eliminates induced PSs from the circuit** and artificially introduces long-range crosstalk between controlled PSs. The reduced matrix is then used to solve the phase-voltage relation efficiently and with **high accuracy**, instead of relying on the pseudo-inverse of rectangular crosstalk matrices severely degrading the control accuracy of PICs.

Reducing a rectangular crosstalk matrix into a square matrix is only feasible if the considered PIC has a sufficient number of controlled PS laid out adequately in its interferometric mesh. **We give and prove a criterion certifying the resilience of a PIC to crosstalk**, that is its ability to fully cancel crosstalk. The criterion uses a mathematical graph to represent PICs and enables to rapidly test the resilience to crosstalk of a given PIC. Universal interferometers such as the Reck [36], Clements [37] and Bell-Walmsley [38] are found to be crosstalk-resilient.

Scaling up the number of modes and photons with universal PICs is challenging due to the sheer number of on-chip components. It is therefore likely that future large-scale photonic quantum computing devices will be based on specialized interferometers instead. To enforce robustness to crosstalk, it is possible to equip every waveguide of a PIC with a controlled PS at the design stage. Such an approach to PIC design would however affect negatively the footprint, control complexity, power consumption, heat dissipation capabilities and optical transmission of integrated

devices. **Our criterion comes here into play to design PICs with reduced numbers of controlled PSs**, while maintaining a sufficient number of degrees of freedom to mitigate crosstalk.

The presence of physical phenomena in PICs, such as induced PSs, could be inferred from the unphysical long-range crosstalk in estimated crosstalk matrices. Other imperfections such as detector nonlinearities, variations of the beamsplitter reflectivity with crosstalk and internal losses in the PIC do not leave apparent traces in the estimated parameters. We implement physical models for such imperfections, but **do not observe any improvement in the prediction accuracy of the virtual replica**. The physical effect limiting the virtual replica prediction accuracy in experimental validations remains elusive. Deciphering the shortcomings of our virtual replica or measurement protocols is still an active area of research.

Conclusion and emerging challenges in high-fidelity integrated photonic QI processing

In this PhD thesis, we have advanced the field of photonic integrated circuits (PICs) for quantum information (QI) processing, focusing on their **characterization, control, and applications**. As integrated photonics forms the foundation for scalable photonic quantum computing, it is crucial for achieving universal fault-tolerant quantum computers. We interface bright single-photon emitters based on *Quandela* semiconductor quantum dots, producing a stable stream of pure, indistinguishable photons, with silica and silicon nitride PICs, enabling compact and stable quantum light manipulation.

In the first part of the work, we performed QI protocols with specialized PICs, generating path-encoded postselected entangled states and manipulating them via arbitrary single-qubit gates. We carried out **randomness certification** with a 4-mode PIC featuring 4 reconfigurable phase shifters harnessing a Bell state. Our experiment constitutes the first certified randomness generation experiment on a chip, accounting for inter-agent communication by measuring the signaling fraction. Given that the presence of signaling reduces the amount of final certified random bits in the experiment, we stabilized the optical equipment and established our first PIC control scheme, using optical phase measurement to calibrate the implemented measurement bases. **This enabled us to conduct a 94-hour experiment, yielding a certified bit rate of 21 bits per second with a signaling fraction of 0.5 %, largely attributed to finite statistical noise.**

We then leveraged our knowledge in control and stabilization to generate and manipulate a 4-GHZ (Greenberger-Horne-Zeilinger) state on a second dedicated PIC. We achieved full tomography of a **high-fidelity 4-GHZ state in $\approx$ 50 hours**, faster than previous benchmarks in integrated platforms, owing to the brightness of our single-photon source and stability granted by the PIC. **The measured state fidelity of 86 % and purity of 76 % are remarkable for photonic 4-GHZ state generation**, and can be improved with a better single-photon source and more refined PIC imperfection mitigation.

Subsequently, we moved from specialized to universal-scheme PICs. Sampling-based tasks consisting of sampling output states from an implemented unitary matrix are central to near-term photonic quantum computing, making universal PICs particularly relevant for this QI era. These versatile PICs can implement any unitary matrix on photons but are notoriously complex, with numerous interconnected beamsplitters and phase shifters. Working with increasingly large-scale universal integrated architectures,required a major shift in our numerical methods to tackle PIC control. To address this, **we developed a machine learning-based characterization process which combines machine learning with physical models, that we patented**. Our process relies on a virtual replica of the physical PIC to characterize, which retrieves physical parameters, such as crosstalk, beamsplitter reflectivity errors and output losses, to replicate the behavior of the PIC. The knowledge of these parameters is difficult to access otherwise, and when combined with an imperfection mitigation, enables to compensate reflectivity errors and cancel thermal crosstalk. **We demonstrated an unprecedented 99.77 % average amplitude fidelity between target and implemented matrices on a 12-mode silicon nitride Clements interferometer, featuring 132 beamsplitters and 126 phase shifters.** Our work paves the way for high-fidelity photonic quantum computing on large-scale devices.

Intriguingly, the prediction accuracy of our virtual replica remains in experimental runs systematically one order of magnitude higher than expected from the detector noise. This hints towards at an unexplained physical phenomenon, not taken into account by the physical model of our virtual replica. This led us to **refine our phase shifter crosstalk model, accounting for the influence of crosstalk on empty waveguides**, that is not equipped with a controlled phase shifter. Virtual replicas equipped with the extended crosstalk model, using rectangular rather than square crosstalk matrices, converged more quickly and accurately captured short-range crosstalk. We established a framework for exactly cancelling crosstalk in the extended crosstalk model. **Our mitigation framework led us additionally to the discovery of a graphical criterion that certifies the robustness of a given interferometer mesh to crosstalk**. Our criterion is relevant in particular for future demonstrations of photonic QI processing, scaling beyond 30 photonic qubits, that will likely require specialized interferometers. Our criterion will be a safeguard for the design of these specialized interferometers, guaranteeing that they feature a sufficient number of degrees of freedom adequately laid out to entirely cancel crosstalk.

Despite extending the crosstalk model and incorporating additional imperfections like detector noise, beamsplitter crosstalk, and internal losses, the underlying cause of the experimental limitations affecting the prediction accuracy of the virtual replica remains unresolved. Whether large-scale photonic systems can be controlled with a noise-limited accuracy is still an open question and a focus of ongoing research.

Another challenge is the scalability of our machine learning-assisted characterization protocol. Its duration and memory usage scale approximately as m^6 for universal interferometers, where m is the number of modes. This scaling includes an m^2 factor from the interferometer size and an m^4 contribution from the crosstalk matrix. Current efforts on 24-mode universal PICs (not covered in this manuscript) are directed at improving scalability by restricting the crosstalk matrix estimated by the virtual replica to the neighborhood of its diagonal, keeping only dominant crosstalk coefficients. Efficient characterization is crucial, as each PIC typically requires several recalibrations over its lifetime of use. For instance, a calibration is required after switching to a different single-photon source, as the emission wavelength of each quantum dot is different, which in turn affects the physical parameters of the circuit such as the beamsplitter reflectivities.

Periodic calibration every few months also allow to account for the gradual degradation of phase shifters over time. This wear may be attenuated thanks to recent advancements not covered in this manuscript. Current investigations suggest that a new approach to imperfection mitigation, building on the mathematical framework developed for extended crosstalk mitigation in Chapter IV, substantially reduces PIC power consumption. The method involves using gradient descent to find a set of voltages that approximate a target unitary matrix while penalizing high-power solutions. This reduction in power dissipation is expected to extend the lifetime of on-chip phase shifters and alleviate the demands on thermal dissipation equipment.

Optimal control is key to the broader adoption of PICs across various fields, from radiofrequency signal processing to quantum sensing. Many challenges remain, but with progress in machine learning, PIC design, and fabrication, we aim at Quandela to fully understand and mitigate device imperfections, paving the way for fault-tolerant photonic architectures of the future.

A - *Unravel*: real-time source characterization

During this thesis, I developed *Unravel* (see Fig. A.1), a tool designed for the real-time characterization of pulsed single-photon sources and for the automated processing of saved data during post-processing. This graphical tool provides immediate feedback during tasks such as rotating waveplates or aligning fiber collimators, significantly reducing the time required for setup optimization. *Unravel* leverages multi-threading to maintain a responsive user interface and includes features like automated peak detection, dark count subtraction, demultiplexer pulse envelope corrections, and rapid measurement uncertainty estimations. *Unravel* has become the primary internal tool for source characterization within Quandela. The histogram correlation processing backend is used for $g^{(2)}(0)$ and V_{HOM} measurements in *Quandela*'s quantum computing hardware.

Figure A.1: V_{HOM} measurement with *Unravel*.

B - Supplementary material to Chapter II

This appendix contains details about the optical setups of Chapter II used for **certified quantum random number generation (C-QRNG)** and **4-GHZ state tomography**.

B.1 - C-QRNG optical setup

The optical setup is shown on Fig. II.6. We discuss each element of the setup:

- The **single-photon source** "Alyx" generates single-photons at $925.16\,\mathrm{nm}$ using the phonon-assisted excitation scheme. Characteristics of the source:
  - First-lens brightness: $B_{\mathrm{FL}} \approx 39 \pm 3\,\%$
  - Photon purity (with etalon): $g^{(2)}(0) \approx 2.31 \pm 0.03\,\%$
  - Photon indistinguishability: $V_{\mathrm{HOM}} \approx 93.09 \pm 0.04\,\%$
  - Mean wave-packet overlap: $M_s \approx 97.65 \pm 0.06\,\%$

  A voltage of the order of -1.5 V is applied on the quantum dot to bring the emission wavelength in line with its cavity.
- The **excitation laser** is a mode-locked femtosecond laser with a repetition rate of $79.08\,\mathrm{MHz}$, corresponding to a duration $\tau_{\mathrm{rep}} \approx 12.6\,\mathrm{ns}$ between consecutive pulses. The spectrally broad pulses are shaped using a filtering setup based on a 4f line principle, which includes a Bragg grating splitting incoming wavelengths into different directions, a slit for wavelength selection, and another grating recombining the light into a single beam, ensuring optimal narrow pumping of the source. We align the filtering setup such that it yields pulses around $924.24\,\mathrm{nm}$ with a spectral full width at half maximum of $\approx 0.1\,\mathrm{nm}$, corresponding to a pulse duration of $\approx 12\,\mathrm{ps}$.
- To increase the bitrate of the experiment, the **excitation pulse rate is doubled** using a fibered Mach-Zehnder interferometer with an approximately $\tau_{\mathrm{rep}}/2$ delay line on one arm (see Fig. II.6.a).
- A **filtering stage** separates the emitted single-photons from parasitic reflected pump laser. The stage consists of three optical bandpass filters (10^{-3} transmission at $924\,\mathrm{nm}$, $850\,\mathrm{pm}$ FWHM). The photons are in addition spectrally filtered to increase their purity with a Fabry-Perot etalon (FSR $204\,\mathrm{pm}$ and finesse 14 at $925\,\mathrm{nm}$, $59 \pm 1\,\%$ single-photon transmission).
- To inject two photons simultaneously in the PIC, we use a **passive demultiplexer** ($80 \pm 1\,\%$ transmission) as shown on Fig. II.6.b. A polarization beamsplitter separates the photon stream into two. One of its arms is connected to a τ_{rep} delay line. Because of its passive nature, only $1/4$ of all consecutive photon pairs are correctly demultiplexed. Indeed, injecting two consecutive photons yields two photons arriving at the same time when the first photon takes the long path and the second photon takes the short one. Other components in the demultiplexer are:

- a polarizer, configured such that the polarizing beamsplitter acts as a symmetric beamsplitter. The polarizer additionally filters the emitted single-photons in polarization. The preceding quarter- and half-wave plates are set to maximize the number of photons transmitted by the polarizer.
- a motorized shutter that allows to select the input state that is sent to the PIC. We can choose between a single- and a two-photon state.
- a fibered polarization controller used to enforce that both input photons share the same polarization in the PIC. This is crucial for guaranteeing photon indistinguishability.

- The silica glass **PIC** used for single-photon manipulation features femtosecond laser-written waveguides. The optical transmission of the chip is $58 \pm 1\,\%$, averaged over the two used inputs. The PIC features also a waveguide crossing, where one of the waveguides passes under the other in 3D, thanks to the laser writing technique.

- The output state is sent to a **detection system** consisting of superconducting nanowire single photon detectors (SNSPD, 70% detection efficiency) followed by a correlator for photon times of arrival processing.

B.1.1 - PIC phase-voltage relation

We use the notation of Section II.4.2 for the voltages and phase shifters of the PIC. The PIC phase-voltage relation given by the manufacturer is

$$\begin{bmatrix} \psi_x^A \\ \psi_y^B \end{bmatrix} = \begin{bmatrix} 1.2890 & -0.0785 \\ 0.0988 & -1.2777 \end{bmatrix} \begin{bmatrix} V_x^A \\ V_y^B \end{bmatrix}^{\odot 2} - \begin{bmatrix} 0.0192 & -0.0009 \\ 0.0012 & -0.0203 \end{bmatrix} \begin{bmatrix} V_x^A \\ V_y^B \end{bmatrix}^{\odot 4} \tag{B.1}$$

$$\begin{bmatrix} \phi_x^A \\ \phi_y^B \end{bmatrix} = \begin{bmatrix} 0.2703 \\ -0.2799 \end{bmatrix} + \begin{bmatrix} 1.4693 & -0.1111 \\ 0.1120 & -1.4776 \end{bmatrix} \begin{bmatrix} U_x^A \\ U_y^B \end{bmatrix}^{\odot 2} - \begin{bmatrix} 0.0351 & -0.0026 \\ 0.0027 & -0.0343 \end{bmatrix} \begin{bmatrix} U_x^A \\ U_y^B \end{bmatrix}^{\odot 4} \tag{B.2}$$

where the phases are expressed in radians, the voltages in Volts, and $^{\odot}$ is component-wise exponentiation. Off-diagonal elements represent thermal crosstalk. From the numerical values we quantify:

- an average **crosstalk strength** of $7.2\,\%$ by comparing the off-diagonal elements to the diagonal ones
- an average **nonlinearity strength** of $1.9\,\%$ by comparing order 2 and order 4 diagonal elements
- the **orders 2 and 4 matrix similarity** measures by how much the order 4 matrix is a scaled down version of the order 2 matrix. For the ψ phases, the average relative difference between the order 4 and scaled order 2 matrix is $48\,\%$ per element, while it is only $5.8\,\%$ for the ϕ phases

B.2 - PIC calibration protocols

We give here the detailed protocols for calibrating the ϕ and ψ phases of Alice and Bob's interferometers.

Protocol B.2.1: MZI ϕ phase calibrations

Requires:

A function $f(\phi^A, \phi^B) = (U^A, U^B)$ that takes as input a pair of phases ϕ^A and ϕ^B, solves the phase-voltage equation Eq. B.2 and applies the solved voltages (U^A, U^B) on Alice's and Bob's ϕ phase shifter.

Input:

Target phases $\phi^{A/B}_{\text{tar},(x,y)}$ for each measurement context, as specified in Table II.2.

Returns:

Corrected phases $\phi^{A/B}_{\text{sol},(x,y)}$ for each context, such that when given to f, measurement contexts (x, y) is applied on the PIC.

Protocol:

For each measurement context (x, y):

1. **Initial state**
   We define a pair of initial phases $\phi^{A/B}_{0,(x,y)}$ which serve as a starting point for the optimization procedure.
   - If a calibration has been previously performed, set $\phi^{A/B}_{0,(x,y)}$ to be the previous solution.
   - Else, set $\phi^{A/B}_{0,(x,y)}$ to be the input target phases: $\phi^{A/B}_{0,(x,y)} = \phi^{A/B}_{\text{tar},(x,y)}$
2. **Input phase sweep** Simultaneously sweep Alice's and Bob's input phases from $\phi^{A/B}_{0,(x,y)} - 50\,\text{mrad}$ to $\phi^{A/B}_{0,(x,y)} + 50\,\text{mrad}$ with $5\,\text{mrad}$ steps. At each step, measure Alice's and Bob's interferometer phases following Sec. II.4.3.A.
3. **Data processing** The acquired data for each measurement context has the following form:

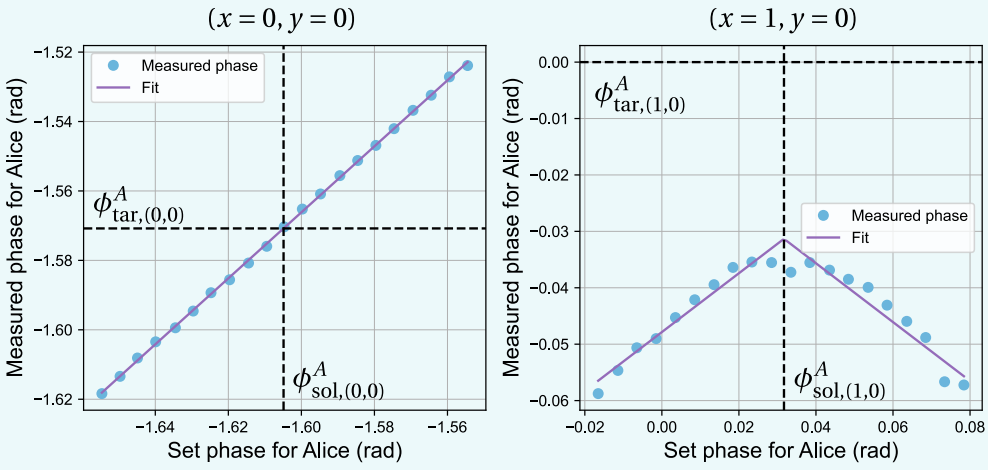

The data is fitted with a line or a triangle depending on the context (purple lines in the plots). The fit is used to determine the input phases $\phi^A_{\text{sol},(x,y)}$ and $\phi^B_{\text{sol},(x,y)}$ that implement the target phases. Horizontal black dashed lines indicate the target phase to reach, and vertical black dashed lines the optimal input phase.

Protocol B.2.2: External ψ phase calibration for Alice

Requires:

A function $f(\psi^A) = (V^A, V^B)$ that takes as input a pair a phase ψ^A, solves the phase-voltage equation Eq. B.1 with the constraint $\psi^B = 0$ on Bob's phase shifter and applies the solved voltages (V^A, V^B) on Alice's and Bob's ψ phase shifter.

Input:

Calibrated $\phi^{A/B}_{(x,y)}$ phases, using Protocol B.2.1

Returns:

Phase ψ^A_{sol} such that when given to f, the CHSH inequality value I_{CHSH} is maximal.

Protocol:

1. **Initial state**
   We define an initial phase ψ^A_0 which serve as a starting point for the optimization procedure.
   - If a calibration has been previously performed, set ψ^A_0 to be the previous solution.
   - Else, set $\psi^A_0 = 0$.
2. **Input phase sweep** Sweep Alice's phase around ψ^A_0 and measure the CHSH inequality violation for each point using the calibrated measurement contexts.
3. **Data processing**
   The acquired data has the following form:

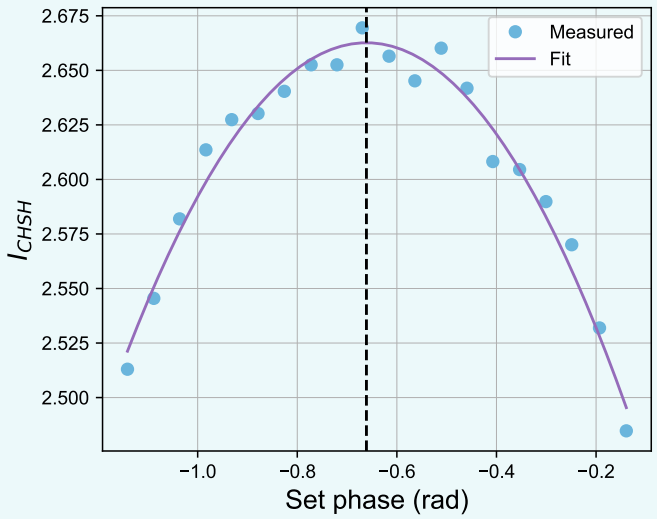

   The data is fitted with a quadratic polynomial (purple line). The fit is used to determine the input phases ψ^A_{sol} that maximally violates CHSH (vertical black dashed line).

C - Derivation of the CHSH inequality expression

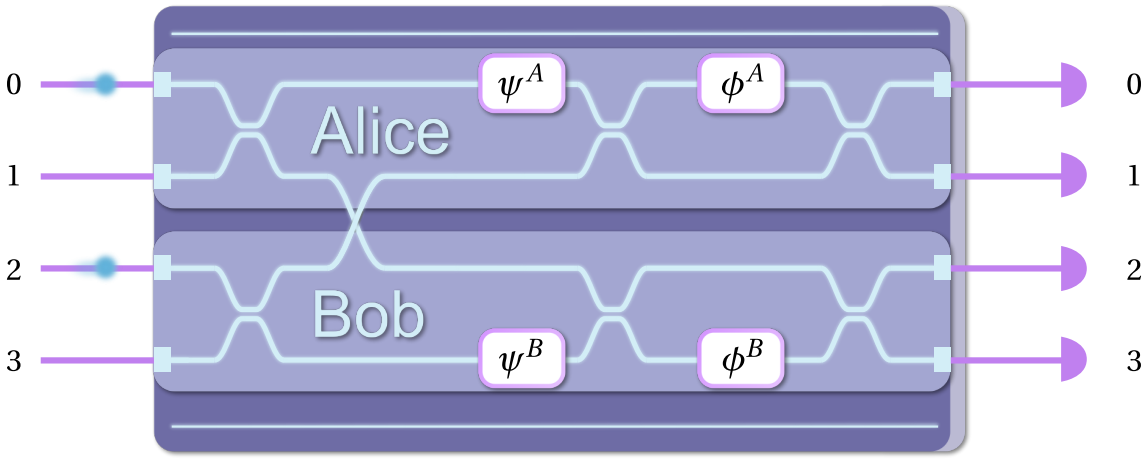

Figure C.1: Simplified scheme of the photonic integrated circuit for randomness generation.

We derive in this appendix the expression of the CHSH inequality value I_{CHSH} as function of photon indistinguishability and Alice's and Bob's phase shift choice. We show that the measurement bases of our experiment are optimal and that I_{CHSH} depends linearly on V_{HOM} according to the relation

$$I_{\text{CHSH}} = \sqrt{2}(V_{\text{HOM}} + 1) \tag{C.1}$$

The **photonic integrated circuit (PIC)** used for randomness generation is shown on Fig. C.1. For the derivation we use Fock state notation with mode labelling from 0 to 3. We use the creation operator formalism:

$$|0:1\rangle = a_0^\dagger |\text{vac}\rangle \tag{C.2}$$
$$|1:1\rangle = a_1^\dagger |\text{vac}\rangle \tag{C.3}$$
$$|2:1\rangle = a_2^\dagger |\text{vac}\rangle \tag{C.4}$$
$$|3:1\rangle = a_3^\dagger |\text{vac}\rangle \tag{C.5}$$

In addition, we do not assume that the two input photons are identical. Sources of distinguishability are time of arrival, polarization and wavelength. These extra degrees of freedom are encoded in configuration wavefunction $|\alpha\rangle$ (resp. $|\beta\rangle$) for the top (resp. bottom) photon. Hence, $|0_\alpha:1\rangle = a_{0,\alpha}^\dagger |\text{vac}\rangle$ represents a photon travelling in mode 0 with configuration $|\alpha\rangle$. Also, we have

$$\langle\alpha|\beta\rangle = 0 \iff \text{the photons are completely distinguishable} \tag{C.6}$$
$$\langle\alpha|\beta\rangle = 1 \text{ (up to a phase)} \iff \text{the photons are indistinguishable} \tag{C.7}$$

C.1 - Bell state generation

The two input photons initialize the quantum state in

$$\left|0_\alpha:1,2_\beta:1\right\rangle = a^\dagger_{0,\alpha}a^\dagger_{2,\beta}|\text{vac}\rangle\,. \tag{C.8}$$

Applying a symmetric beamsplitter on each pair of modes and a waveguide crossing yields the state

$$\frac{1}{2}\left(a^\dagger_{0,\alpha}a^\dagger_{1,\beta} + i\,a^\dagger_{0,\alpha}a^\dagger_{3,\beta} + i\,a^\dagger_{2,\alpha}a^\dagger_{1,\beta} - a^\dagger_{2,\alpha}a^\dagger_{3,\beta}\right)|\text{vac}\rangle \tag{C.9}$$

After postselection on 2-photon coincidences between Alice and Bob and discarding the global phase, the entangled state is

$$\frac{1}{\sqrt{2}}\left(a^\dagger_{0,\alpha}a^\dagger_{3,\beta} + a^\dagger_{2,\alpha}a^\dagger_{1,\beta}\right)|\text{vac}\rangle \tag{C.10}$$

C.2 - Output state

Alice's and Bob's individual interferometer is represented by the unitary matrix

$$U(\psi,\phi) = \frac{1}{\sqrt{2}}\begin{bmatrix}1 & i\\ i & 1\end{bmatrix}\begin{bmatrix}e^{i\phi} & 0\\ 0 & 1\end{bmatrix}\frac{1}{\sqrt{2}}\begin{bmatrix}1 & i\\ i & 1\end{bmatrix}\begin{bmatrix}e^{i\psi} & 0\\ 0 & 1\end{bmatrix} = ie^{i\phi/2}\begin{bmatrix}\sin\left(\frac{\phi}{2}\right)e^{i\psi} & \cos\left(\frac{\phi}{2}\right)\\ \cos\left(\frac{\phi}{2}\right)e^{i\psi} & -\sin\left(\frac{\phi}{2}\right)\end{bmatrix} \tag{C.11}$$

acting on the Fock states. Discarding the global phase factor of the matrix because the detectors are not sensitive to phases and enforcing $\psi = 0$ to simplify the calculations results in a simplified unitary matrix

$$U(\phi) = \begin{bmatrix}\sin\left(\frac{\phi}{2}\right) & \cos\left(\frac{\phi}{2}\right)\\ \cos\left(\frac{\phi}{2}\right) & -\sin\left(\frac{\phi}{2}\right)\end{bmatrix}. \tag{C.12}$$

The full output state is then:

$$\begin{aligned}\left|\psi_{\text{out}}\right\rangle = \frac{1}{\sqrt{2}}&\left[\sin\left(\frac{\phi^A}{2}\right)a^\dagger_{0,\alpha} + \cos\left(\frac{\phi^A}{2}\right)a^\dagger_{1,\alpha}\right]\times\left[\cos\left(\frac{\phi^B}{2}\right)a^\dagger_{2,\beta} - \sin\left(\frac{\phi^B}{2}\right)a^\dagger_{3,\beta}\right]|\text{vac}\rangle\\ &+\frac{1}{\sqrt{2}}\left[\sin\left(\frac{\phi^B}{2}\right)a^\dagger_{2,\alpha} + \cos\left(\frac{\phi^B}{2}\right)a^\dagger_{3,\alpha}\right]\times\left[\cos\left(\frac{\phi^A}{2}\right)a^\dagger_{0,\beta} - \sin\left(\frac{\phi^A}{2}\right)a^\dagger_{1,\beta}\right]|\text{vac}\rangle\,.\end{aligned} \tag{C.13}$$

We then express the configuration $\left|\beta\right\rangle$ as a function of $|\alpha\rangle$. We decompose $\left|\beta\right\rangle$ as a part that is indistinguishable with respect to $|\alpha\rangle$ and a second part that is completely distinguishable:

$$\left|\beta\right\rangle = c_\parallel|\alpha\rangle + c_\perp|\alpha_\perp\rangle \tag{C.14}$$

with $|\alpha_\perp\rangle$ a unit vector such that $\langle\alpha|\alpha_\perp\rangle = 0$, and $|c_\parallel|^2 + |c_\perp|^2 = 1$. As a result,

$$a^\dagger_\beta = c_\parallel a^\dagger_\alpha + c_\perp a^\dagger_{\alpha_\perp} \tag{C.15}$$

Injecting this expression in the output state yields

$$\begin{aligned}\left|\psi_{\text{out}}\right\rangle = \frac{1}{\sqrt{2}}&\left[\sin\left(\frac{\phi^A}{2}\right)a^\dagger_{0,\alpha} + \cos\left(\frac{\phi^A}{2}\right)a^\dagger_{1,\alpha}\right]\\ &\times\left[c_\parallel\cos\left(\frac{\phi^B}{2}\right)a^\dagger_{2,\alpha} + c_\perp\cos\left(\frac{\phi^B}{2}\right)a^\dagger_{2,\alpha_\perp} - c_\parallel\sin\left(\frac{\phi^B}{2}\right)a^\dagger_{3,\alpha} - c_\perp\sin\left(\frac{\phi^B}{2}\right)a^\dagger_{3,\alpha_\perp}\right]|\text{vac}\rangle\\ &+\frac{1}{\sqrt{2}}\left[\sin\left(\frac{\phi^B}{2}\right)a^\dagger_{2,\alpha} + \cos\left(\frac{\phi^B}{2}\right)a^\dagger_{3,\alpha}\right]\\ &\times\left[c_\parallel\cos\left(\frac{\phi^A}{2}\right)a^\dagger_{0,\alpha} + c_\perp\cos\left(\frac{\phi^A}{2}\right)a^\dagger_{0,\alpha_\perp} - c_\parallel\sin\left(\frac{\phi^A}{2}\right)a^\dagger_{1,\alpha} - c_\perp\sin\left(\frac{\phi^A}{2}\right)a^\dagger_{1,\alpha_\perp}\right]|\text{vac}\rangle\,.\end{aligned} \tag{C.16}$$

C.3 - Computation of outcome probabilities

Let $\mathbb{P}(a,b|\phi^A,\phi^B)$ be the probability that Alice and Bob measure respectively a and b with their interferometer phases set to ϕ^A and ϕ^B. Alice measures $a=0$ (resp. $a=1$) when the detector on mode 0 (resp. 1) clicks. We compute $p(a,b|\phi^A,\phi^B)$ from the expression of $|\psi_{\text{out}}\rangle$ by pairing the creation operators corresponding to an outcome (a,b) and summing the modulus square of the coefficients. For instance, the outcome $(a=0,b=0)$ corresponds to the operator pairs $a^\dagger_{0,\alpha}a^\dagger_{2,\alpha}$, $a^\dagger_{0,\alpha}a^\dagger_{2,\alpha_\perp}$, $a^\dagger_{2,\alpha}a^\dagger_{0,\alpha}$ and $a^\dagger_{2,\alpha}a^\dagger_{0,\alpha_\perp}$ in $|\psi_{\text{out}}\rangle$. Notice that $a^\dagger_{0,\alpha}a^\dagger_{2,\alpha}=a^\dagger_{2,\alpha}a^\dagger_{0,\alpha}$. The raw expression of the probability of outcome $(0,0)$ is thus:

$$\mathbb{P}(0,0|\phi^A,\phi^B)=\left|\frac{c_\parallel}{\sqrt{2}}\left(\sin\left(\frac{\phi^A}{2}\right)\cos\left(\frac{\phi^B}{2}\right)+\sin\left(\frac{\phi^B}{2}\right)\cos\left(\frac{\phi^A}{2}\right)\right)\right|^2 + \left|\frac{c_\perp}{\sqrt{2}}\sin\left(\frac{\phi^A}{2}\right)\cos\left(\frac{\phi^B}{2}\right)\right|^2+\left|\frac{c_\perp}{\sqrt{2}}\sin\left(\frac{\phi^B}{2}\right)\cos\left(\frac{\phi^A}{2}\right)\right|^2 \tag{C.17}$$

Computing all probabilities and simplifying the expressions yields

$$\mathbb{P}(0,0|\phi^A,\phi^B)=p(1,1|\phi^A,\phi^B)=\frac{|c_\parallel|^2-1}{8}\cos\left(\phi^A-\phi^B\right)-\frac{|c_\parallel|^2+1}{8}\cos\left(\phi^A+\phi^B\right)+\frac{1}{4}, \tag{C.18}$$

$$\mathbb{P}(0,1|\phi^A,\phi^B)=p(1,0|\phi^A,\phi^B)=-\frac{|c_\parallel|^2-1}{8}\cos\left(\phi^A-\phi^B\right)+\frac{|c_\parallel|^2+1}{8}\cos\left(\phi^A+\phi^B\right)+\frac{1}{4}. \tag{C.19}$$

C.4 - Link with HOM visibility

Photon indistinguishability is quantified by the HOM visibility V_{HOM}, which is measured by letting two photons interfere on a symmetric beamsplitter. V_{HOM} is then defined as

$$V_{\text{HOM}}=1-2p_{\text{coinc}} \tag{C.20}$$

where p_{coinc} is the coincidence probability. Using the same mathematical treatment as above, we show that

$$V_{\text{HOM}}=|\langle\alpha|\beta\rangle|^2=|c_\parallel|^2. \tag{C.21}$$

Injecting this expression in the probabilities gives us

$$\mathbb{P}(0,0|\phi^A,\phi^B)=\mathbb{P}(1,1|\phi^A,\phi^B)=\frac{V_{\text{HOM}}-1}{8}\cos\left(\phi^A-\phi^B\right)-\frac{V_{\text{HOM}}+1}{8}\cos\left(\phi^A+\phi^B\right)+\frac{1}{4} \tag{C.22}$$

$$\mathbb{P}(0,1|\phi^A,\phi^B)=\mathbb{P}(1,0|\phi^A,\phi^B)=-\frac{V_{\text{HOM}}-1}{8}\cos\left(\phi^A-\phi^B\right)+\frac{V_{\text{HOM}}+1}{8}\cos\left(\phi^A+\phi^B\right)+\frac{1}{4}. \tag{C.23}$$

C.5 - Expression of behavior and CHSH inequality value

Using our formulas and our choices for Alice's and Bob's phases in each measurement context (x,y), we compute the theoretical behavior shown in Fig. C.2. From this, we compute the CHSH inequality value as a function of photon indistinguishability.

$$I_{\text{CHSH}}=\sqrt{2}(V_{\text{HOM}}+1) \tag{C.24}$$

		Measurement			
		(x, y)			
		$(0, 0)$	$(0, 1)$	$(1, 0)$	$(1, 1)$
Result (a, b)	$(0, 0)$	$c_+(V_{\text{HOM}})$	$c_-(V_{\text{HOM}})$	$c_-(1)$	$c_-(1)$
	$(0, 1)$	$c_-(V_{\text{HOM}})$	$c_+(V_{\text{HOM}})$	$c_+(1)$	$c_+(1)$
	$(1, 0)$	$c_-(V_{\text{HOM}})$	$c_+(V_{\text{HOM}})$	$c_+(1)$	$c_+(1)$
	$(1, 1)$	$c_+(V_{\text{HOM}})$	$c_-(V_{\text{HOM}})$	$c_-(1)$	$c_-(1)$

Figure C.2: Behavior of CHSH experiment as a function of V_{HOM} with $c_\pm(x) = \frac{2 \pm \sqrt{2}x}{8}$.

D - Phase-voltage equation solvers

The most general phase-voltage equation is a nonlinear matrix equation of the form (we focus on voltage-controlled phase shifters for clarity, but the formalism is equivalent when using current-controlled phase shifters)

$$\vec{\phi} = \sum_{k \neq 0} C_k \vec{V}^{\odot k} + \vec{c}_0 \tag{D.1}$$

where

- $\vec{\phi}$ is the vector containing the implemented phase shifts
- $\vec{V}$ is the vector whose components are the applied voltages
- C_k are $n_{\mathrm{PS}} \times n_{\mathrm{PS}}$ matrices with n_{PS} the number of phase shifters. Diagonal elements contain the self-heating coefficients and off-diagonal elements account for crosstalk.
- $^{\odot}$ is element-wise exponentiation
- $\vec{c}_0$ is the vector containing the passive phases

Such matrix equations are challenging to solve efficiently. In practice, we also have the additional constraint that the voltages that we can apply on the phase shifters must be positive and below some safe value. A good solver should harness the fact that the crosstalk matrices C_k have dominant diagonals and that the phases are defined up to 2π to return a valid set of voltages. In this section we present the different phase-voltage equation solvers that were devised, tested and used during our experiments.

D.1 - DI-QRNG phase-voltage equation solver

The DI-QRNG PIC has a phase-voltage equation with order 2 and order 4 dependence. The PIC is relatively simple with only two phase shifters that need to be reconfigured frequently (Alice's and Bob's Mach-Zehnder interferometer phase shifters ϕ^A and ϕ^B). Hence, our devised solving method does not try to solve the phase-voltage equation in the general case, but is tailored for the PIC we use.

A preliminary study starts by exploring the set of all joint phases (ϕ^A, ϕ^B) that can be implemented while staying below the safe voltage of $2.5\,\mathrm{V}$. We plot this region of implementable phases denoted $\mathscr{X}$ on Fig. D.1. We then choose a square region $\mathscr{Y}$ of side 2π that lies entirely inside the set of implementable phases.

During standard operation, given target phases $\left(\phi^A_{\mathrm{target}}, \phi^B_{\mathrm{target}}\right)$ to implement, we subtract or add 2π as many times as needed until the target phases lie in $\mathscr{Y}$, as shown on Fig. D.1. When both target phases are located in the square region $\mathscr{Y}$, it is guaranteed that there is a valid voltage solution that implements the target phases. From there, the solution is straightforwardly approximated using `scipy.optimize.minimize` with the `COBYLA` gradient-free method (Constrained Optimization by Linear Approximation).

D.2 - 4-GHZ solver

The 4-GHZ PIC has a phase-current equation only with order 2 dependence. There are two groups of 4 phase shifters that need to be frequently reconfigured: the external phases ψ and

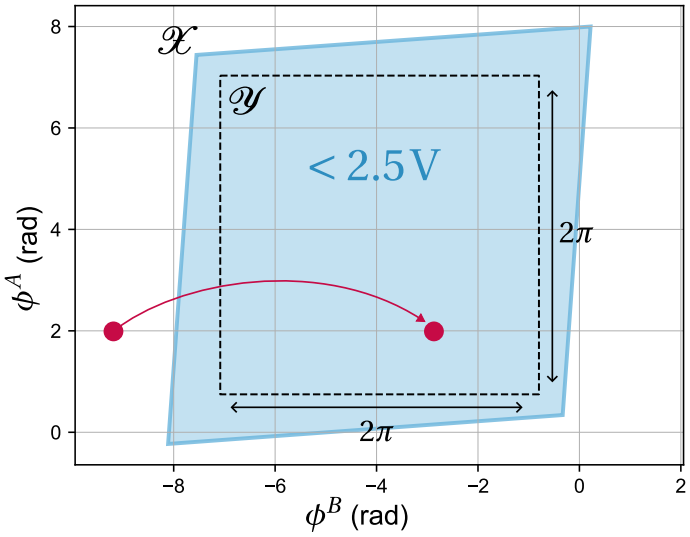

Figure D.1: Phase shifts map for Alice's and Bob's Mach-Zehnder interferometer (MZI) The blue area indicates the set $\mathscr{X}$ implementable MZI phases with voltages below the safe limit of $2.5\,\mathrm{V}$. The dashed square delimits a square region $\mathscr{Y}$ of side 2π. The red dots represent target phases that are displaced by 2π to fit into the region $\mathscr{Y}$.

the Mach-Zehnder interferometer phases ϕ. We do not use the method from the previous section where we seek a region of side 2π in which all phases can be continuously swept, because it would require searching this volume in a 4-dimensional space. Instead, the solver based on `scipy.optimize.minimize` applies randomly 2π offsets on the target phases until the solution is a valid set of voltages. This brute force method works well for small-sized PICs only.

D.3 - Stepper

The *stepper* algorithm is our first attempt to design a general phase-voltage equation solver. Let $\vec{\phi}$ be the target phases. The algorithm starts with $\vec{V} = 0$. At each iteration,

1. $\vec{\phi}(\vec{V})$ is computed from Eq. D.1,
2. the phase difference $\Delta\vec{\phi} = \vec{\phi} - \vec{\phi}(\vec{V})$ is computed modulo 2π,
3. each voltage V_i is updated with a step proportional to $\Delta\phi_i$,
4. each V_i is cast within $[0, V_{\text{max}}]$ by a module operation, where V_{max} is the safe operation voltage threshold.

The algorithm terminates when the amplitude of each $\Delta\vec{\phi}$ component is below a specified threshold, usually set to 0.1 mrad. If the algorithm remains stuck in a local minimum, a random vector is added to $\vec{V}$. The scaling of the *stepper* algorithm is $O(n_{\text{PS}}^3)$, with n_{PS} the number of phase shifters. This is because Step 1 of the iteration is $O(n_{\text{PS}}^2)$ and the number of iterations is observed to scale with n_{PS} (see Fig. D.2b).

D.4 - Matrix perturbation solver

The *matrix perturbation solver* is an improvement over the *stepper* of Section D.3 in terms of algorithmic scaling: $O(n_{\text{PS}}^2)$ against $O(n_{\text{PS}}^3)$. In addition, the *matrix perturbation solver* is compatible with rectangular crosstalk matrices and has fewer parameters.

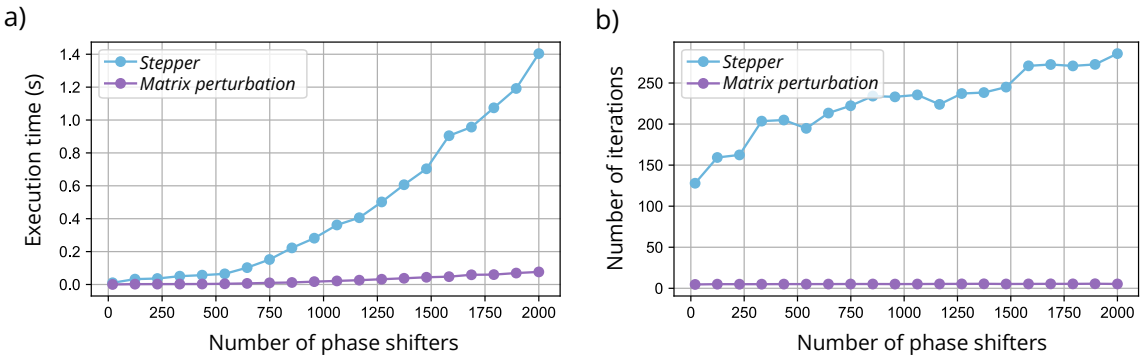

Figure D.2: Comparison between *stepper* and *matrix perturbation* phase-voltage relation solvers. a) Execution time and **b)** number of iterations as a function of number of phase shifters. The phase voltage relation to solve has a dominant V^2 term and a minor V^4 term. Each point represents 50 tests.

The solver starts with $\vec{V} = 0$. At each iteration, the voltage solution is updated according to the following rule inspired from perturbation theory:

$$\vec{V}^{\odot 2} \leftarrow C_2^{-1} \cdot \left(\vec{\phi}_{\text{target}} - \vec{c}_0 - \sum_{k \neq 2} C_k \cdot \vec{V}^{\odot k} \right) \tag{D.2}$$

This assumes that the V^2 terms in Eq. D.1 is dominant. Before applying a component-wise square root on $\vec{V}^{\odot 2}$, the algorithm checks that all components are positive and below the safe voltage bound. Else, 2π terms are subtracted or added to the corresponding components of $\vec{\phi}$ until all bound conditions are met.

The solver exits the iterative approximation process when all components of $\vec{\phi}(\vec{V})$ are close to $\vec{\phi}_{\text{target}}$ within some specified accuracy value, typically 0.1 mrad. Note that when the phase-voltage relation contains only the V^2 term, the solver delivers the solution in a single iteration.

We compare the *stepper* and *matrix perturbation* solvers on Fig. D.2.

E - Article in preparation

Resource-efficient crosstalk mitigation for the high-fidelity operation of photonic integrated circuits with induced phase shifters

Andreas Fyrillas,[1,2] Nicolas Heurtel,[1,3] Simone Piacentini,[1] Nicolas Maring,[1] Jean Senellart,[1] and Nadia Belabas[2]

[1] *Quandela, 7 Rue Léonard de Vinci, 91300 Massy, France*
[2] *Centre for Nanosciences and Nanotechnologies, CNRS, Université Paris-Saclay, UMR 9001, 10 Boulevard Thomas Gobert, 91120, Palaiseau, France*
[3] *Université Paris-Saclay, CNRS, ENS Paris-Saclay, Inria, Laboratoire Méthodes Formelles, 91190, Gif-sur-Yvette, France*

Photonic integrated circuits (PICs) are key platforms for the compact and stable manipulation of classical and quantum light. Imperfections arising from fabrication constraints, tolerances, and operation wavelength limit the accuracy of intended operations on light and impede the practical utility of current PICs. In particular, crosstalk between reconfigurable phase shifters is challenging to characterize due to the large number of parameters to estimate and the difficulty in isolating individual parameters. Previous studies have attempted to model crosstalk solely as an interaction between controlled phase shifters, overlooking the broader scope of this issue. We introduce the concept of induced phase shifter, arising from crosstalk on bare waveguide sections as predicted by simulations, resulting in an exhaustive description and systematic analysis of crosstalk. We characterize induced phase shifters in physical devices using a machine learning-based method and propose a mitigation framework. This framework further allows to establish a criterion certifying that a given interferometer has a sufficient number of degrees of freedom adequately laid out to fully mitigate crosstalk. Our approach is experimentally validated on a 12-mode Clements interferometer. We demonstrate the efficacy of our extended crosstalk model to accurately recover physical crosstalk properties of the PIC and cancel induced phase shifters following our mitigation framework.

I. INTRODUCTION

Photonic integrated circuits (PICs) embark optical components in a tightly integrated platform for light manipulation with enhanced compactness, scalability and stability. PICs are essential both for classical [1] and quantum optics [2], with applications ranging from microwave photonics [3], optical beamforming [4], and high-precision sensing [5] to quantum computing [6, 7], quantum communication [8], quantum cryptography [9], and quantum sensing [10]. We consider here programmable PICs for light manipulation, featuring directional couplers, and reconfigurable phase shifters (PSs). Directional couplers act as beamsplitters of fixed reflectivity, while PSs, controlled by voltage or electric current, enable the PIC to perform a wide variety of operations on input light states. Reconfigurable PSs harness thermo-optic effects [11], strain-induced birefringence [12] or electro-optic effects [13] to apply phase shifts on the guided light.

In general, crosstalk between PSs is an expected consequence of their compact integration. Our focus is here on voltage-controlled thermo-optic PSs and thermal crosstalk, which is the most widely used PS technology. Thermo-optic PSs generate heat and leverage the temperature dependence of the refractive index. The generated heat then diffuses within the PIC and manifests as crosstalk between the circuit's PSs. Crosstalk between PSs is recognized as a major imperfection in the integrated photonics litterature [14]. The mitigation of crosstalk presents a considerable challenge due to the multitude of contributing parameters and the complexity of interferometer meshes, which hinder the isolation and control of individual crosstalk components. The formalism used in [15] to account for thermal crosstalk was first introduced in [16, 17] as a matrix relation between the target phases and the actual implemented phase shifts on each PS. A similar matrix-based approach is used in [9, 18–21] to relate the implemented phase shifts to the applied voltages or electric currents. In particular, our previous work [20] achieved the highest recorded fidelity for implemented unitary matrices by using a machine-learning assisted method to retrieve the phase-voltage relation parameters of a physical PIC. The recovered phase-voltage relation exhibits unphysical long-range crosstalk. This hints towards a mechanism overlooked by current crosstalk models, and suggests that a physically accurate and systematic crosstalk description for PICs is still missing. In this work,

- we extend existing crosstalk descriptions by introducing an effective optical component accounting for parasitic phase shifts on bare waveguide sections, confirmed in simulations (Section II).
- We provide and benchmark a machine learning based-method for measuring crosstalk in PICs in the extended crosstalk paradigm (Section III).
- We mitigate crosstalk in the extended crosstalk framework, which demonstrates that mitigation is fundamentally infeasible in certain interferometer meshes. Based on this new understanding, effectively mitigating crosstalk through optimized PIC designs is key to improving control, scalability, and fidelity, while minimizing the number of on-chip components. We es-

tablish a criterion for certifying the inherent ability of a given interferometer to cancel crosstalk (Section IV).

- Finally, we experimentally assess the improvements achieved thanks to the extended crosstalk model (Section V).

II. CROSSTALK MODEL EXTENSION WITH INDUCED PHASE SHIFTERS

Given a PIC, let n_{CPS} be the number of *controlled* PSs, that is the number of phase shifters that are physically fabricated as such on the PIC and directly controlled by voltage. PIC crosstalk models usually describe crosstalk as a mutual influence between controlled PSs [14–16, 20, 22]. This influence is captured by a matrix relation relating the applied voltages $\vec{V}$ to the implemented phase shifts $\vec{\phi}^{(\mathrm{res})}$ restricted to controlled PSs. Hence, the phase-voltage relation of a PIC in what we call the *restricted crosstalk model* has the general form

$$\vec{\phi}^{(\mathrm{res})} = \sum_{k\neq 0} C_k^{(\mathrm{res})} \cdot \vec{V}^{\odot k} + \vec{c}_0^{(\mathrm{res})} \tag{1}$$

where $C_k^{(\mathrm{res})}$ are crosstalk matrices of size $n_{\mathrm{CPS}} \times n_{\mathrm{CPS}}$, $^{\odot}$ is element-wise exponentiation and $\vec{c}_0^{(\mathrm{res})}$ is the vector containing the n_{CPS} passive phases. The diagonal elements of a crosstalk matrix $C_k^{(\mathrm{res})}$ correspond to the *self-heating* coefficients. Self-heating coefficients quantify the efficiency with which PS heaters modify the phase of light propagating in the waveguide they are located on. Off-diagonal elements of crosstalk matrices account for crosstalk between PSs. For ideal thermo-optic phase shifters, only the $k = 2$ term remains in Eq. 1. We will consider for simplicity PICs with phase-voltage relations of the form $\vec{\phi}^{(\mathrm{res})} = C_2^{(\mathrm{res})} \cdot \vec{V}^{\odot 2} + \vec{c}_0^{(\mathrm{res})}$.

Restricted crosstalk models do, however, not reflect the physical reality of actual crosstalk. Physical crosstalk, related to heat diffusion for thermo-optic PSs, is indeed expected to also create phase shifts on waveguide portions that do not feature any controlled PS. Analogous effects may also exist for mechanical and electro-optic phase shifters, by spread of strain or stray electric fields to neighboring waveguides. To demonstrate this effect for thermo-optic PSs, we perform numerical simulations on a silicon nitride (SiN) PIC featuring 6 *modes* (number of waveguides running through the PIC), shown on Fig. 1a. The impact of crosstalk is assessed by computing the generated phase shifts in waveguides neighboring an active controlled PS (see Methods and App. A for details on the simulations). The PIC, consistent with typical designs, is fitted with trenches to increase phase shifter efficiency and reduce heat diffusion in the circuit [23, 24] (see cross section on Fig. 1b). The resulting phase shifts displayed on Fig. 1c confirm that waveguides that do not initially feature a PS heater acquire an unwanted phase shift due to heat diffusion. This effect is not included in the restricted crosstalk model, which by definition only accounts for crosstalk between controlled PSs.

We show on Fig. 1d that the presence of induced PSs significantly impacts interferometer behavior. To evaluate this, we implement a set of target unitary matrices on the simulated PIC featuring induced PSs. Each matrix encodes the action of the interferometer on light [25]. Following the procedure in Methods ("Measurement of amplitude fidelity"), the target matrices are implemented considering only crosstalk between controlled PSs to compute the applied voltages. The resulting average amplitude fidelity between targeted and implemented matrices is 99.3 % due to the presence of induced PSs. The amplitude fidelity between two unitary matrices U and V is defined as [19]

$$\mathscr{F}_a(U,V) = \frac{\mathrm{Tr}\left(|U|^T \cdot |V|\right)}{m} \tag{2}$$

where the absolute value is applied element-wise and m is the number of modes. For comparison, the highest experimentally achieved average amplitude fidelity between implemented and target Haar-random unitary matrices is 99.7 % (in [20] on a 12-mode Clements interferometer).

To account for these parasitic induced phase shifts, we propose to extend the standard restricted crosstalk models by introducing *induced* PSs in the circuit. Induced PSs are not directly controlled by voltage, but arise from the refraction index change caused by heat diffusion in bare waveguide sections. We thus consider in the extended crosstalk model that all the circuit waveguide portions feature either an initially present controlled PS, or an added induced PS. This is shown on Fig. 2b. As a result, the restricted square crosstalk matrix $C_2^{(\mathrm{res})}$ of size $n_{\mathrm{CPS}} \times n_{\mathrm{CPS}}$ (see Fig. 2c) is augmented to an extended rectangular matrix $C_2^{(\mathrm{ext})}$ of size $n_{\mathrm{PS}} \times n_{\mathrm{CPS}}$ (see Fig. 2d) with n_{PS} the total number of on-chip PSs (including controlled and induced ones).

Note that extended crosstalk matrices contain only positive coefficients, because crosstalk increases the phase of each PS (assuming that the refractive index increases with temperature, as is the case for silica glass or SiN). In the restricted model, controlled PSs in Mach-Zehnder interferometers (MZI) can have a negative crosstalk coefficient due to the situation depicted in Fig. 2e.

Similarly, the vector of implemented phases $\vec{\phi}^{(\mathrm{res})}$ and the passive phase vector $\vec{c}_0^{(\mathrm{res})}$ are promoted from n_{CPS} to n_{PS} components in their extended versions $\vec{\phi}^{(\mathrm{ext})}$ and $\vec{c}_0^{(\mathrm{ext})}$ which include controlled and induced PSs. We set the passive phase of induced PSs to zero by convention, such that the restricted and extended crosstalk models yield the same PIC state when no voltage is applied. The extended phase-voltage relation reads

$$\vec{\phi}^{(\mathrm{ext})} = C_2^{(\mathrm{ext})} \cdot \vec{V}^{\odot 2} + \vec{c}_0^{(\mathrm{ext})}. \tag{3}$$

III. CHARACTERIZATION OF CROSSTALK USING MACHINE LEARNING

We discuss in this section a method for experimentally measuring extended crosstalk matrices $C_2^{(\mathrm{ext})}$ of PICs, based

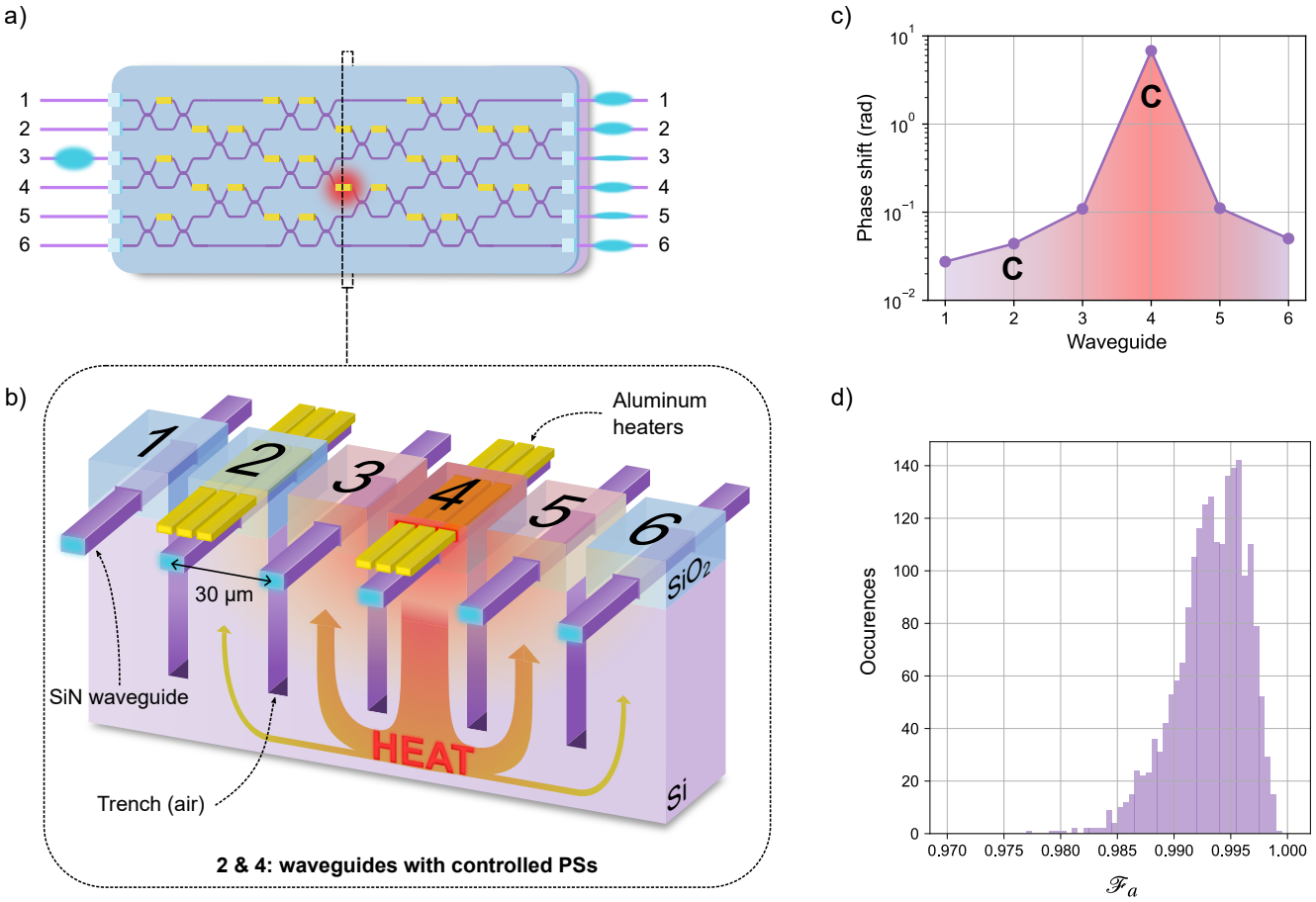

FIG. 1. **Thermal crosstalk in photonic integrated circuits induces parasitic phase shifts in neighboring waveguides.** **a)** 6-mode Clements interferometer with thermo-optic phase shifters (PSs). Yellow rectangles indicate the location of controlled phase shifters. Red area indicates an active controlled PS generating heat that induces a target phase shift on light propagating through its associated waveguide portion. **b)** Cross section of photonic circuit (not to scale, see App. A). The controlled PS on waveguide 4 is actuated and generates heat which diffuses. Blue: silicon dioxide (SiO_2) layer. Dark purple: silicon nitride (SiN) waveguides. Light purple: silicon (Si) substrate. Yellow: aluminum heaters. The trenches are etched in the Si substrate and filled with air. Only waveguides 2 and 4 feature a controlled PS (the controlled PS on waveguide 2 is not actuated here). **c)** Simulated values of induced phase shifts in each waveguide of the cross section (see Methods). The letter "C" indicates the waveguides featuring a controlled PS. The applied bias voltage on the actuated controlled PS of waveguide 4 is 14 V, which is the value inducing a 2π phase shift on waveguide 4 with realistic parameters (see Methods). **d)** Histogram of amplitude fidelities between target unitary matrices and implemented matrices on PIC. Only crosstalk between controlled PSs is taken into account when solving the phase-voltage relation of the PIC (see Methods "Measurement of amplitude fidelity"). The average amplitude fidelity is 99.3 %.

on the machine learning-assisted method we introduced in [20]. The method adopts a clear-box approach to PIC characterization. In the clear-box approach, the machine learning model (MLM) acting as the virtual replica of the PIC to characterize is built on a physical PIC model. This is in contrast with methods using virtual replicas based on black-box neural networks [26, 27]. The clear-box MLM is trained to replicate the behavior of the hardware PIC to characterize. This requires a training and a test dataset of samples acquired on the PIC. For each sample, light is injected into a PIC input port i, a list of random voltages $\vec{V}$ is applied on the PIC and the resulting light intensity output distribution $\vec{p}$ is measured (normalized to sum to 1), yielding a sample $(\vec{V}, i, \vec{p})$. The restricted MLM of [20] is extended by adding induced PSs to the machine learning model. As described in Sec. II, induced PSs are not directly controlled by a voltage in the model, but emerge from a realistic crosstalk that is described by an rectangular crosstalk matrix $C_2^{(\mathrm{ext})}$.

We compare the ability of the MLMs equipped with restricted and extended crosstalk models to learn the behavior of crosstalk in a hardware PIC. The hardware device to characterize is here replaced by a simulated idealized PIC whose only imperfection is crosstalk, i.e. all beamsplitters are symmetric, the PIC is perfectly transmissive but the crosstalk matrices $C_2^{(\mathrm{res})}$ and $C_2^{(\mathrm{ext})}$ have nonzero off-diagonal elements. The simulated PIC has an extended crosstalk model whose parameters are unknown to the MLMs (see Methods). During the training process,

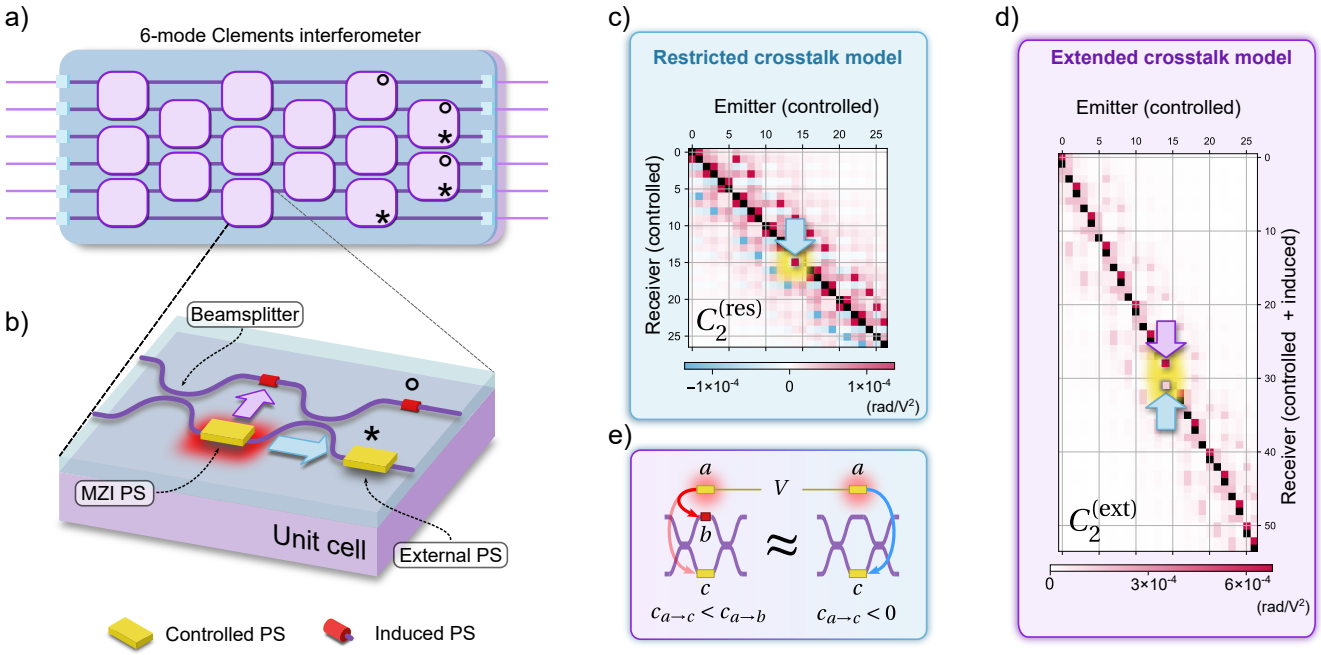

FIG. 2. **Extended crosstalk model taking into account induced phase shifters. a)** Schematic of 6-mode Clements interferometer. The basic unit cell **b)** of the interferometer contains two beamsplitters, two controlled phase shifters (PSs): one Mach-Zehnder interferometer (MZI) PS and one external PS. The unit cell also features two induced PSs. "*" or "°" symbols on unit cells in a) indicate that the unit cell lacks PSs marked with the same symbols on b), as they do not produce any measurable effect on light intensity detectors. Overall, the PIC has $n_{\mathrm{PS}} = 54$ PSs, among which $n_{\mathrm{CPS}} = 27$ are controlled. **c)** Simulated restricted crosstalk matrix. The restricted crosstalk model only considers interactions between controlled PSs via a square crosstalk matrix $C_2^{(\mathrm{res})}$ in the restricted phase-voltage relation (Eq. 1). The $C_2^{(\mathrm{res})}$ matrix displayed here is simulated from the circuit layout (see Methods, "Simulation benchmark of the training process"). The blue arrow on $C_2^{(\mathrm{res})}$ points at the coefficient corresponding to the influence symbolized by the blue arrow on the unit cell b). Diagonally dominant coefficients are masked. **d)** Simulated extended crosstalk matrix. The extended crosstalk model includes induced PSs representing phase shifts appearing due to crosstalk on waveguides devoid of any controlled PS. The associated simulated extended crosstalk matrix $C_2^{(\mathrm{ext})}$ is displayed, along with two colored arrows pointing at the coefficients corresponding to the influence symbolized by the color-coded arrows on b). **e)** Configuration leading to negative coefficients in the restricted crosstalk matrix. $c_{x\to y}$ denotes the crosstalk coefficient associated to the influence of PS x on PS y. Left: extended crosstalk model. A voltage V is applied on the heat emitter a. The MZI has an induced PS b on the top arm and a controlled PS c on the bottom arm. PS b is closer to a, thus $0 < c_{a\to b} < c_{a\to c}$. As a result, the phase difference between the two arms $\phi_c - \phi_b = (c_{a\to c} - c_{a\to b})V^2 < 0$ decreases with increasing voltage V. In addition, the unitary matrix of the MZI acquires a global phase $e^{i(c_{a\to c}+c_{a\to b})V^2}$. The impact of crosstalk on the phase difference can be taken into account in the restricted crosstalk model (right), in which the MZIs only have a controlled PS, with $c_{a\to c} < 0$. The impact on the global phase is however not captured by the restricted crosstalk model.

the MLMs attempt to converge to adequate parameters for their crosstalk matrix such that the mean square error (MSE) between the training dataset light intensity distributions $\vec{p}$ and the model predictions $\hat{\vec{p}}$ is minimized (quantities with a hat represent MLM predictions). In practice, the estimated crosstalk matrix $\hat{C}_2^{(\mathrm{res})}$ (resp. $\hat{C}_2^{(\mathrm{ext})}$) of the restricted (resp. extended) MLM is tuned via gradient-descent (see Methods), where each step is denoted *epoch*. This corresponds to the machine learning stages denoted "ML" in Figure 2 of [20].

The distance between a dataset light intensity distribution $\vec{p}$ and its corresponding prediction $\hat{\vec{p}}$ is quantified by the total variation distance (TVD):

$$\mathrm{TVD}\left(\vec{p},\hat{\vec{p}}\right) = \frac{1}{2}\sum_i |p_i - \hat{p}_i| \tag{4}$$

where TVD = 0 means $\vec{p} = \hat{\vec{p}}$ and TVD = 1 signifies that $\vec{p}$ and $\hat{\vec{p}}$ are maximally different. The prediction accuracy of an MLM is gauged by the average TVD on the test dataset and denoted $\mathrm{TVD}_{\mathrm{test}}$.

a. Benchmark on a Clements interferometer and training sample requirement The restricted and extended MLMs are trained on a 12-mode Clements interferometer [28] ($n_{\mathrm{PS}} = 252$ PSs, among which $n_{\mathrm{CPS}} = 126$ are controlled) with an increasing number of training samples. The number of parameters to train in the restricted (resp. extended) crosstalk model is the number of matrix elements in $C_2^{(\mathrm{res})}$ (resp. $C_2^{(\mathrm{ext})}$), that is $n_{\mathrm{CPS}} \times n_{\mathrm{CPS}} \approx 16000$ (resp. $n_{\mathrm{CPS}} \times n_{\mathrm{PS}} \approx 32000$). Fig. 3a reveals that the number of training samples required to train the extended MLM does not increase compared to the restricted MLM. The invariance of the *data-to-parameter ratio* (number of training samples / number

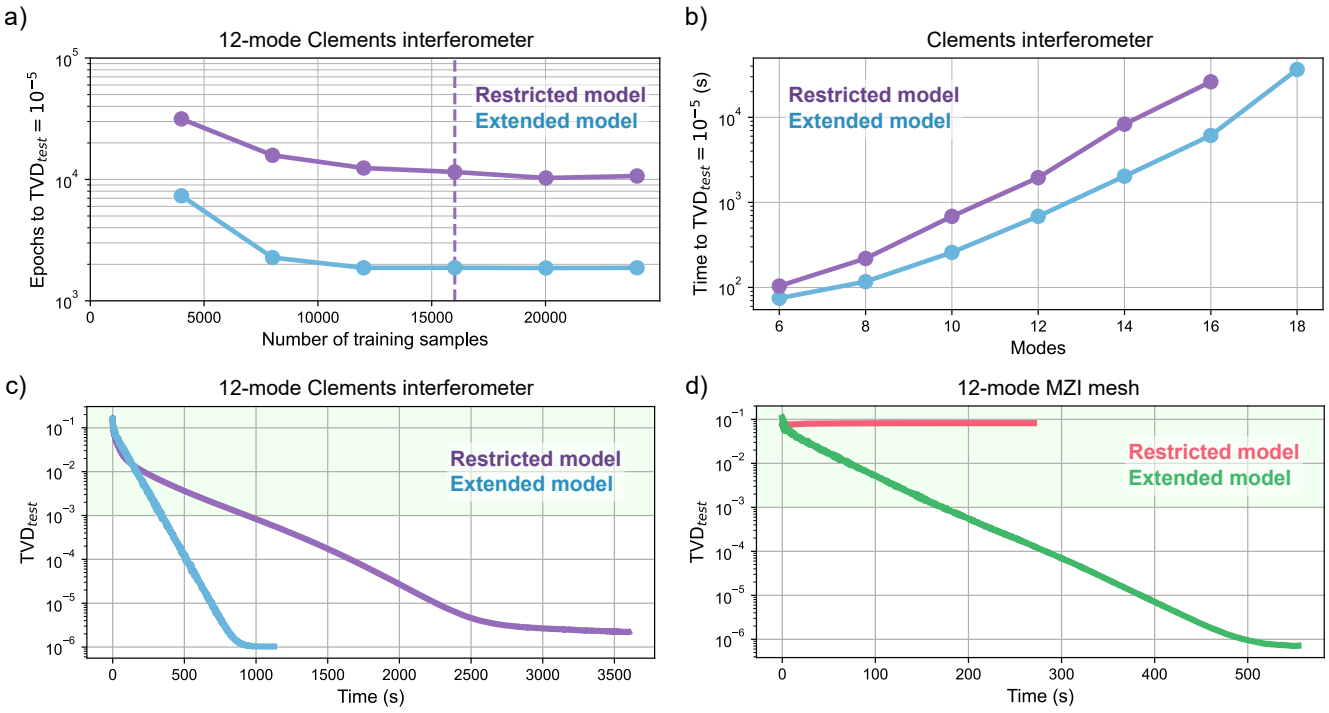

FIG. 3. **Simulation benchmarking the characterization of induced phase shifters.** The simulations are performed on simulated 12-mode photonic integrated circuits (PICs) (see Methods) featuring induced phase shifters (PSs). We compare the training performance of machine learning models (MLMs) equipped with restricted and extended crosstalk models. **a)** Number of epochs needed to reach $\mathrm{TVD}_{\mathrm{test}} = 10^{-5}$ versus the number of training samples used for training the restricted and extended crosstalk models on a 12-mode Clements interferometer. The purple dashed line indicates the number of samples corresponding to a data-to-parameter ratio of 1 for the restricted model. From here on, to train the restricted and extended models, we always use a number of training samples corresponding to a data-to-parameter ratio of 1 for the restricted model **b)** Elapsed time needed for the restricted and extended MLMs to reach $\mathrm{TVD}_{\mathrm{test}} = 10^{-5}$ for Clements interferometers with increasing numbers of modes. **c)** $\mathrm{TVD}_{\mathrm{test}}$ as a function of elapsed training time in the case of a 12-mode Clements interferometer for restricted and extended MLMs. The number of training samples in both cases is 16 000 (data-to-parameter ratio equal to 1 for the restricted model). Green area indicates experimentally accessible values of $\mathrm{TVD}_{\mathrm{test}}$. **d)** Same as c) for a mesh of MZIs, which is a Clements interferometer whose external controlled PSs (see Fig. 2b) have been converted into induced PSs ($n_{\mathrm{PS}} = 252$ PSs, among which $n_{\mathrm{CPS}} = 66$ are controlled). Both models were trained with ≈ 4000 samples (data-to-parameter ratio equal to 1 for the restricted model).

of MLM parameters) is especially relevant for practical aspects of characterization. Indeed the temporal bottleneck in the characterization protocol is the collection of the training and test datasets [20], which are themselves limited by the PIC reconfiguration and detector integration times (see Methods). In the following, we always train the restricted and extended MLMs with a number of training samples corresponding to a data-to-parameter ratio of 1 for the restricted model. This corresponds to 16 000 training samples for the 12-mode Clements interferometer.

Interestingly, the extended MLM requires significantly fewer gradient descent epochs to reach a target $\mathrm{TVD}_{\mathrm{test}}$ value, which we attribute in part to the doubled amount of degrees of freedom granted by the extended crosstalk matrix $\hat{C}_2^{(\mathrm{ext})}$. Consequently, each epoch is longer to compute for the extended MLM (302 ms against 235 ms for the restricted MLM). There is nevertheless a substantial net time gain when training the extended MLM, as shown on Fig. 3b. Fig. 3c displays the evolution of $\mathrm{TVD}_{\mathrm{test}}$ during training for the restricted and extended MLMs.

When using single-photon detectors, the count rate measurements are affected by Poisson shot noise, which limits $\mathrm{TVD}_{\mathrm{test}}$ to values above 0.1 % as demonstrated in [20]. Empirically, the $\mathrm{TVD}_{\mathrm{test}}$ is similar when performing the characterization with a continuous-wave laser and powermeters. Hence, the advantage of the extended model over the restricted model in terms of attained $\mathrm{TVD}_{\mathrm{test}}$ values is not experimentally relevant in our case.

b. Benchmark on an MZI mesh We repeat the simulation of the previous paragraph with an interferometer featuring only the MZIs of a 12-mode Clements interferometer. The external PSs of the Clements mesh (see Fig. 2b) are replaced by induced PSs in the MZI mesh. We observe on 3d that the restricted model does not converge. On the contrary, the extended model manages to replicate the PIC behavior. Hence, the extended MLM converges on more interferometer meshes, featuring induced PSs, compared to the restricted model. This observation is justified in Section IV C.

We verify that the the inability of the restricted model to

converge is indeed due to the presence of realistic induced PSs and not tied to the particular MZI mesh chosen here. Indeed, removing the induced PSs from the simulated MZI mesh allows the restricted model to converge.

IV. CROSSTALK MITIGATION IN THE EXTENDED FRAMEWORK

It is assumed in this section that the crosstalk matrix $C_2^{(\mathrm{res/ext})}$ of the hardware device is known. In practice, $C_2^{(\mathrm{res/ext})}$ is approximated by the crosstalk matrix $\hat{C}_2^{(\mathrm{res/ext})}$ estimated from characterization by the restricted/extended MLM of Section III. Mitigating crosstalk consists in solving the phase-voltage relation (restricted Eq. 1 or extended Eq. 3) of the device to find a set of voltages achieving the specified target phases. This requires the inverse of the crosstalk matrix (see App. B for a description of our solver). Square crosstalk matrices $C_2^{(\mathrm{res})}$ are usually invertible by diagonal dominance. However, in extended crosstalk models, the crosstalk matrix $C_2^{(\mathrm{ext})}$ is rectangular (see Section II), thus the inverse is not defined. Specifically, $C_2^{(\mathrm{ext})}$ has more rows than columns, which entails that the phase-voltage relation is an underdetermined system of equations.

In the rectangular case, the algebraic matrix inverse may be replaced by the Moore-Penrose pseudo-inverse. The induced phase shifts are set to zero in the target phases vector $\vec{\phi}^{(\mathrm{ext})}$ given to the solver, to implement only the desired phases on the controlled PSs. We demonstrate now that this strategy does not provide an accurate control of the PIC. On a simulated 12-mode Clements interferometer, the generated relation (see Methods "Simulation benchmark of the training process") featuring a rectangular extended crosstalk matrix $C_2^{(\mathrm{ext})}$ is inverted using the pseudo-inverse in our solver. The calculated voltage solution yields on average 6 mrad errors on controlled phases and 140 mrad residual phase shifts on induced PSs. As a result, the amplitude fidelity (see Eq. 2) of implemented matrices with respect to the target is degraded to $\mathscr{F}_a = 97.7 \pm 0.6\,\%$ (error bar is one standard deviation) as shown on Fig. 4d (blue histogram). In contrast, the case of simulated PICs without induced PSs, i.e. with square crosstalk matrices, our solver achieves $\mathscr{F}_a = 100\,\%$. Mitigation of induced PSs thus requires to transform the rectangular crosstalk matrix $C_2^{(\mathrm{ext})}$ into an invertible square matrix.

To mitigate crosstalk in the extended framework, we introduce in Subsection IV A a method called *crosstalk matrix reduction*, which turns rectangular crosstalk matrices into square invertible crosstalk matrices. The matrix reduction process uses invariant phase transformations. We lay the foundations for finding such phase transformations in Subsection IV B using circuit rewriting rules. From the rewriting rules, we devise an efficient algorithm for finding invariant phase transformations on a given circuit (see App. D). Subsection IV C gives a practical criterion for straightforwardly certifying the ability of a given PIC to fully cancel crosstalk.

A. Matrix reduction from invariant phase transformations mitigates induced PSs

Crosstalk matrix reduction, which plays a pivotal role in induced PS mitigation, hinges on the existence of *invariant PIC transformation*. Invariant PIC transformations are modifications of the PIC properties that leave the *measurable outcomes* of the physical experiment invariant, while keeping the same voltages applied to the PIC. The measurable outcomes may be the light intensity, photon countrates or photon coincidence counts

Theorem 1 allows us to remove induced PSs from a given PIC by applying an invariant transformation on the PIC.

Theorem 1. *(Crosstalk matrix row deletion)*

Consider a PIC with PSs labeled $1,2,...,n$ *(including controlled and induced PSs) and extended crosstalk matrix* $C_2^{(ext)}$*. We denote* ϕ_i *the phase shift value implemented by the i-th PS.*

Suppose that the k-th PS is an induced PS and that there exists an invariant phase transformation of the form

$$\begin{aligned} &\phi_i \longrightarrow \phi_i + \alpha_i \phi_k \quad \textit{for} \quad i \neq k \\ &\phi_k \longrightarrow 0 \end{aligned} \tag{5}$$

that holds for all values of $\phi_k \in [0, 2\pi[$ *and where the coefficients* $\alpha_1, ..., \alpha_n$ *are in* $\mathbb{R}$*.*

Then we may apply the following invariant transformation to the PIC:

1. *Apply the transformation*

$$R_i \longrightarrow R_i + \alpha_i R_k \quad \textit{for} \quad i \neq k \tag{6}$$

   to the crosstalk matrix $C_2^{(ext)}$ *of the PIC, where* R_i *designates the i-th row of* $C_2^{(ext)}$*.*

2. *Delete* R_k*.*

3. *Remove the k-th PS from the circuit.*

In Theorem 1, *invariant phase transformations* are modifications of the implemented PIC phase shifts that leave the measurable outcomes invariant. Invariant phase transformations are a property both of the PIC and the optical setup. For instance, if the PIC is followed by light intensity detectors, then applying additional phase shifts to the output modes of the PIC does not produce any measurable effect. We then say that the output ports are *phase-invariant*. Similarly, if the PIC is used to manipulate single photons as in [7], then the input ports are phase-invariant as well. Note that induced and controlled PSs located on phase-invariant input and output ports may be discarded.

The crosstalk matrix row deletion procedure of Theorem 1 is illustrated on Fig. 4a,b. Note that every usage of Theorem 1 deletes a row from the crosstalk matrix and removes effectively an induced PS from the circuit. By applying the

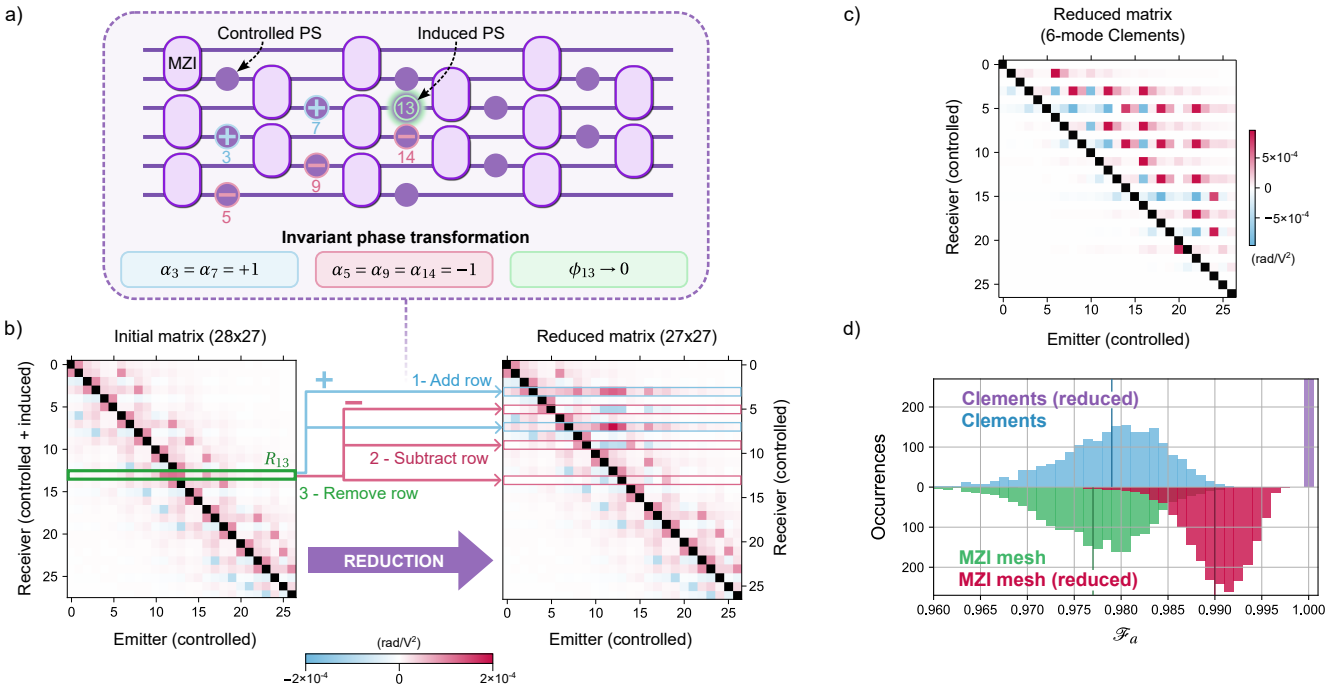

FIG. 4. **Mitigation of induced phase shifters (PSs) by matrix reduction.** All input and output ports are here assumed to be phase-invariant (see Section IV A). **a) + b)** Matrix reduction is illustrated on a 6-mode Clements interferometer featuring a single induced PS. The circuit features $n_{\mathrm{PS}} = 28$ PSs, among which $n_{\mathrm{CPS}} = 27$ are controlled. We consider that all of the input and output ports of the circuit are phase-invariant (see Section IV A) **a)** Schematic of the circuit. The purple squares represent Mach-Zehnder interferometers (MZIs, each featuring one controlled PS), and the purple disks depict controlled PSs. The induced PS (green disk) indexed as PS 13 implements a phase shift ϕ_{13}. The circuit admits an invariant phase transformation of the form Eq. 5 which consists in setting ϕ_{13} to 0, adding ϕ_{13} to the phase of PSs indexed 3 and 7 (PSs with a "+" sign) and subtracting ϕ_{13} from the phase of PSs indexed 5, 9 and 14 (PSs with a "-" sign). The invariant phase transformation is of the form Eq. 5 with coefficients $\alpha_3 = \alpha_7 = +1$ and $\alpha_5 = \alpha_9 = \alpha_{14} = -1$ for $\phi_{13} \to 0$. **b)** Illustration of the reduction process. By Theorem 1, the invariant phase transformation shown in a) is associated to an invariant crosstalk matrix transformation. We select the 13-th row (green frame), denoted R_{13} of the initial rectangular crosstalk matrix of size $n_{\mathrm{PS}} \times n_{\mathrm{CPS}}$. The dominant diagonal coefficients with approximate value $0.034\,\mathrm{rad/V^2}$ are masked for readability. According to the coefficients α_i, R_{13} is added ($\alpha_i = 1$, blue frames) to or subtracted ($\alpha_i = -1$, red frames) from the rows of the initial matrix. The process yields a square reduced matrix of size $n_{\mathrm{CPS}} \times n_{\mathrm{CPS}}$ after deletion of R_{13}. **c)** Reduced crosstalk matrix of the 6-mode Clements interferometer to reduce the rectangular crosstalk matrix displayed in Fig. 2d. The crosstalk matrix row deletion procedure of Theorem 1 is applied to every induced PS. **d)** Histogram of amplitude fidelities with vertical bars indicating the average value. We simulate two 12-mode circuits featuring induced phase shifters, whose initial rectangular crosstalk matrix is generated from the circuit layout in the extended crosstalk framework (see Methods "Simulation benchmark of the training process"), i.e. every waveguide either has a controlled or an induced PS. For each circuit, the amplitude fidelity with respect to target matrices is measured on 2000 target phase configurations (see Methods "Measurement of amplitude fidelity"). Upper half: Clements interferometer with rectangular crosstalk matrix (blue) and with reduced square matrix (purple, all values are 1 up to numerical errors). Lower half: mesh of MZIs (Clements interferometer whose external controlled PSs have been converted into induced PSs, as for Fig. 3d) with rectangular crosstalk matrix before (green) and after (red) reduction. 55 of the initial 186 induced PS cannot not be removed from the MZI mesh, thus the reduced matrix of size 121×66 remains rectangular.

procedure to each induced PS of a given PIC, a rectangular extended crosstalk matrix $C_2^{(\mathrm{ext})}$ may be reduced into a square matrix, depending on the interferometer mesh. For instance, Fig. 4c shows that the extended rectangular crosstalk matrix of a 6-mode Clements interferometer [28] reduces to a square matrix, assuming phase-invariant input and output ports. Fig. 2d displays the initial rectangular crosstalk matrix. Note that the reduction process introduces artificial long-range crosstalk in the reduced matrix to compensate for the removal of induced phase shifters.

To perform the reduction, only invariant PIC transformations are applied to the PIC. As a result, the reduction process is an invariant PIC transformation as well. In other words, the initial rectangular and the reduced crosstalk matrices yield the same measurable outcomes for a given list of voltages $\vec{V}$.

If the reduced crosstalk matrix is square, it is typically also invertible (see Methods). An invertible reduced crosstalk matrix allows to exactly invert the phase-voltage relation and recover the full PIC control accuracy as demonstrated in the upper half of Fig. 4d.

However, the reduction process yields a square matrix, only if we can find an invariant phase transformation for each induced PS. We give in Subsection IV C a criterion on

the circuit for this condition to be fulfilled. For instance, consider a mesh consisting only of MZIs without controlled PSs between them (e.g. the circuit of Fig. 4a without purple dots). The initial rectangular matrix can then only be partially reduced, resulting in a reduced matrix that remains rectangular. Partial reduction nevertheless provides a control accuracy improvement over the initial matrix (see lower half of Fig. 4d).

B. Finding invariant phase transformations from local circuit rewriting rules

Matrix reduction relies on the existence of invariant phase transformations. Such invariant phase transformations can be found by moving the induced PSs out of the circuit using local circuit rewriting rules. In particular, we use the two basis rules ϕ-cross and ϕ-merge depicted on Fig. 5a and also introduced in [29–32].

From the rules ϕ-cross and ϕ-merge, we derive the rule ϕ-remove which is used to move a phase shift by modifying only adjacent phase shifts. PSs are said to be *adjacent* when they are in the configuration displayed in Fig. 5b.

The rule ϕ-remove is an invariant phase transformation of the form Eq. 5. With the notation of Fig. 5b, the coefficients of the transformation are $\alpha_1 = -1$ and $\alpha_2 = \alpha_3 = 1$ for $\phi_0 \to 0$. Thus, if the PS labelled "2" represents an induced PS and PSs labelled "0", "1" and "3" are controlled PSs, then the crosstalk matrix row deletion procedure (Theorem 1) can be applied to remove the induced PS from the circuit and delete its associated row in the crosstalk matrix. If an induced PS is not adjacent to three controlled PSs, then the ϕ-remove rule must be repeatedly applied until all created phase shifts have been merged with controlled PSs or moved out of the circuit (see Fig. 5c). App. D introduces an efficient and generic phase simplification algorithm to find the invariant phase transformation associated to each induced PS, which are then used to reduce crosstalk matrices following Theorem 1.

In the particular case of Reck interferometers [25], [31] showed that there exists a set of deterministic rules , i.e. each step in the process has only one applicable rule ensuring an unambiguous path of execution. These deterministic rules can be used to remove all the induced PSs in Reck interferometers.

To find phase invariant transformations, we only consider linear relationships between PSs found via the ϕ-remove rule (see Fig. 5b) It would be possible to remove additional induced PSs from circuits by also considering nonlinear relationships between phases (e.g. axiom E2 in [32]). This would however greatly complexify the transformations applied to the crosstalk matrix, ultimately rendering the phase-voltage equation challenging to solve.

C. Criterion for crosstalk-robust interferometers: acyclic pruned graphs

We establish in this subsection a graphical criterion for certifying the robustness of a PIC to crosstalk. PICs that are not crosstalk-robust are not suited as experimental platforms, as they do not have the ability to suppress crosstalk entirely. A PIC is *crosstalk-robust* when its initial rectangular crosstalk matrix can be fully reduced to a square matrix following Section IV A, using linear invariant phase transformations derived from the circuit rewriting rule ϕ-remove from Section IV B.

The criterion does not rely on the phase simplification algorithm of App. D, and provides intuition on why certain meshes fail to be crosstalk-robust. We demonstrate how to apply our graphical criterion in Fig. 6. The PIC to investigate is represented as a mathematical graph. The nodes represent the on-chip beamsplitters and the edges interconnecting the nodes symbolize the PIC waveguides. The edges corresponding to PIC waveguide section featuring a controlled PS are marked with a cross. The graph features two additional nodes, called *input* and *output* nodes which are connected by an edge. Every input (resp. output) port of the circuit is connected to the input (resp. output) node. Each of these edges is marked with a cross if the port is phase invariant. We obtain a *pruned graph* by deleting every edge marked with a cross. The pruned graph encodes the robustness of the PIC to crosstalk as stated in Theorem 2, proven in App. E 1.

Theorem 2 (Crosstalk-robustness criterion)**.** *A PIC is crosstalk-robust if and only if its associated pruned graph is acyclic.*

The criterion is illustrated in Fig. 6 on three examples with phase-invariant input and output port. App. F provides an example where phase-invariance is not assumed. Following Theorem 2, the Reck [25], Clements [28] and Bell-Walmsley [29] universal interferometers are crosstalk-robust. On the contrary, specialized interferometers such as [33–36] are not crosstalk-robust for instance. Remarkably, we can highlight that universal schemes are not necessarily crosstalk-robust. Indeed, an MZI followed by two beamsplitters is universal on two modes, but not crosstalk-robust.

A pruned graph containing cycles can be made acyclic by removing additional edges. The minimal number of edges that must be removed corresponds to the circuit rank, as defined in graph theory [37]. In other words, a non-crosstalk-robust interferometer can be made resilient by adding r controlled PSs to the circuit, where r is the circuit rank of its pruned graph. The placement of these additional PSs is discussed in App. E 2.

Robustness to crosstalk also sheds light on the results of Fig. 3c,d. In Fig. 3c, the restricted MLM equipped with a square crosstalk matrix is able to faithfully learn the behavior of the Clements interferometer. This is because Clements interferometers are crosstalk-robust. Thus the

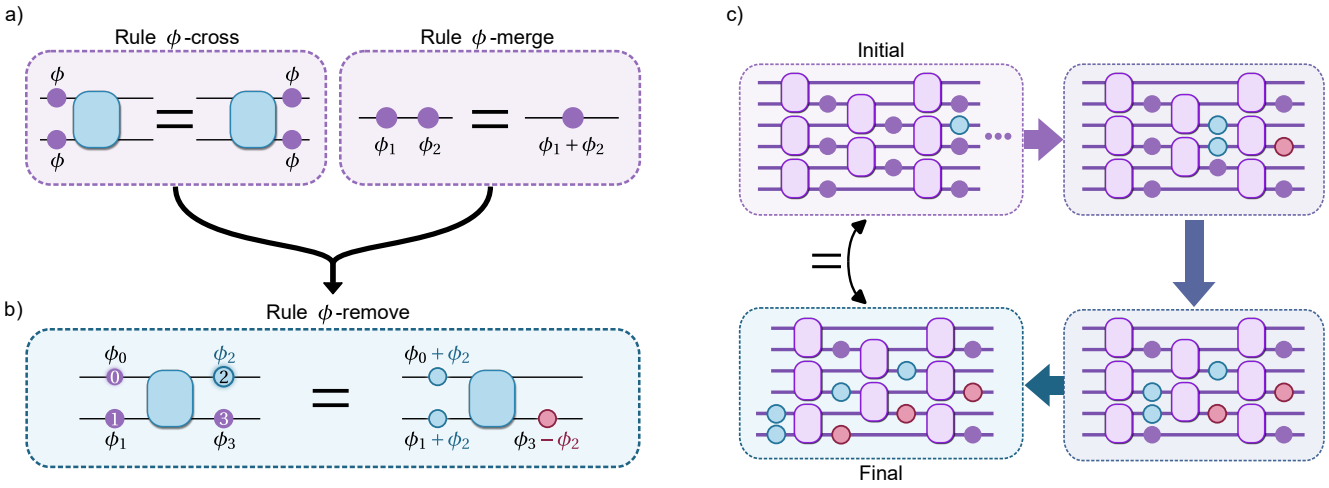

FIG. 5. **Local circuit rewriting rules are used to find invariant phase transformations.** Disks represent phase shifters (PSs). Equality between two circuits means that both implement the same unitary matrix acting on the photons. **a)** Basis rules ϕ-cross and ϕ-merge from which the rule ϕ-remove **b)** is derived. The blue rectangle represents any linear on-chip component on two modes such as a beamsplitter or a Mach-Zehnder interferometer (MZI). The phase shift implemented by each PS is displayed near its corresponding disk. **c)** Derivation of the invariant phase transformation of Fig. 4a. Purple rectangles are MZIs. Purple disks are controlled PSs. In the initial state, the blue disk is an induced PS with a phase ψ to move out of the circuit. The three dots on the right indicate that the circuit has been truncated for readability. The induced phase shift is moved across the circuit by repeatedly applying the rule ϕ-remove from b). The rule ϕ-remove is applied to cross an MZI. In the intermediate and final states, blue (resp. red) disks represent PSs whose phase has been increased (resp. decreased) by ψ. The process ends when only phase shifts outside of the circuit remain. They are discarded in Fig. 4a because we assume phase-invariant input and output ports in this case (see Section IV A).

crosstalk dynamics of Clements interferometers can be encapsulated into a square crosstalk matrix, which the restricted MLM can then directly learn. On the contrary in Fig. 3d, the restricted MLM cannot converge in the case of a generic mesh of MZIs which is not crosstalk-robust, because its crosstalk is necessarily described by a rectangular matrix.

V. EXPERIMENTAL VALIDATION

We proceed with the comparison of restricted and extended MLMs with a physical PIC. We characterize and control a 12-mode Clements interferometer featuring 126 reconfigurable phase-shifters and 132 beamsplitters [38]. As described in Section III, we acquire ≈ 16 000 training samples and 4 000 test samples on the PIC, corresponding to a data-to-parameter ratio of 1 for the restricted crosstalk model and a train/test dataset ratio of 80/20.

The PIC is first characterized with a restricted MLM following the procedure of [20], consisting in the stages:

- V-IFM (voltage interference fringe measurement): the estimated passive phases $\hat{\vec{c}}_0$ and self-heating coefficients (diagonal elements of the estimated crosstalk matrix $\hat{C}_2^{(\mathrm{res})}$) are coarsely approximated by sweeping the voltage of each controlled PS and fitting the resulting interference fringes.
- ML (machine learning stage): the estimated crosstalk matrix $\hat{C}_2^{(\mathrm{res})}$, beamsplitter reflectivity values $\hat{\vec{R}}$ and output transmissions $\hat{\vec{T}}_{\mathrm{out}}$ are updated via a gradient descent algorithm. Similarly to Section III, the algorithm seeks to minimize the mean squared error between the measured output light intensity distributions $\vec{p}$ in the training dataset and the distributions $\hat{\vec{p}}$ predicted by the model.
- ϕ-IFM (phase interference fringe measurement): the estimated passive phases $\hat{\vec{c}}_0$ are updated by sweeping successively each PS phase from 0 to 2π. This measurement makes use of the knowledge acquired in the preceding ML stage by the MLM to 1) compensate crosstalk for improved phase shifter control using the estimated crosstalk matrix $\hat{C}_2^{(\mathrm{res})}$ and 2) to generate the expected interference fringes using the learned beamsplitter reflectivity values $\hat{\vec{R}}$ and output losses $\hat{\vec{T}}_{\mathrm{out}}$. The measured fringes are compared to the expected ones to deduce the passive phase update.
- The protocol iterates between ML and ϕ-IFM stages until the prediction accuracy of the model stagnates, measured by the average TVD (see Section III) on the test dataset.

The restricted MLM achieves $\mathrm{TVD}_{\mathrm{test}}^{(\mathrm{res})} = 7.5\,\%$ at the end of the protocol, after 2 (ML + ϕ-IFM) iterations. The estimated crosstalk matrix $\hat{C}_2^{(\mathrm{res})}$ is displayed in Fig. 7a. The difference between our value for $\mathrm{TVD}_{\mathrm{test}}$ and the one of [20] ($\mathrm{TVD}_{\mathrm{test}}^{(\mathrm{res})} = 2.9\,\%$) resides in our use of an attenuated laser instead of a true single-photon source as the light source (see Methods).

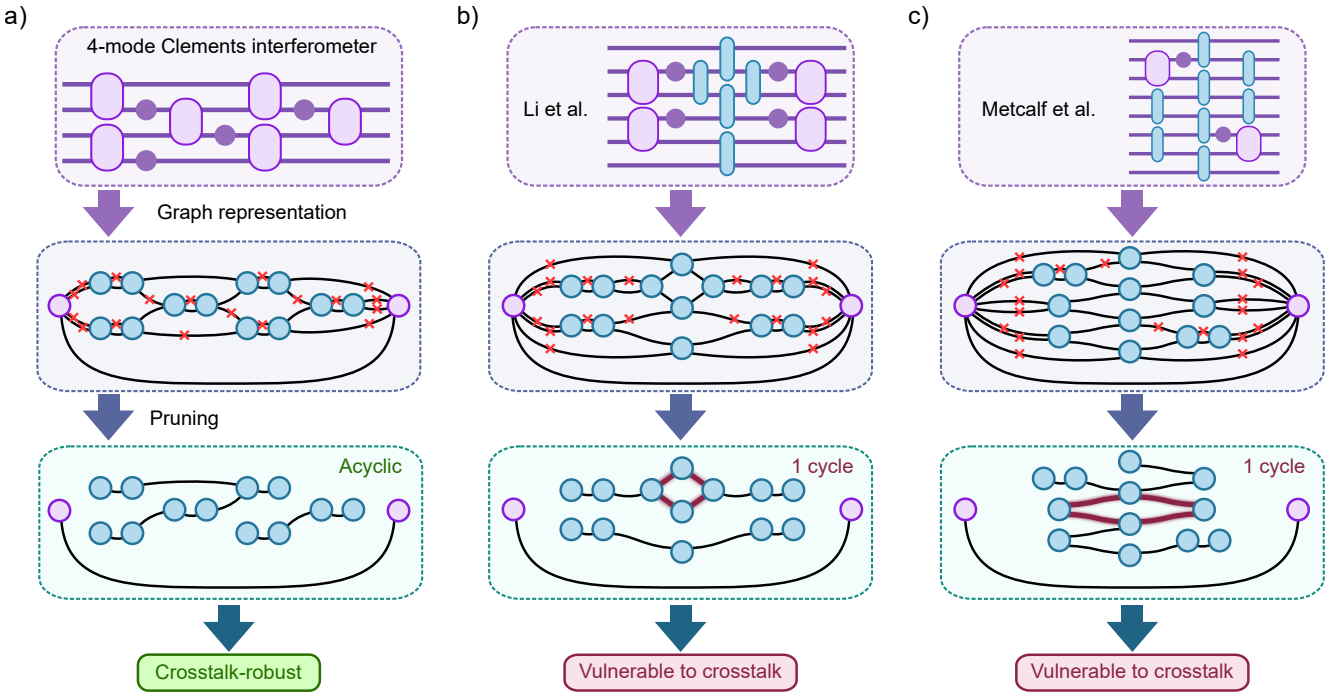

FIG. 6. **Certification of robustness to crosstalk using graph theory** The crosstalk robustness criterion (Theorem 2) is illustrated for **a)** a 4-mode Clements interferometer [28] and the interferometers of **b)** [33] and **c)** [34]. Each circuit is drawn in the respective top panel, with controlled phase shifters (PSs) represented as purple disks, beamsplitters as blue rectangles and Mach-Zehnder interferometers with the PS on the top mode as purple rectangles. Each circuit is associated to a mathematical graph, where the blue nodes symbolize the circuit beamsplitters, the purple nodes are the input and output nodes and the graph edges are laid out to reproduce the circuit waveguide mesh. Here we assume that all the ports are phase invariant (see Section IV A). Phase invariant input and output ports and waveguides featuring a controlled PS are marked with a cross. The graph is then pruned according to Section IV C by deleting all the marked edges. The pruned graph of a) is acyclic which proves that the 4-mode Clements interferometer is crosstalk-robust. On the contrary, the pruned graphs of b) and c) contain one cycle, thus the interferometers cannot entirely cancel crosstalk.

We then equip the MLM with an extended phase-voltage relation (see Eq. 3) and repeat the characterization process, with 2 (ML + ϕ-IFM) iterations as well. For this, we introduce a modification in the protocol where the rectangular crosstalk matrix $\hat{C}_2^{(\mathrm{ext})}$ is reduced to a square crosstalk matrix before entering each ϕ-IFM stage following our crosstalk matrix reduction procedure from Section IV. The reduction is necessary to effectively mitigate crosstalk when sweeping each PS in phase. The extended crosstalk model achieves $\mathrm{TVD}_{\mathrm{test}}^{(\mathrm{ext})} = 7.6\,\%$. As predicted from our simulations (see Fig 3c) and justified in Section IV C, the restricted and extended MLMs yield similar $\mathrm{TVD}_{\mathrm{test}}$ values for Clements interferometers. The estimated extended crosstalk matrix $\hat{C}_2^{(\mathrm{ext})}$ is shown in Fig. 7b.

We quantify the PIC control accuracy by the amplitude fidelity $\mathscr{F}_a$ between measured and implemented phase configurations on the PIC. Empirically, we observe that $\mathscr{F}_a \approx 1-\mathrm{TVD}_{\mathrm{test}}^2$. Consequently, the comparable $\mathrm{TVD}_{\mathrm{test}}$ achieved by the restricted and extended MLMs implies that using the estimated physical parameters of either model yields a similar PIC control accuracy. Indeed, the amplitude fidelity $\mathscr{F}_a$ on the physical PIC is the same for both models within error bars (see Fig. 7e).

The total time spent in the 2 ML stages is 3.9 minutes for the restricted MLM (see Methods "Simulation benchmark of the training process" for the duration of an epoch). On the other hand, the extended MLM offers a speed up as observed in Fig. 3b, requiring only 1.5 minutes to reach the same $\mathrm{TVD}_{\mathrm{test}}$.

The restricted MLM is able to account for induced phase shifters in the case of Clements interferometers, as simulated in Fig. 3b and discussed in Section IV C. The restricted MLM achieves this by introducing long-range crosstalk in the estimated restricted matrix $\hat{C}_2^{(\mathrm{res})}$ (see Fig. 7a). The resulting estimated matrix is akin to the reduced version of an extended crosstalk matrix (see Fig. 4a). Due to the artificial long-range crosstalk, the average off-diagonal amplitude of the estimated restricted crosstalk matrix $\hat{C}_2^{(\mathrm{res})}$ is $\approx 1\times10^{-4}$, whereas it is only $\approx 5\times10^{-5}$ for the extended crosstalk matrix $\hat{C}_2^{(\mathrm{ext})}$. As a consequence, physical short-range crosstalk is obscured in the restricted crosstalk matrix $\hat{C}_2^{(\mathrm{res})}$, whereas it is clearly visible in the extended matrix $\hat{C}_2^{(\mathrm{ext})}$. In particular, the extended matrix shows the presence of crosstalk between adjacent MZI columns (see Fig. 7c). Furthermore, reconstructing crosstalk as a function of distance between components in Fig. 7d shows that the crosstalk is more short-ranged in the extended matrix $\hat{C}_2^{(\mathrm{ext})}$ than in the re-

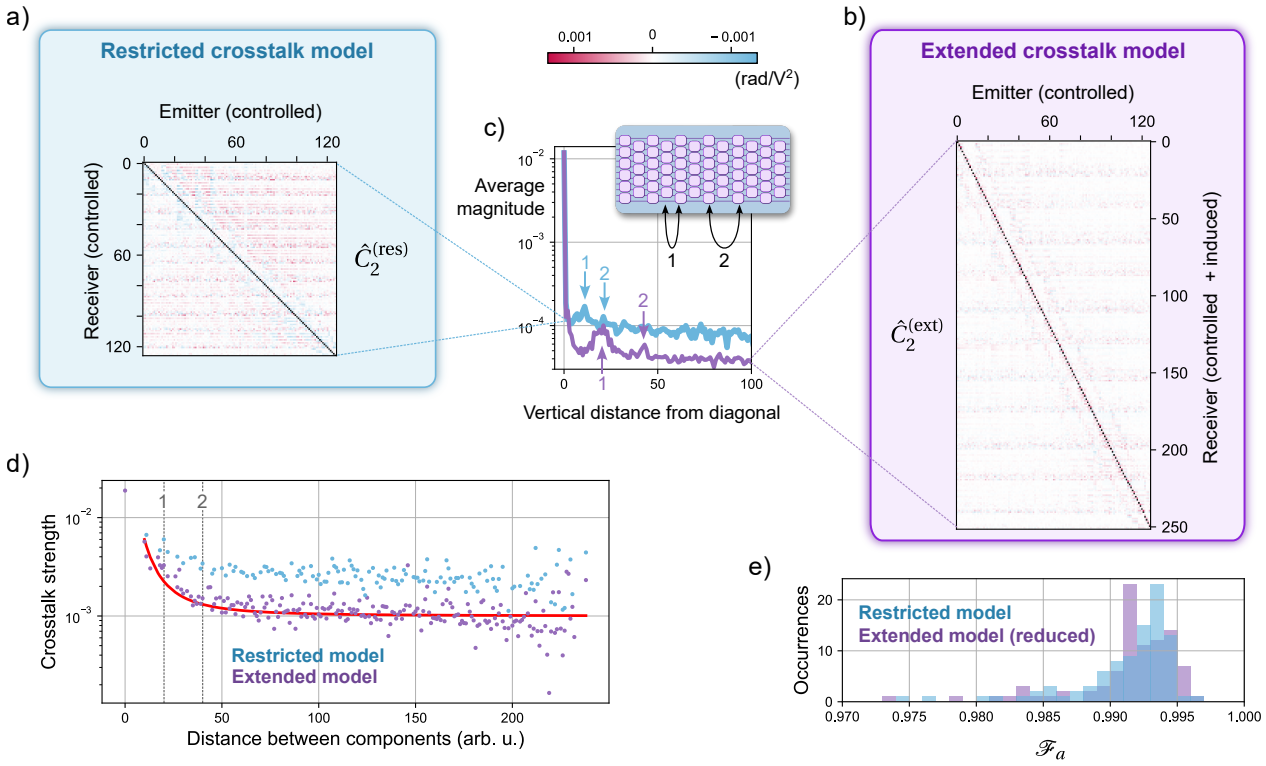

FIG. 7. **Experimental characterization of a 12-mode Clements interferometer with restricted and extended crosstalk machine learning models (MLMs). a)** (resp. **b)**) Estimated crosstalk matrix $\hat{C}_2^{(res)}$ (resp. $\hat{C}_2^{(ext)}$) of the trained MLM equipped with a restricted (resp. extended) crosstalk model. The self-heating coefficients on the diagonal are masked. **c)** Averaged magnitude of matrix elements as a function of vertical distance from the diagonal along vertical sections of $\hat{C}_2^{(res)}$ and $\hat{C}_2^{(ext)}$. Arrows labelled "1" and "2" indicate distances from the diagonal corresponding to unit cell column jumps as indicated in the inset. **d)** Crosstalk strength in $\hat{C}_2^{(res)}$ and $\hat{C}_2^{(ext)}$ as a function of the distance between components. Crosstalk strength is defined as the crosstalk coefficient value divided by the average diagonal coefficient. The distance is estimated from a 2D layout of the physical device described (see Methods "Simulation benchmark of the training process"). The red continuous curve shows the crosstalk-versus-distance function used for the simulations, with an additional offset of 1e-3 for clarity due to the log scale. The vertical grey lines labelled "1" and "2" indicate the distance between consecutive unit cell columns (see inset of c)). **e)** The PIC control accuracy provided by the restricted and extended MLM characterizations is measured for 100 phase configurations (see Methods "Measurement of amplitude fidelity"). The extended crosstalk matrix $\hat{C}_2^{(ext)}$ is reduced to a square matrix prior to the measurement following Section IV to enable crosstalk mitigation. The accuracy is measured by the amplitude fidelity $\mathcal{F}_a$ between with measured and expected output light intensity distributions. The average value for the restricted (resp. extended) MLM is $98.7 \pm 0.2\,\%$ (resp. $98.6 \pm 0.2\,\%$) (error bar is the statistical uncertainty on the 100 experiments).

stricted matrix $\hat{C}_2^{(res)}$. Thus, extended crosstalk models capture a more realistic picture of crosstalk, offering a valuable method for assessing PIC design and fabrication improvements in large-scale integrated structures.

VI. CONCLUSION AND DISCUSSION

We propose an extended crosstalk model including induced PSs, providing a systematic and physically faithful approach to modeling PS crosstalk in PICs. We use machine learning to estimate crosstalk matrices of physical devices and demonstrate in simulations that MLMs equipped with an extended crosstalk model generally converge faster than MLMs equipped with a restricted model. This behavior is demonstrated on Clements interferometers [28] , and further confirmed in separate simulations on Bell-Walmsley interferometers [29] (see App. G). The restricted and extended model require the same number of data samples for training. Additionally, the extended MLM successfully converges on a larger class of interferometers than the restricted MLM.

Our crosstalk mitigation framework is able to achieve optimal control of PICs with known universal-scheme interferometers, such as the Reck [25], Clements [28], and Bell-Walmsley [29] schemes, despite the presence of induced PSs. However, scalability beyond 50 modes, or 25 dual-rail path-encoded qubits, with universal interferometers remains a challenge due to the large number of on-chip components required. Consequently, quantum information processing with a larger number of photonic qubits will likely necessitate specialized interferometers. Our mitiga-

tion framework reveals a significant caveat in this approach: some PIC interferometer designs are fundamentally flawed, preventing effective crosstalk cancellation.

To enforce robustness to crosstalk, it is possible to equip every waveguide of a PIC with a controlled PS at the design stage. Such an approach to PIC design would however affect negatively the footprint, control complexity, power consumption, heat dissipation capabilities and optical transmission of integrated devices. We establish an accessible criterion that certifies the robustness of a given PIC to crosstalk. As such, our criterion can be used to design PICs with reduced numbers of controlled PSs, while maintaining a sufficient number of degrees of freedom to mitigate crosstalk.

Experimentally, the extended MLM proves effective in capturing a physically faithful representation of crosstalk within physical devices. This capability is particularly valuable for PIC design and fabrication processes, offering a direct benchmark for crosstalk reduction strategies in large-scale PICs, in which accessing individual physical parameters is challenging.

Our extended crosstalk model, conclusions on crosstalk characterization and mitigation, as well as the layout rules for designing interferometers resilient to crosstalk are valid for any PS technology.

METHODS

Thermal crosstalk simulations

We use the HEAT and Finite Difference Eigenmode (FDE) solvers of the Ansys Lumerical suite to perform thermal and electromagnetic simulations. We consider the circuit cross section described in Fig. 1b. Further information about the parameters and the results of the simulation can be found in the App. A.

The thermal crosstalk arising when a controlled PS is actuated is estimated by retrieving the temperature profile in the circuit. The steady state temperature reached in each point of the cross section can be calculated by numerically solving the time-independent heat equation

$$-k(x,y)\cdot\nabla^2 T(x,y) = Q(x,y), \tag{7}$$

where k [W/(m · K)] is the thermal conductivity of the material, $\nabla^2 T$ is the Laplacian of the temperature T [K], and $Q = \rho\cdot J^2$ [W/m^3] is the power per unit volume dissipated by Joule effect in a PS of resistivity ρ and biased with a current density J.

Once the temperature has been computed, we find the new refractive index profile $n(x,y,T)$ in the cross section by using the thermo-optic coefficient $\partial n/\partial T$, which depends on the considered material - in this case silicon nitride (SiN) for the core and SiO_2 for the cladding:

$$n(x,y,T) = n(x,y,T_0) + \left.\frac{\partial n}{\partial T}\right|_{(x,y)} dT(x,y). \tag{8}$$

The information about the index profile allows to retrieve the effective refractive index n_{eff} of the fundamental TE (transverse electric) mode by using the FDE solver, which calculates the waveguide eigenmodes by solving Maxwell's equations in the waveguide cross section. Once n_{eff} is known, the phase shift is eventually calculated for each waveguide as

$$\Delta\phi = \phi(T) - \phi(T_0) = \frac{2\pi}{\lambda}\left[n_{\text{eff}}(T) - n_{\text{eff}}(T_0)\right] L\,, \tag{9}$$

with T_0 the temperature in passive conditions, and L [mm] the length of the actuated controlled PS.

Simulation benchmark of the training process

The hardware device is replaced by a simulated PIC with perfectly symmetric beamsplitters and unity input and output transmissions. The passive phases of the simulated PIC are all set to zero, which corresponds to an experimental situation where the passive phases have been precisely estimated. The distance d between the components (MZIs and PSs) is algorithmically computed by drawing the interferometer mesh with a spacing of 10 units between waveguides and 10 units between consecutive components. A distance equal to 0 corresponds to the distance between the two PSs inside an MZI. The off-diagonal crosstalk coefficients are then given by the function

$$f(d) = \begin{cases} 0.5/d^2 & \text{for} \quad d \neq 0 \\ 0.02 & \text{for} \quad d = 0 \end{cases} \tag{10}$$

which reproduces the experimentally observed crosstalk-versus-distance relationship (see Fig. 7d). The diagonal coefficients are all taken to be equal to 0.034.

The MLMs are coded in `Python` using the `PyTorch` package. The `Adam` optimizer is used to minimize the mean square error of the model predictions on the training dataset with β parameters (0.99, 0.9999) with learning rates 10^{-5} for a number of interferometer modes smaller than or equal to 14, 5×10^{-6} for 16 modes and 1×10^{-6} for 18 modes. The training/test dataset ratio is 80/20. We use an i7-12700 CPU with an NVIDIA T1000 8 GB GPU. For a 12-mode Clements interferometer, the restricted (resp. extended MLM) takes 235 ms (resp. 302 ms). The epoch times are significantly shorter than [20] thanks to the GPU acceleration of matrix operations.

Experimental setup

We use a 12-mode Clements interferometer with 126 controlled thermo-optic phase shifters and 132 beamsplitters, a continuous-wave laser at 925 nm and single-photon detectors. The PIC reconfiguration time is 2 s. The coherent light is strongly attenuated before the PIC by decoupling fibers such that the total countrate on all 12 detectors lies between

500 kcounts/s and 1.5 Mcounts/s to avoid detector saturation and validity of the single-photon regime. For every performed countrate measurement, the integration time is 1 s.

Measurement of amplitude fidelity

We describe our protocol for evaluating the circuit control accuracy via the amplitude fidelity, both for simulated and hardware experiments. A specified number of target phase configurations are applied successively on the physical or simulated PIC. Each phase shift is uniformly chosen between 0 and 2π. Note that the resulting unitary matrices are not uniformly distributed for the Haar measure. Each phase configuration is converted into voltages using a specified phase-voltage relation and our solver described in App. B. For each phase configuration, the amplitude matrix implemented by the interferometer is measured by acquiring the output light intensity distribution for light injected successively into every other input port (light is injected into a single input port at a time). The component-wise square root of the measured distributions are the columns of the measured matrices. The expected matrices are computed from the phase configurations.

For Fig. 1, 2000 phase configurations are generated. The phase-voltage relation is solved taking into account only crosstalk between controlled PSs. The behavior of crosstalk in the simulated circuit is set to match the results from Fig. 1c. Note that our crosstalk simulations were performed only on transverse cross-sections such as Fig. 1b, thus we consider here that crosstalk only propagates vertically in the PIC drawn in Fig. 1a. In reality, heat is expected to also diffuse horizontally. For each phase configuration, the amplitude fidelity $\mathscr{F}_a$ (see Eq. 2) of the implemented matrix is measured with respect to the target matrix computed from the phase configuration.

In the case of the experimental run, the estimated beamsplitter reflectivity values $\hat{\vec{R}}$ and the estimated output transmissions $\hat{\vec{T}}_{\text{out}}$ by the MLM are used as well to generate the expected matrices. The amplitude fidelity values are computed between the measured and expected matrices from Eq. 2.

Invertibility of reduced matrix

If the reduced crosstalk matrix is square, it is typically invertible, although this depends on the number of modes and the strength of crosstalk. For small interferometers or weak crosstalk, the reduced matrix is diagonally dominant and therefore invertible. As the number of modes increases, the off-diagonal coefficients of the crosstalk matrix, which account for induced phase shifts, increase in magnitude. This increase can compromise the diagonal dominance of the reduced matrix.

We generate simulated crosstalk matrices using the process described in the Methods section ("Simulation benchmark of the training process"). For Clements interferometers with realistic crosstalk values, the reduced matrix is diagonally dominant up to 150 modes. We verified that up to 160 modes, the reduced matrix remains invertible, even though it is not diagonally dominant. In contrast, for a 50-mode interferometer with crosstalk increased 30-fold beyond experimental values, the reduced matrix becomes non-invertible.

ACKNOWLEDGEMENTS

This work has been co-funded by the European Commission as part of the EIC accelerator program, under the grant agreement 190188855. We acknowledge funding from the Plan France 2030 through the project ANR-22-PETQ-0013.

COMPETING INTERESTS

The authors declare that there are no competing interests.

AUTHOR CONTRIBUTIONS

A.F. formulated the original idea, conducted machine-learned characterization and carried out experimental validations. S.P. performed numerical crosstalk simulations. A.F. and N.H. designed mitigation strategies, with N.H. developing the algorithm and criteria for mitigation. A.F. and N.B. wrote the manuscript and designed the visualisations. N.B. supervised the project. N.M. and J.S. provided general oversight.

DATA AND CODE AVAILABILITY

The codebase and data generated as part of this work are available to research groups upon reasonable request to the corresponding author.

[1] Bogaerts, W. *et al.* Programmable photonic circuits. *Nature* **586**, 207–216 (2020).

[2] Wang, J., Sciarrino, F., Laing, A. & Thompson, M. G. Integrated photonic quantum technologies. *Nature Photonics* **14**, 273–284 (2020).

[3] Marpaung, D., Yao, J. & Capmany, J. Integrated microwave photonics. *Nature Photonics* **13**, 80–90 (2019).

[4] Heck, M. J. R. Highly integrated optical phased arrays: photonic integrated circuits for optical beam shaping and beam steering. *Nanophotonics* **6**, 93–107 (2017).

[5] Luan, E., Shoman, H., Ratner, D. M., Cheung, K. C. & Chrostowski, L. Silicon photonic biosensors using label-free detection. *Sensors* **18** (2018). URL https://www.mdpi.com/1424-8220/18/10/3519.

[6] Zhong, H.-S. *et al.* Quantum computational advantage using photons. *Science* **370**, 1460–1463 (2020).

[7] Maring, N. *et al.* A versatile single-photon-based quantum computing platform. *Nature Photonics* 1–7 (2024).

[8] Luo, W. *et al.* Recent progress in quantum photonic chips for quantum communication and internet. *Light: Science and Applications* **12**, 175 (2023).

[9] Fyrillas, A. *et al.* Certified randomness in tight space. *PRX Quantum* **5**, 020348 (2024).

[10] Polino, E. *et al.* Experimental multiphase estimation on a chip. *Optica* **6**, 288–295 (2019).

[11] Harris, N. C. *et al.* Efficient, compact and low loss thermo-optic phase shifter in silicon. *Optics Express* **22**, 10487–10493 (2014).

[12] Dong, M. *et al.* High-speed programmable photonic circuits in a cryogenically compatible, visible–near-infrared 200 mm cmos architecture. *Nature Photonics* **16**, 59–65 (2022).

[13] Li, M. *et al.* Lithium niobate photonic-crystal electro-optic modulator. *Nature Communications* **11**, 4123 (2020).

[14] Banerjee, S., Nikdast, M. & Chakrabarty, K. Characterizing coherent integrated photonic neural networks under imperfections. *Journal of Lightwave Technology* **41**, 1464–1479 (2023). ArXiv:2207.10835 [cs, eess].

[15] Bandyopadhyay, S. *et al.* Single chip photonic deep neural network with accelerated training (2022). URL http://arxiv.org/abs/2208.01623. ArXiv:2208.01623 [physics].

[16] Milanizadeh, M., Aguiar, D., Melloni, A. & Morichetti, F. Canceling thermal cross-talk effects in photonic integrated circuits. *Journal of Lightwave Technology* **37**, 1325–1332 (2019).

[17] Milanizadeh, M. *et al.* Control and calibration recipes for photonic integrated circuits. *IEEE Journal of Selected Topics in Quantum Electronics* **26**, 1–10 (2020).

[18] Pont, M. *et al.* High-fidelity four-photon ghz states on chip. *npj Quantum Information* **10**, 1–7 (2024).

[19] Pentangelo, C. *et al.* High-fidelity and polarization-insensitive universal photonic processors fabricated by femtosecond laser writing. *Nanophotonics* (2024). URL https://www.degruyter.com/document/doi/10.1515/nanoph-2023-0636/html.

[20] Fyrillas, A., Faure, O., Maring, N., Senellart, J. & Belabas, N. Scalable machine learning-assisted clear-box characterization for optimally controlled photonic circuits. *Optica* **11**, 427–436 (2024).

[21] Rodari, G. *et al.* Semi-device independent characterization of multiphoton indistinguishability (2024). URL http://arxiv.org/abs/2404.18636. ArXiv:2404.18636 [quant-ph].

[22] Zhu, Y. *et al.* Countering variations and thermal effects for accurate optical neural networks. In *Proceedings of the 39th International Conference on Computer-Aided Design*, 1–7 (ACM, Virtual Event USA, 2020). URL https://dl.acm.org/doi/10.1145/3400302.3415682.

[23] Alemany, R., Muñoz, P., Pastor, D. & Domínguez, C. Thermo-optic phase tuners analysis and design for process modules on a silicon nitride platform. *Photonics* **8** (2021). URL https://www.mdpi.com/2304-6732/8/11/496.

[24] Ceccarelli, F. *et al.* Low power reconfigurability and reduced crosstalk in integrated photonic circuits fabricated by femtosecond laser micromachining. *Laser & Photonics Reviews* **14**, 2000024 (2020). URL https://onlinelibrary.wiley.com/doi/abs/10.1002/lpor.202000024.

https://onlinelibrary.wiley.com/doi/pdf/10.1002/lpor.202000024.

[25] Reck, M., Zeilinger, A., Bernstein, H. J. & Bertani, P. Experimental realization of any discrete unitary operator. *Physical Review Letters* **73**, 58–61 (1994).

[26] Cimini, V. *et al.* Calibration of multiparameter sensors via machine learning at the single-photon level. *Physical Review Applied* **15**, 044003 (2021).

[27] Youssry, A. *et al.* Experimental graybox quantum system identification and control (2023). URL http://arxiv.org/abs/2206.12201. ArXiv:2206.12201 [physics, physics:quant-ph].

[28] Clements, W. R., Humphreys, P. C., Metcalf, B. J., Kolthammer, W. S. & Walmsley, I. A. Optimal design for universal multiport interferometers. *Optica* **3**, 1460–1465 (2016).

[29] Bell, B. A. & Walmsley, I. A. Further compactifying linear optical unitaries. *APL Photonics* **6**, 070804 (2021).

[30] Pont, M. *et al.* Quantifying n-photon indistinguishability with a cyclic integrated interferometer. *Physical Review X* **12**, 031033 (2022).

[31] Clément, A., Heurtel, N., Mansfield, S., Perdrix, S. & Valiron, B. Lov-calculus: A graphical language for linear optical quantum circuits (2022). URL http://arxiv.org/abs/2204.11787. ArXiv:2204.11787 [quant-ph].

[32] Heurtel, N. A complete graphical language for linear optical circuits with finite-photon-number sources and detectors (2024). URL http://arxiv.org/abs/2402.17693. ArXiv:2402.17693 [quant-ph].

[33] Li, H. W. *et al.* Calibration and high fidelity measurement of a quantum photonic chip. *New Journal of Physics* **15**, 063017 (2013). ArXiv:1306.1719 [quant-ph].

[34] Metcalf, B. J. *et al.* Quantum teleportation on a photonic chip. *Nature Photonics* **8**, 770–774 (2014).

[35] Shadbolt, P. J. *et al.* Generating, manipulating and measuring entanglement and mixture with a reconfigurable photonic circuit. *Nature Photonics* **6**, 45–49 (2012).

[36] Peruzzo, A. *et al.* A variational eigenvalue solver on a photonic quantum processor. *Nature Communications* **5**, 4213 (2014).

[37] Berge, C. *The Theory of Graphs*. Dover books on mathematics (Dover Publications, 2001).

[38] Taballione, C. *et al.* A universal fully reconfigurable 12-mode quantum photonic processor. *Materials for Quantum Technology* **1**, 035002 (2021).

[39] Palik, E. D. *Handbook of optical constants of solids*, vol. 3 (Academic press, 1998).

[40] Philipp, H. R. Optical properties of silicon nitride. *Journal of the Electrochemical Society* **120**, 295 (1973).

[41] Berge, C. *Graphs and Hypergraphs*, vol. 6 of *North-Holland Mathematical Library* (North-Holland Publishing Company, Amsterdam, 1973), revised edn.

Appendix A: PARAMETERS AND RESULTS OF THE THERMAL SIMULATIONS

A detail of the phase shifter (PS) cross section considered for the thermal and electromagnetic simulation is represented in the inset in Fig. 8. The SiN waveguide, with a thickness of 150 nm and a width of 800 nm, is placed under a PS composed of three aluminum alloy microheaters with a thickness of 400 nm, a width of 2 µm and a pitch of 5 µm. The distance between neighboring waveguides is 45 µm. Insulating trenches, with a depth of 200 µm, are etched in the silica (SiO_2) and silicon (Si) layers in the middle of each waveguides pair, and are considered filled with air. The total thickness of the device is set to 250 µm. The simulation region also includes a layer of air on top of the oxide, to estimate the heat dissipation occurring in air by conduction; both convection and irradiation channels are neglected.

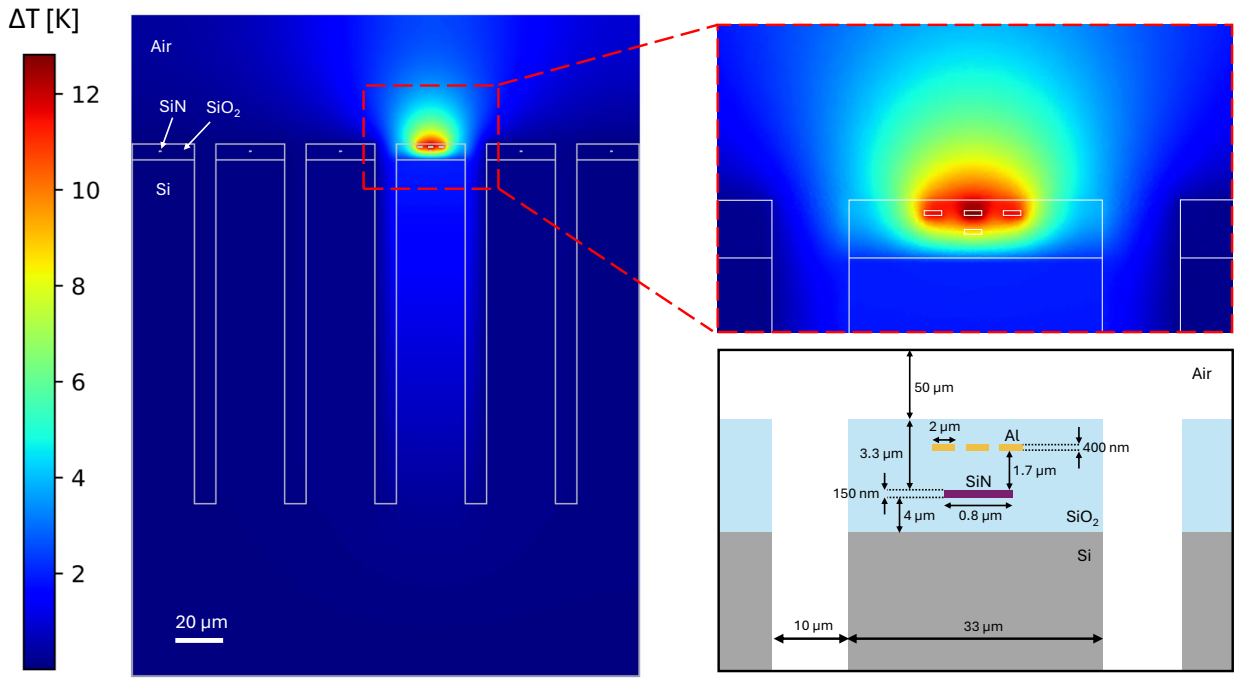

FIG. 8. Simulated cross-section and temperature profile obtained when applying a bias current of 18 mA to the controlled phase shifter. In the insets, a detail of the temperature increase around the phase shifter, and a zoomed cross-section (not to scale) showing the main geometric parameters used for the simulation.

A boundary condition of $T = 298$ K is set at the bottom of the silicon layer, to simulate the behavior of an active temperature controller. Moreover, the size of the simulation area is chosen by performing convergence tests to ensure that the results are not affected by its choice. A non-uniform mesh is used in order to capture fast changes of temperature or electromagnetic fields only where necessary: for instance, the mesh size of the waveguides and the heaters is set to 20 nm, while for the silicon layer it is equal to 1 µm. Convergence tests were performed as well to choose the adequate mesh size. The physical parameters used in the simulation, and in particular necessary for solving Eqs. 7, 8 and 9, are listed in Tab. I. The considered light wavelength is $\lambda = 925$ nm.

In Fig. 8, we also show the simulated temperature profile when applying a bias current of 18 mA, corresponding to a voltage drop of 14 V on the 5 mm-long microheaters, which ensures a phase shift of 2π on the controlled waveguide. The maximum temperature difference induced in the material is equal to 12.5 K, with a temperature increase in the waveguide of 9 K. The simulation shows the insulating effect of the trenches, which are confining the heat in the column under the PS. It is also possible to notice how the remaining silicon layer is responsible for the heat transfer to the adjacent waveguides, due to the fact that the trenches are not etched through the whole thickness of the device.

Appendix B: PHASE-VOLTAGE EQUATION SOLVER

Consider a photonic integrated circuit (PIC) with n_{CPS} controlled phase shifters (PSs) and n_{PS} PSs (controlled and induced). The general phase-voltage relation relating the implemented phase shifts $\vec{\phi}$ to the applied voltages $\vec{V}$ is of the form

Material	n	k [W/(m · K)]	ρ [Ω · m]	$\partial n/\partial T$ [K^{-1}]
SiN	1.990	30	-	$3.0 \cdot 10^{-5}$
SiO_2	1.452	1.4	-	$8.7 \cdot 10^{-6}$
Al alloy	$1.771 + 8.641i$	200	$3.6 \cdot 10^{-8}$	-
Si	$3.605 + 0.001i$	130	-	$1.8 \cdot 10^{-4}$
Air	1.000	0.03	-	$1.0 \cdot 10^{-6}$

TABLE I. Refractive index n, thermal conductivity k, electrical resistivity ρ and thermo-optic coefficient $\partial n/\partial T$ at T = 298 K and λ = 925 nm for the materials considered in the simulation [39, 40]. If a value is not present, it is either not defined or not needed for the simulation.

[20]:

$$\vec{\phi} = \sum_{k\geq 1} C_k \cdot \vec{V}^{\odot k} + \vec{c}_0, \tag{B1}$$

where C_k are crosstalk matrices of size $n_{\mathrm{PS}} \times n_{\mathrm{CPS}}$, $^{\odot}$ is element-wise exponentiation and $\vec{c}_0$ is the vector containing the n_{PS} passive phases. Additional features and constraints of the phase-voltage relation are

- the components of $\vec{\phi}$ are defined up to 2π
- the voltages assume positive values below a safe voltage operation bound.
- the diagonal of the crosstalk matrices dominates the off-diagonal terms
- for usual thermo-optic PSs, the order 2 term is dominant. Order 4, 6... terms may be added to account for heater resistance change with increasing temperature

Given $\vec{\phi} = \vec{\phi}(\vec{V})$, we usually seek to invert the relation to obtain a set of voltages $\vec{V}$ that implements a target phase configuration $\vec{\phi}_{\mathrm{target}}$. General nonlinear matrix equations are notoriously hard to solve, nevertheless our custom solver harnesses the characteristic traits of the phase-voltage relation to provide an approximate solution.

We use an iteration-based solver. At each iteration, the voltage solution is updated according to the following rule inspired from perturbation theory:

$$\vec{V}^{\odot 2} \leftarrow C_2^{-1} \cdot \left(\vec{\phi}_{\mathrm{target}} - \vec{c}_0 - \sum_{k\neq 2} C_k \cdot \vec{V}^{\odot k} \right) \tag{B2}$$

Before applying a component-wise square root on $\vec{V}^{\odot 2}$, the algorithm checks that all components are positive and below the safe voltage bound. Else, 2π terms are subtracted or added to the corresponding components of $\vec{\phi}$ until all bound conditions are met.

The solver exits the iterative approximation process when all components of $\vec{\phi}(\vec{V})$ are close to $\vec{\phi}_{\mathrm{target}}$ within some specified accuracy value, typically 0.1 mrad. Note that when the phase relation contains only the order 2 term, the solver delivers the solution in a single iteration.

The described solver bears two major improvements with respect to the one presented in [20]:

- our solver is compatible with rectangular crosstalk matrices. In that case, C_2^{-1} is the Moore-Penrose pseudo-inverse. The solution $\vec{\phi}(\vec{V})$ may however not approximate $\vec{\phi}_{\mathrm{target}}$ within the specified accuracy value.
- the solver scales with $O(n_{\mathrm{PS}}^2)$ (in comparison to the $O(n_{\mathrm{PS}}^3)$ scaling of [20]). It is indeed sufficient to compute C_2^{-1} only once before operating the PIC. Each iteration consists then of $O(n_{\mathrm{PS}}^2)$ operations due to matrix-vector multiplication. In addition, the number of iterations needed to approximate a solution is empirically independent of the number of phase shifters.

Appendix C: CROSSTALK MATRIX REDUCTION THEOREMS

The number of phase shifters (PSs) in a photonic integrated circuit (PIC) is denoted n_{PS} (controlled and induced) and the number of controlled PSs is n_{CPS}. ϕ_k denotes the phase shift value implemented by the PS labelled k.

1. Lemma for C 2

a. Statement Consider a PIC with PSs labeled $1,...,n_{\mathrm{PS}}$ (including controlled and induced phase shifters) and extended crosstalk matrix C of size $n_{\mathrm{PS}} \times n_{\mathrm{CPS}}$.

Suppose that there exists an invariant phase transformation (see Section IV A) of the form

$$\forall i \in [\![1, n_{\mathrm{PS}}]\!], \quad \phi_i \longrightarrow \phi_i + \alpha_i \psi \tag{C1}$$

that holds for all values of $\psi \in [0, 2\pi[$. The coefficients $\alpha_1, ..., \alpha_n$ are in $\mathbb{R}$.

Then the following transformation acting on C is an invariant crosstalk matrix transformation:

$$\forall i \in [\![1, n_{\mathrm{PS}}]\!], \forall j \in [\![1, n_{\mathrm{CPS}}]\!], \quad C_{ij} \longrightarrow C_{ij} + \alpha_i \Delta c_j \tag{C2}$$

with $\Delta c_j \in \mathbb{R}$ for all $j \in [\![1, n_{\mathrm{CPS}}]\!]$.

b. Proof The extended phase-voltage relation of the PIC is $\vec{\phi}^{(\mathrm{ext})} = C \cdot \vec{V}^{\odot 2} + \vec{c}_0^{(\mathrm{ext})}$ as stated in Eq. 3. Each phase shift is then expressed as

$$\phi_i = \sum_{j=1}^{n_{\mathrm{CPS}}} C_{ij} V_j^2 + (c_0)_i \tag{C3}$$

We apply the matrix transformation specified in the above statement to the crosstalk matrix C. The phase shifts evolve according to $\phi_i \longrightarrow \phi_i + \Delta\phi_i$, with

$$\Delta\phi_i = \alpha_i \sum_{j=1}^{n_{\mathrm{CPS}}} \Delta c_j V_j^2 \tag{C4}$$

Note that the phase shift variation is of the form $\Delta\phi_i = \alpha_i \psi$, which defines an invariant phase transformation by assumption. Thus we have proven that the stated crosstalk matrix transformation is invariant. □

2. Proof of Theorem 1 (Crosstalk matrix row deletion)

a. Statement Consider a PIC with PSs labeled $1,...,n_{\mathrm{PS}}$ (including controlled and induced phase shifters) and extended crosstalk matrix C of size $n_{\mathrm{PS}} \times n_{\mathrm{CPS}}$.

Suppose that PS k is an induced PS and that there exists an invariant phase transformation of the form

$$\forall i \in [\![1, n_{\mathrm{PS}}]\!], \quad \phi_i \to \begin{cases} \phi_i + \alpha_i \phi_k & \text{for } \ i \neq k \\ 0 & \text{for } \ i = k \end{cases} \tag{C5}$$

that holds for all values of $\phi_k \in [0, 2\pi[$. The coefficients $\alpha_1, ..., \alpha_n$ are in $\mathbb{R}$.

Then we can apply the following invariant transformation to the crosstalk matrix C, where R_i designates the i-th row of C:

$$\forall i \in [\![1, n_{\mathrm{PS}}]\!], \quad R_i \to \begin{cases} R_i + \alpha_i R_k & \text{for } \ i \neq k \\ 0 & \text{for } \ i = k \end{cases} \tag{C6}$$

The row R_k is then deleted.

b. Proof The stated invariant transformation can be condensed into

$$\forall i \in [\![1, n_{\mathrm{PS}}]\!], \quad \phi_i \to \phi_i + \alpha_i \phi_k \tag{C7}$$

by setting $\alpha_k = -1$. Let us focus on a single column j of the crosstalk matrix C. By Lemma C 1, the following transformation is an invariant crosstalk matrix transformation:

$$\forall i \in [\![1, n_{\mathrm{PS}}]\!], \quad C_{ij} \to C_{ij} + \alpha_i \Delta c_j \tag{C8}$$

with $\Delta c_j \in \mathbb{R}$. Taking $\Delta c_j = C_{kj}$, we have

$$\forall i \in [\![1, n_{\mathrm{PS}}]\!], \quad C_{ij} \to \begin{cases} C_{ij} + \alpha_i C_{kj} & \text{for } i \neq k \\ 0 & \text{for } i = k \end{cases}, \tag{C9}$$

Note that the matrix element of column j corresponding to ϕ_k has been zeroed. Applying the same procedure for every column of C, we zero the entire row R_k and retrieve the stated transformation on the rows of C in the statement of the theorem. Because the row corresponding to ϕ_k is zero everywhere, the phase shift value is then always zero, hence we can remove the induced PS k from the circuit and delete the associated row in the matrix. □

Appendix D: PHASE SIMPLIFICATION ALGORITHM

1. Algorithm

We introduce a phase simplification algorithm to efficiently find the removable induced phase shifters (PSs) in a given photonic integrated circuit (PIC) and the associated invariant phase transformations (see Section IV B). We say that an induced PS is *removable* when its implemented phase shift can be moved out of the circuit as exemplified in Fig. 5c. This yields an invariant phase transformation of the form Eq. 5 that enables the removal of the induced PSs from the circuit, following Theorem 1.

An induced PS is removable if and only if it is adjacent (see Section IV B) to three components of the types

- phase-invariant input/output port,
- controlled PS,
- removable induced PS.

We can then indeed apply the rule ϕ-remove (see Fig. 5b) to propagate the phase shift out of the circuit. Note that as the matrix reduction procedure progresses, some removable induced PSs may become *non-removable* due to the gradual deletion of induced PSs in the circuit.

One approach to finding the removable induced PSs of a given circuit would be to start from each induced PSs and use a recursive function to determine if the adjacent induced PSs are removable themselves. Our phase simplification algorithm does the opposite by starting from the induced PSs that are trivially removable, i.e. adjacent to three controlled PSs or phase-invariant input/output ports. These trivially removable induced PSs are labelled as removable by the algorithm and the associated linear reduction coefficients (α_k in Fig. 4a) are stored. The algorithm subsequently processes in the same way induced PSs adjacent to the newly labelled induced PSs. The procedure is iterated until no new adjacent removable induced PSs can be found.

If there are however still induced PSs left in the circuit at this stage, this implies that the circuit features at least one non-removable induced PS. In that case, the algorithm randomly designates one of the remaining induced PSs as non-removable. Non-removable induced PSs are on equal footing with controlled PSs in the sense that they are static in the circuit and can absorb adjacent phase shifts. The algorithm then resumes its iterative procedure until all induced PSs have been labelled. We prove in App. E 2 that the number of non-removable induced PSs found by our phase simplification algorithm is minimal.

The presence of a non-removable induced PS in a circuit entails that its initial rectangular crosstalk matrix cannot be reduced to a square matrix by linear transformations by repeated application of Theorem 1. As shown on Fig. 4d, this does not provide an optimal PIC control accuracy but improves nevertheless the control accuracy of the circuit.

The presented phase simplification algorithm is flexible as it can be extended with additional rules for removing induced PSs if the circuit features components other than phase shifters and beamsplitters. This would just change the definition of a removable induced PS.

2. Algorithmic complexity

We now discuss the complexity of the phase simplification algorithm. We consider first the general case. The total number of induced PSs to label is less than n_{PS}, as we never reconsider already labelled induced PSs. Establishing a phase relationship between PSs is at most of complexity n_{PS} because a relation could involve all the on-chip PSs. Therefore, the complexity of the full procedure is $O(n_{\mathrm{PS}}^2)$ in the worst case.

In our case, the linear phase relationships are local, thus the relations do not always involve all the on-chip PSs. Thus the stated upper bound is not attained in practice. The reduction algorithm is benchmarked on Clements interferometers with

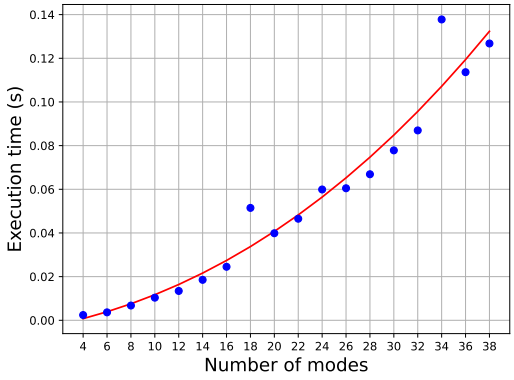

FIG. 9. **Reduction algorithm evaluation on Clements interferometers**. The algorithm is implemented in Python. Each blue point consists in 10 repetitions of the algorithm. We only benchmark the algorithm that establishes the linear relations between the phase shifters, not the crosstalk matrix transformation process. The red curve is a third degree polynomial fit.

the execution time graphed on Fig. 9. We observe that the algorithm scales with $O(m^3)$ with m the number of modes. In a Clements interferometer, the number of phase shifters n_{PS} is related to m via $m \approx \sqrt{n_{\mathrm{PS}}}$. Hence, the scaling of the algorithm is $O(n_{\mathrm{PS}}^{3/2})$ in our case.

Appendix E: PROOF OF CROSSTALK-ROBUSTNESS CRITERION

We prove the graphical criterion of Section IV C that certifies the robustness of a given photonic integrated circuit (PIC) with respect to crosstalk.

1. Proof of Theorem 2 (Crosstalk-robustness criterion)

a. Statement A PIC is crosstalk-robust if and only if its associated pruned graph is acyclic.

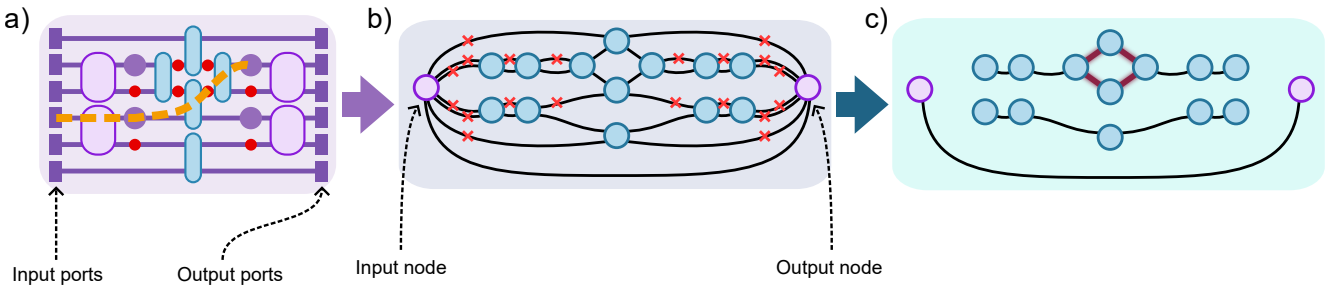

FIG. 10. Graph representation of Fig. 6b. Red edges indicate phase invariant input/output ports. Edges corresponding to waveguides featuring a controlled PS are marked with a red cross.

b. Proof Let us consider an arbitrary PIC, such as the one of Fig. 10a. We call *path* a sequence of phase shifters (PSs) that extends from one PS/input port/output port to another PS/input port/output port (see orange path on Fig. 10a).

Let us consider an induced PS in the PIC. From the rule ϕ-remove (see Fig. 5b) and App. D, the induced PS is removable when it is adjacent to three components of the following type

- phase invariant input/output port,
- controlled PS,
- removable PS.

By this observation, an induced PS is removable to the left (resp. right) when all paths starting from the left (resp. right) of the induced PS eventually reach a phase invariant input/output port or a controlled PS. An induced PS is removable when it is removable to the left or to the right. Consequently, an induced PS is non-removable when it is non-removable to the left and to the right. In other words, an induced PS is non-removable when one of the paths to the left and to the right ends on a phase-dependent input/output port or performs a cycle.

We now convert the PIC into a mathematical graph. The nodes represent the on-chip beamsplitters and the edges interconnecting the nodes symbolize the PIC waveguides. The edges corresponding to PIC waveguide section featuring a controlled PS are marked with a cross. The graph features two additional nodes, called *input* and *output* nodes. Every input (resp. output) port of the circuit is connected to the input (resp. output) node, marked with a cross if the port is phase invariant. The input and output nodes are connected by an edge as well. Any path in the PIC has a corresponding path in the graph.

We obtain a *pruned graph* by deleting every edge marked with a cross. Internal cycles in the pruned graph (connecting beamsplitter nodes) mark cyclic paths in the PIC consisting only of induced PSs, which is the signature of the presence of a non-removable induced PS.

Note that if an induced PS in the PIC has paths to the left and to the right leading to phase-dependent input/output ports, it is non-removable. As the input and output nodes are connected in the graph, this non-removability also manifests as the presence of a cycle.

This proves the theorem. □

2. Proof of maximal reduction for non-crosstalk-robust interferometers: circuit rank of the pruned graphs

When the interferometer is not crosstalk-robust, then by definition its crosstalk matrix cannot be fully reduced to a square matrix (see Section IV C). Non crosstalk-robust interferometers feature induced PSs that cannot be removed from the circuit. We prove here that the number of removed induced PSs following our phase-simplification algorithm of App. D is maximal. Equivalently, this shows that the number of remaining rows in the reduced crosstalk matrix is minimal.

We use the pruned graph formalism introduced in Section IV C. As stated by Theorem 2 and shown in App. E 1, an induced PS cannot be removed if its corresponding edge in the pruned graph belongs to a cycle (see Fig. 10). Reciprocally, if the pruned graph is acyclic, then every induced PS can be removed from the circuit. The remaining edges in the pruned graph represent the induced PSs of the circuit. Therefore, the minimal number of non-removable PSs is the minimal number of edges to remove in the pruned graph to make it acyclic. This number is known as the circuit rank [37], leading to the following theorem:

Theorem 3 (Minimal number of non-removable PS)**.** *The minimal number of non-removable PS in a given PIC is the circuit rank of its associated pruned graph.*

As the pruned graph is undirected, the circuit rank r is straightforward to compute from

$$r = e - v + c, \tag{E1}$$

where e is the number of edges, v is the number of vertices, and c is the number of connected components in the pruned graph. For instance in Fig. 10, we have $e = 13$, $v = 15$ and $c = 3$, yielding indeed $r = 1$, i.e. a single edge must be removed from graph to make it acyclic.

Remarkably, it is possible to find a minimum set of edges breaking all the pruned graph cycles using a greedy algorithm [41]. At each step, the greedy algorithm chooses to cut an edge belonging to at least one cycle of the pruned graph, and continues until there is no cycle. A cut edge by the algorithm in the pruned graph corresponds, in the phase simplification algorithm, to label a non-removable induced PS. More precisely, our phase-simplification algorithm of App. D follows the greedy approach: when no additional induced PS can be identified as removable, the algorithm randomly selects one of the remaining unlabeled induced PS and designates it as non-removable (cutting a random edge in a cycle) and continues until every PS is removable (until the pruned graph is acyclic). The greedy algorithm being optimal for finding the minimum set of edges breaking all the cycles, the phase simplification algorithm gives the minimum number of non-removable PSs, thus the reduction is maximal.

Appendix F: CROSSTALK-ROBUSTNESS CRITERION WITH PHASE-DEPENDENT INPUT PORTS

We illustrate in Fig. 11 the crosstalk-robustness criterion of Section IV C for an interferometer with phase-dependent (opposite of phase-invariant) input and output ports. In practice, this is the case when using the interferometer with coherent states of light and the output lead to a second PIC for instance. The considered interferometer is a variant of the 6-mode

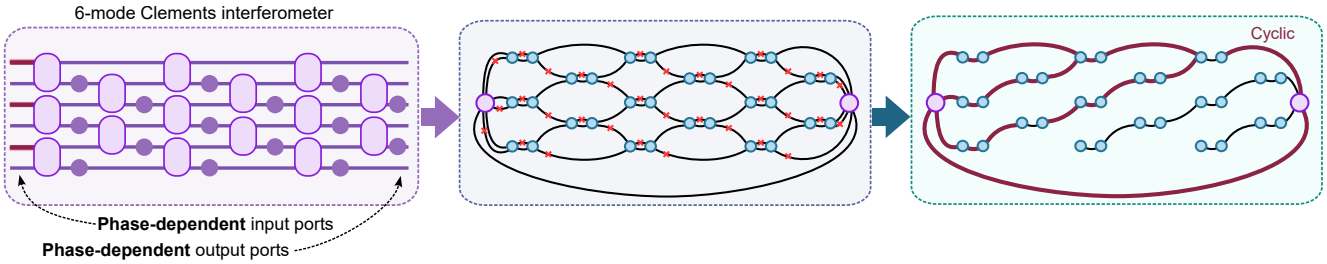

FIG. 11. **Applying the crosstalk-robustness criterion for an interferometer with phase-dependent input ports**.

Clements interferometer with controlled phase shifters (PSs) on some output ports. Applying the crosstalk-robustness criterion reveals that in this configuration, the Clements interferometer is vulnerable to crosstalk, because its pruned graph contains cycles. Adding controlled PSs outside of the MZI mesh, such as in the original Clements mesh [28], restores the crosstalk-robustness of the scheme.

Appendix G: CONVERGENCE COMPARISON WITH BELL-WALMSLEY INTERFEROMETER

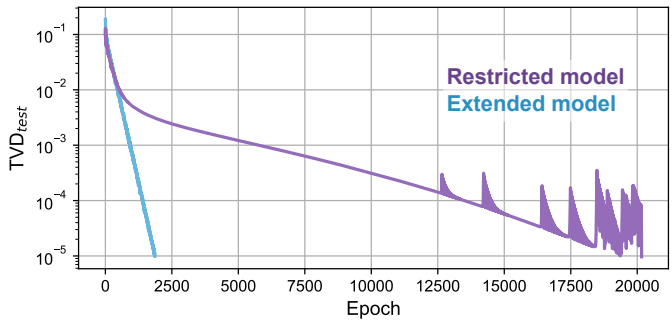

FIG. 12. $\mathrm{TVD}_{\mathrm{test}}$ as a function of the number of epochs processed for characterizing a 12-mode Bell interferometer. The purple (resp. purple) curve is associated to a machine learning model equipped with a restricted (resp. extended) crosstalk model.

Similarly to Section III, we train machine learning models (MLMs) equipped with restricted and extended crosstalk models to characterize a 12-mode Bell-Walmsley interferometer [29]. Fig. 12 shows that the extended MLM converges in substantially fewer epochs to the $\mathrm{TVD}_{\mathrm{test}}$ target of 10^{-5} than the restricted MLM. The characterization duration is 6.5 minutes for the extended MLM and 53.3 minutes for the restricted MLM. All the simulation and training parameters are the same as described in the Methods section, but the simulation was performed with a different CPU and GPU. The ripples in the purple curve in Fig. 12 can be removed by decreasing the learning rate of the model, at the cost of slower descent.

Bibliography

[1] Heurtel, N. *et al.* Perceval: A Software Platform for Discrete Variable Photonic Quantum Computing. *Quantum* **7**, 931 (2023). URL https://quantum-journal.org/papers/q-2023-02-21-931/. Publisher: Verein zur Förderung des Open Access Publizierens in den Quantenwissenschaften.

[2] Maring, N. *et al.* One Nine Availability of a Photonic Quantum Computer on the Cloud Toward HPC Integration. In *2023 IEEE International Conference on Quantum Computing and Engineering (QCE)*, vol. 02, 112–116 (2023). URL https://ieeexplore.ieee.org/document/10313716.

[3] Fyrillas, A. *et al.* Certified Randomness in Tight Space. *PRX Quantum* **5**, 020348 (2024). URL https://link.aps.org/doi/10.1103/PRXQuantum.5.020348. Publisher: American Physical Society.

[4] Pont, M. *et al.* High-fidelity four-photon GHZ states on chip. *npj Quantum Information* **10**, 1–7 (2024). URL https://www.nature.com/articles/s41534-024-00830-z. Publisher: Nature Publishing Group.

[5] Maring, N. *et al.* A versatile single-photon-based quantum computing platform. *Nature Photonics* 1–7 (2024). URL https://www.nature.com/articles/s41566-024-01403-4. Publisher: Nature Publishing Group.

[6] Fyrillas, A., Faure, O., Maring, N., Senellart, J. & Belabas, N. Scalable machine learning-assisted clear-box characterization for optimally controlled photonic circuits. *Optica* **11**, 427–436 (2024). URL https://opg.optica.org/optica/abstract.cfm?uri=optica-11-3-427. Publisher: Optica Publishing Group.

[7] Fyrillas, A. *et al.* (In preparation) Resource-efficient crosstalk mitigation for the high-fidelity operation of photonic integrated circuits with induced phase shifters.

[8] Feynman, R. P. Simulating Physics with Computers. In *Feynman And Computation* (CRC Press, 2002). Num Pages: 21.

[9] Gisin, N. & Thew, R. Quantum communication. *Nature Photonics* **1**, 165–171 (2007). URL https://www.nature.com/articles/nphoton.2007.22. Publisher: Nature Publishing Group.

[10] Krantz, P. *et al.* A quantum engineer's guide to superconducting qubits. *Applied Physics Reviews* **6**, 021318 (2019). URL https://aip.scitation.org/doi/full/10.1063/1.5089550. Publisher: American Institute of Physics.

[11] Bruzewicz, C. D., Chiaverini, J., McConnell, R. & Sage, J. M. Trapped-ion quantum computing: Progress and challenges. *Applied Physics Reviews* **6**, 021314 (2019). URL https://doi.org/10.1063/1.5088164.

[12] Flamini, F., Spagnolo, N. & Sciarrino, F. Photonic quantum information processing: a review. *Reports on Progress in Physics* **82**, 016001 (2018). URL https://doi.org/10.1088/1361-6633/aad5b2. Publisher: IOP Publishing.

[13] Slussarenko, S. & Pryde, G. J. Photonic quantum information processing: A concise review. *Applied Physics Reviews* **6**, 041303 (2019). URL https://aip.scitation.org/doi/full/10.1063/1.5115814. Publisher: American Institute of Physics.

[14] Aaronson, S. & Arkhipov, A. The Computational Complexity of Linear Optics. *Theory of Computing* **9**, 143–252 (2013). URL https://theoryofcomputing.org/articles/v009a004/. Number: 4 Publisher: Theory of Computing.

[15] Zhong, H.-S. *et al.* Phase-Programmable Gaussian Boson Sampling Using Stimulated Squeezed Light. *Physical Review Letters* **127**, 180502 (2021). URL https://link.aps.org/doi/10.1103/PhysRevLett.127.180502. Publisher: American Physical Society.

[16] Madsen, L. S. *et al.* Quantum computational advantage with a programmable photonic processor. *Nature* **606**, 75–81 (2022). URL https://www.nature.com/articles/s41586-022-04725-x. Number: 7912 Publisher: Nature Publishing Group.

[17] Politi, A., Cryan, M. J., Rarity, J. G., Yu, S. & O'Brien, J. L. Silica-on-Silicon Waveguide Quantum Circuits. *Science* **320**, 646–649 (2008). URL https://www.science.org/doi/10.1126/science.1155441. Publisher: American Association for the Advancement of Science.

[18] Taballione, C. *et al.* 20-Mode Universal Quantum Photonic Processor. *Quantum* **7**, 1071 (2023). URL https://quantum-journal.org/papers/q-2023-08-01-1071/. Publisher: Verein zur Förderung des Open Access Publizierens in den Quantenwissenschaften.

[19] Knill, E., Laflamme, R. & Milburn, G. J. A scheme for efficient quantum computation with linear optics. *Nature* **409**, 46–52 (2001). URL https://www.nature.com/articles/35051009. Publisher: Nature Publishing Group.

[20] Kok, P. *et al.* Linear optical quantum computing with photonic qubits. *Reviews of Modern Physics* **79**, 135–174 (2007). URL https://link.aps.org/doi/10.1103/RevModPhys.79.135. Publisher: American Physical Society.

[21] Mower, J., Harris, N. C., Steinbrecher, G. R., Lahini, Y. & Englund, D. High-fidelity quantum state evolution in imperfect photonic integrated circuits. *Physical Review A* **92**, 032322 (2015). URL https://link.aps.org/doi/10.1103/PhysRevA.92.032322. Publisher: American Physical Society.

[22] Milanizadeh, M., Aguiar, D., Melloni, A. & Morichetti, F. Canceling Thermal Cross-Talk Effects in Photonic Integrated Circuits. *Journal of Lightwave Technology* **37**, 1325–1332 (2019). Conference Name: Journal of Lightwave Technology.

[23] Bandyopadhyay, S., Hamerly, R., Hamerly, R. & Englund, D. Hardware error correction for programmable photonics. *Optica* **8**, 1247–1255 (2021). URL https://opg.optica.org/optica/abstract.cfm?uri=optica-8-10-1247. Publisher: Optica Publishing Group.

[24] Kumar, S. P. *et al.* Mitigating linear optics imperfections via port allocation and compilation (2021). URL http://arxiv.org/abs/2103.03183. ArXiv:2103.03183 [physics, physics:quant-ph].

[25] Tran, M. A. *et al.* Ultra-Low-Loss Silicon Waveguides for Heterogeneously Integrated Silicon/III-V Photonics. *Applied Sciences* **8**, 1139 (2018). URL https://www.mdpi.com/2076-3417/8/7/1139. Number: 7 Publisher: Multidisciplinary Digital Publishing Institute.

[26] Desiatov, B., Shams-Ansari, A., Zhang, M., Wang, C. & Lončar, M. Ultra-low-loss integrated visible photonics using thin-film lithium niobate. *Optica* **6**, 380–384 (2019). URL https://opg.optica.org/optica/abstract.cfm?uri=optica-6-3-380. Publisher: Optica Publishing Group.

[27] Chunnilall, C. J., Degiovanni, I. P., Kück, S., Müller, I. & Sinclair, A. G. Metrology of single-photon sources and detectors: a review. *Optical Engineering* **53**, 081910 (2014). URL https://www.spiedigitallibrary.org/journals/optical-engineering/volume-53/issue-8/081910/Metrology-of-single-photon-sources-and-detectors-a-review/10.1117/1.OE.53.8.081910.full. Publisher: SPIE.

[28] Scheel, S. Single-photon sources–an introduction. *Journal of Modern Optics* **56**, 141–160 (2009). URL https://doi.org/10.1080/09500340802331849. Publisher: Taylor & Francis _eprint: https://doi.org/10.1080/09500340802331849.

[29] Vigliar, C. *et al.* Error-protected qubits in a silicon photonic chip. *Nature Physics* **17**, 1137–1143 (2021). URL https://www.nature.com/articles/s41567-021-01333-w. Publisher: Nature Publishing Group.

[30] Bao, J. *et al.* Very-large-scale integrated quantum graph photonics. *Nature Photonics* **17**, 573–581 (2023). URL https://www.nature.com/articles/s41566-023-01187-z. Number: 7 Publisher: Nature Publishing Group.

[31] van der Meer, R. *et al.* Experimental simulation of loop quantum gravity on a photonic chip. *npj Quantum Information* **9**, 1–7 (2023). URL https://www.nature.com/articles/s41534-023-00702-y. Number: 1 Publisher: Nature Publishing Group.

[32] Somaschi, N. *et al.* Near-optimal single-photon sources in the solid state. *Nature Photonics* **10**, 340–345 (2016). URL https://www.nature.com/articles/nphoton.2016.23. Number: 5 Publisher: Nature Publishing Group.

[33] Ding, X. *et al.* High-efficiency single-photon source above the loss-tolerant threshold for efficient linear optical quantum computing (2023). URL http://arxiv.org/abs/2311.08347. ArXiv:2311.08347 [quant-ph].

[34] Wang, H. *et al.* Boson Sampling with 20 Input Photons and a 60-Mode Interferometer in a $1{0}^{14}$-Dimensional Hilbert Space. *Physical Review Letters* **123**, 250503 (2019). URL https://link.aps.org/doi/10.1103/PhysRevLett.123.250503. Publisher: American Physical Society.

[35] Chen, S. *et al.* Heralded three-photon entanglement from a single-photon source on a photonic chip (2023). URL http://arxiv.org/abs/2307.02189. ArXiv:2307.02189 [quant-ph].

[36] Reck, M., Zeilinger, A., Bernstein, H. J. & Bertani, P. Experimental realization of any discrete unitary operator. *Physical Review Letters* **73**, 58–61 (1994). URL https://link.aps.org/doi/10.1103/PhysRevLett.73.58. Publisher: American Physical Society.

[37] Clements, W. R., Humphreys, P. C., Metcalf, B. J., Kolthammer, W. S. & Walmsley, I. A. Optimal design for universal multiport interferometers. *Optica* **3**, 1460–1465 (2016). URL https://opg.optica.org/optica/abstract.cfm?uri=optica-3-12-1460. Publisher: Optica Publishing Group.

[38] Bell, B. A. & Walmsley, I. A. Further compactifying linear optical unitaries. *APL Photonics* **6**, 070804 (2021). URL https://doi.org/10.1063/5.0053421.

[39] Cohen-Tannoudji, C., Laloe, F. & Diu, B. *Mécanique Quantique - Tome 1: Nouvelle édition* (EDP sciences, 2018). Google-Books-ID: 3jRyDwAAQBAJ.

[40] Chambert-Loir, A. *Information Theory: Three Theorems by Claude Shannon*, vol. 144 of *UNITEXT* (Springer International Publishing, Cham, 2022). URL https://link.springer.com/10.1007/978-3-031-21561-2.

[41] Grifone, J. *Algèbre Linéaire 6E Édition* (Éditions Cépaduès, 2019). Google-Books-ID: uRvZwAEACAAJ.

[42] Dukish, B. Computers and the Binary System. In Dukish, B. (ed.) *Coding the Arduino: Building Fun Programs, Games, and Electronic Projects*, 17–36 (Apress, Berkeley, CA, 2018). URL https://doi.org/10.1007/978-1-4842-3510-2_2.

[43] Schlosshauer, M. Quantum decoherence. *Physics Reports* **831**, 1–57 (2019). URL https://www.sciencedirect.com/science/article/pii/S0370157319303084.

[44] Schrödinger, E. An Undulatory Theory of the Mechanics of Atoms and Molecules. *Physical Review* **28**, 1049–1070 (1926). URL https://link.aps.org/doi/10.1103/PhysRev.28.1049. Publisher: American Physical Society.

[45] Hall, B. C. *Lie Groups, Lie Algebras, and Representations: An Elementary Introduction*, vol. 222 of *Graduate Texts in Mathematics* (Springer International Publishing, Cham, 2015). URL https://link.springer.com/10.1007/978-3-319-13467-3.

[46] Nielsen, M. A. & Chuang, I. L. *Quantum Computation and Quantum Information: 10th Anniversary Edition* (Cambridge University Press, 2010).

[47] Aaronson, S. & Gottesman, D. Improved simulation of stabilizer circuits. *Physical Review A* **70**, 052328 (2004). URL https://link.aps.org/doi/10.1103/PhysRevA.70.052328. Publisher: American Physical Society.

[48] Barenco, A. *et al.* Elementary gates for quantum computation. *Physical Review A* **52**, 3457–3467 (1995). URL https://link.aps.org/doi/10.1103/PhysRevA.52.3457. Publisher: American Physical Society.

[49] Boykin, P. O., Mor, T., Pulver, M., Roychowdhury, V. & Vatan, F. A new universal and fault-tolerant quantum basis. *Information Processing Letters* **75**, 101–107 (2000). URL https://www.sciencedirect.com/science/article/pii/S0020019000000843.

[50] Shi, Y. Both Toffoli and Controlled-NOT need little help to do universal quantum computation (2002). URL http://arxiv.org/abs/quant-ph/0205115. ArXiv:quant-ph/0205115.

[51] Wootters, W. K. & Zurek, W. H. A single quantum cannot be cloned. *Nature* **299**, 802–803 (1982). URL https://www.nature.com/articles/299802a0. Publisher: Nature Publishing Group.

[52] Herbert, N. FLASH—A superluminal communicator based upon a new kind of quantum measurement. *Foundations of Physics* **12**, 1171–1179 (1982). URL https://doi.org/10.1007/BF00729622.

[53] Kalckar, J. *Foundations of Quantum Physics II (1933-1958)* (Elsevier, 2013). Google-Books-ID: yet5P7f_630C.

[54] Khrennikov, A. Roots of quantum computing supremacy: superposition, entanglement, or complementarity? *The European Physical Journal Special Topics* **230**, 1053–1057 (2021). URL https://doi.org/10.1140/epjs/s11734-021-00061-9.

[55] Aiello, A., Töppel, F., Marquardt, C., Giacobino, E. & Leuchs, G. Quantumlike nonseparable structures in optical beams. *New Journal of Physics* **17**, 043024 (2015). URL https://dx.doi.org/10.1088/1367-2630/17/4/043024. Publisher: IOP Publishing.

[56] Khrennikov, A. Quantum Versus Classical Entanglement: Eliminating the Issue of Quantum Nonlocality. *Foundations of Physics* **50**, 1762–1780 (2020). URL https://doi.org/10.1007/s10701-020-00319-7.

[57] Jackson, J. D. *Classical electrodynamics* (Wiley, New York, 1999), 3. ed edn. OCLC: 925677836.

[58] Griffiths, D. J. Introduction to Electrodynamics (2023). URL https://www.cambridge.org/highereducation/books/introduction-to-electrodynamics/FD23E188E2BDCDB40199CFE3386EC08F. ISBN: 9781009397735 Publisher: Cambridge University Press.

[59] Grynberg, G., Aspect, A. & Fabre, C. *Introduction to Quantum Optics: From the Semi-classical Approach to Quantized Light* (Cambridge University Press, Cambridge, 2010). URL https://www.cambridge.org/core/books/introduction-to-quantum-optics/F45DCE785DC8226D4156EC15CAD5FA9A.

[60] Johns, O. *Analytical Mechanics for Relativity and Quantum Mechanics* (OUP Oxford, 2005). Google-Books-ID: zocpxybmGfoC.

[61] Loudon, R. *The Quantum Theory of Light* (OUP Oxford, 2000). Google-Books-ID: AEkfajgqldoC.

[62] Cohen-Tannoudji, C., Laloe, F. & Diu, B. *Mécanique quantique - tome III* (EDP sciences, 2017). Google-Books-ID: Nng2DwAAQBAJ.

[63] Scheel, S. Permanents in linear optical networks (2004). URL http://arxiv.org/abs/quant-ph/0406127. ArXiv:quant-ph/0406127.

[64] Mandel, L. & Wolf, E. *Optical Coherence and Quantum Optics* (Cambridge University Press, Cambridge, 1995). URL https://www.cambridge.org/core/books/optical-coherence-and-quantum-optics/F8CB94C70FA64CD3FB60890CA2048168.

[65] Baus, M. & Tejero, C. F. *Equilibrium Statistical Physics: Phases of Matter and Phase Transitions* (Springer Science & Business Media, 2007). Google-Books-ID: EosodCy8qGIC.

[66] Beck, M. Comparing measurements of $g^{(2)}(0)$ performed with different coincidence detection techniques. *JOSA B* **24**, 2972–2978 (2007). URL https://opg.optica.org/josab/abstract.cfm?uri=josab-24-12-2972. Publisher: Optica Publishing Group.

[67] Spagnolo, N. *et al.* General Rules for Bosonic Bunching in Multimode Interferometers. *Physical Review Letters* **111**, 130503 (2013). URL https://link.aps.org/doi/10.1103/PhysRevLett.111.130503. Publisher: American Physical Society.

[68] Hong, C. K., Ou, Z. Y. & Mandel, L. Measurement of subpicosecond time intervals between two photons by interference. *Physical Review Letters* **59**, 2044–2046 (1987). URL https://link.aps.org/doi/10.1103/PhysRevLett.59.2044. Publisher: American Physical Society.

[69] Ollivier, H. *et al.* Hong-Ou-Mandel Interference with Imperfect Single Photon Sources. *Physical Review Letters* **126**, 063602 (2021). URL https://link.aps.org/doi/10.1103/PhysRevLett.126.063602. Publisher: American Physical Society.

[70] Pont, M. *et al.* Quantifying n-Photon Indistinguishability with a Cyclic Integrated Interferometer. *Physical Review X* **12**, 031033 (2022). URL https://link.aps.org/doi/10.1103/PhysRevX.12.031033. Publisher: American Physical Society.

[71] Pont, M. *Multi-photon quantum interference and entanglement*. PhD Thesis (2023). URL http://www.theses.fr/2023UPASP162/document.

[72] Takeoka, M., Jin, R.-B. & Sasaki, M. Full analysis of multi-photon pair effects in spontaneous parametric down conversion based photonic quantum information processing. *New Journal of Physics* **17**, 043030 (2015). URL https://dx.doi.org/10.1088/1367-2630/17/4/043030. Publisher: IOP Publishing.

[73] Meyer-Scott, E., Silberhorn, C. & Migdall, A. Single-photon sources: Approaching the ideal through multiplexing. *Review of Scientific Instruments* **91**, 041101 (2020). URL https://doi.org/10.1063/5.0003320.

[74] Billard, M. *Practical and efficient solid-state sources of single and indistinguishable photons for quantum applications*. These de doctorat, université Paris-Saclay (2021). URL https://theses.fr/2021UPASP015.

[75] Kimble, H. J., Dagenais, M. & Mandel, L. Photon Antibunching in Resonance Fluorescence. *Physical Review Letters* **39**, 691–695 (1977). URL https://link.aps.org/doi/10.1103/PhysRevLett.39.691. Publisher: American Physical Society.

[76] Keller, M., Lange, B., Hayasaka, K., Lange, W. & Walther, H. A calcium ion in a cavity as a controlled single-photon source. *New Journal of Physics* **6**, 95 (2004). URL https://dx.doi.org/10.1088/1367-2630/6/1/095.

[77] Lounis, B. & Moerner, W. E. Single photons on demand from a single molecule at room temperature. *Nature* **407**, 491–493 (2000). URL https://www.nature.com/articles/35035032. Publisher: Nature Publishing Group.

[78] Aharonovich, I., Englund, D. & Toth, M. Solid-state single-photon emitters. *Nature Photonics* **10**, 631–641 (2016). URL https://www.nature.com/articles/nphoton.2016.186. Publisher: Nature Publishing Group.

[79] Esmann, M., Wein, S. C. & Antón-Solanas, C. Solid-state single-photon sources: recent advances for novel quantum materials (2023). URL http://arxiv.org/abs/2312.09280. ArXiv:2312.09280.

[80] Senellart, P., Solomon, G. & White, A. High-performance semiconductor quantum-dot single-photon sources. *Nature Nanotechnology* **12**, 1026–1039 (2017). URL https://www.nature.com/articles/nnano.2017.218. Publisher: Nature Publishing Group.

[81] Giesz, V. *Cavity-enhanced Photon-Photon Interactions With Bright Quantum Dot Sources*. phdthesis, Université Paris Saclay (COmUE) (2015). URL https://theses.hal.science/tel-01272948.

[82] Ollivier, H. *Quantum purity and symmetry control of single-photon sources based on semiconductor quantum dots*. phdthesis, Université Paris-Saclay (2021). URL https://theses.hal.science/tel-03378446.

[83] Baskaran, A. & Smereka, P. Mechanisms of Stranski-Krastanov growth. *Journal of Applied Physics* **111**, 044321 (2012). URL https://doi.org/10.1063/1.3679068.

[84] Dousse, A. *et al.* Controlled Light-Matter Coupling for a Single Quantum Dot Embedded in a Pillar Microcavity Using Far-Field Optical Lithography. *Physical Review Letters* **101**, 267404 (2008). URL https://link.aps.org/doi/10.1103/PhysRevLett.101.267404. Publisher: American Physical Society.

[85] Purcell, E. M., Torrey, H. C. & Pound, R. V. Resonance Absorption by Nuclear Magnetic Moments in a Solid. *Physical Review* **69**, 37–38 (1946). URL https://link.aps.org/doi/10.1103/PhysRev.69.37. Publisher: American Physical Society.

[86] Ramsay, A. J. *et al.* Phonon-Induced Rabi-Frequency Renormalization of Optically Driven Single $\mathrm{InGaAs}/\mathrm{GaAs}$ Quantum Dots. *Physical Review Letters* **105**, 177402 (2010). URL https://link.aps.org/doi/10.1103/PhysRevLett.105.177402. Publisher: American Physical Society.

[87] Wang, H. *et al.* Towards optimal single-photon sources from polarized microcavities. *Nature Photonics* **13**, 770–775 (2019). URL https://www.nature.com/articles/s41566-019-0494-3. Publisher: Nature Publishing Group.

[88] Thomas, S. *et al.* Bright Polarized Single-Photon Source Based on a Linear Dipole. *Physical Review Letters* **126**, 233601 (2021). URL https://link.aps.org/doi/10.1103/PhysRevLett.126.233601. Publisher: American Physical Society.

[89] Quilter, J. *et al.* Phonon-Assisted Population Inversion of a Single $\mathrm{InGaAs}/\mathrm{GaAs}$ Quantum Dot by Pulsed Laser Excitation. *Physical Review Letters* **114**, 137401 (2015). URL https://link.aps.org/doi/10.1103/PhysRevLett.114.137401. Publisher: American Physical Society.

[90] Cosacchi, M., Ungar, F., Cygorek, M., Vagov, A. & Axt, V. Emission-Frequency Separated High Quality Single-Photon Sources Enabled by Phonons. *Physical Review Letters* **123**, 017403 (2019). URL https://link.aps.org/doi/10.1103/PhysRevLett.123.017403. Publisher: American Physical Society.

[91] Gustin, C. & Hughes, S. Efficient Pulse-Excitation Techniques for Single Photon Sources from Quantum Dots in Cavities (2019). URL http://arxiv.org/abs/1906.06447. ArXiv:1906.06447.

[92] Wenniger, I. M. d. B. *Impact of photon-number coherence on the performance and energetics of quantum optics protocols*. phdthesis, Université Paris-Saclay (2023). URL https://theses.hal.science/tel-04128680.

[93] Kuhlmann, A. V. *et al.* Charge noise and spin noise in a semiconductor quantum device. *Nature Physics* **9**, 570–575 (2013). URL https://www.nature.com/articles/nphys2688. Number: 9 Publisher: Nature Publishing Group.

[94] Dong, B. *et al.* Silicon-on-Insulator Waveguide Devices for Broadband Mid-Infrared Photonics. *IEEE Photonics Journal* **9**, 1–10 (2017). URL https://ieeexplore.ieee.org/document/7914632/?arnumber=7914632. Conference Name: IEEE Photonics Journal.

[95] Ceccarelli, F. *et al.* Low Power Reconfigurability and Reduced Crosstalk in Integrated Photonic Circuits Fabricated by Femtosecond Laser Micromachining. *Laser & Photonics Reviews* **14**, 2000024 (2020). URL https://onlinelibrary.wiley.com/doi/abs/10.1002/lpor.202000024. _eprint: https://onlinelibrary.wiley.com/doi/pdf/10.1002/lpor.202000024.

[96] Peruzzo, A., Laing, A., Politi, A., Rudolph, T. & O'Brien, J. L. Multimode quantum interference of photons in multiport integrated devices. *Nature Communications* **2**, 224 (2011). URL https://www.nature.com/articles/ncomms1228. Number: 1 Publisher: Nature Publishing Group.

[97] Hill, M., Leijtens, X., Khoe, G. & Smit, M. Optimizing imbalance and loss in 2 × 2 3-dB multimode interference couplers via access waveguide width. *Journal of Lightwave Technology* **21**, 2305–2313 (2003). URL https://ieeexplore.ieee.org/document/1236502. Conference Name: Journal of Lightwave Technology.

[98] Maese-Novo, A. *et al.* Wavelength independent multimode interference coupler. *Optics Express* **21**, 7033–7040 (2013). URL https://opg.optica.org/oe/abstract.cfm?uri=oe-21-6-7033. Publisher: Optica Publishing Group.

[99] Harris, N. C. *et al.* Efficient, compact and low loss thermo-optic phase shifter in silicon. *Optics Express* **22**, 10487–10493 (2014). URL https://opg.optica.org/oe/abstract.cfm?uri=oe-22-9-10487. Publisher: Optica Publishing Group.

[100] Sattari, H. *et al.* Compact broadband suspended silicon photonic directional coupler. *Optics Letters* **45**, 2997–3000 (2020). URL https://opg.optica.org/ol/abstract.cfm?uri=ol-45-11-2997. Publisher: Optica Publishing Group.

[101] Orlandi, P. *et al.* Tunable silicon photonics directional coupler driven by a transverse temperature gradient. *Optics Letters* **38**, 863–865 (2013). URL https://opg.optica.org/ol/abstract.cfm?uri=ol-38-6-863. Publisher: Optica Publishing Group.

[102] Shen, B., Wang, P., Polson, R. & Menon, R. An integrated-nanophotonics polarization beamsplitter with 2.4 × 2.4 m2 footprint. *Nature Photonics* **9**, 378–382 (2015). URL https://www.nature.com/articles/nphoton.2015.80. Publisher: Nature Publishing Group.

[103] Lammers, K., Alberucci, A., Jisha, C. P., Szameit, A. & Nolte, S. Electro-optical control of polarization in femtosecond-laser written waveguides using an embedded liquid crystal cell. *Optical Materials Express* **14**, 836–846 (2024). URL https://opg.optica.org/ome/abstract.cfm?uri=ome-14-4-836. Publisher: Optica Publishing Group.

[104] Piekarek, M. *et al.* High-extinction ratio integrated photonic filters for silicon quantum photonics. *Optics Letters* **42**, 815–818 (2017). URL https://opg.optica.org/ol/abstract.cfm?uri=ol-42-4-815. Publisher: Optica Publishing Group.

[105] Politi, A., Matthews, J. C. F. & O'Brien, J. L. Shor's Quantum Factoring Algorithm on a Photonic Chip. *Science* **325**, 1221–1221 (2009). URL https://www.science.org/doi/10.1126/science.1173731. Publisher: American Association for the Advancement of Science.

[106] Li, H. W. *et al.* Calibration and High Fidelity Measurement of a Quantum Photonic Chip. *New Journal of Physics* **15**, 063017 (2013). URL http://arxiv.org/abs/1306.1719. ArXiv:1306.1719 [quant-ph].

[107] Metcalf, B. J. *et al.* Multiphoton quantum interference in a multiport integrated photonic device. *Nature Communications* **4**, 1356 (2013). URL https://www.nature.com/articles/ncomms2349. Number: 1 Publisher: Nature Publishing Group.

[108] Metcalf, B. J. *et al.* Quantum teleportation on a photonic chip. *Nature Photonics* **8**, 770–774 (2014). URL https://www.nature.com/articles/nphoton.2014.217. Number: 10 Publisher: Nature Publishing Group.

[109] Shor, P. Algorithms for quantum computation: discrete logarithms and factoring. In *Proceedings 35th Annual Symposium on Foundations of Computer Science*, 124–134 (1994). URL https://ieeexplore.ieee.org/document/365700.

[110] Shadbolt, P. J. *et al.* Generating, manipulating and measuring entanglement and mixture with a reconfigurable photonic circuit. *Nature Photonics* **6**, 45–49 (2012). URL https://www.nature.com/articles/nphoton.2011.283. Number: 1 Publisher: Nature Publishing Group.

[111] Peruzzo, A. *et al.* A variational eigenvalue solver on a photonic quantum processor. *Nature Communications* **5**, 4213 (2014). URL https://www.nature.com/articles/ncomms5213. Publisher: Nature Publishing Group.

[112] Mills, J. & Mezher, R. Mitigating photon loss in linear optical quantum circuits: classical post-processing methods outperforming postselection (2024). URL http://arxiv.org/abs/2405.02278. ArXiv:2405.02278 [quant-ph].

[113] Fldzhyan, S. A., Saygin, M. Y. & Kulik, S. P. Optimal design of error-tolerant reprogrammable multiport interferometers. *Optics Letters* **45**, 2632–2635 (2020). URL https://opg.optica.org/ol/abstract.cfm?uri=ol-45-9-2632. Publisher: Optica Publishing Group.

[114] Saygin, M. *et al.* Robust Architecture for Programmable Universal Unitaries. *Physical Review Letters* **124**, 010501 (2020). URL https://link.aps.org/doi/10.1103/PhysRevLett.124.010501. Publisher: American Physical Society.

[115] Hamerly, R., Bandyopadhyay, S. & Englund, D. Asymptotically fault-tolerant programmable photonics. *Nature Communications* **13**, 6831 (2022). URL https://www.nature.com/articles/s41467-022-34308-3. Number: 1 Publisher: Nature Publishing Group.

[116] Hamerly, R., Basani, J. R., Sludds, A., Vadlamani, S. K. & Englund, D. Towards the Information-Theoretic Limit of Programmable Photonics (2024). URL http://arxiv.org/abs/2408.09673. ArXiv:2408.09673 [physics].

[117] Bogaerts, W. *et al.* Programmable photonic circuits. *Nature* **586**, 207–216 (2020). URL https://www.nature.com/articles/s41586-020-2764-0. Number: 7828 Publisher: Nature Publishing Group.

[118] Pérez-López, D., López, A., DasMahapatra, P. & Capmany, J. Multipurpose self-configuration of programmable photonic circuits. *Nature Communications* **11**, 6359 (2020). URL https://www.nature.com/articles/s41467-020-19608-w. Number: 1 Publisher: Nature Publishing Group.

[119] Rausell-Campo, J. R., Pérez-López, D. & Francoy, J. C. Universal Unitary Transformations on a Programmable Integrated Photonic Processor. In *2024 IEEE Photonics Society Summer Topicals Meeting Series (SUM)*, 1–2 (2024). URL https://ieeexplore.ieee.org/abstract/document/10614542. ISSN: 2376-8614.

[120] Luo, W. *et al.* Recent progress in quantum photonic chips for quantum communication and internet. *Light: Science & Applications* **12**, 175 (2023). URL https://www.nature.com/articles/s41377-023-01173-8. Publisher: Nature Publishing Group.

[121] Roeloffzen, C. G. H. *et al.* Low-Loss Si3N4 TriPleX Optical Waveguides: Technology and Applications Overview. *IEEE Journal of Selected Topics in Quantum Electronics* **24**, 1–21 (2018). URL http://ieeexplore.ieee.org/document/8259277/.

[122] Taballione, C. *et al.* A universal fully reconfigurable 12-mode quantum photonic processor. *Materials for Quantum Technology* **1**, 035002 (2021). URL https://doi.org/10.1088/2633-4356/ac168c. Publisher: IOP Publishing.

[123] Pentangelo, C. *et al.* High-fidelity and polarization-insensitive universal photonic processors fabricated by femtosecond laser writing. *Nanophotonics* (2024). URL https://www.degruyter.com/document/doi/10.1515/nanoph-2023-0636/html. Publisher: De Gruyter.

[124] Dong, M. *et al.* High-speed programmable photonic circuits in a cryogenically compatible, visible–near-infrared 200 mm CMOS architecture. *Nature Photonics* **16**, 59–65 (2022). URL https://www.nature.com/articles/s41566-021-00903-x. Number: 1 Publisher: Nature Publishing Group.

[125] Li, M. *et al.* Lithium niobate photonic-crystal electro-optic modulator. *Nature Communications* **11**, 4123 (2020). URL https://www.nature.com/articles/s41467-020-17950-7. Number: 1 Publisher: Nature Publishing Group.

[126] Carolan, J. *et al.* Universal linear optics. *Science (New York, N.Y.)* **349**, 711–716 (2015).

[127] Goede, M. d. *et al.* High Fidelity 12-Mode Quantum Photonic Processor Operating at InGaAs Quantum Dot Wavelength. In *Optica Advanced Photonics Congress 2022 (2022), paper ITu4B.3*, ITu4B.3 (Optica Publishing Group, 2022). URL https://opg.optica.org/abstract.cfm?uri=IPRSN-2022-ITu4B.3.

[128] Arrazola, J. M. *et al.* Quantum circuits with many photons on a programmable nanophotonic chip. *Nature* **591**, 54–60 (2021). URL https://www.nature.com/articles/s41586-021-03202-1. Number: 7848 Publisher: Nature Publishing Group.

[129] Ashtiani, F., Geers, A. J. & Aflatouni, F. An on-chip photonic deep neural network for image classification. *Nature* **606**, 501–506 (2022). URL https://www.nature.com/articles/s41586-022-04714-0. Number: 7914 Publisher: Nature Publishing Group.

[130] Bandyopadhyay, S. *et al.* Single chip photonic deep neural network with accelerated training (2022). URL http://arxiv.org/abs/2208.01623. ArXiv:2208.01623 [physics].

[131] Dyakonov, I. V. *et al.* Reconfigurable Photonics on a Glass Chip. *Physical Review Applied* **10**, 044048 (2018). URL https://link.aps.org/doi/10.1103/PhysRevApplied.10.044048. Publisher: American Physical Society.

[132] Ceccarelli, F. *et al.* Universal photonic processors in a glass-based femtosecond laser writing platform. In *Photonics in Switching and Computing 2021 (2021), paper W2A.3*, W2A.3 (Optica Publishing Group, 2021). URL https://opg.optica.org/abstract.cfm?uri=PSC-2021-W2A.3.

[133] Giordani, T. *et al.* Experimental certification of contextuality, coherence, and dimension in a programmable universal photonic processor. *Science Advances* **9**, eadj4249 (2023). URL https://www.science.org/doi/full/10.1126/sciadv.adj4249. Publisher: American Association for the Advancement of Science.

[134] Kondratyev, I. V. *et al.* Large-scale error-tolerant programmable interferometer fabricated by femtosecond laser writing (2023). URL http://arxiv.org/abs/2308.13452. ArXiv:2308.13452 [physics, physics:quant-ph].

[135] Rodari, G. *et al.* Semi-device independent characterization of multiphoton indistinguishability (2024). URL http://arxiv.org/abs/2404.18636. ArXiv:2404.18636 [quant-ph].

[136] Zhong, H.-S. *et al.* Quantum computational advantage using photons. *Science* **370**, 1460–1463 (2020). URL https://www.science.org/doi/10.1126/science.abe8770. Publisher: American Association for the Advancement of Science.

[137] Fukui, K. & Takeda, S. Building a large-scale quantum computer with continuous-variable optical technologies. *Journal of Physics B: Atomic, Molecular and Optical Physics* **55**, 012001 (2022). URL https://dx.doi.org/10.1088/1361-6455/ac489c. Publisher: IOP Publishing.

[138] Cimini, V. *et al.* Calibration of Multiparameter Sensors via Machine Learning at the Single-Photon Level. *Physical Review Applied* **15**, 044003 (2021). URL https://link.aps.org/doi/10.1103/PhysRevApplied.15.044003. Publisher: American Physical Society.

[139] Mezher, R., Carvalho, A. F. & Mansfield, S. Solving graph problems with single-photons and linear optics (2023). URL http://arxiv.org/abs/2301.09594. ArXiv:2301.09594 [quant-ph].

[140] Sansoni, L. *et al.* Two-Particle Bosonic-Fermionic Quantum Walk via Integrated Photonics. *Physical Review Letters* **108**, 010502 (2012). URL https://link.aps.org/doi/10.1103/PhysRevLett.108.010502. Publisher: American Physical Society.

[141] Crespi, A. *et al.* Anderson localization of entangled photons in an integrated quantum walk. *Nature Photonics* **7**, 322–328 (2013). URL https://www.nature.com/articles/nphoton.2013.26. Publisher: Nature Publishing Group.

[142] Brod, D. J. *et al.* Photonic implementation of boson sampling: a review. *Advanced Photonics* **1**, 034001 (2019). URL https://www.spiedigitallibrary.org/journals/advanced-photonics/volume-1/issue-3/034001/Photonic-implementation-of-boson-sampling-a-review/10.1117/1.AP.1.3.034001.full. Publisher: SPIE.

[143] Heurtel, N., Mansfield, S., Senellart, J. & Valiron, B. Strong simulation of linear optical processes. *Computer Physics Communications* **291**, 108848 (2023). URL https://www.sciencedirect.com/science/article/pii/S0010465523001935.

[144] Hamilton, C. S. *et al.* Gaussian Boson Sampling. *Physical Review Letters* **119**, 170501 (2017). URL https://link.aps.org/doi/10.1103/PhysRevLett.119.170501. Publisher: American Physical Society.

[145] Schnabel, R. Squeezed states of light and their applications in laser interferometers (2017). URL http://arxiv.org/abs/1611.03986. ArXiv:1611.03986.

[146] Deng, Y.-H. *et al.* Gaussian Boson Sampling with Pseudo-Photon-Number Resolving Detectors and Quantum Computational Advantage (2023). URL http://arxiv.org/abs/2304.12240. ArXiv:2304.12240 [quant-ph].

[147] Paesani, S. *et al.* Generation and sampling of quantum states of light in a silicon chip. *Nature Physics* **15**, 925–929 (2019). URL https://www.nature.com/articles/s41567-019-0567-8. Publisher: Nature Publishing Group.

[148] Cerezo, M. *et al.* Variational quantum algorithms. *Nature Reviews Physics* **3**, 625–644 (2021). URL https://www.nature.com/articles/s42254-021-00348-9. Publisher: Nature Publishing Group.

[149] Biamonte, J. *et al.* Quantum machine learning. *Nature* **549**, 195–202 (2017). URL https://www.nature.com/articles/nature23474. Publisher: Nature Publishing Group.

[150] Havlíček, V. *et al.* Supervised learning with quantum-enhanced feature spaces. *Nature* **567**, 209–212 (2019). URL https://www.nature.com/articles/s41586-019-0980-2. Publisher: Nature Publishing Group.

[151] Bartkiewicz, K. *et al.* Experimental kernel-based quantum machine learning in finite feature space. *Scientific Reports* **10**, 12356 (2020). URL https://www.nature.com/articles/s41598-020-68911-5. Publisher: Nature Publishing Group.

[152] Ralph, T. C., Langford, N. K., Bell, T. B. & White, A. G. Linear optical controlled-NOT gate in the coincidence basis. *Physical Review A* **65**, 062324 (2002). URL https://link.aps.org/doi/10.1103/PhysRevA.65.062324. Publisher: American Physical Society.

[153] Knill, E. Quantum gates using linear optics and postselection. *Physical Review A* **66**, 052306 (2002). URL https://link.aps.org/doi/10.1103/PhysRevA.66.052306. Publisher: American Physical Society.

[154] Ralph, T. C., White, A. G., Munro, W. J. & Milburn, G. J. Simple scheme for efficient linear optics quantum gates. *Physical Review A* **65**, 012314 (2001). URL https://link.aps.org/doi/10.1103/PhysRevA.65.012314. Publisher: American Physical Society.

[155] Bennett, C. H. *et al.* Teleporting an unknown quantum state via dual classical and Einstein-Podolsky-Rosen channels. *Physical Review Letters* **70**, 1895–1899 (1993). URL https://link.aps.org/doi/10.1103/PhysRevLett.70.1895.

[156] Gottesman, D. & Chuang, I. L. Demonstrating the viability of universal quantum computation using teleportation and single-qubit operations. *Nature* **402**, 390–393 (1999). URL https://www.nature.com/articles/46503. Publisher: Nature Publishing Group.

[157] Pirandola, S., Eisert, J., Weedbrook, C., Furusawa, A. & Braunstein, S. L. Advances in quantum teleportation. *Nature Photonics* **9**, 641–652 (2015). URL https://www.nature.com/articles/nphoton.2015.154. Publisher: Nature Publishing Group.

[158] Raussendorf, R. & Briegel, H. J. A One-Way Quantum Computer. *Physical Review Letters* **86**, 5188–5191 (2001). URL https://link.aps.org/doi/10.1103/PhysRevLett.86.5188. Publisher: American Physical Society.

[159] Briegel, H. J., Browne, D. E., Dür, W., Raussendorf, R. & Van den Nest, M. Measurement-based quantum computation. *Nature Physics* **5**, 19–26 (2009). URL https://www.nature.com/articles/nphys1157. Publisher: Nature Publishing Group.

[160] Hein, M. *et al.* Entanglement in Graph States and its Applications (2006). URL http://arxiv.org/abs/quant-ph/0602096. ArXiv:quant-ph/0602096.

[161] Ciampini, M. A. *et al.* Path-polarization hyperentangled and cluster states of photons on a chip. *Light: Science & Applications* **5**, e16064–e16064 (2016). URL https://www.nature.com/articles/lsa201664. Number: 4 Publisher: Nature Publishing Group.

[162] Adcock, J. C., Vigliar, C., Santagati, R., Silverstone, J. W. & Thompson, M. G. Programmable four-photon graph states on a silicon chip. *Nature Communications* **10**, 3528 (2019). URL https://www.nature.com/articles/s41467-019-11489-y. Number: 1 Publisher: Nature Publishing Group.

[163] Coste, N. *et al.* High-rate entanglement between a semiconductor spin and indistinguishable photons. *Nature Photonics* **17**, 582–587 (2023). URL https://www.nature.com/articles/s41566-023-01186-0. Publisher: Nature Publishing Group.

[164] Browne, D. E. & Rudolph, T. Resource-efficient linear optical quantum computation. *Physical Review Letters* **95**, 010501 (2005). URL http://arxiv.org/abs/quant-ph/0405157. ArXiv:quant-ph/0405157.

[165] Huang, J. *et al.* Demonstration of hypergraph-state quantum information processing. *Nature Communications* **15**, 2601 (2024). URL https://www.nature.com/articles/s41467-024-46830-7. Publisher: Nature Publishing Group.

[166] Galton, F. Dice for Statistical Experiments. *Nature* **42**, 13–14 (1890). URL https://www.nature.com/articles/042013a0. Number: 1070 Publisher: Nature Publishing Group.

[167] Mannalath, V., Mishra, S. & Pathak, A. A Comprehensive Review of Quantum Random Number Generators: Concepts, Classification and the Origin of Randomness (2022). URL http://arxiv.org/abs/2203.00261. ArXiv:2203.00261 [quant-ph].

[168] James, F. A review of pseudorandom number generators. *Computer Physics Communications* **60**, 329–344 (1990). URL https://www.sciencedirect.com/science/article/pii/001046559090032V.

[169] Zhun, H. & Hongyi, C. A truly random number generator based on thermal noise. In *ASICON 2001. 2001 4th International Conference on ASIC Proceedings (Cat. No.01TH8549)*, 862–864 (2001).

[170] Herrero-Collantes, M. & Garcia-Escartin, J. C. Quantum random number generators. *Reviews of Modern Physics* **89**, 015004 (2017). URL https://link.aps.org/doi/10.1103/RevModPhys.89.015004. Publisher: American Physical Society.

[171] Rarity, J., Owens, P. & Tapster, P. Quantum Random-number Generation and Key Sharing. *Journal of Modern Optics* **41**, 2435–2444 (1994). URL https://doi.org/10.1080/09500349414552281. Publisher: Taylor & Francis _eprint: https://doi.org/10.1080/09500349414552281.

[172] Hensen, B. *et al.* Loophole-free Bell inequality violation using electron spins separated by 1.3 kilometres. *Nature* **526**, 682–686 (2015). URL https://www.nature.com/articles/nature15759. Number: 7575 Publisher: Nature Publishing Group.

[173] Liu, Y. *et al.* Device-independent quantum random-number generation. *Nature* **562**, 548–551 (2018). URL https://www.nature.com/articles/s41586-018-0559-3. Number: 7728 Publisher: Nature Publishing Group.

[174] Bierhorst, P. *et al.* Experimentally generated randomness certified by the impossibility of superluminal signals. *Nature* **556**, 223–226 (2018). URL https://www.nature.com/articles/s41586-018-0019-0. Number: 7700 Publisher: Nature Publishing Group.

[175] Zhang, Y. *et al.* Experimental Low-Latency Device-Independent Quantum Randomness. *Physical Review Letters* **124**, 010505 (2020). URL https://link.aps.org/doi/10.1103/PhysRevLett.124.010505. Publisher: American Physical Society.

[176] Li, M.-H. *et al.* Experimental Realization of Device-Independent Quantum Randomness Expansion. *Physical Review Letters* **126**, 050503 (2021). URL https://link.aps.org/doi/10.1103/PhysRevLett.126.050503. Publisher: American Physical Society.

[177] Shalm, L. K. *et al.* Device-independent randomness expansion with entangled photons. *Nature Physics* **17**, 452–456 (2021). URL https://www.nature.com/articles/s41567-020-01153-4. Number: 4 Publisher: Nature Publishing Group.

[178] Pironio, S. *et al.* Random Numbers Certified by Bell's Theorem. *Nature* **464**, 1021–1024 (2010). URL http://arxiv.org/abs/0911.3427. ArXiv:0911.3427 [quant-ph].

[179] Liu, W.-Z. *et al.* Device-independent randomness expansion against quantum side information. *Nature Physics* **17**, 448–451 (2021). URL https://www.nature.com/articles/s41567-020-01147-2. Number: 4 Publisher: Nature Publishing Group.

[180] Brunner, N., Cavalcanti, D., Pironio, S., Scarani, V. & Wehner, S. Bell nonlocality. *Reviews of Modern Physics* **86**, 419–478 (2014). URL https://link.aps.org/doi/10.1103/RevModPhys.86.419. Publisher: American Physical Society.

[181] Clauser, J. F., Horne, M. A., Shimony, A. & Holt, R. A. Proposed Experiment to Test Local Hidden-Variable Theories. *Physical Review Letters* **23**, 880–884 (1969). URL https://link.aps.org/doi/10.1103/PhysRevLett.23.880. Publisher: American Physical Society.

[182] Abramsky, S. & Brandenburger, A. The sheaf-theoretic structure of non-locality and contextuality. *New Journal of Physics* **13**, 113036 (2011). URL https://iopscience.iop.org/article/10.1088/1367-2630/13/11/113036.

[183] Budroni, C., Cabello, A., Gühne, O., Kleinmann, M. & Larsson, J.- Kochen-Specker contextuality. *Reviews of Modern Physics* **94**, 045007 (2022). URL https://link.aps.org/doi/10.1103/RevModPhys.94.045007. Publisher: American Physical Society.

[184] Abramsky, S., Barbosa, R. S. & Mansfield, S. The contextual fraction as a measure of contextuality. *Physical Review Letters* **119**, 050504 (2017). URL http://arxiv.org/abs/1705.07918. ArXiv:1705.07918 [quant-ph].

[185] Vallée, K. *et al.* Corrected Bell and non-contextuality inequalities for realistic experiments. *Philosophical Transactions of the Royal Society A: Mathematical, Physical and Engineering Sciences* **382**, 20230011 (2024). URL https://royalsocietypublishing.org/doi/full/10.1098/rsta.2023.0011. Publisher: Royal Society.

[186] Miller, C. A. & Shi, Y. Universal Security for Randomness Expansion from the Spot-Checking Protocol. *SIAM Journal on Computing* **46**, 1304–1335 (2017). URL https://epubs.siam.org/doi/10.1137/15M1044333. Publisher: Society for Industrial and Applied Mathematics.

[187] Krawczyk, H. New Hash Functions for Message Authentication. In Guillou, L. C. & Quisquater, J.-J. (eds.) *Advances in Cryptology — EUROCRYPT '95*, 301–310 (Springer, Berlin, Heidelberg, 1995).

[188] Trevisan, L. Extractors and Pseudorandom Generators. *Journal of the ACM* **48**, 860–879 (2001).

[189] Ma, X. *et al.* Postprocessing for quantum random-number generators: Entropy evaluation and randomness extraction. *Physical Review A* **87**, 062327 (2013). URL https://link.aps.org/doi/10.1103/PhysRevA.87.062327. Publisher: American Physical Society.

[190] De, A., Portmann, C., Vidick, T. & Renner, R. Trevisan's Extractor in the Presence of Quantum Side Information. *SIAM Journal on Computing* **41**, 915–940 (2012). URL https://epubs.siam.org/doi/abs/10.1137/100813683. Publisher: Society for Industrial and Applied Mathematics.

[191] Wein, S. C. Modelling Markovian light-matter interactions for quantum optical devices in the solid state (2021). URL http://arxiv.org/abs/2105.06580. ArXiv:2105.06580 [quant-ph].

[192] Navascues, M., Pironio, S. & Acin, A. A convergent hierarchy of semidefinite programs characterizing the set of quantum correlations (2008). URL https://arxiv.org/abs/0803.4290v1.

[193] Larsson, J.- & Gill, R. D. Bell's inequality and the coincidence-time loophole. *Europhysics Letters* **67**, 707 (2004). URL https://iopscience.iop.org/article/10.1209/epl/i2004-10124-7/meta. Publisher: IOP Publishing.

[194] Christensen, B. G. *et al.* Analysis of coincidence-time loopholes in experimental Bell tests. *Physical Review A* **92**, 032130 (2015). URL https://link.aps.org/doi/10.1103/PhysRevA.92.032130. Publisher: American Physical Society.

[195] Storz, S. *et al.* Loophole-free Bell inequality violation with superconducting circuits. *Nature* **617**, 265–270 (2023). URL https://www.nature.com/articles/s41586-023-05885-0. Number: 7960 Publisher: Nature Publishing Group.

[196] Liu, Y. *et al.* High-Speed Device-Independent Quantum Random Number Generation without a Detection Loophole. *Physical Review Letters* **120**, 010503 (2018). URL https://link.aps.org/doi/10.1103/PhysRevLett.120.010503. Publisher: American Physical Society.

[197] Shen, L. *et al.* Randomness Extraction from Bell Violation with Continuous Parametric Down-Conversion. *Physical Review Letters* **121**, 150402 (2018). URL https://link.aps.org/doi/10.1103/PhysRevLett.121.150402. Publisher: American Physical Society.

[198] Um, M. *et al.* Randomness Expansion Secured by Quantum Contextuality. *Physical Review Applied* **13**, 034077 (2020). URL https://link.aps.org/doi/10.1103/PhysRevApplied.13.034077. Publisher: American Physical Society.

[199] Altman, D. G. & Bland, J. M. Standard deviations and standard errors. *BMJ : British Medical Journal* **331**, 903 (2005). URL https://www.ncbi.nlm.nih.gov/pmc/articles/PMC1255808/.

[200] Wang, X.-L. *et al.* 18-Qubit Entanglement with Six Photons' Three Degrees of Freedom. *Physical Review Letters* **120**, 260502 (2018). URL https://link.aps.org/doi/10.1103/PhysRevLett.120.260502. Publisher: American Physical Society.

[201] Li, J.-P. *et al.* Multiphoton Graph States from a Solid-State Single-Photon Source. *ACS Photonics* **7**, 1603–1610 (2020). URL https://doi.org/10.1021/acsphotonics.0c00192. Publisher: American Chemical Society.

[202] Hillery, M., Bužek, V. & Berthiaume, A. Quantum secret sharing. *Physical Review A* **59**, 1829–1834 (1999). URL https://link.aps.org/doi/10.1103/PhysRevA.59.1829. Publisher: American Physical Society.

[203] Chae, E., Choi, J. & Kim, J. An elementary review on basic principles and developments of qubits for quantum computing. *Nano Convergence* **11**, 11 (2024). URL https://doi.org/10.1186/s40580-024-00418-5.

[204] Acharya, R. *et al.* Suppressing quantum errors by scaling a surface code logical qubit. *Nature* **614**, 676–681 (2023). URL https://www.nature.com/articles/s41586-022-05434-1. Publisher: Nature Publishing Group.

[205] Roffe, J. Quantum Error Correction: An Introductory Guide. *Contemporary Physics* **60**, 226–245 (2019). URL http://arxiv.org/abs/1907.11157. ArXiv:1907.11157 [quant-ph].

[206] Zong, Z. *et al.* Optimization of a Controlled-Z Gate with Data-Driven Gradient-Ascent Pulse Engineering in a Superconducting-Qubit System. *Physical Review Applied* **15**, 064005 (2021). URL https://link.aps.org/doi/10.1103/PhysRevApplied.15.064005. Publisher: American Physical Society.

[207] Banerjee, S., Nikdast, M. & Chakrabarty, K. Characterizing Coherent Integrated Photonic Neural Networks under Imperfections. *Journal of Lightwave Technology* **41**, 1464–1479 (2023). URL http://arxiv.org/abs/2207.10835. ArXiv:2207.10835 [cs, eess].

[208] Marcatili, E. a. J. Dielectric Rectangular Waveguide and Directional Coupler for Integrated Optics. *Bell System Technical Journal* **48**, 2071–2102 (1969). URL https://onlinelibrary.wiley.com/doi/abs/10.1002/j.1538-7305.1969.tb01166.x. _eprint: https://onlinelibrary.wiley.com/doi/pdf/10.1002/j.1538-7305.1969.tb01166.x.

[209] Russell, N. J., Chakhmakhchyan, L., O'Brien, J. L. & Laing, A. Direct dialling of Haar random unitary matrices. *New Journal of Physics* **19**, 033007 (2017). URL https://dx.doi.org/10.1088/1367-2630/aa60ed. Publisher: IOP Publishing.

[210] Burgwal, R. *et al.* Using an imperfect photonic network to implement random unitaries. *Optics Express* **25**, 28236–28245 (2017). URL https://opg.optica.org/oe/abstract.cfm?uri=oe-25-23-28236. Publisher: Optica Publishing Group.

[211] Yang, Y. *et al.* Phase coherence length in silicon photonic platform. *Optics Express* **23**, 16890–16902 (2015). URL https://opg.optica.org/oe/abstract.cfm?uri=oe-23-13-16890. Publisher: Optica Publishing Group.

[212] Ruder, S. An overview of gradient descent optimization algorithms (2017). URL http://arxiv.org/abs/1609.04747. ArXiv:1609.04747 [cs].

[213] Nelder, J. A. & Mead, R. A Simplex Method for Function Minimization. *The Computer Journal* **7**, 308–313 (1965). URL https://doi.org/10.1093/comjnl/7.4.308.

[214] Bartz-Beielstein, T., Branke, J., Mehnen, J. & Mersmann, O. Evolutionary Algorithms. *WIREs Data Mining and Knowledge Discovery* **4**, 178–195 (2014). URL https://onlinelibrary.wiley.com/doi/abs/10.1002/widm.1124. _eprint: https://onlinelibrary.wiley.com/doi/pdf/10.1002/widm.1124.

[215] Garnett, R. *Bayesian Optimization* (Cambridge University Press, 2023). Google-Books-ID: MBCrEAAAQBAJ.

[216] Laing, A. & O'Brien, J. L. Super-stable tomography of any linear optical device (2012). URL http://arxiv.org/abs/1208.2868. ArXiv:1208.2868 [quant-ph].

[217] Dhand, I., Khalid, A., Lu, H. & Sanders, B. C. Accurate and precise characterization of linear optical interferometers. *Journal of Optics* **18**, 035204 (2016). URL https://dx.doi.org/10.1088/2040-8978/18/3/035204. Publisher: IOP Publishing.

[218] Spagnolo, N. *et al.* Learning an unknown transformation via a genetic approach. *Scientific Reports* **7**, 14316 (2017). URL https://www.nature.com/articles/s41598-017-14680-7. Number: 1 Publisher: Nature Publishing Group.

[219] Rahimi-Keshari, S. *et al.* Direct characterization of linear-optical networks. *Optics Express* **21**, 13450–13458 (2013). URL https://opg.optica.org/oe/abstract.cfm?uri=oe-21-11-13450. Publisher: Optica Publishing Group.

[220] Hamerly, R., Bandyopadhyay, S. & Englund, D. Accurate Self-Configuration of Rectangular Multiport Interferometers. *Physical Review Applied* **18**, 024019 (2022). URL https://link.aps.org/doi/10.1103/PhysRevApplied.18.024019. Publisher: American Physical Society.

[221] Hornik, K., Stinchcombe, M. & White, H. Multilayer feedforward networks are universal approximators. *Neural Networks* **2**, 359–366 (1989). URL https://www.sciencedirect.com/science/article/pii/0893608089900208.

[222] Kuzmin, S., Dyakonov, I. & Kulik, S. Architecture agnostic algorithm for reconfigurable optical interferometer programming. *Optics Express* **29**, 38429–38440 (2021). URL https://opg.optica.org/oe/abstract.cfm?uri=oe-29-23-38429. Publisher: Optica Publishing Group.

[223] Bantysh, B., Katamadze, K., Chernyavskiy, A. & Bogdanov, Y. Fast reconstruction of programmable integrated interferometers. *Optics Express* **31**, 16729–16742 (2023). URL https://opg.optica.org/oe/abstract.cfm?uri=oe-31-10-16729. Publisher: Optica Publishing Group.

[224] Hiai, F. & Petz, D. *Introduction to Matrix Analysis and Applications*. Universitext (Springer International Publishing, Cham, 2014). URL https://link.springer.com/10.1007/978-3-319-04150-6.

[225] Mele, A. A. Introduction to Haar Measure Tools in Quantum Information: A Beginner's Tutorial. *Quantum* **8**, 1340 (2024). URL https://quantum-journal.org/papers/q-2024-05-08-1340/. Publisher: Verein zur Förderung des Open Access Publizierens in den Quantenwissenschaften.

[226] Youssry, A. *et al.* Experimental graybox quantum system identification and control. *npj Quantum Information* **10**, 1–9 (2024). URL https://www.nature.com/articles/s41534-023-00795-5. Publisher: Nature Publishing Group.

[227] Zheng, J.-H. *et al.* Global calibration of large-scale photonic integrated circuits (2024). URL http://arxiv.org/abs/2407.02207. ArXiv:2407.02207 [physics, physics:quant-ph].

[228] Youssry, A., Chapman, R. J., Peruzzo, A., Ferrie, C. & Tomamichel, M. Modeling and control of a reconfigurable photonic circuit using deep learning. *Quantum Science and Technology* **5**, 025001 (2020). URL https://dx.doi.org/10.1088/2058-9565/ab60de. Publisher: IOP Publishing.

[229] Alexiev, C., Mak, J. C. C., Sacher, W. D. & Poon, J. K. S. Calibrating rectangular interferometer meshes with external photodetectors. *OSA Continuum* **4**, 2892–2904 (2021). URL https://opg.optica.org/osac/abstract.cfm?uri=osac-4-11-2892. Publisher: Optica Publishing Group.

[230] Kingma, D. P. & Ba, J. Adam: A Method for Stochastic Optimization (2017). URL http://arxiv.org/abs/1412.6980. ArXiv:1412.6980 [cs].

[231] Milanizadeh, M. *et al.* Control and Calibration Recipes for Photonic Integrated Circuits. *IEEE Journal of Selected Topics in Quantum Electronics* **26**, 1–10 (2020). Conference Name: IEEE Journal of Selected Topics in Quantum Electronics.

[232] Clément, A., Heurtel, N., Mansfield, S., Perdrix, S. & Valiron, B. LOv-Calculus: A Graphical Language for Linear Optical Quantum Circuits (2022). URL http://arxiv.org/abs/2204.11787. ArXiv:2204.11787 [quant-ph].

[233] Heurtel, N. A Complete Graphical Language for Linear Optical Circuits with Finite-Photon-Number Sources and Detectors (2024). URL http://arxiv.org/abs/2402.17693. ArXiv:2402.17693 [quant-ph].

[234] Natarajan, C. M., Tanner, M. G. & Hadfield, R. H. Superconducting nanowire single-photon detectors: physics and applications. *Superconductor Science and Technology* **25**, 063001 (2012). URL https://dx.doi.org/10.1088/0953-2048/25/6/063001. Publisher: IOP Publishing.

[235] Ceccarelli, F. *et al.* Recent Advances and Future Perspectives of Single-Photon Avalanche Diodes for Quantum Photonics Applications. *Advanced Quantum Technologies* **4**, 2000102 (2021). URL https://onlinelibrary.wiley.com/doi/abs/10.1002/qute.202000102. _eprint: https://onlinelibrary.wiley.com/doi/pdf/10.1002/qute.202000102.

[236] Renema, J. J. *et al.* Universal response curve for nanowire superconducting single-photon detectors. *Physical Review B* **87**, 174526 (2013). URL https://link.aps.org/doi/10.1103/PhysRevB.87.174526. Publisher: American Physical Society.

[237] Haldar, S., Sehrawat, A. & Balasubramanian, K. B. Modelling response time contrasts in superconducting nanowire single photon detectors (2024). URL http://arxiv.org/abs/2403.07299. ArXiv:2403.07299 [cond-mat].

[238] Yu, D. F. & Fessler, J. A. Mean and variance of single photon counting with deadtime. *Physics in Medicine & Biology* **45**, 2043 (2000). URL https://dx.doi.org/10.1088/0031-9155/45/7/324.

[239] Hutcheson, L. D., White, I. A. & Burke, J. J. Comparison of bending losses in integrated optical circuits. *Optics Letters* **5**, 276–278 (1980). URL https://opg.optica.org/ol/abstract.cfm?uri=ol-5-6-276. Publisher: Optica Publishing Group.